

A Study of Power Cycles Using Supercritical Carbon Dioxide as the
Working Fluid

by

Andrew Urban Schroder

Bachelor of Science, Mechanical Engineering, University of Cincinnati, 2007

Master of Science, Mechanical Engineering, University of Cincinnati, 2011

A thesis submitted to the
Faculty of the Graduate School of the
University of Cincinnati in partial fulfillment
of the requirements for the degree of
Doctor of Philosophy
Department of Aerospace Engineering
College of Engineering

Committee Chair: Dr. Mark Turner

Monday, March 14th, 2016 A.D.

©2016 Andrew Urban Schroder

Abstract

A real fluid heat engine power cycle analysis code has been developed for analyzing the zero dimensional performance of a general recuperated, recompression, precompression supercritical carbon dioxide power cycle with reheat and a unique shaft configuration. With the proposed shaft configuration, several smaller compressor-turbine pairs could be placed inside of a pressure vessel in order to avoid high speed, high pressure rotating seals. The small compressor-turbine pairs would share some resemblance with a turbocharger assembly. Variation in fluid properties within the heat exchangers is taken into account by discretizing zero dimensional heat exchangers. The cycle analysis code allows for multiple reheat stages, as well as an option for the main compressor to be powered by a dedicated turbine or an electrical motor. Variation in performance with respect to design heat exchanger pressure drops and minimum temperature differences, precompressor pressure ratio, main compressor pressure ratio, recompression mass fraction, main compressor inlet pressure, and low temperature recuperator mass fraction have been explored throughout a range of each design parameter. Turbomachinery isentropic efficiencies are implemented and the sensitivity of the cycle performance and the optimal design parameters is explored. Sensitivity of the cycle performance and optimal design parameters is studied with respect to the minimum heat rejection temperature and the maximum heat addition temperature. A hybrid stochastic and gradient based optimization technique has been used to optimize critical design parameters for maximum engine thermal efficiency. A parallel design exploration mode was also developed in order to rapidly conduct the parameter sweeps in this design space exploration. A cycle thermal efficiency of 49.6% is predicted with a 320 K [47°C] minimum temperature and 923 K [650°C] maximum temperature.

In addition to the recuperated, recompression, precompression supercritical carbon dioxide power cycle with reheat, the real fluid heat engine power cycle analysis code was expanded to

study a theoretical recuperated Lenoir cycle using supercritical carbon dioxide as the working fluid. There have been no prior studies of recuperated Lenoir cycles besides the present work. An ideal cycle thermal efficiency of 45.6% is predicted for the recuperated Lenoir cycle with a 320 K [47°C] minimum temperature and 923 K [650°C] maximum temperature.

The real fluid cycle analysis code was also enhanced to study a combined cycle engine cascade. Two engine cascade configurations were studied. The first consisted of a traditional open loop gas turbine, coupled with a series of recuperated, recompression, precompression supercritical carbon dioxide power cycles, with a predicted combined cycle thermal efficiency of 65.0% using a peak temperature of 1,890 K [1,617°C]. The second configuration consisted of a hybrid natural gas powered solid oxide fuel cell and gas turbine, coupled with a series of recuperated, recompression, precompression supercritical carbon dioxide power cycles, with a predicted combined cycle thermal efficiency of 73.1%. Both configurations had a minimum temperature of 306 K [33°C]. The hybrid stochastic and gradient based optimization technique was used to optimize all engine design parameters for each engine in the cascade such that the entire engine cascade achieved the maximum thermal efficiency. The parallel design exploration mode was also utilized in order to understand the impact of different design parameters on the overall engine cascade thermal efficiency.

Two dimensional conjugate heat transfer (CHT) numerical simulations of a straight, equal height channel heat exchanger using supercritical carbon dioxide were conducted at various Reynolds numbers and channel lengths. The Star-CCM+ computational fluid dynamics software suite was used with variable fluid properties. The results are compared to the zero dimensional heat exchanger model that was developed as part of the real fluid heat engine cycle analysis code. Highly unusual results due to the radically non-linear fluid properties are presented. The results indicate that if a heat exchanger is used with a long enough length that entrance effects are negligible, the zero dimensional heat exchanger model can be used to rapidly and accurately predict heat exchanger inlet and/or outlet enthalpy weighted average temperatures when a minimum heat exchanger temperature difference is specified, and that the zero dimensional heat exchanger model's results are appropriate for use in the real fluid heat engine power cycle analysis code. An additional simulation of heat transfer between channels at reduced pressure and increased temperature was conducted to demonstrate what a heat exchanger solution would look like in the absence of large fluid property variations.

Contact Information

Telephone (PSTN): +1.859.652.3582

Electronic Mail (SMTP): info@AndySchroder.com

Geographic Location: Fort Mitchell, KY, U.S.A.

PGP Public Key Fingerprint: 893F 9F58 D7AE CF9D F0F7 72F5 34FA EFDB 2D44 186B

PGP Public Key:

-----BEGIN PGP PUBLIC KEY BLOCK-----
Version: GnuPG v1.4.11 (GNU/Linux)

```
mQENBFD3HqABCADXMSjjwfbroE7n98HE5BSqqlSSnzzlIntr09o3c1wzNhAbUe+fg
w0YSLgoPIbjFmtXZAhTVhN6DftNeepl8Rg7SSDeK3F7CeZ0bVKf5LJQI438stzzK
GctPZ31m6XFqCktPV59pbGRt5M6x1RX38sheAJNrLv7aDDch04bS/yRkiNzOUPxw
2sINDz5klorCFKace9oxL8RK25zXickJdprRfbuyKPFve11Rsh5btHmV+D/KDD1y
iUapbkGEkCNrecdRyG144863RQ401GHb3j/HAXdtq1Lz9BFiaZxwQG1nBAXVD/x/
YmZvyXUD2j4WryHGCK7LLCxq/8irJ/1aDcMFABEBAAQJUFuZHkgU2Nocm9kZXIga
PGluZm9AQW5keVNjaHJvZGVyLmNvbT6JAT4EEwECACgFA1D3HqACGwMFCQ1mAYAG
CwkIBwMCBhUIAgkKCwQWAgMBAh4BAheAAAOJEDT679stRBhrezcIAL/2B44bfTdb
OiELHmuqdPYGJQo1jC3LQzUelIQFMkwyJfh8oRmKen8QcdWnuGGYdXFMS/zXcZwq
ERQ+nsnf1xnuYXbBK3I6/LdLHjZ8vYgB1erlGmB4quRuU/vYjCO57cfMdeyppq5yZ
Ww8h3iHkgj2y9CwOCq8je0tgJf28beDnv2c2GKzP6I/WccAzpppNkkccBZNb7H7S
Rc88o/Na5kc7Vd2nGK0xIiLU17ui0ylZP59f+wkGA10OpVwiBgLth1knjf9tXRNq
tzITyP019PHIs1Nwv7EP1/T5YMBcc0CrPjB1nCamowJXbxiwpeEQ0toBEH+NMr8ZP
16dWLnMqs4G5AQ0EUPceoAEIALSJqTfAJcTJA23kLsRmTpWSKaMxv58wj2F9GrEH
7GOJl14sNjQVVInfB6pfzK2+vRt3Eq2qNOMg2uS2StLgsLU7B7PyluMj3ALnyvcQ
NfzKNM6rdESxuCc/Faq9fVTMc95P4199hwx4DMKtSL2b9awtz1oHlOr/x/Awt1UL
j/i6kmI1pdGqdSmbTVg4hV6vH1PRXVhECKw5uAD0zMINomp/6Pyb6AgJuLSQBkmq
rhWC8M2vDM+K5uFXr1tIeymLfn+sbM/xwtTMXa/br9qw1FF40vv58qKR+mw7upMx
L9Q+hDvGrfhXGTfxTzoRBAUwbBDjVp5sd0FqihixXA8RQPsAEQEAAyKBJQYQAQIA
DwUCUPceoAIBDAUJCWYBgAAKCRAO+u/bLUQYa0KRB/45Czrrb8vVq5sQTn191bE6
gmPonMH0pyLLZr6NemqBC6WVh/IBkh8AUmXVLgJs70W2zQavemMGA58KifJYDu9y
oRDinyNcc9jB0oVh0iqzVH2IyY3aBr6CFGA5P9vo191apCPgz1hUXRqhK3bHiHbz
rPICNqEH+LI7Ds69AY19Ql1gG2Q2Ewpw+xs6JPvt2RfHCPhe/5N1zt5BTft0p2ed
0a8IYwtIRJkeXv/5sSYvVB5ZlMjvIjww/qc8MD/0ZiBKZ5tsadQsMKH/7o7uu+Ub
1QHk3x6QFGLo8B+sQQMgqHemJ/igSAuzQ2guAyRQSYu4TB9XtacAJSpuIA0tva/e
=T0y4
```

-----END PGP PUBLIC KEY BLOCK-----

Acknowledgements

I'd like to thank my advisor Dr. Mark Turner for his support throughout my time as a doctoral student. Mark's diverse viewpoints and technical interests have made this study possible. I'm grateful that Mark was willing to advise me on a topic that was completely new to the both of us, despite the fact that no financial support was able to be obtained during the entirety of the project. Being given the freedom to explore a completely new area has been proven to be rewarding experience. I'd like to also thank my committee members, Dr. Milind Jog and Dr. Shaaban Abdallah for reviewing my work and providing critical feedback on this thesis. I'd like to thank Dr. Rory Roberts for his help with the combined cycle that included a solid oxide fuel cell. Rory's expertise in fuel cells was invaluable and made that study possible. I'd like to thank CD-Adapco for providing a complementary academic license and technical support for their Star-CCM+ computational fluid dynamics package, which was used for the 2-D conjugate heat transfer simulations. I'd like to thank fellow doctoral students, Dr. Robert Knapke and (soon to be Dr.) Kiran Siddappaji for their technical feedback and advice along the way, as well as lively discussions on a variety of topics. Finally, I'd like to thank Rob Ogden for his excellent support and management of the computing cluster in the Gas Turbine Simulation Laboratory at U.C.. The expertise and computing tips and tricks that Rob has shared were an invaluable part of my education.

Contents

Abstract	iii
Contact Information	v
Acknowledgements	vi
Contents	ix
List of Figures	xiii
List of Tables	xxi
Nomenclature	xxiii
1 Introduction	1
1.1 Overview of Thermodynamic Cycles	1
1.2 Supercritical Carbon Dioxide Power Cycles	7
1.3 Layout of the Dissertation	9
2 A Recuperated, Recompression, Precompression Supercritical Carbon Dioxide Power Cycle with Intercooling, Improved Regeneration, and Reheat	11
2.1 Introduction	11
2.2 Prior Work	13
2.3 Methodology	14
2.3.1 Cycle Layout	14

2.3.2	Computer Code Overview	19
2.3.3	Real Fluid Heat Exchangers	25
2.3.4	Cycle Simulation	36
2.3.5	Design Exploration	37
2.4	Results	40
2.5	Conclusions and Recommended Future Work	67
3	A Closed Loop Recuperated Lenoir Cycle using Supercritical Carbon Dioxide	69
4	Combined Cycle Engine Cascades Achieving High Efficiency	83
4.1	Introduction	83
4.2	Methodology	84
4.2.1	Cycle Layouts	84
4.2.2	Fuel Cell and Combustion Chemistry	88
4.2.3	Cycle Analysis and Optimization	90
4.3	Results	92
4.3.1	Combined Cycle With Simple Gas Turbine	92
4.3.2	Combined Cycle With Fuel Cell	102
4.4	Conclusions	107
4.5	Recommended Future Work	108
5	Conjugate Heat Transfer With Supercritical Carbon Dioxide As the Working Fluid	111
5.1	Introduction	111
5.2	Problem Scope and Methodology	112
5.2.1	Details of Computational Tools Utilized	113
5.2.2	Flow Configuration and Simulation Setup	114
5.2.3	Post Processing	117
5.3	Results	118
5.3.1	Grid Dependency Studies	118
Laminar		119

Turbulent	124
5.3.2 Case I: High Pressure Inlet $Re_{D_h}=10$, Laminar, 1m Long	130
5.3.3 Case II: High Pressure Inlet $Re_{D_h}=50$, Laminar, 1m Long	138
5.3.4 Case III: High Pressure Inlet $Re_{D_h}=3,000$, Turbulent, 1m Long	144
5.3.5 Case IV: High Pressure Inlet $Re_{D_h}=4,000$, Turbulent, 1m Long	152
5.3.6 Case V: High Pressure Inlet $Re_{D_h}=3,000$, Turbulent, 10m Long	158
5.3.7 Case VI: High Pressure Inlet $Re_{D_h}=3,000$, Turbulent, 10m Long, Nearly Constant and Nearly Similar Specific Heats	165
5.4 Conclusions and Recommended Future Work	172
6 Conclusions and Recommended Future Work	175
References	179
Appendices	185
A Zero Dimensional Heat Exchanger Parameter Sweeps	185
A.1 Sweep ΔT_{min}	185
A.2 Sweep Mass Fraction	197
B Additional Conjugate Heat Transfer Results	209
B.1 Case I: High Pressure Inlet $Re_{D_h}=10$, Laminar, 1m Long	209
B.2 Case III: High Pressure Inlet $Re_{D_h}=3,000$, Turbulent, 1m Long	213

List of Figures

2.1	Specific Heat (c_p) vs Temperature at various Pressures for Carbon Dioxide. The blue line indicates the critical pressure of 7.4MPa.	12
2.2	Example System Layout Showing Two Low Temperature Recuperators - Temperature Entropy Diagram	15
2.3	Proposed Supercritical Carbon Dioxide Power Cycle Layout. There are four rotating shafts, three compressors, four turbines, and up to four recuperators.	15
2.4	Single Shaft Test Layout	19
2.5	Compressor and Turbine Isentropic Efficiency vs Pressure Ratio at Various Polytropic Efficiencies, and a Constant Ratio of Specific Heats of 1.3	24
2.6	Sample Heat Exchanger Solution	30
2.7	Sample heat exchanger solution with nearly constant and similar specific heats . . .	32
2.8	Sample heat exchanger solution with nearly constant but dissimilar heat capacities .	33
2.9	Sample heat exchanger solution where the heat exchanger is pinched at both ends .	34
2.10	Sample heat exchanger solution where the heat exchanger is pinched in the middle and at the high temperature end	34
2.11	Sample heat exchanger solution where the heat exchanger is pinched only at the low temperature end	35
2.12	Cycle Efficiency Percentage Point Increase Relative to Lowest Case vs Differential Evolution Optimizer Tolerance and Population Size	38
2.13	Temperature Entropy Diagram for the Proposed System Layout, Specific Heat at Constant Pressure Contour Level Background	43

2.14	Temperature Entropy Diagram for the Proposed System Layout, Density Contour Level Background	44
2.15	Temperature Entropy Diagram for the Proposed System Layout, Ratio of Specific Heat at Constant Pressure to the Specific Heat at Constant Volume Contour Level Background	45
2.16	Temperature Entropy Diagram for the Proposed System Layout, Compressibility Factor Contour Level Background	45
2.17	Temperature Entropy Diagram for the Proposed System Layout, Enthalpy Contour Level Background	46
2.18	Enthalpy Entropy Diagram for the Proposed System Layout, Temperature Contour Level Background	46
2.19	Pressure Specific Volume Diagram for the Proposed System Layout, Specific Heat at Constant Pressure Contour Level Background	47
2.20	Pressure Specific Volume Diagram for the Proposed System Layout, Entropy Contour Level Background	47
2.21	Pressure Specific Volume Diagram for the Proposed System Layout, Temperature Contour Level Background	48
2.22	Temperature Pressure Diagram for the Proposed System Layout, Specific Heat at Constant Pressure Contour Level Background	48
2.23	Cycle Efficiency vs Maximum and Minimum Temperature	50
2.24	Cycle Exergy Efficiency vs Maximum and Minimum Temperature	51
2.25	Optimal ReCompression Fraction vs Maximum and Minimum Temperatures	52
2.26	Optimal Main Compressor Outlet Pressure vs Maximum and Minimum Temperatures	52
2.27	Cycle Efficiency vs PreCompressor and Main Compressor Pressure Ratios	53
2.28	Cycle Efficiency vs PreCompressor and Main Compressor Pressure Ratios, With a Nearly Zero Heat Exchanger Minimum Temperature Difference	53
2.29	Optimal ReCompression Fraction vs PreCompressor and Main Compressor Pressure Ratios	54
2.30	Cycle Efficiency vs Heat Exchanger Minimum Temperature Difference	55
2.31	Cycle Efficiency vs ReCompression Fraction	56

2.32	Optimal Main Compressor Pressure Ratio vs ReCompression Fraction	56
2.33	Optimal PreCompressor Pressure Ratio vs ReCompression Fraction	57
2.34	Optimal Overall Pressure Ratio vs ReCompression Fraction	57
2.35	Cycle Efficiency vs Main Compressor Outlet Pressure	58
2.36	Optimal Main Compressor Pressure Ratio vs Main Compressor Outlet Pressure . . .	59
2.37	Optimal PreCompressor Pressure Ratio vs Main Compressor Outlet Pressure	59
2.38	Optimal Overall Pressure Ratio vs Main Compressor Outlet Pressure	60
2.39	Cycle Efficiency vs Main Compressor Isentropic Efficiency	61
2.40	Optimal Main Compressor Pressure Ratio vs Main Compressor Isentropic Efficiency	61
2.41	Optimal PreCompressor Pressure Ratio vs Main Compressor Isentropic Efficiency .	62
2.42	Optimal Recompression Fraction vs Main Compressor Isentropic Efficiency	62
2.43	Cycle Efficiency vs Power Turbine Isentropic Efficiency	63
2.44	Temperature Entropy Diagram for the System Layout Without Reheat	64
2.45	Temperature Entropy Diagram for the System Layout With Reheat	65
2.46	Temperature Entropy Diagram for the System Layout With Reheat and 2 InterTur- bine Reheat Stages	65
2.47	Temperature Entropy Diagram for the System Layout With Reheat and 5 InterTur- bine Reheat Stages	66
2.48	Cycle Efficiency vs Number of Reheat Stages	66
3.1	Constant Volume Heat Exchanger Concept	70
3.2	Lenoir Cycle - Efficiency, Maximum Pressure, Maximum Temperature, and Pressure Ratio vs Minimum Pressure	73
3.3	Recuperated Lenoir Cycle - Efficiency, Maximum Pressure, Maximum Temperature, and Pressure Ratio vs Minimum Pressure	74
3.4	Recuperated Lenoir Cycle - Temperature Entropy, contour background is $\gamma, c_p/c_v$.	75
3.5	Recuperated Lenoir Cycle - Temperature Entropy, contour background is Density .	76
3.6	Recuperated Lenoir Cycle - Temperature Entropy, contour background is Compress- ibility Factor	76
3.7	Recuperated Lenoir Cycle - Temperature Pressure, contour background is Density .	77

3.8	Recuperated Lenoir Cycle - Temperature Pressure, contour background is $\gamma, c_p/c_v$	77
3.9	Recuperated Lenoir Cycle - Pressure Specific Volume, contour background is $\gamma, c_p/c_v$	78
3.10	Recuperated Lenoir Cycle - Pressure Specific Volume, contour background is Compressibility Factor	78
3.11	Recuperated Lenoir Cycle - Pressure Specific Volume, contour background is Entropy	79
3.12	Recuperated Lenoir Cycle - Pressure Specific Volume, contour background is Temperature	79
4.1	Solid Oxide Fuel Cell integrated into a Brayton Cycle Engine	85
4.2	General Supercritical Carbon Dioxide Cycle	86
4.3	General Combined Cycle Engine Cascade with Solid Oxide Fuel Cell, Brayton Cycle, and Supercritical Carbon Dioxide Cycles	87
4.4	Combined Cycle With Simple Gas Turbine, All Engines: Temperature Entropy Diagram	93
4.5	Combined Cycle With Simple Gas Turbine, Engine Number 1: Brayton Cycle, Temperature Entropy Diagram	93
4.6	Combined Cycle With Simple Gas Turbine, Engine Number 2: $S - CO_2$ Cycle, Temperature Entropy Diagram with Specific Heat at Constant Pressure Contour Level Background	94
4.7	Combined Cycle With Simple Gas Turbine, Engine Number 3: $S - CO_2$ Cycle, Temperature Entropy Diagram with Specific Heat at Constant Pressure Contour Level Background	94
4.8	Combined Cycle With Simple Gas Turbine, Engine Number 4: $S - CO_2$ Cycle, Temperature Entropy Diagram with Specific Heat at Constant Pressure Contour Level Background	95
4.9	Combined Cycle Efficiency vs $S - CO_2$ Engine Peak Pressure	98
4.10	Combined Cycle Efficiency vs Topping Cycle Turbine Inlet Temperature at Various Ambient Temperatures	99
4.11	Combined Cycle Exergy Efficiency vs Topping Cycle Turbine Inlet Temperature at Various Ambient Temperatures	100

4.12	Combined Cycle Efficiency vs Total Number of Engines	101
4.13	Combined Cycle Efficiency vs Topping Cycle Compressor Isentropic Efficiency . . .	102
4.14	Combined Cycle With Fuel Cell, All Engines: Temperature Entropy Diagram	103
4.15	Combined Cycle With Fuel Cell, Engine Number 1: Hybrid Fuel Cell and Brayton Cycle, Temperature Entropy Diagram	103
4.16	Combined Cycle With Fuel Cell, Engine Number 2: $S - CO_2$ Cycle, Temperature Entropy Diagram with Specific Heat at Constant Pressure Contour Level Background	104
4.17	Combined Cycle With Fuel Cell, Engine Number 3: $S - CO_2$ Cycle, Temperature Entropy Diagram with Specific Heat at Constant Pressure Contour Level Background	104
5.1	Heat Exchanger Sketch	113
5.2	Heat Exchanger Boundary Conditions	115
5.3	Laminar Grid Dependency Study, Effectiveness vs Geometry Grid Levels at Various Fluid Property Grid Levels	120
5.4	Laminar Grid Dependency Study, Effectiveness vs Property Grid Levels at Various Geometry Grid Levels	120
5.5	Laminar Grid Dependency Study, Temperature Difference vs Position at Each Grid Level	122
5.6	Laminar Grid Dependency Study, Temperature Difference vs Position at Each Grid Level Normalized by Highest Resolution Case	123
5.7	Turbulent Grid Dependency Study, Effectiveness vs Geometry Grid Levels at Various Fluid Property Grid Levels	125
5.8	Turbulent Grid Dependency Study, Effectiveness vs Property Grid Levels at Various Geometry Grid Levels	125
5.9	Turbulent Grid Dependency Study, Temperature Difference vs Position at Each Grid Level	126
5.10	Turbulent Grid Dependency Study, Temperature Difference vs Position at Each Grid Level Normalized by Highest Resolution Case	127
5.11	Turbulent Grid Dependency Study, y^+ vs Position at Each Grid Level, Low Pressure Half Channel	128

5.12	Turbulent Grid Dependency Study, y^+ vs Position at Each Grid Level, High Pressure Half Channel	129
5.13	Case I: Reynolds Numbers and Average Dynamic Viscosities vs Length Position . .	131
5.14	Case I: Total Temperature Contours	132
5.15	Case I: Temperatures vs Length Position	133
5.16	Case I: Average Temperature Difference and Specific Heats vs Temperature on the Low Pressure Side	134
5.17	Case I: Heat Fluxes vs Length Position	135
5.18	Case I: Heat Transfer Coefficients and Average Thermal Conductivities vs Length Position	136
5.19	Case I: Average Gauge Total Pressures vs Length Position	137
5.20	Case I: Average Densities vs Length Position	137
5.21	Case II: Reynolds Numbers and Average Dynamic Viscosities vs Length Position . .	139
5.22	Case II: Temperatures vs Length Position	140
5.23	Case II: Average Temperature Difference and Specific Heats vs Temperature on the Low Pressure Side	141
5.24	Case II: Heat Fluxes vs Length Position	142
5.25	Case II: Heat Transfer Coefficients and Average Thermal Conductivities vs Length Position	143
5.26	Case III: Reynolds Numbers and Average Dynamic Viscosities vs Length Position . .	145
5.27	Case III: Total Temperature Contours	146
5.28	Case III: Temperatures vs Length Position	147
5.29	Case III: Average Temperature Difference and Specific Heats vs Temperature on the Low Pressure Side	148
5.30	Case III: Heat Fluxes vs Length Position	149
5.31	Case III: Heat Transfer Coefficients and Average Thermal Conductivities vs Length Position	150
5.32	Case III: Average Gauge Total Pressures vs Length Position	151
5.33	Case III: Average Densities vs Length Position	151
5.34	Case IV: Reynolds Numbers and Average Dynamic Viscosities vs Length Position . .	153

5.35 Case IV: Average Temperature Difference and Specific Heats vs Temperature on the Low Pressure Side	154
5.36 Case IV: Heat Fluxes vs Length Position	155
5.37 Case IV: Heat Transfer Coefficients and Average Thermal Conductivities vs Length Position	156
5.38 Case IV: Average Gauge Total Pressures vs Length Position	157
5.39 Case V: Reynolds Numbers and Average Dynamic Viscosities vs Length Position . .	159
5.40 Case V: Temperatures vs Length Position	160
5.41 Case V: Average Temperature Difference and Specific Heats vs Temperature on the Low Pressure Side	161
5.42 Case V: Heat Fluxes vs Length Position	162
5.43 Case V: Heat Transfer Coefficients and Average Thermal Conductivities vs Length Position	163
5.44 Case V: Average Gauge Total Pressures vs Length Position	164
5.45 Case V: Average Densities vs Length Position	164
5.46 Case VI: Reynolds Numbers and Average Dynamic Viscosities vs Length Position .	166
5.47 Case VI: Temperatures vs Length Position	167
5.48 Case VI: Average Temperature Difference and Specific Heats vs Temperature on the Low Pressure Side	168
5.49 Case VI: Heat Fluxes vs Length Position	169
5.50 Case VI: Heat Transfer Coefficients and Average Thermal Conductivities vs Length Position	170
5.51 Case VI: Average Gauge Total Pressures vs Length Position	171
5.52 Case VI: Average Densities vs Length Position	171
A.1 Sample Heat Exchanger Solution, $\Delta T_{min} = 0K$	186
A.2 Sample Heat Exchanger Solution, $\Delta T_{min} = 5K$	187
A.3 Sample Heat Exchanger Solution, $\Delta T_{min} = 10K$	188
A.4 Sample Heat Exchanger Solution, $\Delta T_{min} = 15K$	189
A.5 Sample Heat Exchanger Solution, $\Delta T_{min} = 20K$	190

A.6	Sample Heat Exchanger Solution, $\Delta T_{min} = 25K$	191
A.7	Sample Heat Exchanger Solution, $\Delta T_{min} = 30K$	192
A.8	Sample Heat Exchanger Solution, $\Delta T_{min} = 35K$	193
A.9	Sample Heat Exchanger Solution, $\Delta T_{min} = 40K$	194
A.10	Sample Heat Exchanger Solution, $\Delta T_{min} = 45K$	195
A.11	Sample Heat Exchanger Solution, $\Delta T_{min} = 50K$	196
A.12	Sample Heat Exchanger Solution, Mass Fraction=0.1	198
A.13	Sample Heat Exchanger Solution, Mass Fraction=0.2	199
A.14	Sample Heat Exchanger Solution, Mass Fraction=0.3	200
A.15	Sample Heat Exchanger Solution, Mass Fraction=0.4	201
A.16	Sample Heat Exchanger Solution, Mass Fraction=0.5	202
A.17	Sample Heat Exchanger Solution, Mass Fraction=0.6	203
A.18	Sample Heat Exchanger Solution, Mass Fraction=0.7	204
A.19	Sample Heat Exchanger Solution, Mass Fraction=0.8	205
A.20	Sample Heat Exchanger Solution, Mass Fraction=0.9	206
A.21	Sample Heat Exchanger Solution, Mass Fraction=1.0	207
B.1	Case I: Specific Heat Contours	210
B.2	Case I: Total Pressure Contours	210
B.3	Case I: Density Contours	211
B.4	Case I: Axial Velocity Contours	211
B.5	Case I: Dynamic Viscosity Contours	212
B.6	Case III: Specific Heat Contours	214
B.7	Case III: Total Pressure Contours	214
B.8	Case III: Density Contours	215
B.9	Case III: Axial Velocity Contours	215
B.10	Case III: Dynamic Viscosity Contours	216

List of Tables

2.1	Summary of State Points	16
2.2	Default Component Performances and Allowable Design Ranges	41
2.3	Optimized Cycle Independent and Dependent Variables	41
4.1	Work Split and Efficiencies: Combined Cycle	95
4.2	Selected Temperatures: Combined Cycle	95
4.3	Work Split and Efficiencies: Combined Cycle With Fuel Cell	105
4.4	Selected Temperatures: Combined Cycle With Fuel Cell	105
5.1	2-D Heat Transfer Cases	117
5.2	Fluid Property Grid I	119
5.3	Geometry Grids	119
5.4	Fluid Property Grid II	166

Nomenclature

ΔT	temperature difference between a heat exchanger's cooled and heated sides $(T_{Cooled} - T_{Heated}), K$
ΔT_{min}	heat exchanger minimum temperature difference, K
\dot{m}_{Cooled}	mass flow rate of a heat exchanger's cooled fluid, kg/s
\dot{m}_{Heated}	mass flow rate of a heat exchanger's heated fluid, kg/s
ϵ	heat exchanger effectiveness
η	thermal/first law efficiency
η_c	compressor isentropic efficiency
η_e	exergy/second law efficiency
η_t	turbine isentropic efficiency
η_{Carnot}	efficiency of a Carnot cycle
γ	ratio of specific heats, c_p/c_v
μ_0	fluid reference viscosity, $kg/(m * s)$
ϕ	fraction of desired heat transferred
c_p	specific heat at constant pressure, $J/(kg * K)$
C_{Cooled}	specific heat at constant pressure of a heat exchanger's cooled fluid, based on the mass flow rate of the heat exchanger's cooled fluid, $J/(kg * K)$
C_{Heated}	specific heat at constant pressure of a heat exchanger's heated fluid, based on the mass flow rate of the heat exchanger's cooled fluid, $J/(kg * K)$
$c_{p,Cooled}$	specific heat at constant pressure of a heat exchanger's cooled fluid, $J/(kg * K)$
$c_{p,Heated}$	specific heat at constant pressure of a heat exchanger's heated fluid, $J/(kg * K)$
d	heat exchanger pressure drop coefficient, Pa/K

e_c	compressor polytropic efficiency
e_t	turbine polytropic efficiency
h	total enthalpy, J/kg
$h_{i,Cooled}$	total enthalpy of a heat exchanger's cooled fluid, at the heat exchanger cooled side inlet, J/kg
$h_{i,Heated}$	total enthalpy of a heat exchanger's heated fluid, at the heat exchanger heated side inlet, J/kg
h_i	total enthalpy at a turbomachine inlet, J/kg
$h_{o,Cooled}$	total enthalpy of a heat exchanger's cooled fluid, at the heat exchanger cooled side outlet, J/kg
$h_{o,Heated}$	total enthalpy of a heat exchanger's heated fluid, at the heat exchanger heated side outlet, J/kg
$h_{o,max,Heated}$	maximum possible total enthalpy of a heat exchanger's heated fluid, at the heat exchanger heated side outlet, J/kg
$h_{o,min,Cooled}$	minimum possible total enthalpy of a heat exchanger's cooled fluid, at the heat exchanger cooled side outlet, J/kg
h_o	total enthalpy at a turbomachine outlet, J/kg
$h_{p,Cooled}$	total enthalpy of a heat exchanger's cooled fluid, at the heat exchanger pinch point, J/kg
$h_{p,Heated}$	total enthalpy of a heat exchanger's heated fluid, at the heat exchanger pinch point, J/kg
p	total pressure, Pa
p_i	turbomachine inlet total pressure, Pa
p_o	turbomachine outlet total pressure, Pa
$p_{i,Cooled}$	total pressure of a heat exchanger's cooled fluid, at the heat exchanger cooled side inlet, Pa
$p_{i,Heated}$	total pressure of a heat exchanger's heated fluid, at the heat exchanger heated side inlet, Pa
$p_{p,Cooled}$	total pressure of a heat exchanger's cooled fluid, at the heat exchanger pinch point, Pa

$p_{p,Heated}$	total pressure of a heat exchanger's heated fluid, at the heat exchanger pinch point, Pa
PR_c	compressor pressure ratio, p_o/p_i
PR_t	turbine expansion pressure ratio, p_i/p_o
Q_{in}	input energy, J/kg
Q_{out}	unusable waste heat energy output, J/kg
S	Sutherland constant, K
s	entropy, J/kg
s_i	turbomachine inlet entropy, J/kg
T	total temperature, K
T_0	fluid reference temperature, K
T_c	Temperature of the cold reservoir, K
T_h	Temperature of the hot reservoir, K
T_i	turbomachine inlet total temperature, K
T_o	turbomachine outlet total temperature, K
T_{Cooled}	heat exchanger cooled side temperature, K
T_{Heated}	heat exchanger heated side temperature, K
$T_{i,Cooled}$	total temperature of a heat exchanger's cooled fluid, at the heat exchanger cooled side inlet, K
$T_{i,Heated}$	total temperature of a heat exchanger's heated fluid, at the heat exchanger heated side inlet, K
$T_{o,Cooled}$	total temperature of a heat exchanger's cooled fluid, at the heat exchanger cooled side outlet, K
$T_{o,Heated}$	total temperature of a heat exchanger's heated fluid, at the heat exchanger heated side outlet, K
$T_{p,Cooled}$	heat exchanger pinch temperature of the cooled fluid, K
$T_{p,Heated}$	heat exchanger pinch temperature of the heated fluid, K
W	compressor or turbine work, J/kg
W_{out}	work output, J/kg

Chapter 1

Introduction

1.1 Overview of Thermodynamic Cycles

Extracting mechanical work from heat or chemical energy is one of the prominent engineering challenges in today's society. A number of solutions exist with different power density, fuel efficiency, fuel cost, and component capital and maintenance costs. Each solution in widespread use today provides a balance of these costs. The second law of thermodynamics limits the amount of energy that can be extracted and the Carnot cycle is a heat engine cycle that illustrates the maximum amount of energy that can be extracted due to the second law of thermodynamics by a heat engine. The thermal efficiency¹, or first law efficiency is a quantification of how much mechanical energy (or work) can be extracted from energy in another form (such as heat or chemical energy). This relationship can be represented as:

$$\eta = \frac{W_{out}}{Q_{in}} = \frac{Q_{in} - Q_{out}}{Q_{in}} = 1 - \frac{Q_{out}}{Q_{in}} \quad (1.1)$$

The efficiency of the Carnot cycle is dependent on the temperature that heat is added and rejected from the system. The Carnot cycle features an isothermal heat addition phase where the gas is allowed to expand during heating, an adiabatic isentropic expansion phase where useful work is extracted, an isothermal heat rejection phase where the gas is compressed during cooling, and an

¹It's important to clarify that anywhere in this text where the word "efficiency" is used by itself is meant to refer to the "thermal efficiency" unless prefixed with a modifier.

adiabatic isentropic work input phase where the gas is further compressed to the higher temperature. For a cycle with these four steps of a Carnot cycle, conservation of energy and the second law of thermodynamics require that:

$$\eta_{Carnot} = 1 - \frac{T_c}{T_h} \quad (1.2)$$

Another metric, known as the exergy efficiency, or second law efficiency is used to quantify how high a cycle's thermal efficiency is to that of the maximum allowable by the second law of thermodynamics. For heat engines, this is the cycle's efficiency relative to a Carnot cycle operating with the same minimum and maximum temperatures. The exergy efficiency for a heat engine can be represented by:

$$\eta_e = \frac{\eta}{\eta_{Carnot}} \quad (1.3)$$

The design and physical construction of a real, low cost, high power heat engine that closely approximates a Carnot cycle proves to be a difficult task. The most common heat engines used today employ the Rankine cycle, the Brayton cycle, the Diesel cycle, and the Otto cycle. Depending on the application, variations of each of these basic cycles are used in order to obtain higher power densities, higher thermal efficiencies, better off design operation, quicker power output variation, and lower engine capital costs and complexity.

The Rankine cycle is a type of engine that usually operates with water in a closed loop as its working fluid. At the low temperature portion of the cycle, water is in a liquid form. The water is compressed to a higher pressure, with negligible change in volume, and a small amount of work input (typical back work ratios of $\sim 1\%$ [1]). The high pressure water is then heated using an external heat source. It is boiled, and at an elevated temperature a gaseous or supercritical water is then expanded through a turbine. The turbine extracts energy from the fluid and converts it to shaft work, which is often used to power an electrical generator. After expanding through a turbine, the water vapor is then cooled and condensed back to a liquid.

With water as their working fluid, Rankine cycles must operate at very high pressure ratios in order to have a high average heat addition temperature and a low average heat rejection temperature due to the boiling and condensation, which accept and reject most (but not all) of the heat at a

nearly constant temperature. The compressor pressure ratio can be on the order of 1000[1]. The high pressure ratio is required in order to allow for higher average heat addition temperatures and as much work to be extracted during expansion as possible, without condensing the water. The pressure ratio and maximum engine temperature are limited by material structural limitations. Because the temperature rise during compression is low and the temperature is limited due to the high system pressures, the average temperature of heat addition in a Rankine cycle engine can be fairly low. The minimum heat addition temperature can be risen some by employing a flow split during the expansion process and using some unexpanded fluid as a preheater, but this approach has its limitations in how much preheating can be done.

When powered by the combustion of a fossil fuel such as coal, the burner increases in efficiency as the burner exhaust temperature decreases, because more energy has been extracted from the air and combustion by-products. With the low boiler inlet temperatures in a Rankine cycle, the burner is fairly efficient without the need for a regenerator. A major strength of the Rankine cycle is that it is externally combusted and used with low cost solid fuels such as coal. The Rankine cycle is also used with other heat sources such as solar and nuclear.

Rankine cycle engines powered by coal and have efficiencies advertised up to 46% [2]. Maximum pressures can be above the critical pressure of water of 22.1 MPa. Minimum pressures are typically below standard atmospheric pressure in order to suppress the boiling/condensation temperature and allow for more work to be extracted in the turbine. Condensation in a turbine typically destroys a turbine due to erosion. The turbine exit temperature is limited by this condensation temperature. The minimum cycle heat rejection temperature is determined by the ambient temperature where the engine is is being operated. This can vary significantly based on geographic location and elevation. Peak temperature are presently limited to ~ 873 K [600°C] at peak operating pressures of 25-29 MPa for these large systems[1, 3, 4].

The Brayton cycle is a type of engine that is often designed to be in an open loop configuration where air from the atmosphere is used as the working fluid. After the air from the atmosphere is ingested into the engine, it is compressed and the temperature rises and the density reduces. There is typically a large amount of work done on the air during this compression process (typical back work ratios of 40% to 80%). After being compressed, a fuel is injected into the engine and burned in a combustion chamber. Brayton cycle engines normally uses natural gas, diesel fuel, jet fuel, or

kerosene as their fuel source. After combustion, the temperature has risen. The high temperature air and combustion by-products are then expanded through a turbine. Some or all of the energy extracted by the turbine is then directed to power the compressor used to initially elevate the pressure of the air before being heated. If the engine is used for propulsion, some additional energy may be extracted using a turbine to power a fan for propulsion, and the remaining fluid is then accelerated through an exhaust nozzle to use for propulsion. If the engine is used for land or marine power generation, the remaining energy is then extracted using the turbine and then decelerated and exhausted back the atmosphere at a medium temperature.

Brayton cycle engines are typically smaller than Rankine cycle engines and because they are internally combusted, have less inertia and heat capacity and are therefore faster to start and change their power output than Rankine cycle engines. As with the Rankine cycle, the minimum cycle temperature is determined by the ambient temperature where the engine is being operated. Internal combustion results in a high burner efficiency. Efficiencies are advertised up to 44% for a simple cycle [5].

For the Brayton cycle, the cycle pressure ratio can vary from 9.8[6] to 42[7] depending on the design configuration (the pressure can be as high as 4.3 MPa (42 standard atmospheres)). Because of the much larger density change during the compression process, more work is done during compression and the temperature rises much higher than in a Rankine cycle. As a result, the pressure ratio is limited in order to obtain reasonable work output from the engine and maintain operation below the melting point of the materials and cooling technologies used in the hot sections. Brayton cycle engines do typically employ higher temperature materials than Rankine cycle engines. The higher temperature materials and lower operating pressures, coupled with the high combustor inlet temperature result in higher average heat addition temperatures than Rankine cycles which results in higher cycle efficiencies at higher ambient temperatures. They have peak temperature limited to $\sim 1,900$ K [1,627°C].

In the Brayton cycle with a much lower compression ratio than the Rankine cycle, the reasonably high temperature air and combustion products that are exhausted to the atmosphere still have some usable energy. A recuperator can be used to transfer some of this energy from the low pressure air to the high pressure air, however, the density of the air at the exit of the turbine is usually very low, requiring a very large heat exchanger, which is not ideal for propulsion applications. For land

based applications, rather than using a recuperator, instead the exhaust gases are typically used to power a Rankine cycle, whose maximum temperature is ideally suited for the gas turbine exhaust temperature. Combined cycles allow for utilization of high temperature heat at lower pressures and lower temperature heat at high pressure, balancing material operating conditions and stresses. In this combined cycle configuration, the heat is added at a much higher average temperature and rejected at a much lower average temperature. Combined cycle engine efficiencies of slightly less than 62% are advertised for the lower heating value of the engine's fuel[8, 9].

The Otto cycle is an open loop engine configuration that is typically used with positive displacement pistons. The fuel is usually gasoline, natural gas, propane, methanol, or ethanol. The Otto cycle's strengths are its low cost, simple components, moderate power density, and rapid startup, changes in engine speeds, and changes in power output. Otto cycle engines are typically the smallest engine type used in industry today.

The ideal Otto cycle features an adiabatic compression process, followed by a constant volume heat addition process, then an adiabatic expansion process, followed by a constant volume cooling process. In a real, open loop Otto cycle engine, an air-fuel mixture is ingested from the atmosphere to be compressed. In order to avoid autoignition during the compression process, compression ratio is typically limited to 13 with high octane fuels. Once the compression is complete, the constant volume heating process occurs when the air-fuel mixture is ignited using a spark plug. After the expansion stroke, the combustion by-products are then exhausted to the atmosphere and the cycle repeats.

The thermal efficiency of the Otto cycle is limited because of its pressure ratio limitation, but is widely used because of its reasonable power density, lower cost (because of the lower pressure ratios involved there are lower stresses involved and therefore thinner components can be used), and because of the availability of gasoline, which is produced at fixed proportions along with other products during the refinement of crude oil. Because of the low pressure ratio, the efficiency is much lower than the Brayton and Rankine cycles. Because of the use of pistons the power density is lower than that of a Rankine and Brayton cycle, and the noise to power ratio is higher. As a result, Otto cycle engines are normally only used for automobile, small aviation, small marine, small utility, and small backup electrical power, and therefore are several orders of magnitude smaller than the Rankine and Brayton cycle engines.

The Diesel cycle is an open loop engine configuration that is typically used with positive displacement pistons. The fuel is usually diesel fuel, kerosene, jet fuel, or biodiesel. The ideal Diesel cycle features an adiabatic compression process, followed by a constant pressure heat addition process, followed by an adiabatic expansion process, followed by a constant volume cooling process. In a real, open loop Diesel cycle engine, air is ingested from the atmosphere to be compressed. During compression, the air is heated. Compression ratios in Diesel cycle engines are typically 16 to 22. After compression, the fuel is injected into the high pressure, high temperature chamber and spontaneously ignites and burns as it is pumped into the chamber. As the fuel burns, the piston moves and maintains a fairly constant pressure. After the fuel completes burning, the piston continues to move. After the expansion process is complete, the combustion by-products are then exhausted to the atmosphere and the cycle repeats.

The Diesel cycle's strengths are its high thermal efficiency relative to the Otto cycle due to the higher pressure ratio, quick startup and changes in engine speeds and power output. Diesel fuel also has a higher volumetric energy density and longer term storage stability than gasoline. The Diesel cycle typically results in engines that produce more torque at lower speeds than Otto cycle engines and are therefore applicable to higher loads without the need for as high of gear ratios. Diesel cycle engines also normally result in more linear power curves with operating speed than Otto cycle engines. The Diesel cycle is a natural complement to the Otto cycle because it presents a use for other products of crude oil refinement. Diesel cycle engines normally have a lower power density than Otto cycle engines because of their high compression ratio (less energy input per unit mass), while using the same working fluid (air). Diesel cycle engines also typically produce more noise than Otto cycle engines. Diesel cycle engines are normally used for freight, automobile, marine, utility, building backup electrical power, and small isolated electrical power grids, and are therefore usually several orders of magnitude smaller than the Rankine and Brayton cycle engines. A large Diesel cycle engine can be several orders of magnitude larger than a small Otto cycle engine.

It's important to note that Diesel fuel will not work in Otto cycle engine because autoignition will occur too fast at a low temperature and pressure. Gasoline will not work in a Diesel cycle engine because autoignition occurs too slow at a high temperature and pressure. Therefore, it's important to have engines that can use both fuels.

In addition to the four major cycles, the Rankine, Brayton, Otto, and Diesel cycles, other

cycles worth noting, although not currently in mass use, are the Humphrey and Ericsson cycles. The Humphrey cycle is an idealization of a modification of an internally combusted, open loop Brayton cycle engine where the combustion and heat addition occur at approximately constant volume during a pulse detonation process, rather than a constant pressure combustion process. This constant volume heating results in a higher efficiency because the pressure rises further and the temperature rises more quickly. Engines utilizing the Humphrey cycle are not in widespread use and the cycle is still in a research and development phase.

The Ericsson cycle is an idealization of a recuperated Brayton cycle with an infinite number of intercooling stages during cooling and compression and reheat stages during heat addition and expansion. With these infinite number of intercooling and reheat stages, the cycle results in isothermal heat addition and isothermal heat rejection and has an ideal efficiency equal to that of a Carnot cycle. Because infinite intercooling and reheat is not possible, the Ericsson cycle is more of a theoretical cycle, but does motivate the use of more intercooling and reheat in the design and construction of Brayton cycle engines.

Fuel cells can utilize natural gas as a fuel and produce work in the form of direct current electricity. Fuel cells are different from Brayton, Rankine, and supercritical carbon dioxide cycles in that they are a chemical process rather than a heat engine. Fuel cells can have an efficiency of 52% operating below 1,273 K [1,000°C]. Fuel cells are still an emerging technology. The world's largest fuel cell power plant is currently 59MW, in Hwasung City, South Korea [10, 11]. Platzer et al. presented a combined cycle utilizing hydrogen and pure oxygen as the fuel with a hydrogen fuel cell that produces 74% thermal efficiency[12].

1.2 Supercritical Carbon Dioxide Power Cycles

Closed loop Brayton cycles utilizing Supercritical CO₂ (S-CO₂) as their working fluid have gained interest in recent years for electrical power generation due to potentially high real cycle thermal efficiencies. The high efficiencies of closed loop Supercritical CO₂ Brayton cycles may be possible because operation with the compression phase near the critical point results in a cycle that possesses favorable qualities of both the closed loop water Rankine Cycle and the traditional open loop air Brayton Cycle. Design of such cycles requires complex analysis to consider completely real fluid

property variations, which are a function of both temperature and pressure.

The S-CO₂ Brayton cycle features low compression work (low back work ratio) when compared to a traditional open loop air Brayton cycle. The lower back work ratio results in a decreased sensitivity of compressor isentropic efficiency (and the isentropic efficiency of the turbine(s) that drive(s) the compressor) on the cycle efficiency. Non-condensing cycles have a narrow heat addition and heat rejection temperatures that does not require evaporative cooling, but still approximates a Carnot cycle better than an open loop Brayton cycle. Because the S-CO₂ Brayton cycle does not have to reject latent heat of vaporization at a constant temperature, more recuperation is possible and the cycle is more appropriate for dry cooling in hot climates than traditional closed loop water Rankine cycles because more of the heat can be rejected at higher temperatures. Proposed S-CO₂ cycles are typically recuperated cycles which also results in a much lower pressure ratio than an unrecuperated cycle. Unrecuperated cycles need higher pressure ratios in order to be efficient because if the pressure ratio is too low, too much energy will not be extracted by the turbine(s) and will be wasted. Recuperated cycles can have lower pressure ratios because they are able to recover energy that is not extracted by the turbine(s) and transfer it back to the high pressure side of the cycle. CO₂ is a gas of choice because it is cheap, inert, non-toxic, and its critical temperature of 304K (31°C) is near ambient temperature, ~294K (21°C). In addition, the S-CO₂ Brayton cycle features high power densities due to the high fluid density that occurs because of the high pressures throughout the cycle and the high molecular weight of CO₂ when compared to water or air.

It's important to recognize that supercritical carbon dioxide power cycles have not seen the incremental growth as many of the other popular engine types that have been just discussed. Because supercritical carbon dioxide power cycles require such a high pressures to be of any benefit, in the past it hasn't been possible to design and test devices that could withstand these pressure and temperature ranges. Incremental technological advancements in Rankine and Brayton cycle engines that have occurred over many decades that have begun to approach the required pressure ranges of supercritical carbon dioxide power cycles have helped to make them a reality. Additionally, the increased capability of computationally based cycle and component design considering the highly non-linear fluid properties of supercritical carbon dioxide has also helped to make the technology not so distant.

Possible applications for S-CO₂ engines include base load terrestrial electrical power generation,

marine, aviation, and spacecraft electrical power generation. A S-CO₂ engine could be configured as a bottoming cycle using waste heat from a traditional open loop gas turbine (traditional Brayton cycle) or as a primary cycle with nuclear and solar energy heat sources.

1.3 Layout of the Dissertation

All of the engine cycles discussed have specific application and energy (fuel) source niches that they serve or attempt to serve based on their strengths and weaknesses. The remainder of this work aims to explore the potential performance and applications of new types of cycles that use Supercritical Carbon Dioxide as the working fluid, and understand how these new cycles may compliment, replace, or change the way existing cycles are used. Chapter 2 focuses on the design of a stand alone Recuperated, Recompression, Precompression Supercritical Carbon Dioxide Power Cycle with Intercooling, Improved Regeneration, and Reheat. Chapter 3 takes a look at a theoretical closed recuperated Lenoir cycle using supercritical carbon dioxide that utilizes a constant volume heating process. In search of higher efficiency than the stand alone Recuperated, Recompression, Precompression Supercritical Carbon Dioxide Power Cycle with Intercooling, Improved Regeneration, and Reheat, Chapter 4 proposes and investigates two combined cycle configurations using supercritical carbon dioxide power cycles in place of a traditional Rankine bottoming cycle. The first combined cycle configuration considers a traditional Brayton cycle engine as its topping cycle. In an effort to obtain even higher efficiencies, the second combined cycle configuration considers the use of a hybrid topping cycle that is composed of a Brayton cycle engine and a fuel cell. Because of the critical role of heat exchangers in supercritical carbon dioxide power cycles, Chapter 5 takes a step back and looks at some fundamental analysis of conjugate heat transfer between two supercritical carbon dioxide fluid streams separated by a solid wall.

Chapter 2

A Recuperated, Recompression, Precompression Supercritical Carbon Dioxide Power Cycle with Intercooling, Improved Regeneration, and Reheat

2.1 Introduction

Although there are many potential advantages of S-CO₂ Brayton cycles, design, development, and testing of the appropriate turbomachinery proves to be a very challenging task. The critical pressure of carbon dioxide is 7.4 MPa. The high pressures required for operation near the critical point results in increased structural loading of components, as well as very high working fluid densities. High working fluid densities result in significantly smaller turbomachinery that must be operated at higher speeds than most familiar turbomachinery and prohibit efficient low power, low speed, low cost prototypes to be developed. These high speed requirements inhibit ease of testing of small turbomachinery and small S-CO₂ Brayton cycles. Strong property gradients near the critical point present additional design challenges due to the variation in fluid properties within the turbomachinery components. Figure 2.1 illustrates the non-linearity of the specific heat of carbon dioxide near the critical point at different temperatures and pressures. Figure 2.1 was created using

REFPROP’s Graphical User Interface [13]. Off design operation subjects the turbomachinery to very different inlet conditions. This presents an additional difficulty in developing appropriate technologies that can operate efficiently and stall free throughout a wider operating range and utilize the lower heat rejection temperatures possible with variations in ambient air temperature with time of day, season, and geographic location. These lower heat rejection temperatures could result in a higher cycle efficiency. These challenges are particularly strong in the main compressor which operates near, or at the critical point of CO₂.

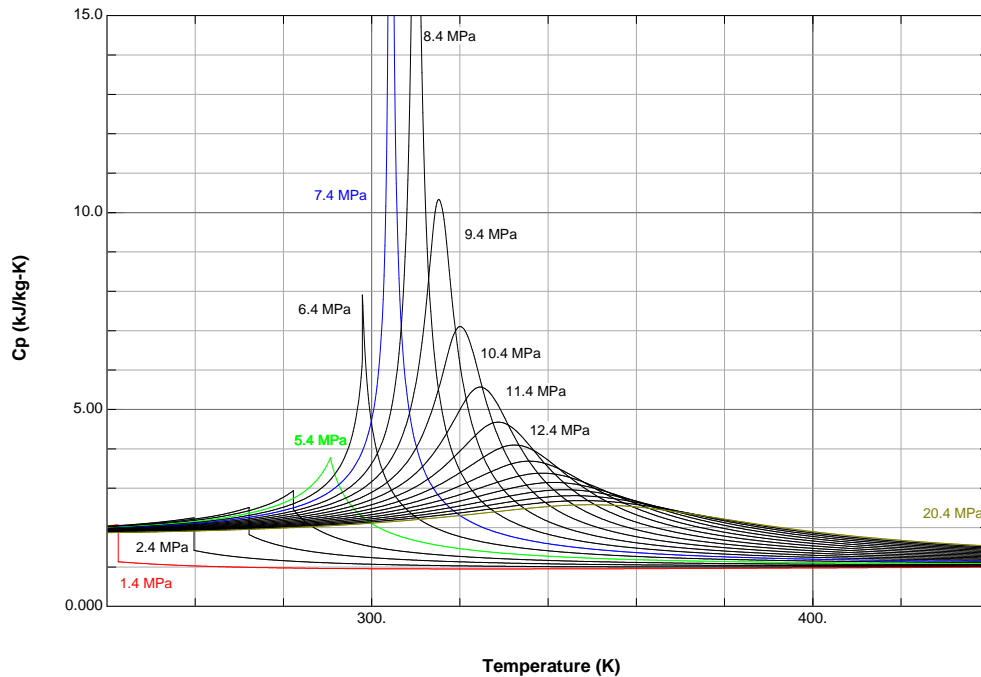


Figure 2.1: Specific Heat (c_p) vs Temperature at various Pressures for Carbon Dioxide. The blue line indicates the critical pressure of 7.4MPa.

The high pressures also present increased structural loading and seal leakage issues, which are even more challenging due to the high operating speeds. Nonlinear specific heat mismatch between the high and low pressure sides of the cycle causes limitations exchanging heat between high and low pressure sides, particularly at lower temperatures and increased complexity in modeling and optimizing the cycle layout. The closed loop design presents additional system complexities.

Because of all of these design challenges, it is important to establish a well directed development process in order to have a successful and efficient maturity of the components and system. This work investigates the impact of system layout, component efficiency, and operating conditions on

sizing of the components in the system and the overall system efficiency. Due to the highly variable fluid properties the sensitivity of component efficiencies will change at different operating conditions. As a result, as cycle layout and component sizes change, the sensitivity of the component efficiencies will also change. Understanding these relationships is important during design and testing because it helps impact the overall direction of the development process. For example, a development engine's layout, components, and overall performance may be radically different from what is targeted for a production engine. One may choose to design an engine with a lower overall performance in order to focus on the design and testing of a particular component that could be installed in a completely different size production engine. One may also design and build components of lower efficiency and different performance than a production engine, just to test an overall cycle layout.

2.2 Prior Work

The earliest reference to a supercritical carbon dioxide power cycle is that of a patent by Sulzer in 1948[14]. Among other efforts within the 1900s, studies conducted by Angelino[15, 16] and Feher[17] in the 1960s were significant contributors to the field. Vaclav Dostal revived interest in supercritical carbon dioxide power cycles with the publication of his doctoral dissertation in 2004[18]. Dostal reviewed and compared a number of cycles and layouts, and primarily analyzed a simple recuperated S-CO₂ cycle with reheat and intercooling and a simple recompression S-CO₂ cycle in his dissertation. He explored heat exchanger volumes and pressure drops in the simple and recompression cycles. Dostal researched application specifics, economic analysis, plant layouts, and control schemes for use of the recompression cycle with nuclear reactors.

Sandia National Laboratories has developed two supercritical CO₂ test rigs with their contractor, Barber-Nichols. Their efforts were initially motivated by nuclear power applications. Sandia's two test rigs have included both a simple S-CO₂ cycle and a recompression S-CO₂ cycle. They have successfully achieved startup of both a main compressor/turbine and recompressor/turbine loop. Their rigs have incorporated turbine alternator/generator compressor assemblies which has limited their operating speeds to that of the maximum speed of the alternator/generator[19, 20]. Bechtel Marine Propulsion Corporation has also been constructing and operating a similar test rig to that of Sandia's[21].

Echogen Power Systems has been developing an engine for waste heat recovery applications since 2007[22]. The United States Department of Energy began subsidizing the development of engines for concentrating solar power applications in mid 2012[23, 24, 25].

2.3 Methodology

2.3.1 Cycle Layout

The layout for the most general cycle considered is shown in Figure 2.2 and a summary of the state points is shown in Table 2.1. Figure 2.3 is a schematic which shows the main component types in the proposed system, which include heat exchangers, turbomachines, shafts, tanks, piping, and a generator. The main compressor is the compressor with the minimum entropy at the inlet (point 1). It is possible that a high recompression fraction will be used and the main compressor will actually not have the bulk of the mass flow, but the name will continue to be used. The precompressor (points 13-14) is used to compress the working fluid and can allow for additional recuperation (improved regeneration), helping with the specific heat mismatch between the high and low pressure sides. The use of the precompressor in addition to the main compressor (points 1-2) also allows for more efficient compression overall since the compression portion of the cycle occurs within a lower temperature range (better approximating a Carnot cycle) and there is additional heat rejection (intercooling).

There is a flow split at the exit of the precompressor (point 14) and some mass flow enters a recompressor and the remaining mass flow passes through an additional recuperator, heat rejection heat exchangers and main compressor. The flow then recombines at the exit of the recompressor (point 4). The fraction of the total mass flow rate that enters the recompressor is called the recompression fraction. The purpose of the flow split is because of the specific heat mismatch between the high and low pressure sides. When the specific heat mismatch is too high, much of the low pressure heat cannot be recuperated. In this case, there is additional entropy created in the heat exchanger because the temperature difference between the high and low pressure fluid streams must be greater in order for heat to be able to transfer and because more external heat has to be added to the cycle at lower temperatures. Rather than operate with heat exchangers with a

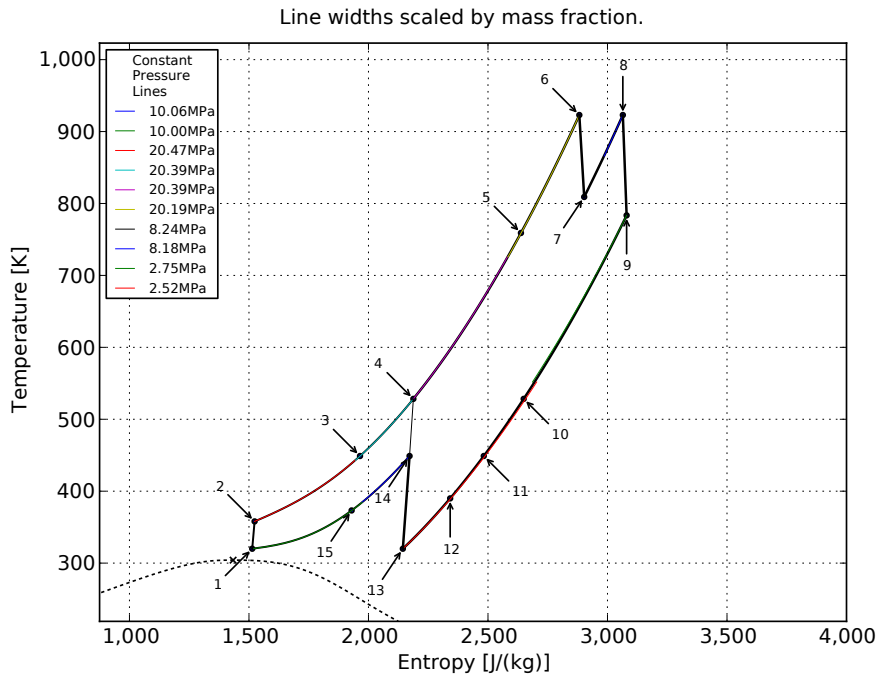


Figure 2.2: Example System Layout Showing Two Low Temperature Recuperators - Temperature Entropy Diagram

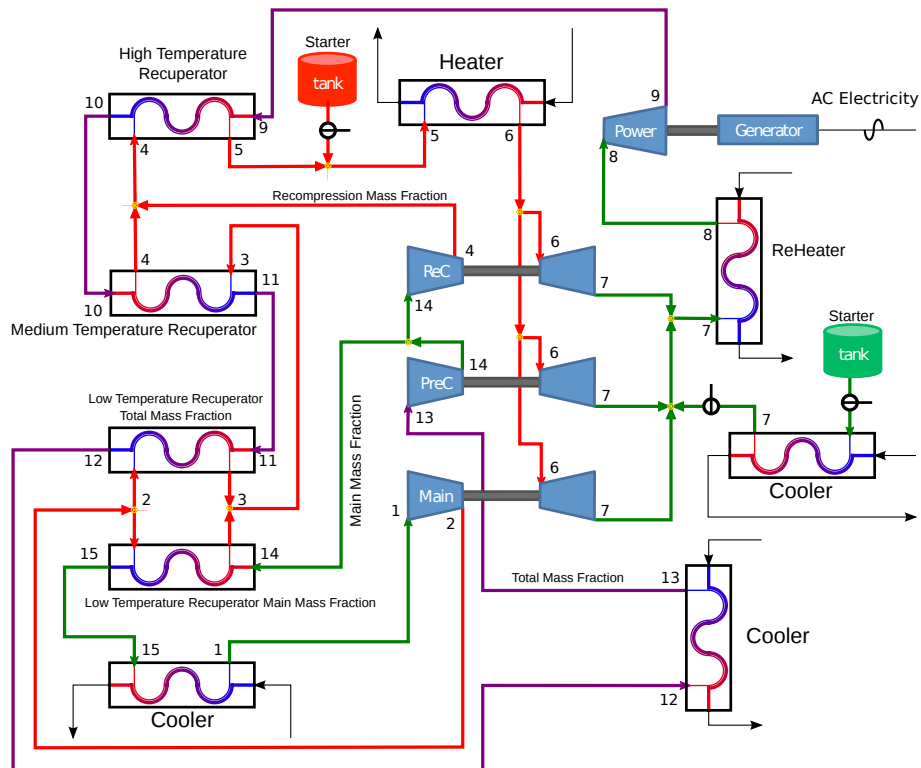


Figure 2.3: Proposed Supercritical Carbon Dioxide Power Cycle Layout. There are four rotating shafts, three compressors, four turbines, and up to four recuperators.

State Point	Component Inlet	Component Outlet
1	Main Compressor	Cooler
2	Low Temperature Recuperators, High Pressure Side	Main Compressor
3	Medium Temperature Recuperator High Pressure Side	Low Temperature Recuperators, High Pressure Side
4	High Temperature Recuperator High Pressure Side	Medium Temperature Recuperator High Pressure Side, Recompressor
5	Heater High Pressure Side	High Temperature Recuperator High Pressure Side
6	High Pressure Turbines	Heater High Pressure Side
7	Reheater High Pressure Side	High Pressure Turbines
8	Power Turbine	Reheater High Pressure Side
9	High Temperature Recuperator Low Pressure Side	Power Turbine
10	Medium Temperature Recuperator Low Pressure Side	High Temperature Recuperator Low Pressure Side
11	Low Temperature Recuperator Total Fraction Low Pressure Side	Medium Temperature Recuperator Low Pressure Side
12	Cooler Low Pressure Side	Low Temperature Recuperator Total Fraction Low Pressure Side
13	Precompressor	Cooler Low Pressure Side
14	Low Temperature Recuperator Main Fraction Low Pressure Side, Recompressor	Precompressor
15	Cooler Low Pressure Side	Low Temperature Recuperator Main Fraction Low Pressure Side

Table 2.1: Summary of State Points

high specific heat mismatch and large entropy generation, some fraction of the fluid is split (the recompression fraction) and recompressed. This results in less mass flow near the critical point on the high pressure side, making the heat capacity (not specific heat capacity) lower. Although the specific enthalpy change (but not necessarily the enthalpy change) in the recompressor is greater than that of the main compressor, making the recompressor's efficiency (and the efficiency of the turbine that powers the recompressor) potentially play a more significant effect on the back work ratio, the benefit gained by better heat capacity matching coupled with a recompression fraction that is not too high can result in overall greater cycle efficiencies by employing a flow split and recompression.

The cycle has three small, high speed turbines which are used to drive the precompressor, recompressor, and main compressor. Each compressor turbine pair is on a different shaft, and can be thought to resemble a turbocharger assembly. If they are all required to share a single shaft, the design of the turbomachinery can't necessarily be optimized very well. After the high pressure fluid is heated by the recuperators (points 2-5) and external heat source (points 5-6), the flow is split (point 6) and enters these three turbines. The flow is split rather than each turbine operating in series in order to reduce the mass flow rate through each turbine so that the turbine will have a larger pressure drop and can operate at a lower speed better matched with the compressor it is powering. In order to simplify the design space, the present study does not explore the relative mass flow rates through each turbine and assumes all three turbines have the same isentropic efficiency. With this layout it actually may be possible (although not necessary) for some of the shafts to be combined (eliminating one or more turbines), if the design of one or more of the compressors happens to be result in a similar enough operating speed, without changing the higher level cycle analysis. After expanding through the turbines (points 6-7), the flow is recombined (point 7) and reheated by the external heat source (points 7-8). After being reheated the fluid then enters a power turbine (points 8-9) which delivers shaft power to the engine's external load (an electrical generator), and is expected to operate at a much lower speed than the 3 smaller turbines. This is believed to be the first formal proposal of such a configuration, and was done so because of the extreme speed difference expected between the power turbine and compressors such that it is not ideal to have a single turbine driving the compressors and electrical generator or alternator.

The other advantage is that the small turbines and compressors could be placed in containment

vessels, eliminating the need for high speed, high pressure rotating seals. The only needed rotating seal would be on the power turbine, which would likely be a larger, slower turbomachine operating at a lower pressure, which would result in a more manageable seal design. The test rigs designed and operated by Sandia National Laboratories were described to have challenges and limitations by utilizing a starter motor/alternator on each shaft, due to speed limitations of the motors and high pressure, high speed rotating seals[19, 20]. In order for this configuration to work with no starter motors connected to the three smaller turbines, a pressurized tank would be required to do a blow down startup procedure in order for the engine to reach its operating speed. It is also possible that a positive displacement pump may be able to be used in place of a tank in order to temporarily provide flow to the smaller turbines.

There is a high temperature recuperator (points 4-5 and 9-10), medium temperature recuperator (points 3-4 and 10-11), and two low temperature recuperators (points 2-3, 11-12, and 14-15). The low temperature recuperators have an additional flow split on the high pressure side (at point 2) directing flow to the two different heat exchangers and then recombining (point 3). When modeling, this more general configuration was assumed and the mass fraction of this additional flow split was explored. The mass fraction on the high pressure side that was explored was called the “Low Temperature Recuperator Main Fraction High Pressure Component Mass Fraction” and represented the mass fraction that was split at point 2 and then went through the heat exchanger which was cooling the main mass fraction flow. The low temperature recuperator cooling the total mass fraction received the complement of the “Low Temperature Recuperator Main Fraction High Pressure Component Mass Fraction” on the high pressure side. Figure 2.2 shows an example of a configuration where two low temperature recuperators are in use. In some cases, one or both of the low temperature recuperators will not exist, and in some cases the medium temperature recuperator also will not exist. Also included in Figure 2.3 are heat rejection heat exchangers. Details related to pressure drop and specific heat of the ambient pressure side of the heat exchanger was not considered in the present analysis and the power required to pump the coolant was considered to be low.

Although the present layout may appear complex, it’s believed that the development could be conducted in stages. Figure 2.4 shows an example layout for testing a single shaft. Also included is an example of the pressure vessel configuration previously mentioned. Initial work could be conducted

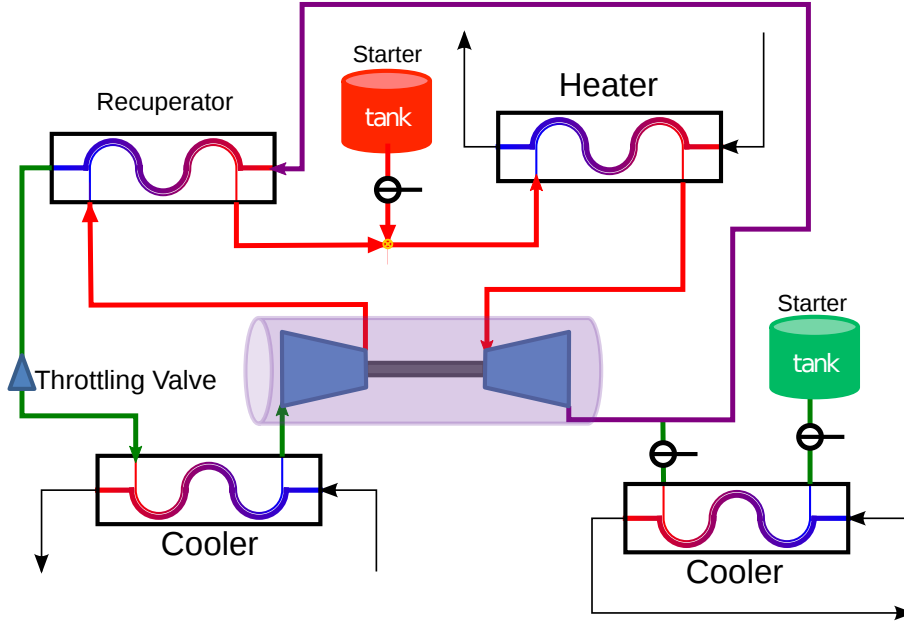


Figure 2.4: Single Shaft Test Layout

on this simplified layout understanding the dynamics and controls of the startup procedure, as well as validating some of the turbomachinery and heat exchanger design. Because the layout is simplified, the turbine would likely be operating off design, but such testing is still believed to be useful. Testing of each shaft could be conducted in simple rigs and once they have all been validated individually, then combined into the larger system shown in Figure 2.3. Because of the incremental development and testing that can occur, coupled with the fact that the high speed rotating seal issues are reduced, the proposed layout is believed to be an overall simpler approach. One point to note, however, is that the placement of the startup tanks in Figures 2.3 and 2.4 has not been optimized. They are primarily included to make the reader aware of their necessity. Additional work would need to be conducted in order to optimize their location for the best balance of reliable startup, cost minimization, and simplicity.

2.3.2 Computer Code Overview

A Supercritical Carbon Dioxide Power Cycle analysis code was created from scratch using Python [26], NumPy [27], SciPy [28], and matplotlib [29]. Variable fluid properties are utilized (i.e. $h = h(T, p)$, $c_p = c_p(T, p)$, and $s = s(T, p)$) throughout the code. Fluid property data was obtained using REFPROP FORTRAN functions[13] and a forked version of the python-refprop module[30]. This

code’s source is expected to be released in April, 2016[31]. A hybrid approach was used to access fluid properties. For commonly accessed properties, property data was populated in advance using REFPROP and stored into RAM for use with an interpolation function. Less commonly used properties are accessed directly from REFPROP as needed. This hybrid approach allowed for an increase in run speed and reliability because the interpolation function call was relatively resource expensive, but more efficient at obtaining multiple values simultaneously. Many REFPROP fluid property function calls were also very unstable in certain regions with certain independent variables, and the data used by the interpolation tables could be generated with more stable choices of independent variables. Even with this hybrid approach, there were still some variations in the REFPROP fluid property data that were perceived to be “noise” that impacted the cycle analysis at some level. Although REFPROP supports many fluids, only carbon dioxide is currently implemented in the present cycle code and all figures shown in the present Chapter are results using carbon dioxide only.

The fluid property functions were setup to accept temperature and pressure (T, p) , temperature and entropy (T, s) , enthalpy and entropy (h, s) , pressure and entropy (p, s) , or enthalpy and pressure (h, p) as inputs. From these inputs, temperature, pressure, enthalpy, entropy, density, specific heat at constant pressure, specific heat at constant volume, speed of sound, dynamic viscosity, thermal conductivity, and compressibility factor could be obtained. Because only two inputs were required the code is not yet setup in a general enough way that it can fully function in regions where mixtures of liquids and vapor can coexist in equilibrium (within the liquid vapor dome), except for plotting of contour level backgrounds. The code assumes all fluids are either supercritical fluids, gases, or vapors. As a result, cycles where condensing may occur are not currently studied. Although liquids should work with the present fluid property lookup technique, they were not considered in order to avoid the chance of a design configuration where some fluid did condense.

The most complicated portion of the code is the real fluid heat exchanger functions. These functions will be discussed in more detail in Section 2.3.3. Although considerably simpler, functions have also been created to model the turbomachines. The isentropic efficiency for a compressor was defined to be:

$$\eta_c = \frac{h_{o,ideal} - h_i}{h_o - h_i} \quad (2.1)$$

where the compressor outlet enthalpy (h_o) can be determined from a known compressor isentropic efficiency (η_c), pressure ratio (PR_c), and inlet temperature (T_i) and pressure (p_i). The compressor inlet enthalpy (h_i) and entropy (s_i) are evaluated using the fluid property functions using the known temperature and pressure as inputs. The ideal compressor outlet has the same entropy as the compressor inlet. The outlet pressure for both the ideal and actual compressor outlet is:

$$p_o = p_i * PR_c \quad (2.2)$$

Using a known pressure and entropy, the ideal compressor outlet enthalpy ($h_{o,ideal}$) can be found using the fluid property functions. With all of these parameters known, the actual compressor outlet enthalpy can be found using the relationship:

$$h_o = \frac{(h_{o,ideal} - h_i)}{\eta_c} + h_i \quad (2.3)$$

With a known compressor outlet enthalpy and pressure, the compressor outlet temperature (T_o) could be found using the fluid property functions.

A similar procedure was used for the turbines. The isentropic efficiency of a turbine was defined to be:

$$\eta_t = \frac{h_i - h_o}{h_i - h_{o,ideal}} \quad (2.4)$$

The turbine inlet enthalpy (h_i) and entropy (s_i) were known in terms of the inlet (T_i) temperature and pressure (p_i). The isentropic efficiency (η_t) was also defined. The ideal turbine outlet entropy ($s_{o,ideal}$) was the same as the inlet entropy (s_i). For the high pressure turbines, the actual outlet enthalpy (h_o) was defined based on the energy (W) required to drive the compressors used in the cycle:

$$h_o = h_i - W \quad (2.5)$$

With a known actual outlet enthalpy and inlet enthalpy, an ideal outlet enthalpy ($h_{o,ideal}$) could be calculated

$$h_{o,ideal} = h_i - \frac{W}{\eta_t} \quad (2.6)$$

Using the ideal outlet enthalpy ($h_{o,ideal}$) and entropy ($s_{o,ideal}$), the turbine outlet pressure could be

determined using the fluid property functions. The ideal turbine outlet pressure was the same as the actual turbine outlet pressure. Using a known turbine outlet enthalpy and pressure, the turbine outlet temperature and entropy could be found using the fluid property functions.

The power turbine was solved in a slightly different way. Rather than matching a work output, the power turbine needed to match the pressure ratio so that the power turbine outlet pressure equaled precompressor inlet pressure plus the high, medium, and low temperature recuperator pressure drops. The iterative process worked by guessing a pressure ratio in the power turbine and then calculating the turbine work output. The guessed turbine outlet pressure is:

$$p_o = p_i / PR_t \quad (2.7)$$

With a guessed outlet pressure (p_o) and a known ideal outlet entropy (s_o), a guessed ideal turbine outlet enthalpy ($h_{o,ideal}$) could be found using the fluid property functions. With a guessed ideal turbine outlet enthalpy known, a guessed actual turbine outlet enthalpy could be calculated as

$$h_o = h_i - \eta_t * (h_i - h_{o,ideal}) \quad (2.8)$$

and the guessed turbine work could then be calculated

$$W = h_i - h_o \quad (2.9)$$

With a guessed turbine outlet pressure and enthalpy the fluid property functions could be used to determine the turbine outlet temperature. The initial guess for the power turbine outlet pressure was based upon no pressure loss in the heat exchangers. After a power turbine outlet temperature was guessed, a guessed size of the heat exchangers and pressures drop could be made. With a new guessed heat exchanger pressure drop, a new power turbine outlet pressure guess could be made. The process repeated until the newly guessed pressure drops stopped changing with subsequent iterations. If the change in pressure from iteration to iteration was less than 0.0001% the pressure was considered to be converged. If the change in pressure from iteration to iteration would not decrease below .0001%, the convergence criteria was relaxed to 0.3%. Once a converged turbine outlet pressure was established, the guessed turbine outlet conditions and turbine work

were assumed to be the actual values. If the relaxed convergence criteria could not be met, an exception was raised. If the process converged to pressure ratio less than 1, an exception was raised because the engine would not be able to start because more work would be required to drive the compressors and overcome the heat exchanger pressure drops than what was being produced.

This iterative process just described was not managed by a turbine specific function, but rather, was managed by a much larger overall function that laid out the entire cycle using the heat exchanger functions and turbomachinery functions. The main cycle layout function also has the capability to iteratively solve for the other unknown pressures within the cycle, the precompressor inlet pressure and the recompressor outlet pressure. The main cycle layout function coordinated the mass splits in the cycle and ensured all of the component inlet and outlet conditions were in agreement. As was mentioned previously, pumping power for the ambient pressure side of the heaters and coolers are assumed to be low and was not considered in the computer code. The heat source currently modeled is that of a constant heat flux (i.e. solar) or a highly regenerated combustion system (heater efficiency is assumed to be 100%) where no heat is wasted in the exhaust flow. With these assumption of low pressure drop, very simple functions were created for the heaters and coolers and were called by the main cycle layout function. The main cycle layout function also totaled all of the energy flows and determined a cycle efficiency. A number of checks were made to ensure that resulting cycle did not violate any thermodynamic laws and that the efficiency was indeed greater than 0.

A set of design exploration functions were created to generate a permutation list and run all permutations of the main cycle layout function in parallel. Another set of functions was developed to plot the results of the design exploration, the layout of the cycle, as well as the temperature variation and fluid properties within the heat exchangers. An earlier version of this work[32] also involved developing, a set of functions to display and interact with all of the results data using a web server and web browser[33]. The results presented in this current work represent an improvement from that earlier web based presentation. At the time of this writing (March 2016), the web based interactive presentation still refers to the older results, however, it may be updated in the future.

It is important to note that the known isentropic efficiencies used in Equations 2.1 and 2.4 are assumed to be fixed. In reality these isentropic efficiencies will be a function of both the turbomachinery inlet conditions and the pressure ratio. For ideal gases with constant properties,

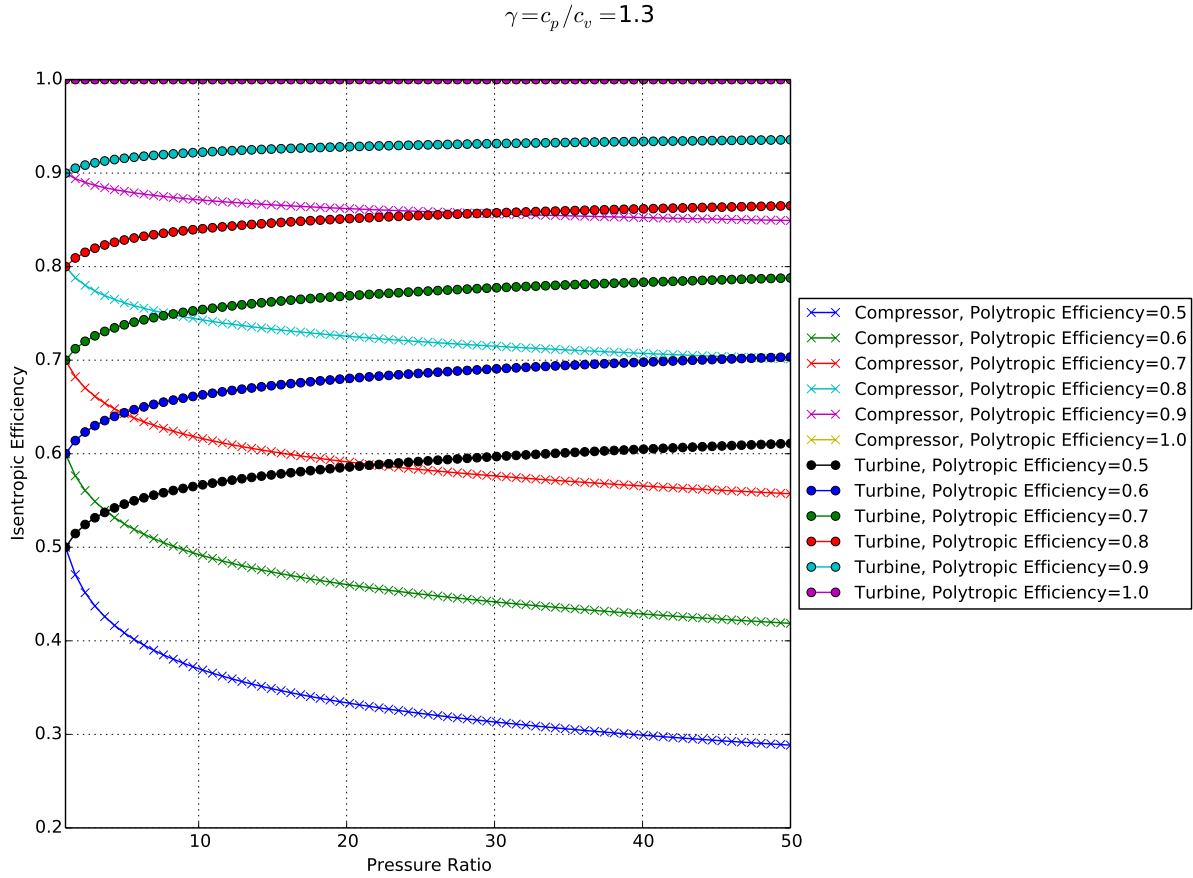


Figure 2.5: Compressor and Turbine Isentropic Efficiency vs Pressure Ratio at Various Polytopic Efficiencies, and a Constant Ratio of Specific Heats of 1.3

the turbomachinery isentropic efficiency is assumed to be a function of just the pressure ratio, the ratio of specific heats, and a polytropic efficiency, as represented below in Equations 2.10 and 2.11 for compressors and turbines, respectively[34].

$$\eta_c = \frac{PR_c^{(\gamma-1)/\gamma} - 1}{PR_c^{(\gamma-1)/(\gamma * e_c)} - 1} \quad (2.10)$$

$$\eta_t = \frac{1 - PR_t^{(1-\gamma)*e_t/\gamma}}{1 - PR_t^{(1-\gamma)/\gamma}} \quad (2.11)$$

As a reference to constant property fluids, Equations 2.10 and 2.11 are plotted for a constant ratio of specific heats of 1.3 and a range of pressure ratios and polytropic efficiencies in Figure 2.5. Variable property fluids will have a much more complex relationship. As a result, the present work assumed fixed turbomachinery isentropic efficiencies and defers variable turbomachinery isentropic

efficiency consideration to be recommended future work. Some impacts of the present constant isentropic efficiency assumption will be discussed later.

2.3.3 Real Fluid Heat Exchangers

Most heat exchangers operate with fluids with nearly constant specific heats and/or are changing phase. Counterflow heat exchangers where both fluids have constant and similar specific heats have a constant and equal slope for the temperature on both the heated and cooled side. Counterflow heat exchangers where the two fluids have constant but dissimilar specific heats are characterized by constant but unequal sloped fluid temperature. Counterflow heat exchangers where the cooled side is condensed and the heated side has a constant specific heat are characterized by a constant temperature on the cooled side and a constant sloped temperature on the heated side. Counterflow heat exchangers where the heated side is vaporized and the cooled side has a constant specific heat are characterized by a constant temperature on the heated side and a constant sloped temperature on the cooled side. For all of these cases, the location of minimum temperature difference between the high and low pressure sides is at an end of the heat exchanger. For the case where the specific heats are constant and similar, the temperature difference is constant throughout the heat exchanger and therefore the location of minimum temperature difference also occurs throughout the entire heat exchanger. The location of minimum temperature difference is sometimes referred to as the pinch point.

Heat exchangers operating with fluids near the critical point possess wildly nonlinear and dissimilar specific heats which dramatically complicates performance analysis. The slope of the fluid temperature is nonlinear and the minimum temperature difference between the heated and cooled fluids may occur in multiple places and not necessarily at the ends of the heat exchanger. Understanding the performance of heat exchanges operating with fluids near the critical point is very important in accurately predicting the performance of real fluid power cycles. The log mean temperature difference and NTU-effectiveness methods described in classic heat transfer textbooks[35] for fluids with constant heat capacities cannot be applied to these cases. An appropriate mean temperature difference (such as a log mean temperature difference) in many situations cannot be defined for fluids with varying heat capacities.

A zero dimensional real fluid counterflow heat exchanger solver has been developed as part of the Supercritical Carbon Dioxide Power Cycle analysis code. This zero dimensional solver takes into account variable fluid specific heats as well as different mass fractions between the high and low pressure side. The primary purpose of this solver is to understand the impact of the variable specific heat on heat transfer. The heat exchanger inlet conditions are defined. The minimum temperature difference within the heat exchanger and the temperatures at the outlets are not computed based on an assumed surface area and convection coefficient or assumed geometry, but rather, the minimum temperature difference (ΔT_{min}) is defined and the outlet temperatures computed given that minimum temperature difference constraint. Conduction along the length of the heat exchanger is assumed to be negligible.

The pressure drop in the heat exchanger is defined as a linear function of the temperature drop, but this pressure drop is not computed based on any assumed geometry. The slope of this linear function is defined by a coefficient, d . The definition of a pressure drop as a function of temperature allows one to explore the impact of the pressure drop in the heat exchanger on the overall power cycle performance that would be required to achieve this limiting case of high convection. This aids the heat exchanger designer by providing a reference on how important it is to minimize pressure loss in order to achieve the very high forced convection coefficients. The assumption that the pressure drop is a linear function of the temperature drop was used because it is assumed that the length of the heat exchanger will be related to the temperature drop in the heat exchanger and the longer the length of the heat exchanger, the larger the pressure drop. This assumption could be improved in many ways, but was utilized because of its simplicity and because low system component pressure drops are anticipated.

The specific heat was evaluated for 200 discrete temperatures in the heat exchanger, on both the high and low pressure sides. The ratio of these specific heats between the high and low pressure side was then calculated at each temperature. Information about the relative specific heat between the high and low pressure side was used to help accelerate the solution process. Key information included the average specific heat ratio, temperatures where the specific heat ratio was equal to 1, the average slope of the specific heat ratios, as well as the average concavity of the specific heat ratios. The logic which utilized these qualities of the specific heat ratios aimed to predict the temperature ($T_{p,Cooled}$) on the cooled/low pressure side where pinching occurred, which was at the

high and/or low temperature end of the heat exchanger, everywhere in the heat exchanger, or in the middle of the heat exchanger (which could be at more than one temperature). The pinch point temperature on the high pressure (heated) and low pressure (cooled) sides of the heat exchanger are related by:

$$T_{p,Heated} = T_{p,Cooled} - \Delta T_{min} \quad (2.12)$$

Knowing the location of a pinch point was desired because it eliminated one unknown from the problem since both the high and low pressure fluid streams were related by the defined minimum temperature difference. With a known temperature where both fluid streams were at nearly the same temperature, the problem reduced to a simple single control volume energy balance with one unknown temperature for cases where the pinching occurred at an inlet or outlet, or two simple control volumes with two unknown temperatures for cases where the pinching occurred in the middle of the heat exchanger.

For the more general case where there were two control volumes, the pressures at the pinch point ($p_{p,Cooled}$ and $p_{p,Heated}$) were defined as

$$p_{p,Cooled} = p_{i,Cooled} - (T_{i,Cooled} - T_{p,Cooled}) * d \quad (2.13)$$

and

$$p_{p,Heated} = p_{i,Heated} - (T_{p,Heated} - T_{i,Heated}) * d \quad (2.14)$$

where $p_{i,Cooled}$ and $T_{i,Cooled}$ are the inlet pressure on the cooled side and $p_{i,Heated}$ and $T_{i,Heated}$ are the inlet pressure on the heated side. With a known temperature and pressure at the pinch point on each side of the heat exchanger, the enthalpy on both the heated ($h_{p,Heated}$) and cooled ($h_{p,Cooled}$) side could be found using the fluid property functions. The enthalpy at the inlet on the heated ($h_{i,Heated}$) and cooled ($h_{i,Cooled}$) sides of the heat exchanger could be found using the fluid property functions. The energy balance for the two control volumes described above can be represented by

$$(h_{p,Heated} - h_{i,Heated}) * \dot{m}_{Heated} = (h_{p,Cooled} - h_{o,Cooled}) * \dot{m}_{Cooled} \quad (2.15)$$

and

$$(h_{o,Heated} - h_{p,Heated}) * \dot{m}_{Heated} = (h_{i,Cooled} - h_{p,Cooled}) * \dot{m}_{Cooled} \quad (2.16)$$

where $h_{o,Heated}$ and $h_{o,Cooled}$ are the enthalpies at the outlet of the heated and cold side of the heat exchanger. \dot{m}_{Heated} and \dot{m}_{Cooled} are the mass flow rates on the heated and cooled sides. Equations 2.15 and 2.16 could then be solved for to find the outlet enthalpies

$$h_{o,Cooled} = h_{p,Cooled} - \frac{(h_{p,Heated} + h_{i,Heated}) * \dot{m}_{Heated}}{\dot{m}_{Cooled}} \quad (2.17)$$

and

$$h_{o,Heated} = \frac{(h_{i,Cooled} - h_{p,Cooled}) * \dot{m}_{Cooled}}{\dot{m}_{Heated}} + h_{p,Heated} \quad (2.18)$$

The outlet temperatures on the heated ($T_{o,Heated}$) and cooled ($T_{o,Cooled}$) sides could then be found using the known outlet enthalpies and the outlet pressures using the fluid property functions. If the pinch point was at an endpoint, a similar, but simpler procedure was used because there were less unknowns.

Once all heat exchanger outlet temperatures were calculated, the solution was verified by using the known inlet and outlet temperatures on the low temperature side of the heat exchanger. For each discrete temperature on the low pressure side, a temperature was calculated on the high pressure side using an energy balance of a simple control volume, using previously calculated temperatures on the low temperature side of the control volume. The resulting temperatures on the high and low pressure side were then compared to check for the actual minimum temperature difference, which would indicate if there was a failure of the logic described above to identify the correct heat exchanger pinch point. For many scenarios, the logic proved to be successful due to an accurate identification of the pinch point, however, the heuristics used to identify the pinch point were not always correct. In order to account for this deficiency, the check for a temperature difference being greater than or less than (potentially being negative) the defined minimum temperature difference, ΔT_{min} , mentioned above, was incorporated in with a root finding function and the correct outlet temperatures found using that root finding function. Because a root finding function was added in order to resolve any deficiencies in the heuristic estimation of the pinch point temperature, the simple control volume approach, mentioned above, was mainly used to provide a good initial guess

for the root finding function.

As was mentioned above, the pressure drops in the heat exchangers were defined to be a function of the temperature changes in the heat exchangers. The technique that was just described for finding the heat exchanger outlet temperatures assumed that the outlet pressures were known. Because the temperature changes in the heat exchanger were initially unknown, an iterative process was required in order to determine appropriate pressure drops. An initial guess for the heat exchanger pressure drops was based upon the low temperature inlet/outlet temperatures being equal and the high temperature inlet/outlet temperatures being equal. Temperature changes within the heat exchangers were found using the guessed pressure drops based upon the initially guessed temperature change. With new guessed pressure drops based on calculated heat exchanger temperature changes, the heat exchanger temperature changes were evaluated again using the process described above. The entire process was repeated until the temperature changes and pressure drops in the heat exchangers stopped changing. If the change in inlet/outlet pressures from iteration to iteration was less than 0.0001%, the solution was considered to be converged. If a change in inlet/outlet pressure of less than 0.0001% could not be achieved, the convergence criteria was relaxed to a change in inlet/outlet pressure of 0.3%. If this relaxation was insufficient, the heat exchanger function raised an exception.

It is important to make it clear that no geometry is assumed in this heat exchanger solver and that the purpose of the solver is to aid cycle and heat exchanger designers in understanding the thermodynamic limit of heat exchanger performance due to the variable specific heat mismatch. Because no geometry is assumed, no length dimension is used when plotting the results, but rather, results are presented as a function of the temperature of the cooled fluid stream. The temperature of the cooled fluid stream is related to the length dimension, but no specific relationship is presently assumed. This technique also has not yet been adapted to handle heat exchangers where a fluid is boiling or condensing.

Figure 2.6 shows an example of a heat exchanger solution. The left plot shows the specific heats of both the heated and cooled sides of the heat exchanger. Two specific heats are presented for each fluid stream. $c_{p,Heated}$ and $c_{p,Cooled}$ are based upon the fluid stream's mass flow, and C_{Heated} and C_{Cooled} are based upon mass flow of the cooled fluid stream and are defined in Equations 2.19 and 2.20.

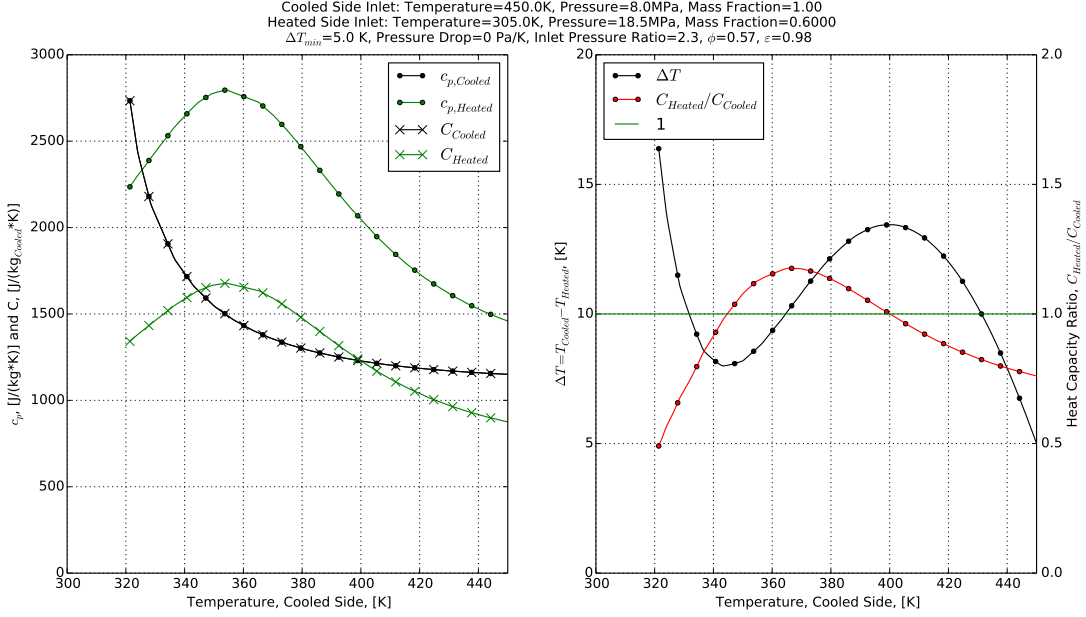


Figure 2.6: Sample Heat Exchanger Solution

$$C_{Heated} = c_{p,Heated} * \frac{\dot{m}_{Heated}}{\dot{m}_{Cooled}} \quad (2.19)$$

$$C_{Cooled} = c_{p,Cooled} * \frac{\dot{m}_{Cooled}}{\dot{m}_{Cooled}} = c_{p,Cooled} \quad (2.20)$$

C_{Heated} and C_{Cooled} are presented so that heat capacity can be compared for heat exchangers with different mass flow rates on the heated and cooled side, which can happen in cycles with recompression. It is important to note that $c_{p,Cooled}$ and C_{Cooled} have the same values and as a result, the curves are overlapping. One can see a highly non-linear and dissimilar c_p for both the heated and cooled sides of the heat exchanger. In the example configuration shown, C is still dissimilar between the heated and cooled sides of the heat exchanger.

An important metric for evaluating heat exchanger performance is the heat exchanger's effectiveness (ϵ), which is defined as

$$\begin{aligned} \epsilon &= \frac{(h_{o,Heated} - h_{i,Heated}) * \dot{m}_{Heated}}{\min((h_{o,max,Heated} - h_{i,Heated}) * \dot{m}_{Heated}, (h_{i,Cooled} - h_{o,min,Cooled}) * \dot{m}_{Cooled})} \\ &= \frac{(h_{i,Cooled} - h_{o,Cooled}) * \dot{m}_{Cooled}}{\min((h_{o,max,Heated} - h_{i,Heated}) * \dot{m}_{Heated}, (h_{i,Cooled} - h_{o,min,Cooled}) * \dot{m}_{Cooled})} \end{aligned} \quad (2.21)$$

where $h_{o,max,Heated}$ is the maximum enthalpy the heated side fluid could have if the heated side outlet could reach the temperature of the cooled side inlet ($T_{i,Cooled}$) and $h_{o,min,Cooled}$ is the minimum enthalpy the cooled side fluid could have if the cooled side outlet could reach the temperature of the heated side inlet ($T_{i,Heated}$). Heat exchanger effectiveness helps one assess how much of the heat that *can* be transferred *is* transferred. An important metric to also consider is the maximum amount of heat that *can* transferred compared to the maximum one may *want* to transfer from either the heated or cooled fluids. In the case of supercritical carbon dioxide power cycle design, one always wants to transfer as much heat as possible, but because of the specific heat mismatch, there isn't always enough heat available to be transferred on the cooled side and there isn't always enough heat that can be accepted on the heated side. No term is known to identify this metric, so a new name will be given as the "Fraction of Desired Heat Transferred" and will be associated with the symbol ϕ and defined as

$$\begin{aligned}\phi &= \frac{(h_{o,Heated} - h_{i,Heated}) * \dot{m}_{Heated}}{\mathbf{max}((h_{o,max,Heated} - h_{i,Heated}) * \dot{m}_{Heated}, (h_{i,Cooled} - h_{o,min,Cooled}) * \dot{m}_{Cooled})} \\ &= \frac{(h_{i,Cooled} - h_{o,Cooled}) * \dot{m}_{Cooled}}{\mathbf{max}((h_{o,max,Heated} - h_{i,Heated}) * \dot{m}_{Heated}, (h_{i,Cooled} - h_{o,min,Cooled}) * \dot{m}_{Cooled})}\end{aligned}\quad (2.22)$$

This new metric can be used to assess how well the specific heats are matched between the heated and the cooled sides. In Figure 2.6 the "Fraction of Desired Heat Transferred" is 0.57, which means that 57% of the heat that one would like to accept on the heated side could be transferred to the heated side, or 57% of the heat that one would like to have available on the cooled side to accept on the heated side could be transferred to the heated side.

In the right plot of Figure 2.6, the temperature difference (ΔT) and ratio of specific heats (C_{Heated}/C_{Cooled}) is presented. A reference horizontal line for a specific heat ratio of 1 is presented in order to illustrate clearly how the heated and cooled sides relative specific heat is changing and which fluid stream has a greater specific heat. The relative specific heats are wildly changing in this particular solution and the temperature difference as a result also changes dramatically within the heat exchanger. It's also important to note in this particular example that the temperature difference changes concavity within the heat exchanger, and the temperature difference is close to zero at one local minima and approximately zero at the absolute minima.

In addition to the example solution shown in Figure 2.6, there are several other example solutions

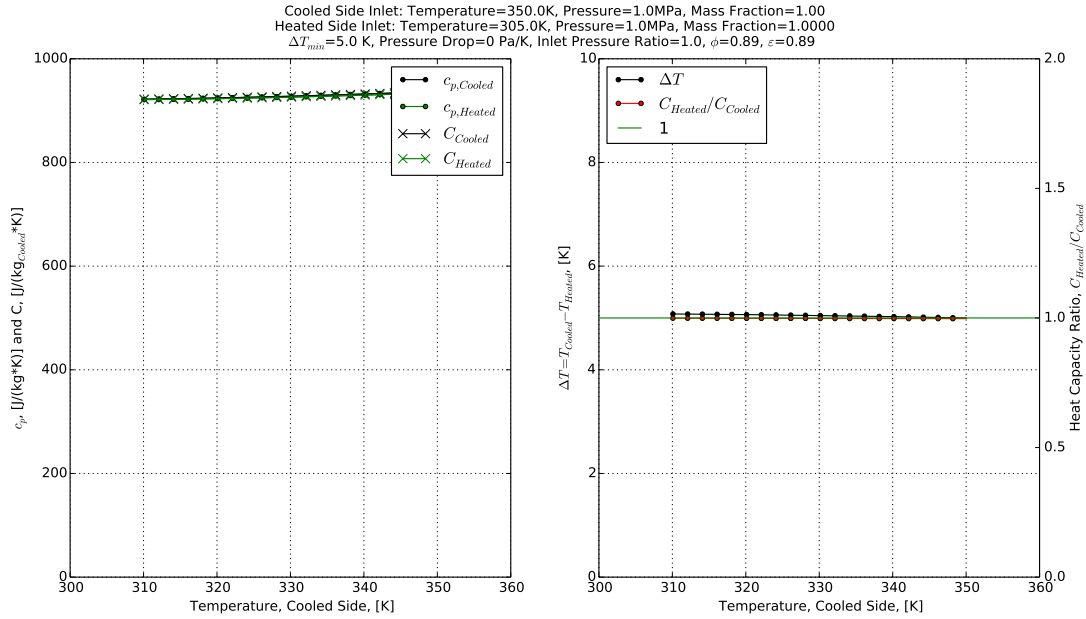


Figure 2.7: Sample heat exchanger solution with nearly constant and similar specific heats

that demonstrate important heat exchanger characteristics. Figure 2.7 shows a heat exchanger with nearly constant and similar specific heats with similar mass flow rates on both the heated and cooled sides. In this example the temperature difference between the heated and cooled sides is constant and minimum throughout the heat exchanger (it is pinched everywhere). The specific heats of both sides are very well matched and the maximum amount of heat that can be transferred is. Figure 2.7 is an example well below the critical pressure, so it is not applicable to supercritical carbon dioxide power cycles, however, it is an important case in understanding the impact of specific heats on heat exchanger performance.

Figure 2.8 shows an example heat exchanger solution where the specific heats are nearly constant (the same pressure as the case in Figure 2.7), but the mass fractions are different so the heat capacities between the heated and cooled sides are different. In this case the heat capacity on the heated side is always lower than the cooled side. Within the operating temperature range defined by the heat exchanger heated and cooled side inlets, there will not be enough heat capacity on the heated side in order to accept all the heat from the cooled side and the cooled side outlet will never reach the inlet temperature of the heated side (the “Fraction of Desired Heat Transferred” is 0.58). The temperature difference varies linearly within the heat exchanger and the location of minimum

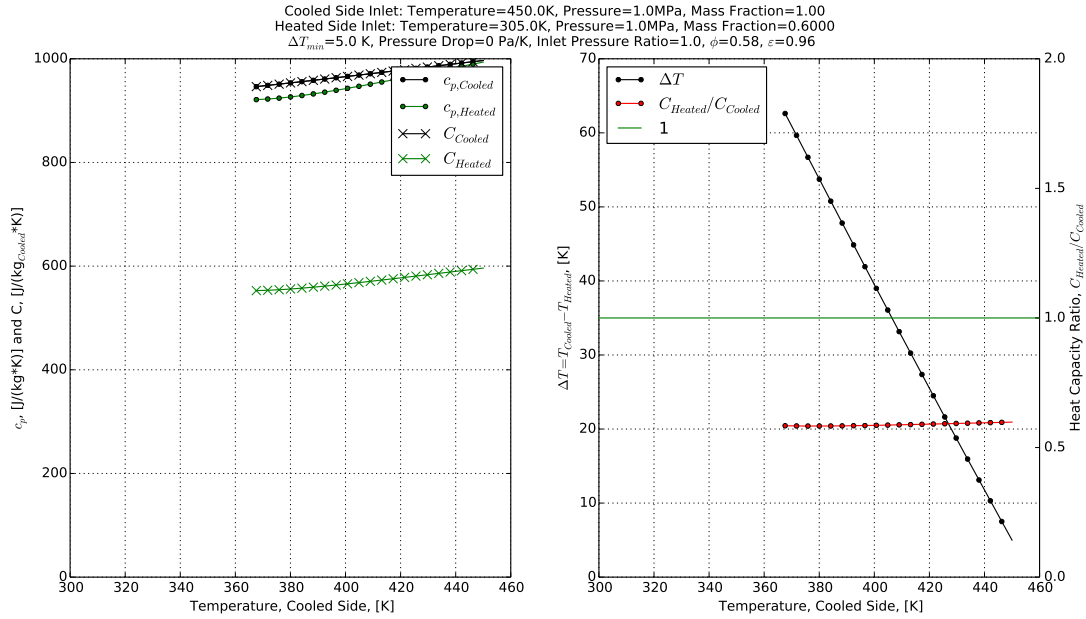


Figure 2.8: Sample heat exchanger solution with nearly constant but dissimilar heat capacities

temperature difference (the pinch point) is at the high temperature end only.

Figure 2.9 shows an example heat exchanger solution where the location of minimum temperature difference (pinch point) occurs at both ends. In this example the specific heats are dissimilar and varying. This particular case is also not applicable to supercritical carbon dioxide power cycles because the heated side is a lower pressure than the cooled side, however, it illustrates a very interesting solution which helps to understand heat exchangers with nonlinear and dissimilar specific heats. In this case the mass fraction was adjusted so that the average heat capacities of the heated and cooled sides are well matched. The heat capacity ratio within the heat exchanger changes from greater than one at the low temperature end of the heat exchanger to less than one at the high temperature end of the heat exchanger. The temperature difference within the heat exchanger is still fairly low away from the ends.

In Figure 2.10 a heat exchanger solution is shown where a pinch point exists at both the high temperature end and in the middle of the heat exchanger. The temperatures and pressures are representative of a heat exchanger operating in a supercritical carbon dioxide power cycle. The specific heat capacities are nonlinear and dissimilar. The mass fraction has been adjusted so that the average heat capacities are nearly the same, which causes the solution to have low temperature

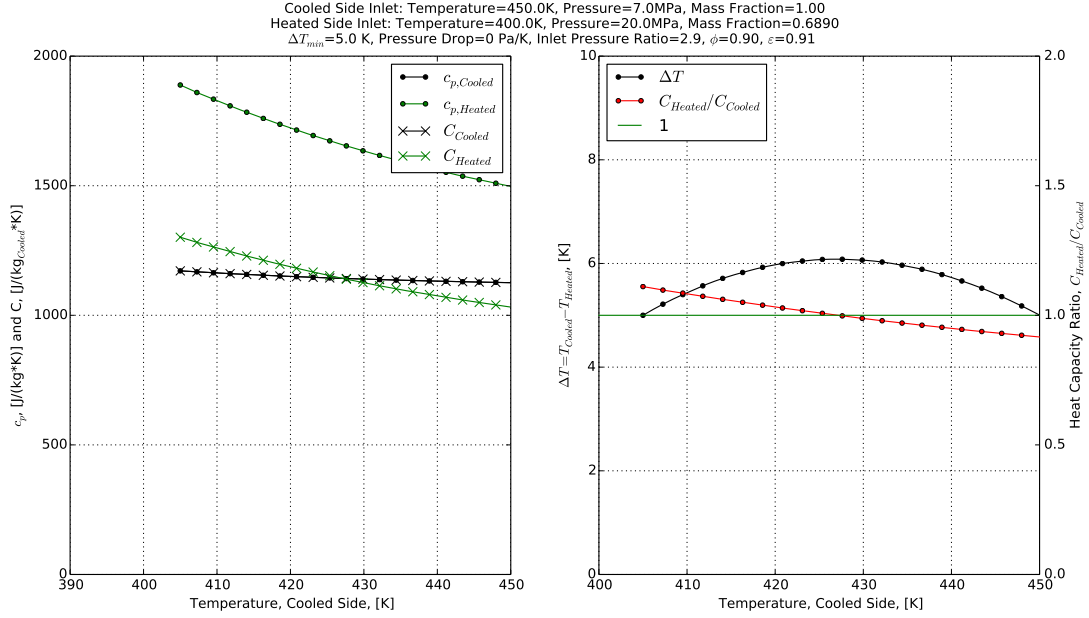


Figure 2.9: Sample heat exchanger solution where the heat exchanger is pinched at both ends

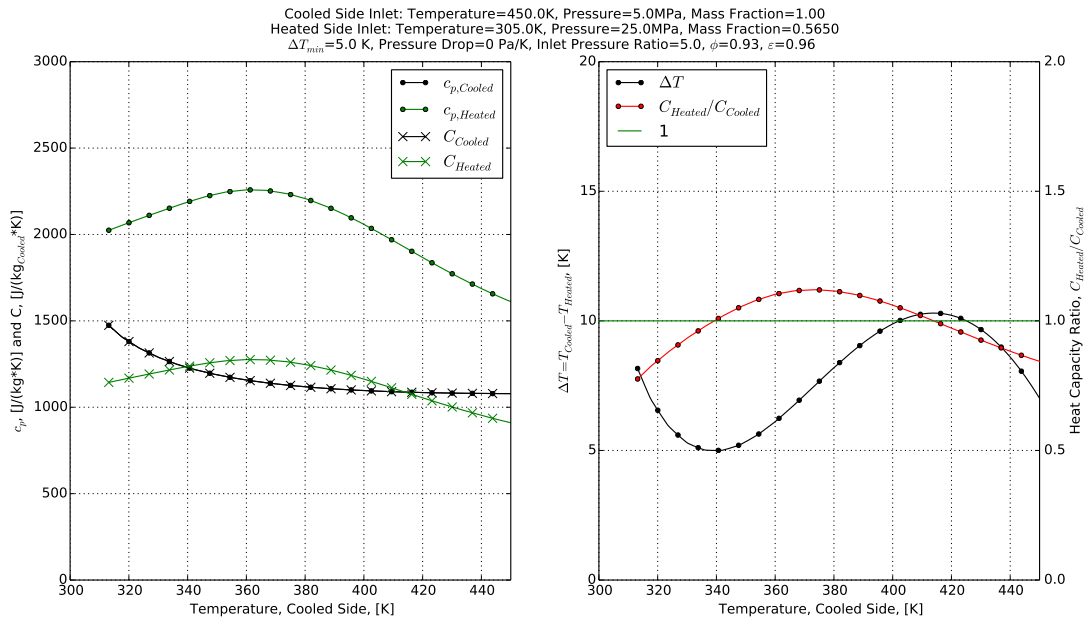


Figure 2.10: Sample heat exchanger solution where the heat exchanger is pinched in the middle and at the high temperature end

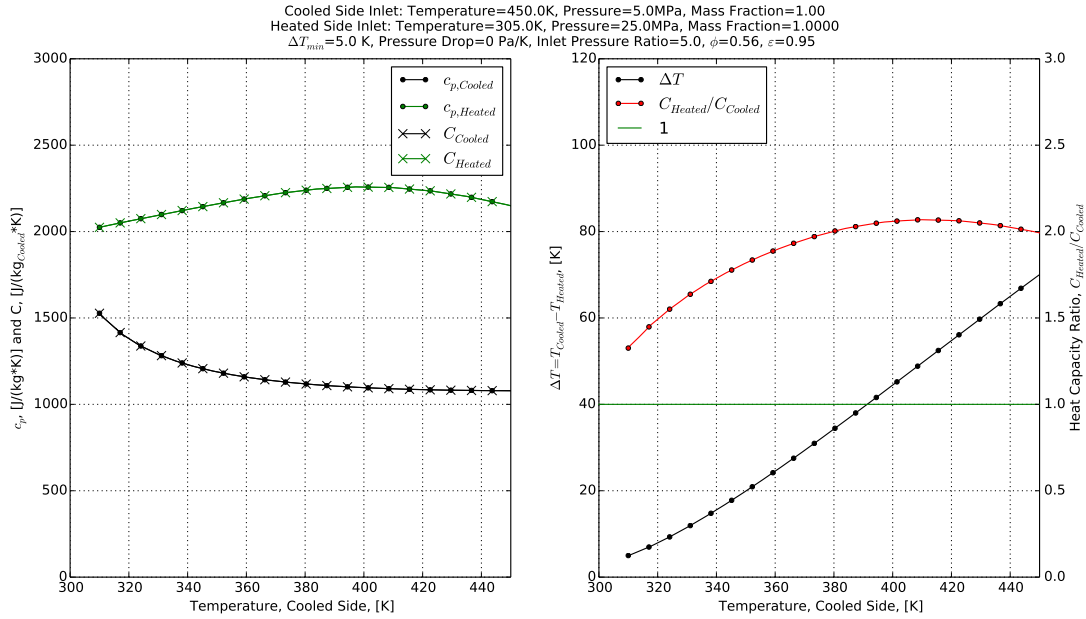


Figure 2.11: Sample heat exchanger solution where the heat exchanger is pinched only at the low temperature end

differences throughout the heat exchanger. This example points out that the pinch point is not necessarily the problem with heat exchangers in supercritical carbon dioxide cycles. The heat exchanger has two pinch points but still has a low temperature difference everywhere so nearly all of the heat from the cooled side is transferred to the heated side (the “Fraction of Desired Heat Transferred” is 0.93). Pinch points may be unusual in heat exchangers with highly nonlinear and dissimilar specific heats, but they are not the problem, just a distinct feature. The location of the pinch point and the temperature away from the pinch point may help to indicate how good or bad the heat capacity match is between the heated and cooled sides.

A case where the heated side specific heat capacity (and heat capacity) is always higher on the heated side than the cooled side is shown in Figure 2.11. In this case the heat exchanger relative heat capacities is always changing within the heat exchanger, but because the heat capacity is always higher on the heated side, the pinch point is only at the low temperature end and the temperature difference is very high at the high temperature end of the heat exchanger. Because the heat capacity on the cooled side is lower, the heated side will never reach the inlet temperature of the cooled side (the “Fraction of Desired Heat Transferred” is 0.56). This case is an example where the single pinch point at the low temperature end clearly indicates that the heat capacity is much

higher on the heated side than the cooled side. It's important to reiterate however that the pinch point itself is not the problem, the heat capacity mismatch is the problem.

All of these example heat exchanger solutions demonstrate some distinct characteristics of heat exchangers with constant, varying, similar, and dissimilar heat capacities. The heat exchanger performance plays a very important part in the performance of a supercritical carbon dioxide power cycle. The present results are useful because they provide a rapid solution and clearly isolate the required temperature difference due to specific heat mismatch. Additional example heat exchangers are presented in Appendix A which show the impact of variation in minimum temperature difference and mass fraction on the solution. Efforts in Chapter 5 will compare some unique 0-D heat exchanger model solutions to that of 2-D heat exchanger numerical simulations in order to provide some validation of the 0-D heat exchanger model, giving further confidence in its applicability in the cycle analysis code.

2.3.4 Cycle Simulation

Inputs of the cycle simulation include maximum temperature, minimum temperature, compressor pressure ratios, turbomachinery component efficiencies, heat exchanger pressure drop, heat exchanger minimum temperature difference, main compressor inlet pressure, and mass fraction for flow splits. An iterative procedure was utilized to find the unknown pressure drop between states 15 and 1 (the Main Fraction Cooler), the ReCompressor Pressure Ratio, and the Power Turbine Pressure ratio. Although an input variable, the linear pressure drop vs temperature drop constant was fixed to the same value for all heat exchangers in the cycle. Individual heat exchangers currently are not able to have different pressure drop constants. The cycle code presently does not include the ability to handle mixing of fluids of different temperatures where the flow is recombined. In order to ensure temperatures were equal when the flow was recombined, some small heaters and coolers were added if necessary on the high and low pressure sides at the inlet or outlet of the the heat exchanger. It is also important to note that only on-design conditions were studied. The code is currently not able to perform transient simulations or off-design studies at this time.

2.3.5 Design Exploration

A design explorer was developed to run the Supercritical Carbon Dioxide Power Cycle analysis code with many different input combinations. The design explorer was developed in such a way that the design space could be explored in parallel by running the Supercritical Carbon Dioxide Power Cycle analysis code on multiple processors simultaneously. The code can use as many processors as are available on a single machine. Some effort was conducted to run different batches of permutations on different machines, however, this functionality was abandoned because of the increased complexity of using multiple machines, and the dramatic increase in the number of processors available on a single machine recently. A 24 processor machine was used for the present study.

In order to effectively eliminate some components such as a low temperature recuperator, the precompressor and/or the recompressor from the system, the “Low Temperature Recuperator Main Fraction High Pressure Component Mass Fraction” could be set to 0 or 1, the precompressor pressure ratio could be set to a pressure ratio of 1 and the recompression fraction could be set to 0 or 1.

An earlier version of this work utilized a parallel brute force design space exploration and optimization process. Although that approach proved to be a reliable and straightforward approach that clearly illustrated the non-linear nature of the design space, unfortunately it was very time consuming and limited the resolution that any one parameter could be explored while simultaneously optimizing the other parameters. The approach was just not practical, and as a result, a more intelligent approach was adopted that resulted in a quicker optimization, with some uncertainty that a true optimum was achieved.

Because the cycle analysis code is based on Python, the available tool sets that were considered was limited to those that can be natively used from within Python. The differential evolution optimizer, part of the SciPy package was used due to its simple interface, responsive developer, and ability to successfully install and run [36]. The differential evolution optimizer is currently not a parallel optimizer. This results in some limitation in achieving a highly converged optimum solution in a short amount of wall time. After several runs, it was identified that reasonable results could be obtained with the current problem in a reasonable amount of time (~ 48 hours).

The differential evolution optimizer is of a class of stochastic population based optimizers. After

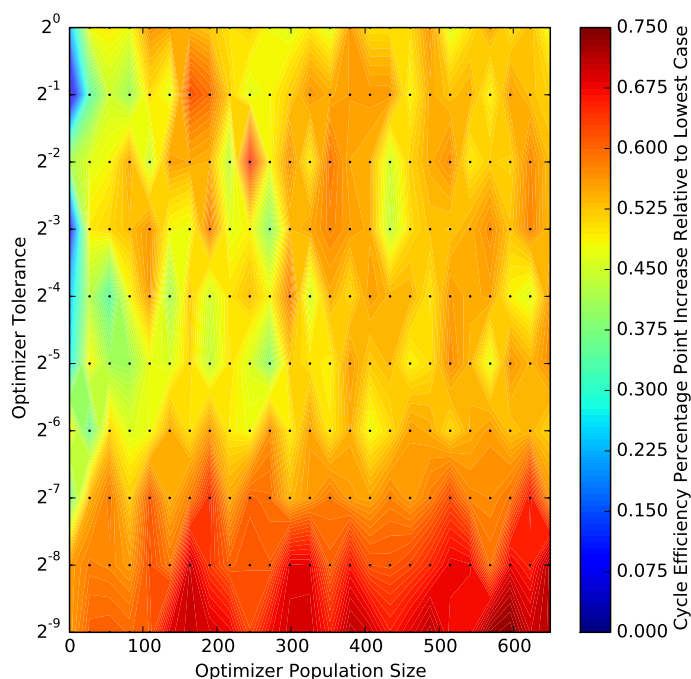


Figure 2.12: Cycle Efficiency Percentage Point Increase Relative to Lowest Case vs Differential Evolution Optimizer Tolerance and Population Size

a solution was found using the differential evolution algorithm, the SciPy “minimize” function was used to “polish” the results more quickly with a gradient based optimizer. The assumption is that the solution obtained using the differential evolution algorithm is close enough to the global optimum that a gradient based optimizer will not drive the solution away to a local, but non global optimum. A tool was developed that allowed any independent variable in the system to be either constrained to a fixed value, optimized, or swept. Since the differential evolution optimizer was not a parallel one, the parameter sweeping was then parallelized instead.

In order to assess the most appropriate parameters to use with the differential evolution optimizer, a sweep of the differential evolution optimizer tolerance and optimizer population size was conducted for a function relevant to the present work. The differential evolution optimizer tolerance and population size were the primary parameters that impacted the optimization time and how close the optimized result was to the true optimum. The results are presented in Figure 2.12 with the differential evolution optimizer tolerance represented using a logarithmic scale and the population size represented using a uniform scale. The population size was swept from 1 to 650 using 25 equally

spaced points. The tolerance was swept from 1 to $2^{-9} \approx 1.95 * 10^{-3}$, using 10 points spaced at integer powers of 2. The exponential tolerance point spacing was used after an initial uniformly spaced study proved to be inappropriate. The contour level magnitude is Cycle Efficiency Percentage Point Increase Relative to Lowest Case. The absolute Cycle Efficiency is not presented because the optimizer parameter sweep was conducted with an older version of the cycle analysis code, and the system that was optimized was that of the Combined Cycle with a Fuel Cell, which will be presented in Chapter 4. As a result, only the relative values are of interest, as this differential evolution optimizer parameter sweep was primarily conducted to assess the relative increase in efficiency possible by increasing the computational time required. The results presented in Figure 2.12 took nearly 18 days of computing time to generate and it was not feasible to re-conduct for every software revision or every cycle layout.

The results exhibit some “noise” because each run with different combinations of tolerance and population size started with a different random population. It could have been possible to start each run with the same starting “seed”, which would have resulted in a smoother change with respect to the optimizer tolerance. However, as population size varied, the same starting seed would have still resulted in a different starting population, and therefore there would still be some “noisy” variation with respect to population size. It was decided that it would be best to start each run with a different starting seed in order to identify the dependency of the optimizer parameters given the optimization starts from any random starting point.

Based on these results, a tolerance of $2^{-8} \approx 3.91 * 10^{-3}$ and a population size of 200 were used for the differential evolution optimizer as a compromise between computational time and accuracy, for all results in the current Chapter as well as Chapter 4. One may notice in Figure 2.12 that there is still some variation, even near the lowest tolerance and largest population size, however, the total variation is still a fraction of a percentage point and the increased optimization time was not deemed to be of considerable benefit. The Combined Cycle with a Fuel Cell had a considerably larger number of parameters to be optimized than the stand alone Supercritical Carbon Dioxide Power Cycle which this Chapter focuses on. Because of this, the results from the differential evolution optimizer parameter sweep for that more complex Combined Cycle with a Fuel Cell are considered to be more than appropriate for the stand alone cycle. The Combined Cycle without a Fuel Cell studied in Chapter 4 is slightly more complex of an optimization process than the Combined Cycle

with a Fuel Cell, but the differential evolution optimizer parameters defined above are still believed to be appropriate.

For all cases, the gradient based, “minimize” function was used with a tolerance of $5 * 10^{-5}$ and a maximum iterations of 200. No extensive study like the one described above was conducted to establish these values. The “minimize” function was considerably faster than the differential evolution optimizer and such a study was not deemed to be as beneficial.

A more sophisticated assessment of the appropriate differential evolution optimizer parameters could have tracked the optimization time in detail and plotted it versus the Cycle Efficiency Percentage Point Increase Relative to Lowest Case, and the corresponding optimizer tolerance and population sizes for each time. The present work did not conduct such a study, but for any follow on work that approach may be recommended. The drawback of that approach is that the optimization time must be interpreted relative to the CPU type of the computer used.

2.4 Results

Table 2.2 provides a summary of the default range of the component performances and allowable design ranges. Parameters that have the same minimum and maximum values were fixed and not optimized. Parameters with dissimilar maximum and minimum values can be optimized or fixed at some value in between the maximum and minimum. Some parameters were not extended to exactly 0 or 1 because the analysis code still assumed some component was present, even if it was essentially non-participating. The maximum system pressure was limited to 35 MPa. A maximum temperature of the cycle was 923 K [650°C] and the minimum temperature 320 K [47°C]. This maximum was believed to be a reasonable one for concentrating solar power applications, and the minimum temperature relevant to the desert operating environments in which a concentrating solar power plant would operate. Fixed turbomachinery component efficiencies were established based on guidance by Dr. Mark Turner. A minimum temperature difference of 5 K, which was used for all CO_2 to CO_2 heat exchangers, was believed to be a reasonable compromise between high effectiveness and cost (Heatric actually advertises counterflow heat exchangers capable of the temperature and pressure ranges needed with approach temperatures as low as 2 K[37]). All results refer to these default parameters unless otherwise specified.

Parameter	Minimum	Maximum
PreCompressor Pressure Ratio	1.0	4.0
Main Compressor Pressure Ratio	1.1	4.1
Recompression Fraction	0.000	0.991
Low Temperature Recuperator Main Fraction High Pressure Component Mass Fraction	0.001	0.991
Main Compressor Outlet Pressure	2 MPa	35 MPa
Maximum Temperature	923 K [650°C]	923 K [650°C]
Minimum Temperature	320 K [47°C]	320 K [47°C]
Main Compressor Isentropic Efficiency	0.850	0.850
PreCompressor Isentropic Efficiency	0.875	0.875
ReCompressor Isentropic Efficiency	0.875	0.875
Power Turbine Isentropic Efficiency	0.930	0.930
Main/Re/Pre Compressor Turbine Isentropic Efficiency	0.890	0.890
Heat Exchanger Minimum Temperature Difference	5 K	5 K
Heat Exchanger Pressure Drop	500 Pa/K	500 Pa/K

Table 2.2: Default Component Performances and Allowable Design Ranges

Parameter	Value
PreCompressor Pressure Ratio	1.7
Main Compressor Pressure Ratio	3.1
Recompression Fraction	35.5%
Low Temperature Recuperator Main Fraction High Pressure Component Mass Fraction	N/A
Main Compressor Outlet Pressure	34.9MPa
ReCompressor Pressure Ratio	3.1
Main/Re/Pre Compressor Turbine Pressure Ratio	1.7
Power Turbine Pressure Ratio	3.0
Main Compressor Back Work Ratio	10.6%
PreCompressor Back Work Ratio	10.6%
ReCompressor Back Work Ratio	11.0%
Total Back Work Ratio	32.2%
Medium Temperature Recuperator Effectiveness	95.9%
Medium Temperature Recuperator Fraction of Desired Heat Transferred	95.0%
High Temperature Recuperator Effectiveness	98.4%
High Temperature Recuperator Fraction of Desired Heat Transferred	83.6%
Medium Temperature Recuperator Heat Exchange Power/Heat Input Power	35.1%
High Temperature Recuperator Heat Exchange Power/Heat Input Power	102.0%
Total Recuperator Heat Exchange Power/Heat Input Power	137.1%
Specific Net Work	167.6 kJ/kg
Thermal Efficiency	49.6%
Exergy Efficiency	75.9%

Table 2.3: Optimized Cycle Independent and Dependent Variables

The optimized cycle configuration based on the default parameters listed in Table 2.2 are shown in Figures 2.13 through 2.22. A summary of the results of the optimization process as well as some key parameters are shown in Table 2.3. This optimized configuration resulted in no low temperature recuperators, just a medium and high temperature recuperator, and had a thermal efficiency of 49.6%. The optimized cycle's exergy efficiency was 75.9%. Other than the absence of the low temperature recuperators, the optimized cycle still featured a precompressor and a recompressor. The work required to power each of the small compressors was fairly similar at 10.6% for the main compressor and precompressor and 11.0% for the recompressor. The recompressor, despite only compressing 35.5% of the mass flow, had the highest work requirement due to its larger enthalpy rise for nearly the same pressure ratio as the main compressor. The power required to power all of the compressors (the back work ratio) was 32.2% of the total power extracted by the 4 turbines at the high temperature end of the cycle. The high temperature recuperator operated over a larger temperature range and also transferred more heat than the medium temperature recuperator. Both recuperators combined transferred 1.37 times the heat from the low pressure to high pressure side than is added to the high pressure side at the high temperature end of the cycle by the two external heaters (the primary heater and reheater). This large amount of recuperation makes it clear how critical the heat exchangers are in this cycle and why the pressure ratios of the turbomachinery components are much lower than more traditional engine types. The specific net work is 167.6 kJ/kg, which is a bit lower than more traditional engine types and is due to the low pressure ratios. Although the specific work is low, the fluid density is still relatively high throughout the entire cycle and therefore the overall power density of the entire engine will likely be much higher than other engine types. Assessing the practical power density of this type of cycle will require some component preliminary design.

In Section 2.3.4 it was mentioned that some small heaters and coolers were added if the heat exchanger inlet or outlet temperatures did not appropriately match up, due to the lack of a mixing model being implemented. Both mixing and the small heaters and coolers would be a poor design and therefore the optimization process naturally discouraged the use of the heaters and coolers. The optimized cycle configuration based on the default parameters listed in Table 2.2 was inspected and no small heaters and coolers actually existed. Other results which specifically vary some of the design parameters from the optimized design based on the default parameters may or may not have

the heaters or coolers, their designs have not yet been specifically inspected.

Figure 2.13 shows the thermodynamic states on a Temperature Entropy diagram ($T - s$). The contours in Figure 2.13 are colored by the specific heat of the fluid of all states within a certain range. Black lines indicate the thermodynamic states throughout the cycle and the numbered points indicate key component inlet and outlet states. Colored lines indicate constant pressure lines starting at each of these numbered state points, and the corresponding pressures are indicated in the legend. Because of the low pressure drop within many components, it is difficult to distinguish the difference in many of these constant pressure lines without magnifying the figure dramatically.

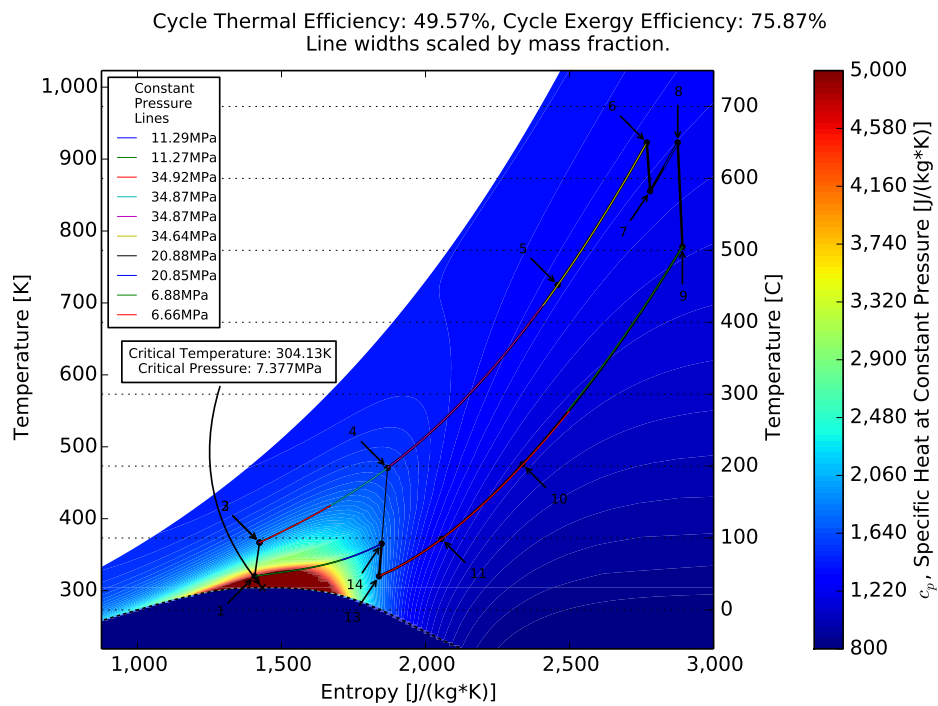


Figure 2.13: Temperature Entropy Diagram for the Proposed System Layout, Specific Heat at Constant Pressure Contour Level Background

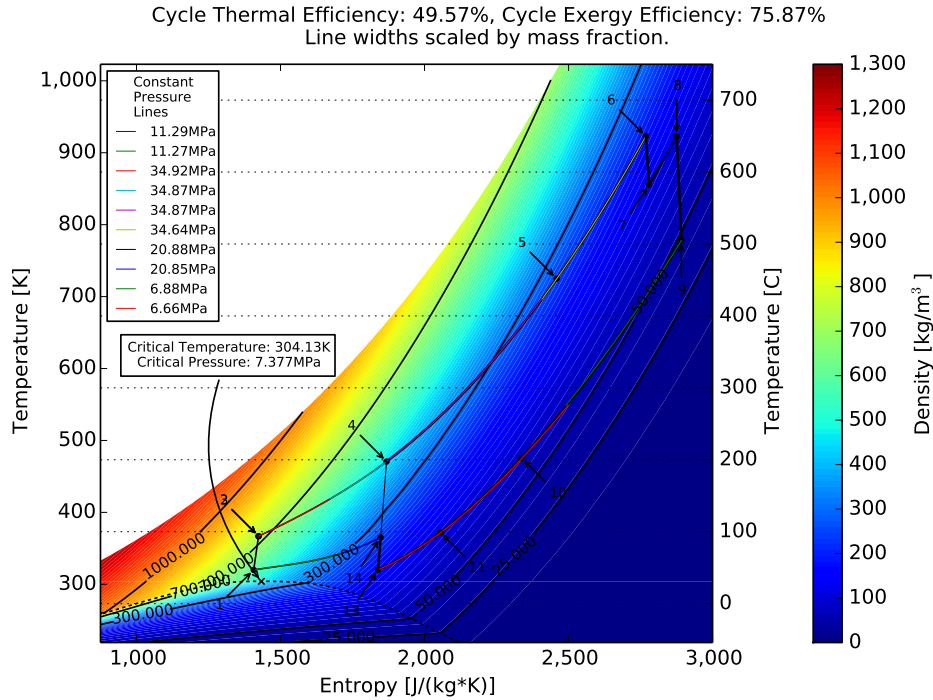


Figure 2.14: Temperature Entropy Diagram for the Proposed System Layout, Density Contour Level Background

Figures 2.14 to 2.17 represent the same layout, but different quantities, Density, Ratio of Specific Heats, Compressibility Factor, and Enthalpy are shown as the contour level backgrounds instead, also emphasizing the highly variable fluid properties. Figure 2.18 shows the cycle on an Enthalpy Entropy diagram with a Temperature contour level background. Figures 2.19 to 2.21 show the cycle layout on a Pressure Specific Volume diagram with Specific Heat at Constant Pressure, Entropy, and Temperature contour level backgrounds. Figure 2.22 is similar to 2.13, except the horizontal axis is pressure instead of Entropy. The fluid type for each region is also labeled. The liquid vapor dome is collapsed to a single line in Temperature Pressure ($T - p$) diagrams.

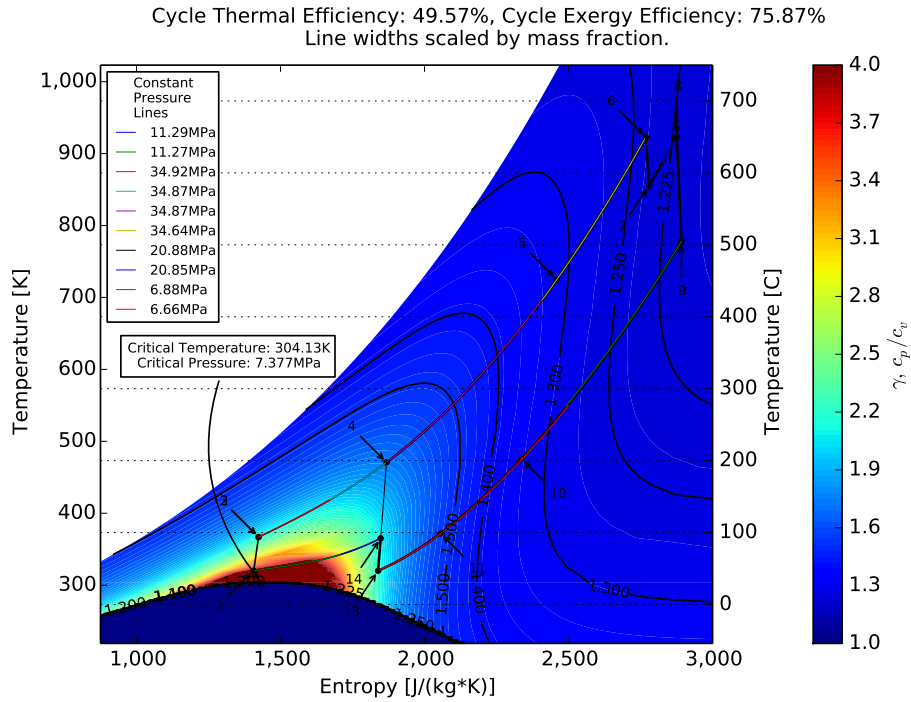


Figure 2.15: Temperature Entropy Diagram for the Proposed System Layout, Ratio of Specific Heat at Constant Pressure to the Specific Heat at Constant Volume Contour Level Background

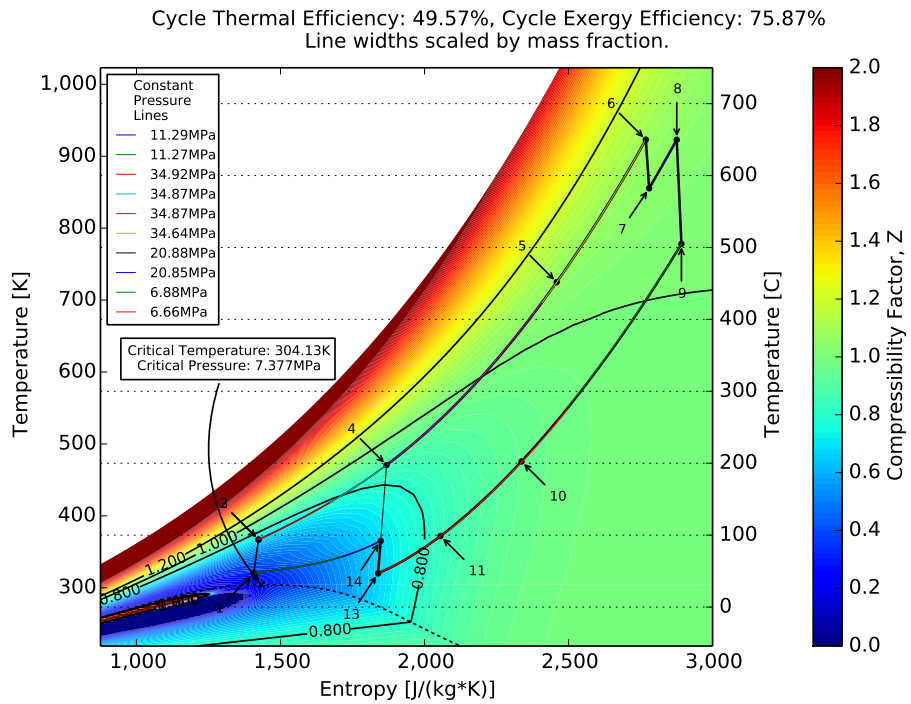


Figure 2.16: Temperature Entropy Diagram for the Proposed System Layout, Compressibility Factor Contour Level Background

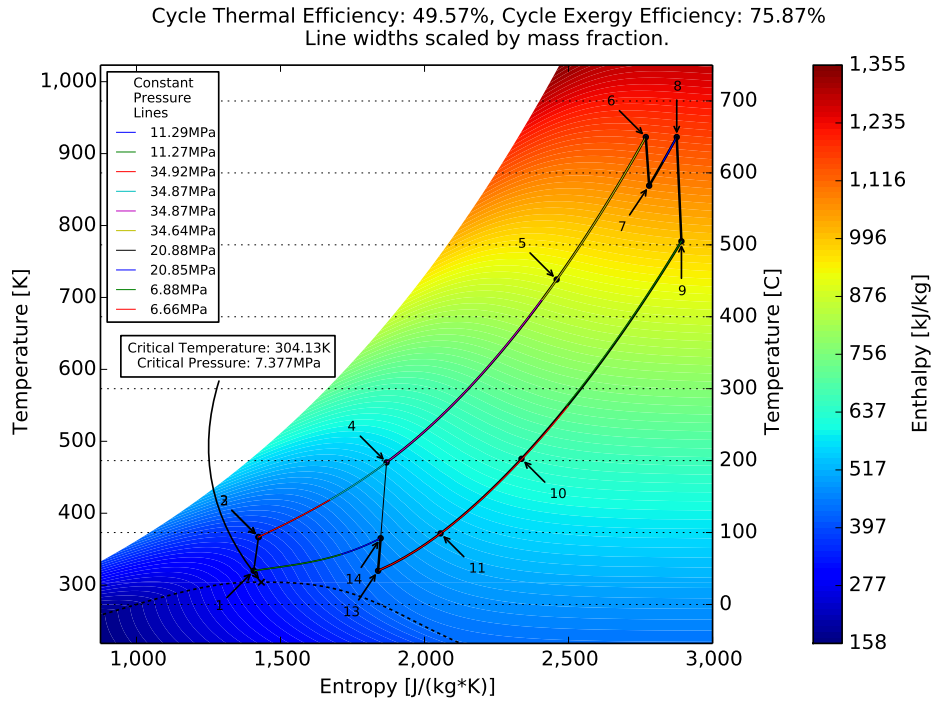


Figure 2.17: Temperature Entropy Diagram for the Proposed System Layout, Enthalpy Contour Level Background

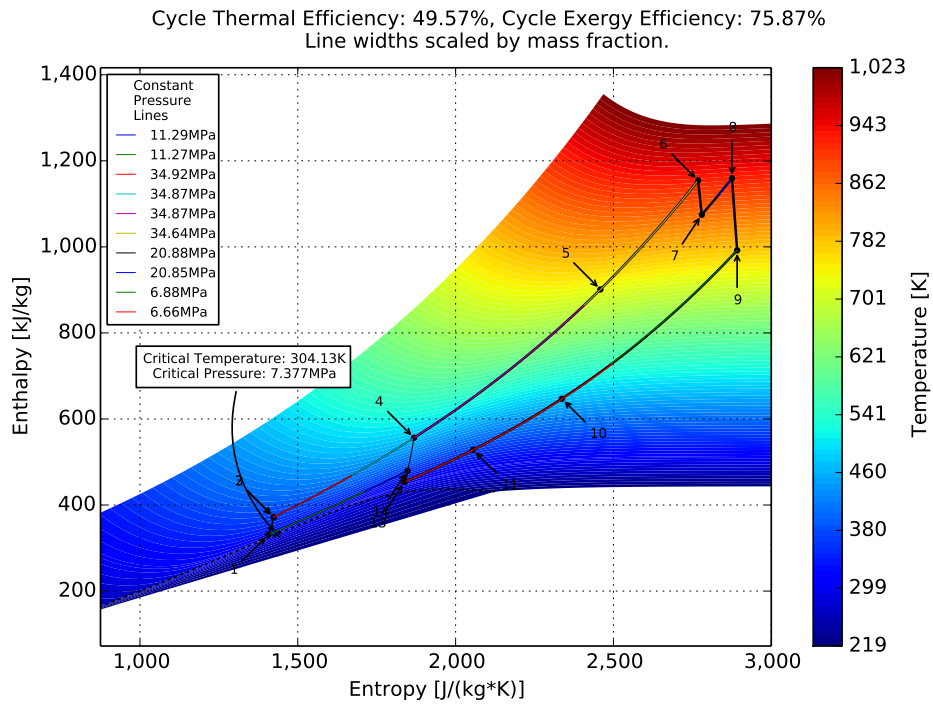


Figure 2.18: Enthalpy Entropy Diagram for the Proposed System Layout, Temperature Contour Level Background

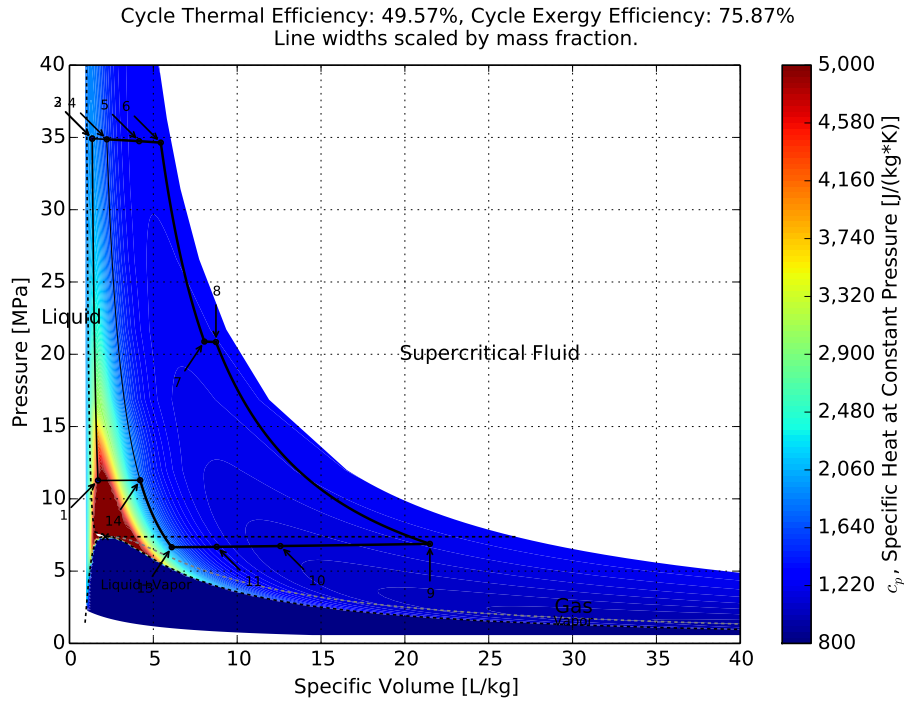


Figure 2.19: Pressure Specific Volume Diagram for the Proposed System Layout, Specific Heat at Constant Pressure Contour Level Background

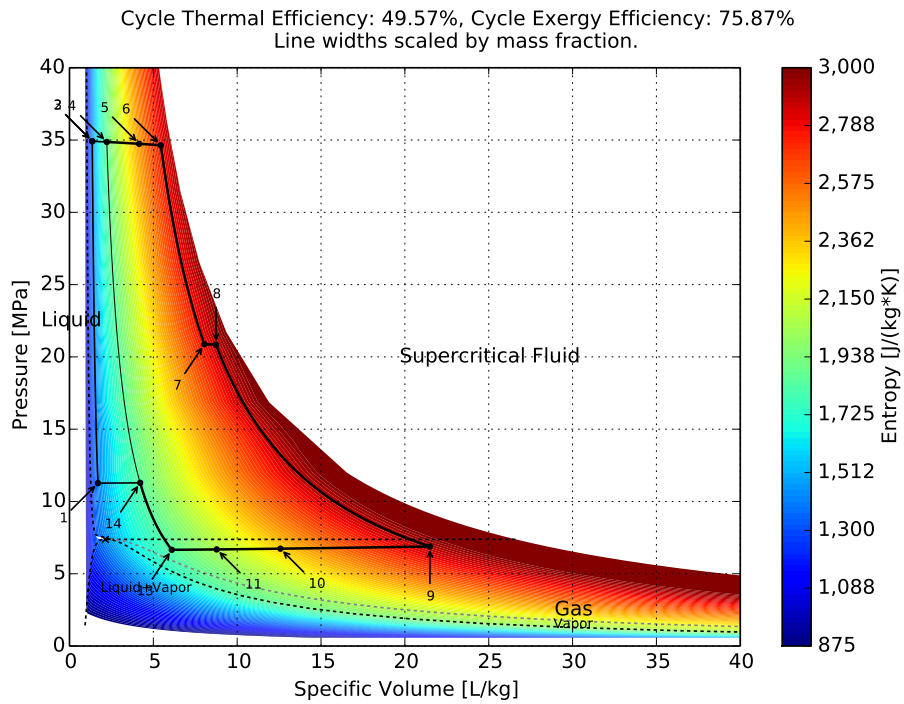


Figure 2.20: Pressure Specific Volume Diagram for the Proposed System Layout, Entropy Contour Level Background

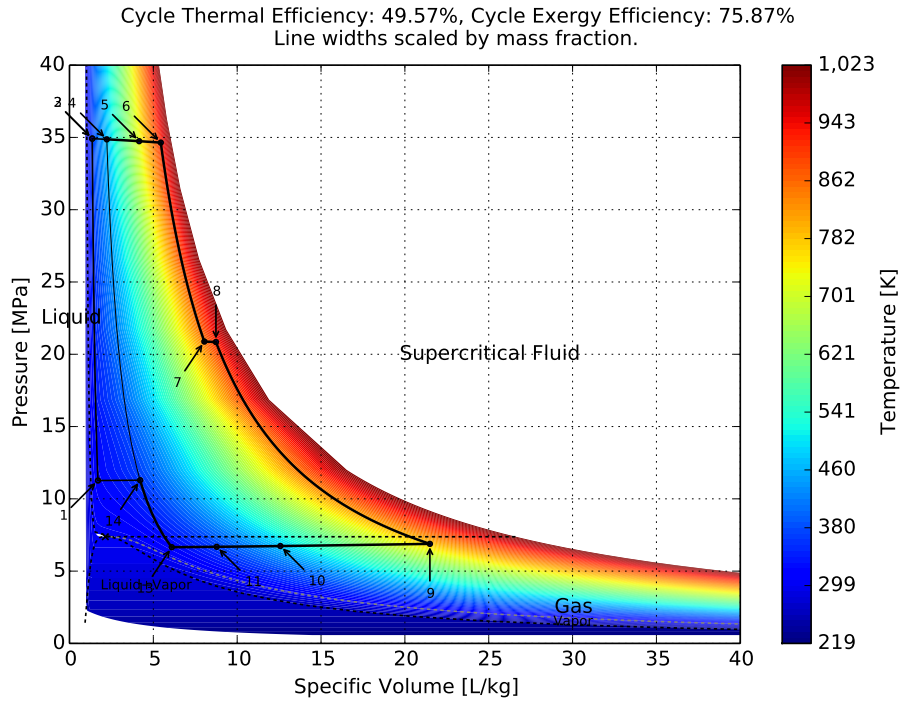


Figure 2.21: Pressure Specific Volume Diagram for the Proposed System Layout, Temperature Contour Level Background

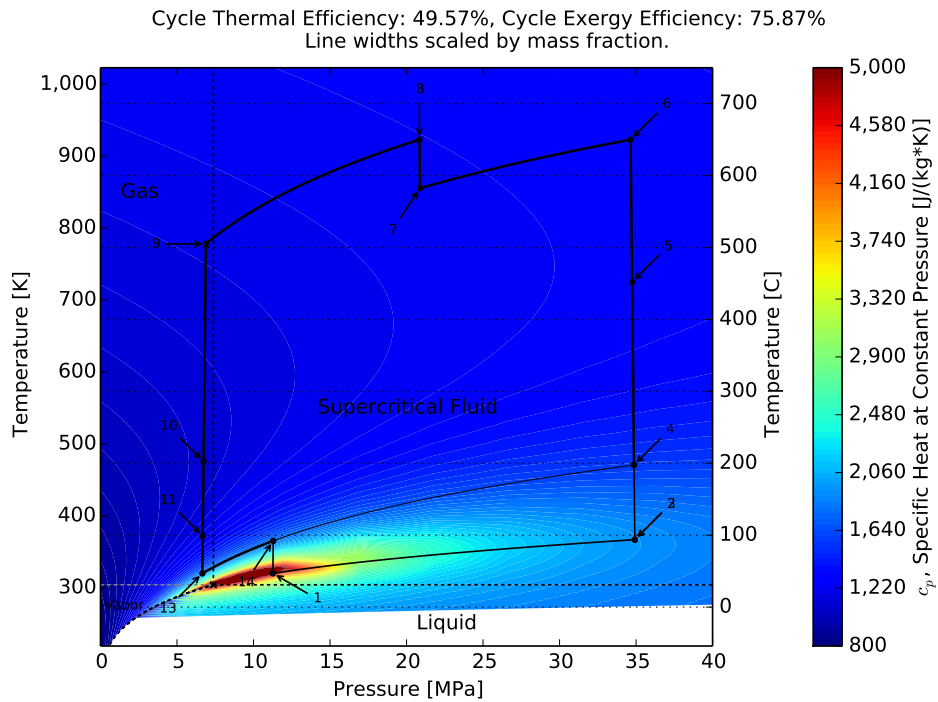


Figure 2.22: Temperature Pressure Diagram for the Proposed System Layout, Specific Heat at Constant Pressure Contour Level Background

Figures 2.23 through 2.48 show additional results that sweep some of the values shown in Table 2.2. Contour plots in this section include dots overlaid over the contour. These dots indicate the data points and all contour values in between the dots have been interpolated.

Figure 2.23 shows the variation in cycle efficiency with respect to the maximum cycle temperature and the minimum cycle temperature. The minimum temperature is swept from 306 K up to 328 K. The maximum temperature is swept from 423 K to 923 K. When the minimum temperature is reduced below the default minimum temperature of 320 K, the cycle efficiency can increase above 50%. Over the wide range of maximum temperatures, the cycle efficiency is non-linearly related to the maximum temperature. A maximum temperature of 423 K results in a cycle efficiency below 15% for minimum temperatures above 310 K. Figure 2.24 shows the variation in cycle exergy efficiency over the same range of minimum and maximum temperatures as in Figure 2.23. According to the results, at intermediate maximum temperatures, there appears to be less sensitivity to the minimum temperature at higher minimum temperatures. Figure 2.25 shows the optimal recompression fraction as it varies significantly with maximum and minimum temperature. Figure 2.26 shows that the optimal main compressor outlet pressure is dependent upon the minimum and maximum temperature.

Figures 2.27 and 2.28 show the cycle efficiency vs pressure ratios. Figure 2.27 is for the default minimum temperature difference of 5 K, and Figure 2.28 is for a minimum temperature difference approaching 0. Both feature similar shapes with different magnitudes. The case with a 5 K minimum temperature difference does have a bit different shaped local maxima near the low pressure ratios. A main take away from Figure 2.27 is that eliminating one of the compressors (i.e. the condition where pressure ratio is 1) will result in several percentage point reduction in overall cycle efficiency, and that when both compressors are used, there is a wide range of combinations of precompressor and main compressor pressure ratios that can give similar cycle efficiencies. Figure 2.29 shows the optimal recompression as it varies with pressure ratios. The sharp discontinuity between 0 and 1 at low precompressor pressure ratios can be explained because as the precompressor pressure ratio approaches 1, the recompressor moves closer and closer to the main compressor and they essentially are nearly the same thing. The optimizer is likely bouncing back and forth between the two possible solutions.

Maximum Thermal Efficiency=52.28%

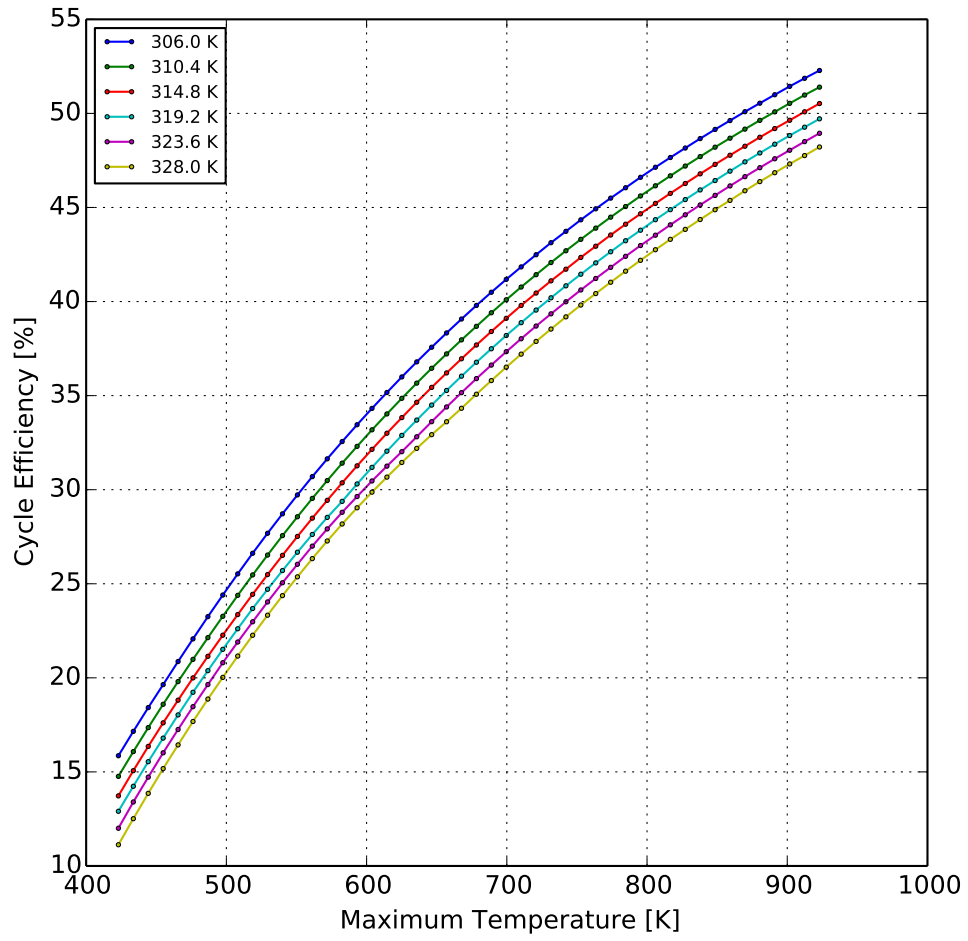


Figure 2.23: Cycle Efficiency vs Maximum and Minimum Temperature

Maximum Exergy Efficiency=78.21%

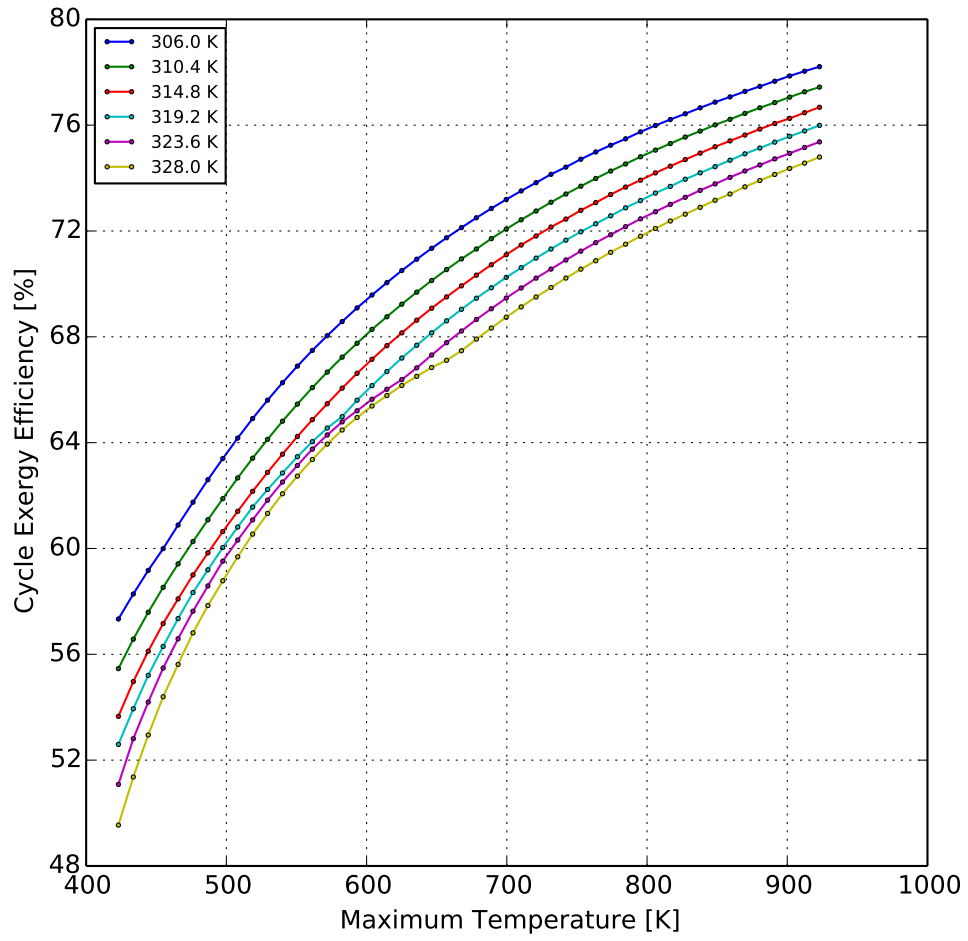


Figure 2.24: Cycle Exergy Efficiency vs Maximum and Minimum Temperature

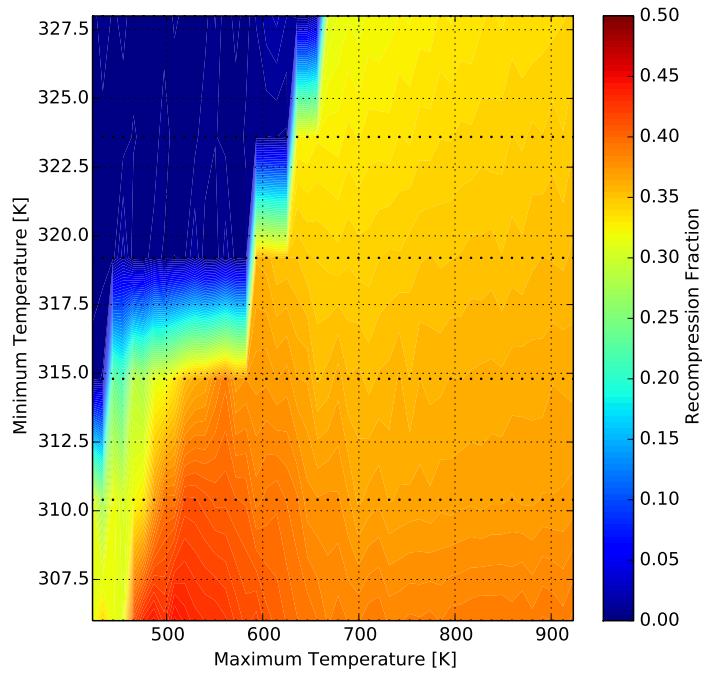


Figure 2.25: Optimal ReCompression Fraction vs Maximum and Minimum Temperatures

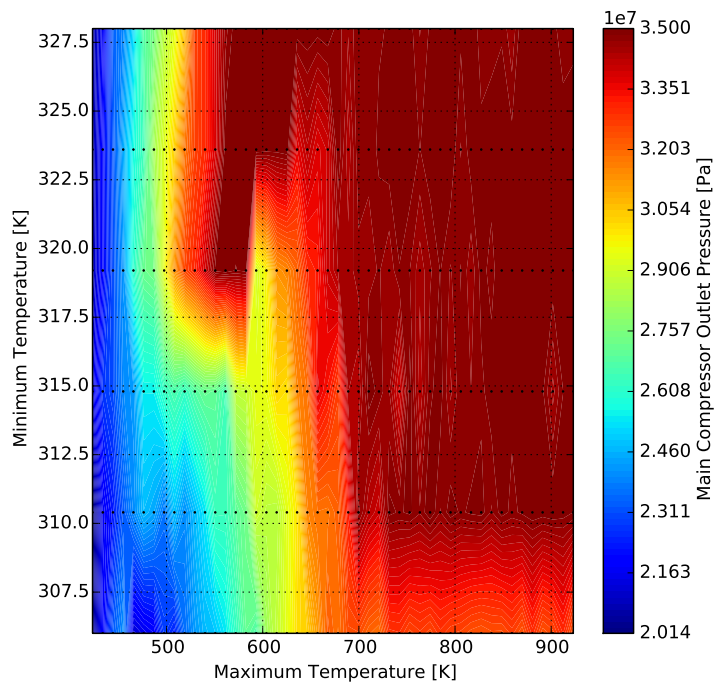


Figure 2.26: Optimal Main Compressor Outlet Pressure vs Maximum and Minimum Temperatures

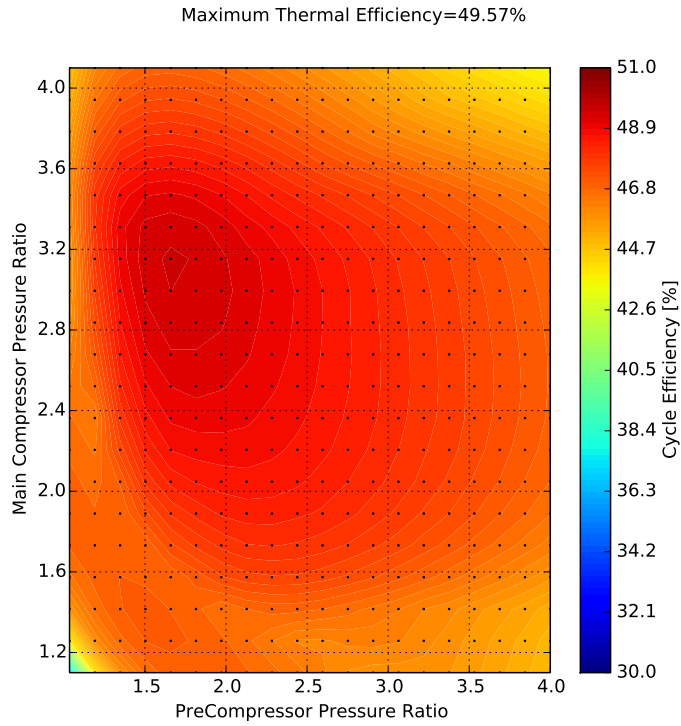


Figure 2.27: Cycle Efficiency vs PreCompressor and Main Compressor Pressure Ratios

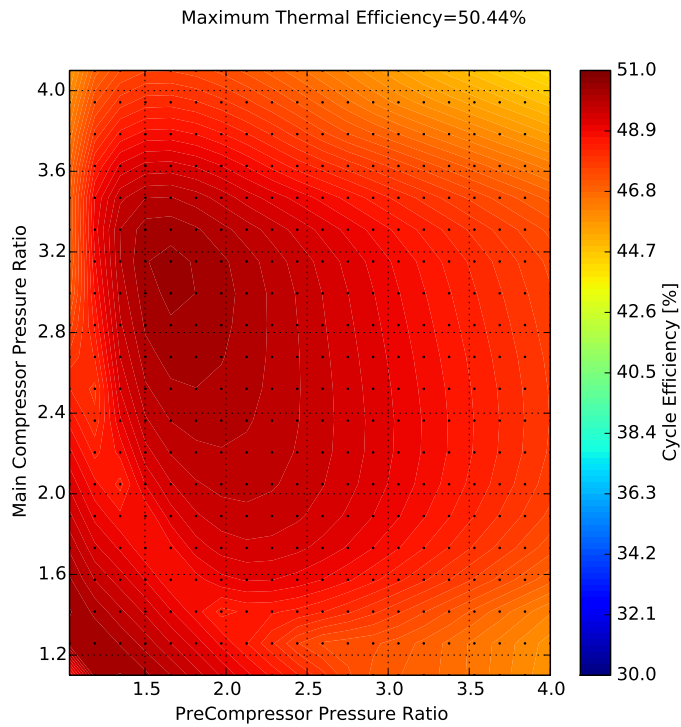


Figure 2.28: Cycle Efficiency vs PreCompressor and Main Compressor Pressure Ratios, With a Nearly Zero Heat Exchanger Minimum Temperature Difference

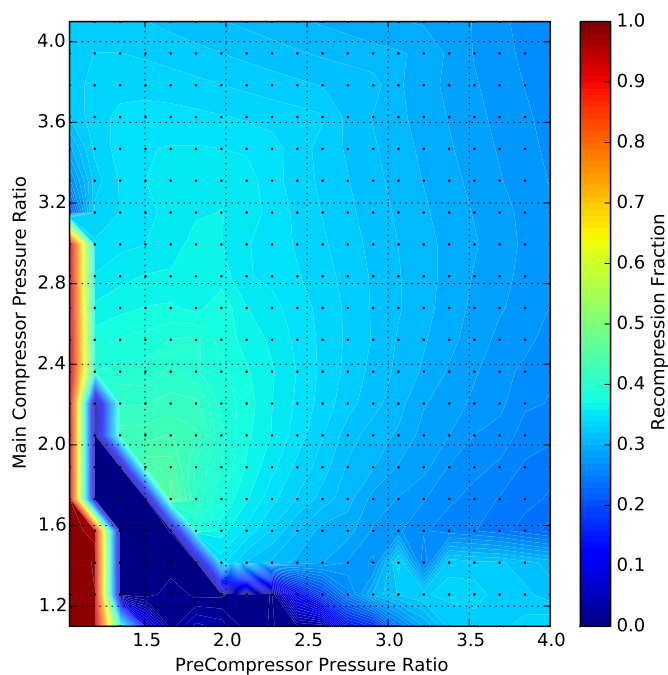


Figure 2.29: Optimal ReCompression Fraction vs PreCompressor and Main Compressor Pressure Ratios

Figure 2.30 shows the variation in cycle efficiency with both the heat exchanger minimum temperature difference and the heat exchanger pressure drop coefficient. At low temperature differences and low pressure drops, there is some unusual behavior. It is not believed to be due to a lack of optimizer convergence. Two different optimization runs with different random starting populations were used and both exhibited nearly the same unusual result. Further efforts were not pursued to assess this behavior because the variation is not extreme and the case with zero pressure drop heat exchangers is not physically realistic anyway.

Figure 2.31 shows the efficiency vs recompression fraction. It's clearly evident that the design is very sensitive to the optimal recompression fraction. A reduction in efficiency of nearly 2.5 percentage points can result if no recompression is used. Figure 2.32 shows the optimal main compressor pressure ratio for each recompression fraction. It's evident that there is a considerable amount of noise in the solution due to a combination of the optimizer not being completely converged and the sensitivity to the main compressor pressure ratio being low. A similar conclusion can be made when reviewing Figures 2.33 and 2.34.

Maximum Thermal Efficiency=53.89%

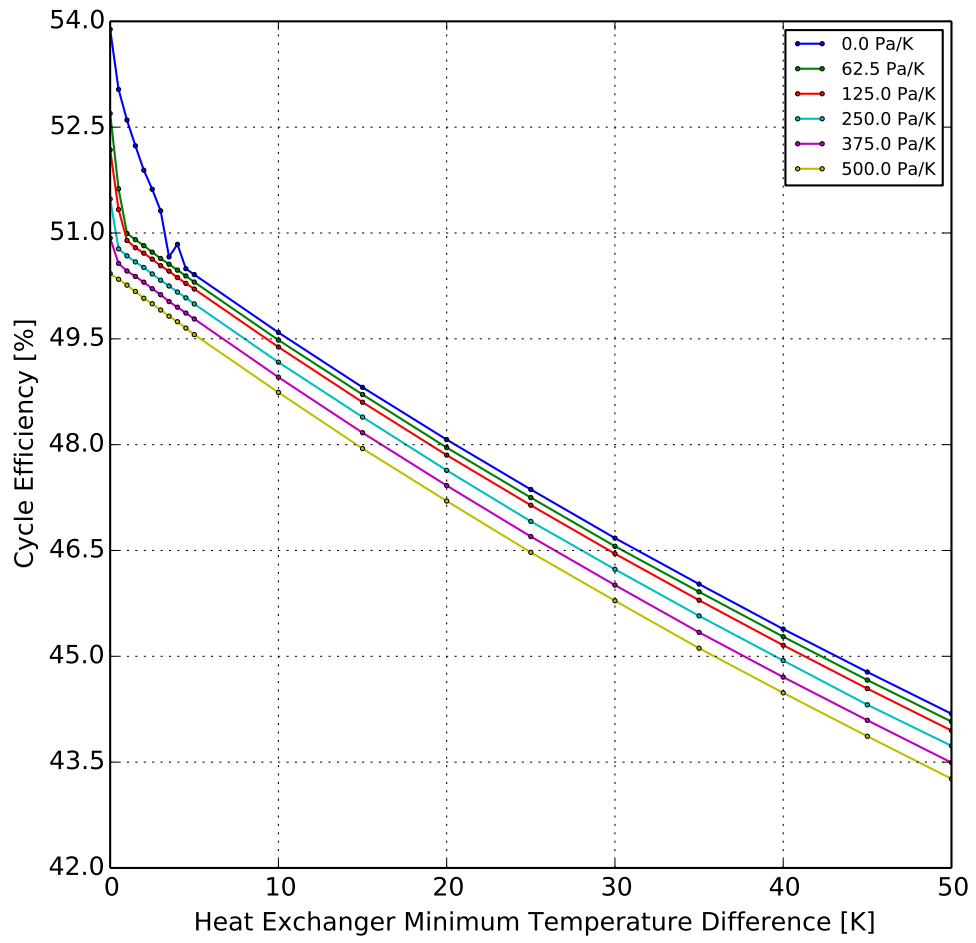


Figure 2.30: Cycle Efficiency vs Heat Exchanger Minimum Temperature Difference

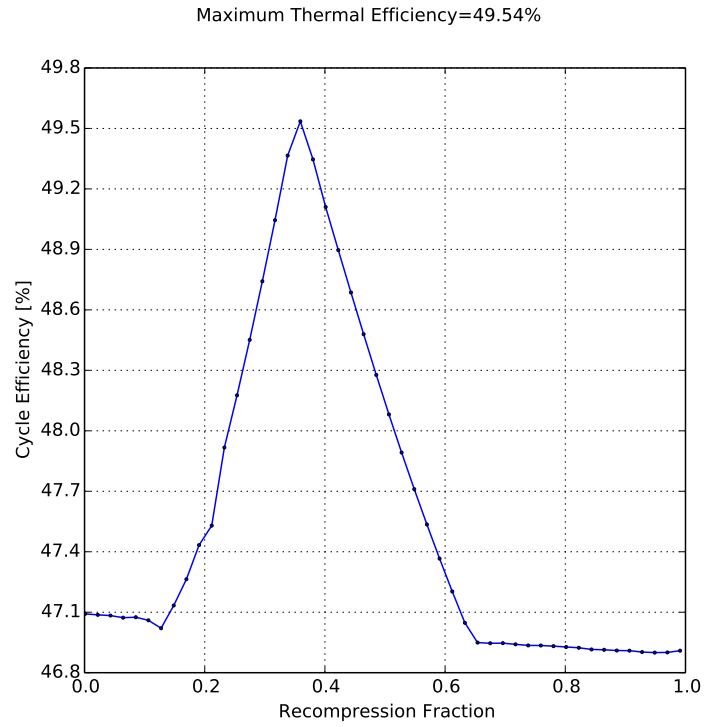


Figure 2.31: Cycle Efficiency vs ReCompression Fraction

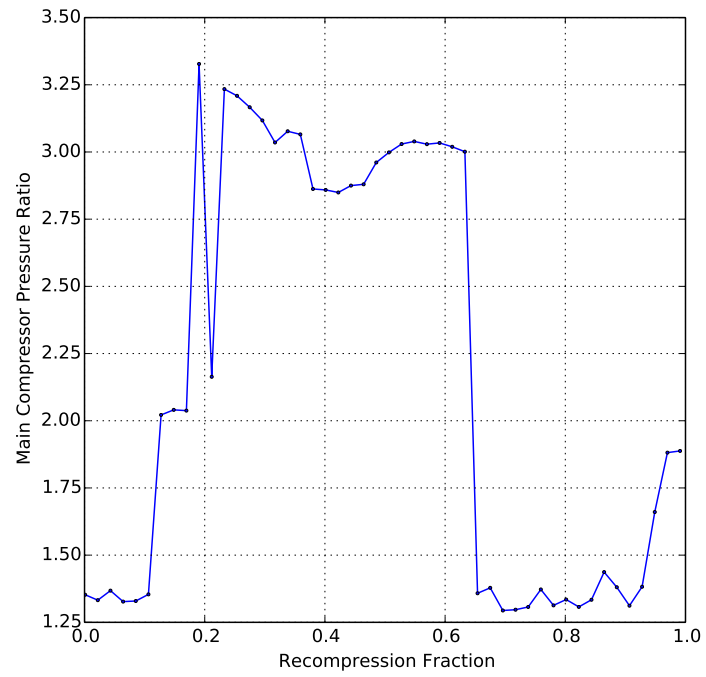


Figure 2.32: Optimal Main Compressor Pressure Ratio vs ReCompression Fraction

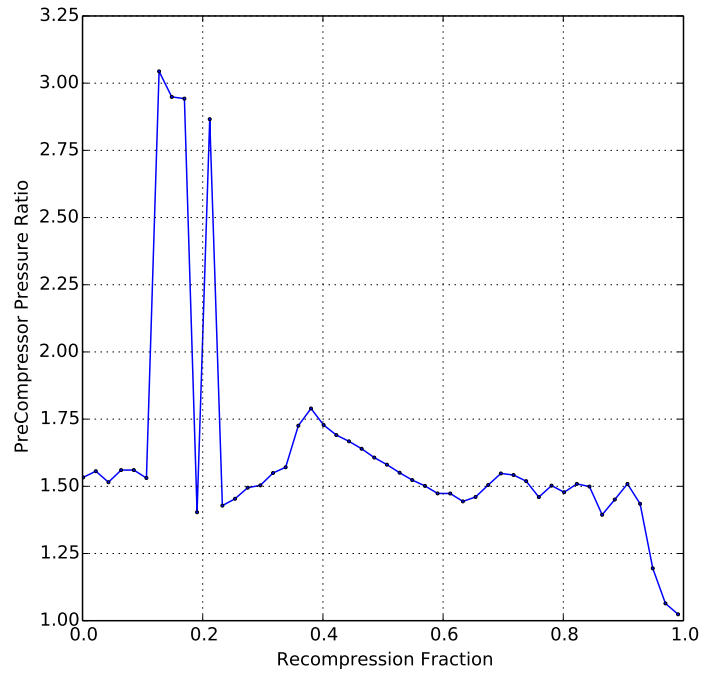


Figure 2.33: Optimal PreCompressor Pressure Ratio vs ReCompression Fraction

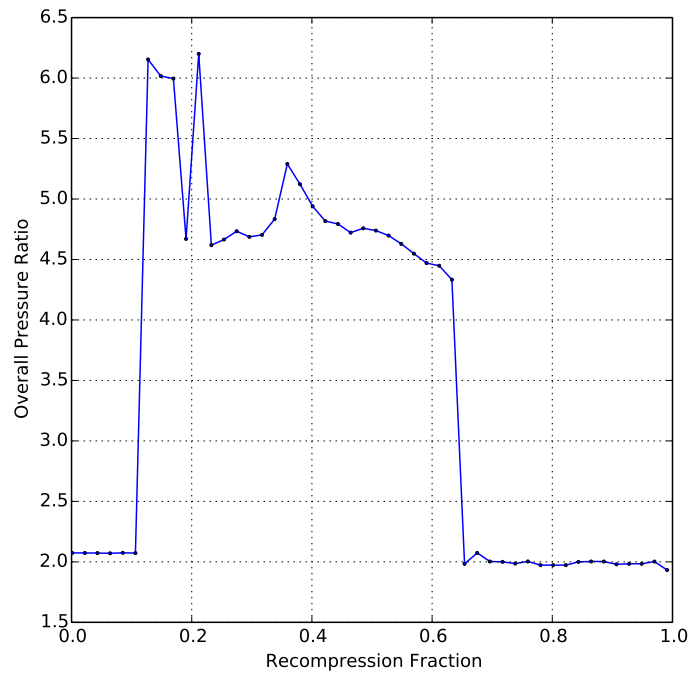


Figure 2.34: Optimal Overall Pressure Ratio vs ReCompression Fraction

Figure 2.35 shows the cycle efficiency vs main compressor outlet pressure. The pressure is swept from 2 MPa up beyond the default maximum pressure of 35 MPa, all the way to 49 MPa. As can be seen, the cycle efficiency continues to increase all the way up to 49 MPa, although the gains begin to diminish around 20 MPa. However, when comparing to Figure 2.26, it's evident that the relationship in Figure 2.35 will change with minimum and maximum temperature, and there is at least a local (and possibly global) optimal main compressor outlet pressure for lower minimum and maximum temperatures. Figure 2.36 shows that the optimal main compressor pressure ratio decreases up to approximately 12 MPa and then begins to increase after 12 MPa all the way up to 49 MPa. The optimal precompressor pressure ratio, shown in Figure 2.37 appears to be a noisier relationship, but appears to be a maximum around 17 MPa. Figure 2.38 then shows the optimal overall pressure ratio, which is the result of multiplying the data in Figures 2.36 and 2.37.

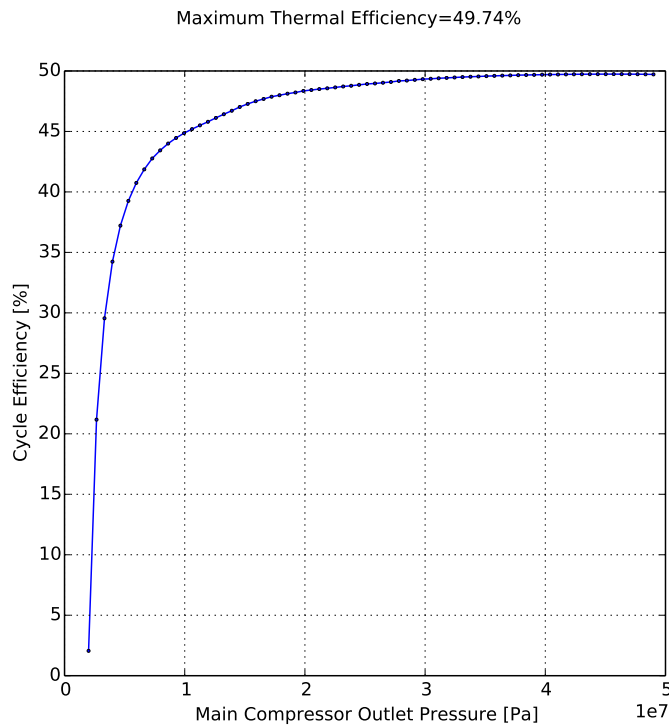


Figure 2.35: Cycle Efficiency vs Main Compressor Outlet Pressure

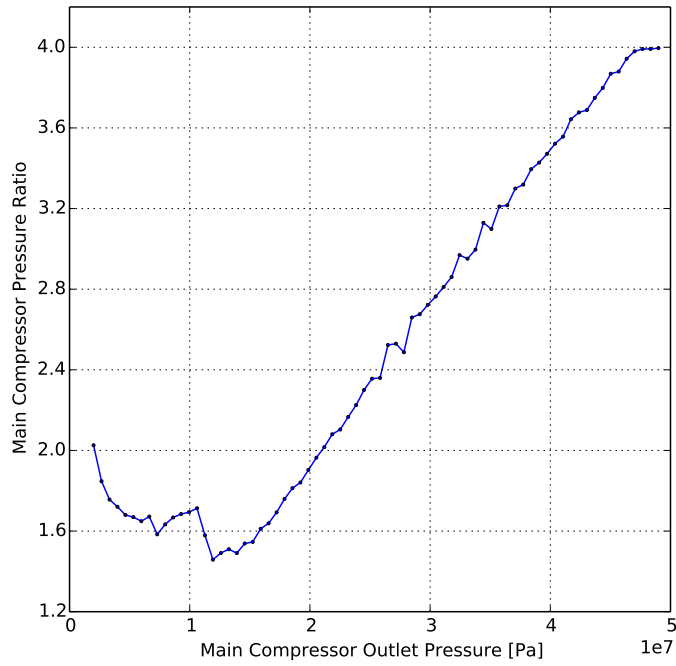


Figure 2.36: Optimal Main Compressor Pressure Ratio vs Main Compressor Outlet Pressure

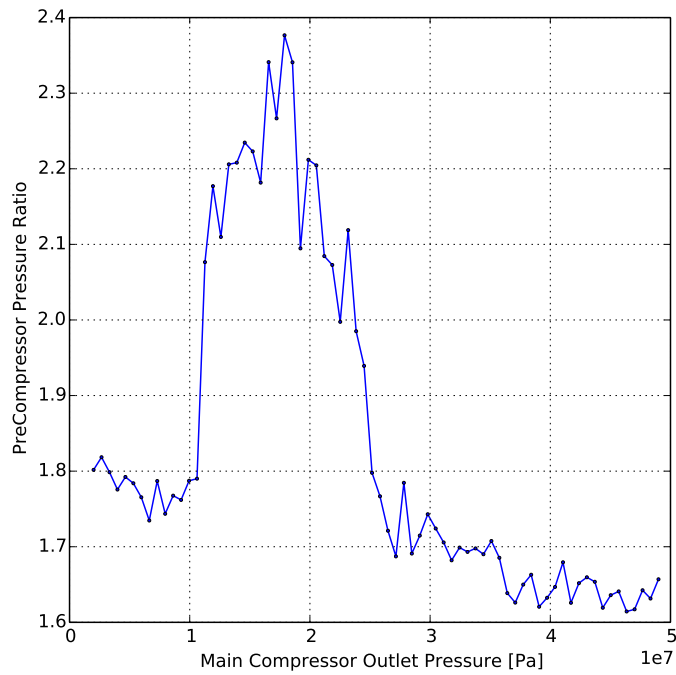


Figure 2.37: Optimal PreCompressor Pressure Ratio vs Main Compressor Outlet Pressure

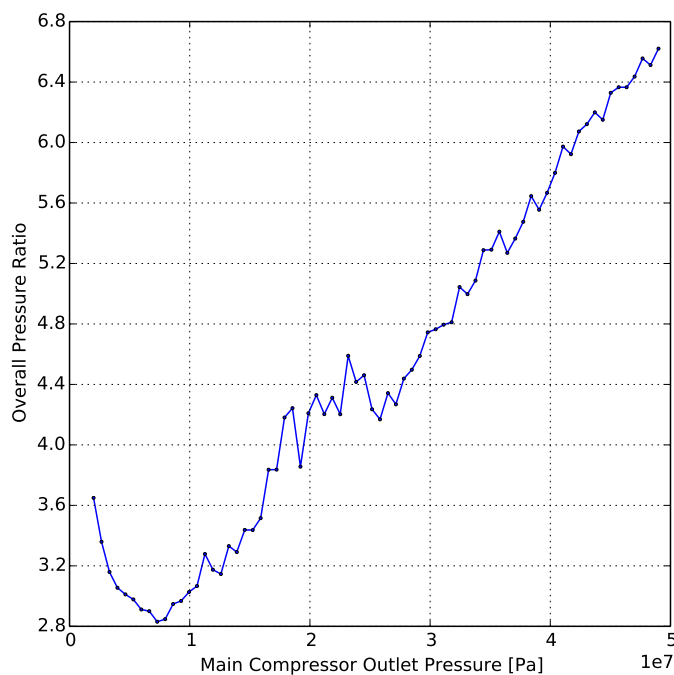


Figure 2.38: Optimal Overall Pressure Ratio vs Main Compressor Outlet Pressure

In order to assess the feasibility of using a positive displacement compressor as a main compressor where the design of a turbomachinery device may be very challenging near the critical point, a parameter sweep of main compressor isentropic efficiency was conducted over a very wide range and the resulting cycle efficiency is shown in Figure 2.39. Two scenarios are considered in Figure 2.39. The first is a main compressor powered by a dedicated turbine, which was previously described. The second is a main compressor that is powered by the power turbine. In the case where the main compressor is powered by the power turbine, the efficiency should be interpreted to be the combined efficiency of the compressor and motor driving the compressor, and generator that is attached to the power turbine. Caution should also be taken when interpreting the results. The present cycle analysis code only considers fixed turbomachinery efficiencies, and therefore the turbomachinery efficiencies are not dependent on the operating range. The operating range can change, however, based on the other design parameters. In the case of a reduced main compressor efficiency, the optimization process will tend to prefer a higher recompression fraction as the main compressor efficiency drops. As the recompression fraction rises, the precompressor pressure ratio will then be reduced and the precompressor inlet pressure increased in order to move the recompressor

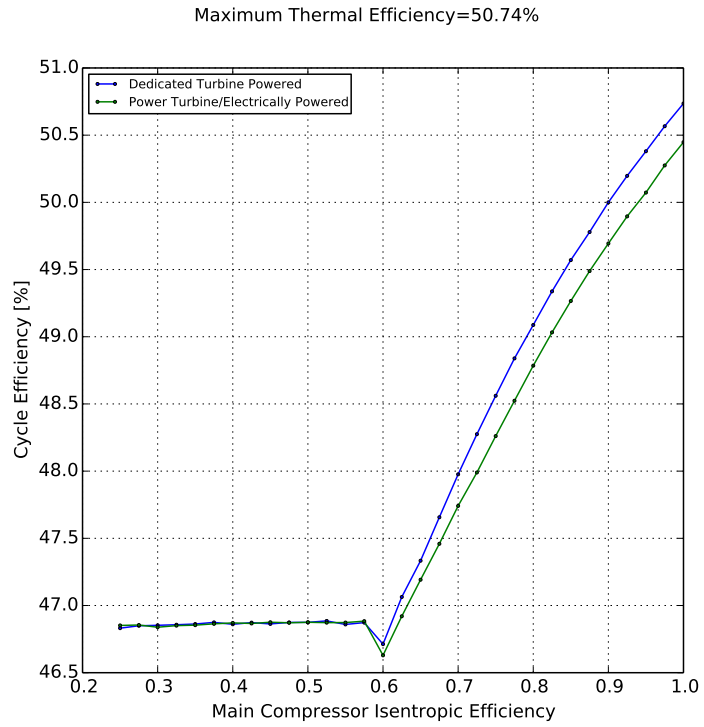


Figure 2.39: Cycle Efficiency vs Main Compressor Isentropic Efficiency

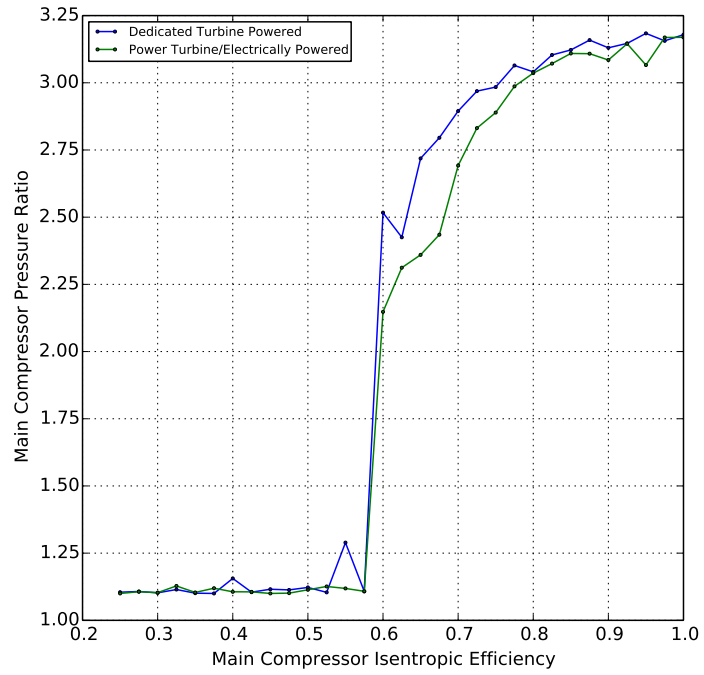


Figure 2.40: Optimal Main Compressor Pressure Ratio vs Main Compressor Isentropic Efficiency

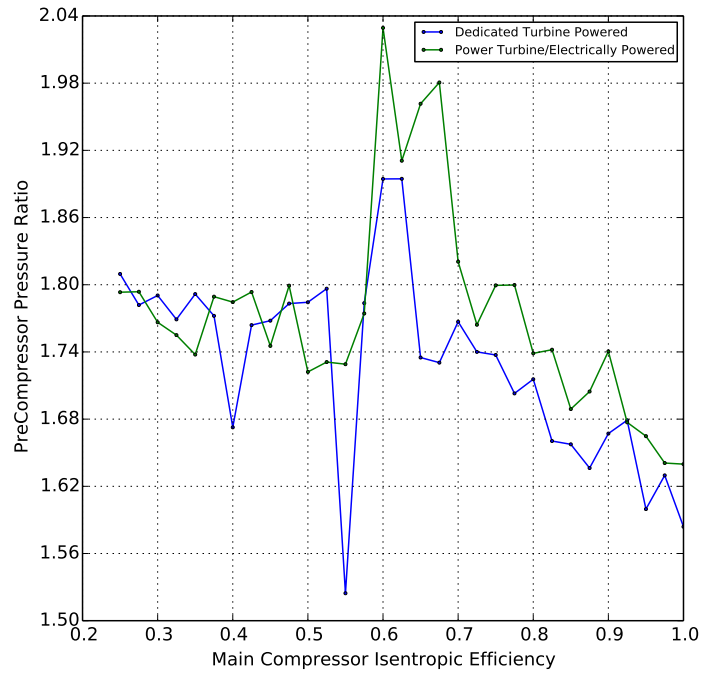


Figure 2.41: Optimal PreCompressor Pressure Ratio vs Main Compressor Isentropic Efficiency

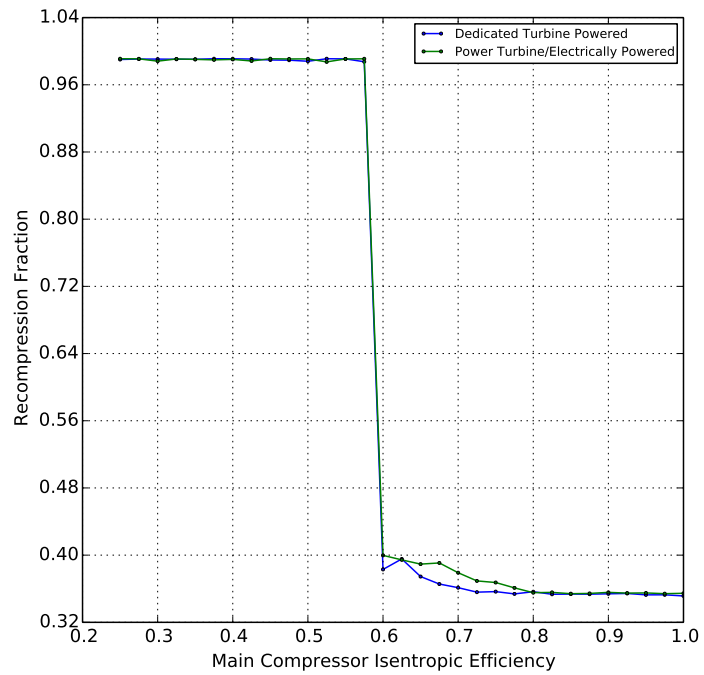


Figure 2.42: Optimal Recompression Fraction vs Main Compressor Isentropic Efficiency

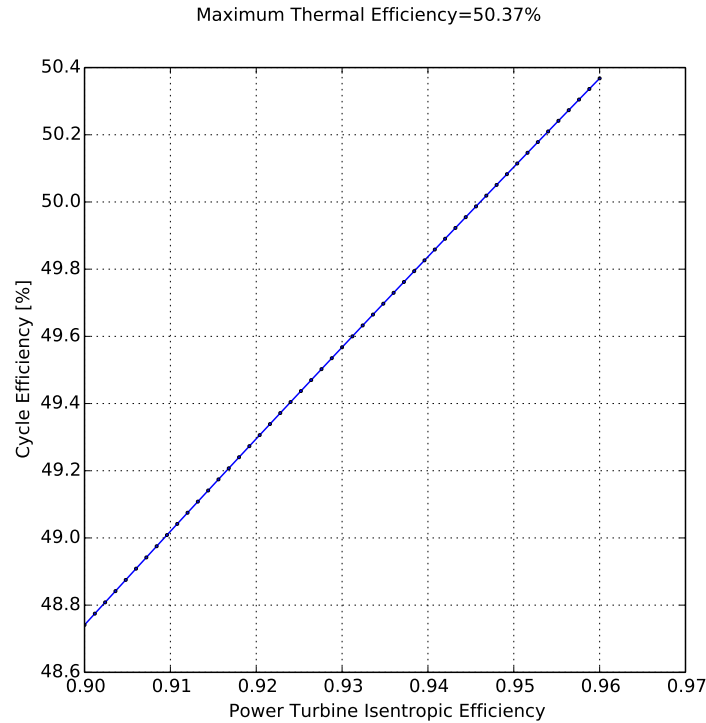


Figure 2.43: Cycle Efficiency vs Power Turbine Isentropic Efficiency

inlet to a lower entropy level. As the optimizer drives the recompressor in this direction, it gets closer to the critical point and is then in the region of wild fluid property variation and using a component isentropic efficiency that is no longer appropriate. An alternate scenarios is that the main compressor and recompressor pressure ratio is decreased as low as possible and then the precompressor is moved to the same operating range as the main compressor. As a result of this deficiency in the optimization processes, it's recommended not to consider results below main compressor isentropic efficiencies of 70%. It is readily evident in Figure 2.40 that the main compressor pressure ratio rapidly decreases below 70% efficiency, and the precompressor pressure ratio is shown to go up below 70% efficiency in Figure 2.41. Figure 2.42 shows an abrupt increase in recompression fraction below 70% main compressor isentropic efficiency.

Figure 2.43 shows the sensitivity of the cycle thermal efficiency to the power turbine isentropic efficiency. The results were obtained in a slightly different way than all of the other parameter sweeps that are presented. One will notice that the range of power turbine isentropic efficiencies is quite low and there is no optimizer “noise”. There was no optimization conducted. Because of the small range explored, the cycle design was fixed to that which is presented in Figures 2.13 through

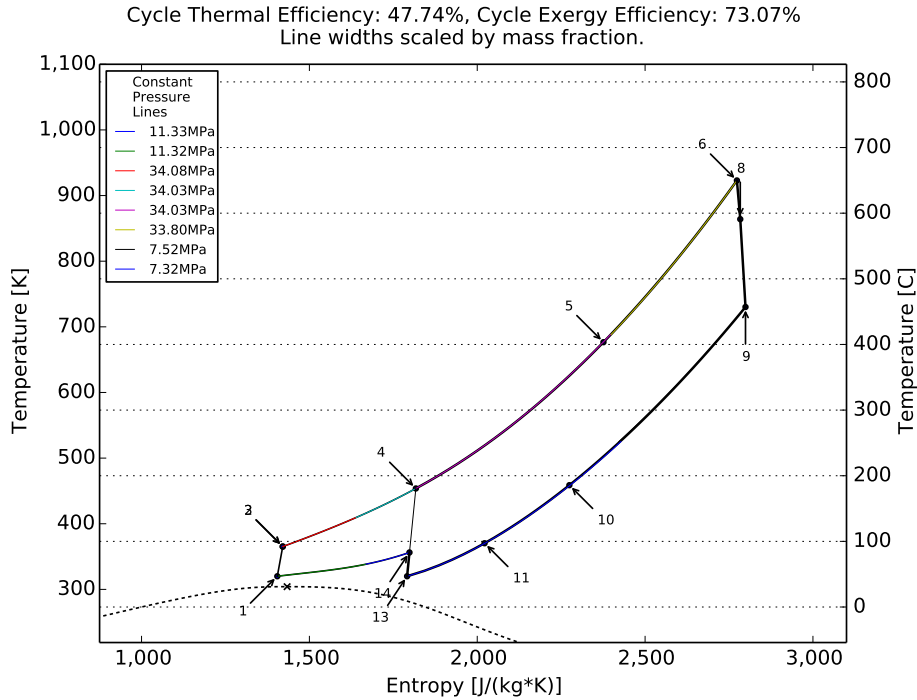


Figure 2.44: Temperature Entropy Diagram for the System Layout Without Reheat

2.22. Only the power turbine isentropic efficiency was changed during this parameter sweep. Figure 2.43 shows a very linear relationship between the power turbine isentropic efficiency and the overall cycle thermal efficiency over this small range. For every 1 percentage point increase in power turbine isentropic efficiency there is 0.26667 percentage point increase in cycle thermal efficiency.

Another study was conducted to assess the impact of reheat on the cycle efficiency. The default cycle described previously included a single reheat stage. That single reheat stage can be eliminated. On the contrary, additional reheat stages can be added. Figure 2.44 shows an optimized cycle with no reheat stages. Figure 2.45 is the default case presented in Figures 2.13 through 2.22, without the contour level background. The most innovative way to increase the number of reheat stages would be to integrate heat exchangers into the stator vanes of each stage in the power turbine. Such a design could be even more possible using additive manufacturing processes in order to open up the design space of the hybrid heat exchanger stator. It's most likely that the power turbine would be a three stage turbine, and therefore, two additional reheat stages could be added in the second and third turbine stages. Figure 2.46 shows an optimized cycle with two reheat stages added in between turbine stages in the power turbine. Figure 2.47 shows an optimized cycle with five reheat stages

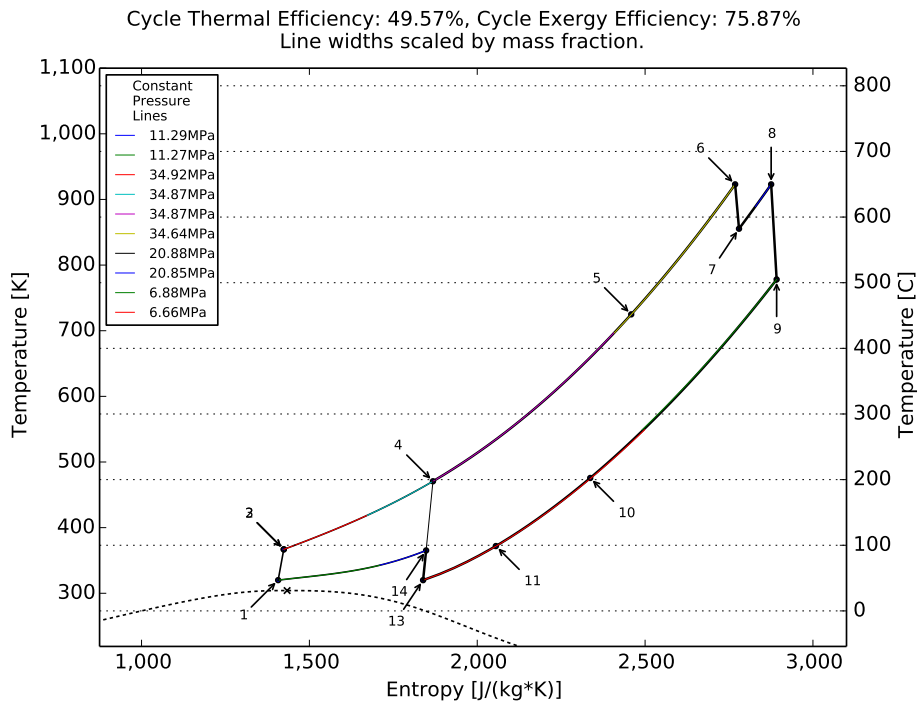


Figure 2.45: Temperature Entropy Diagram for the System Layout With Reheat

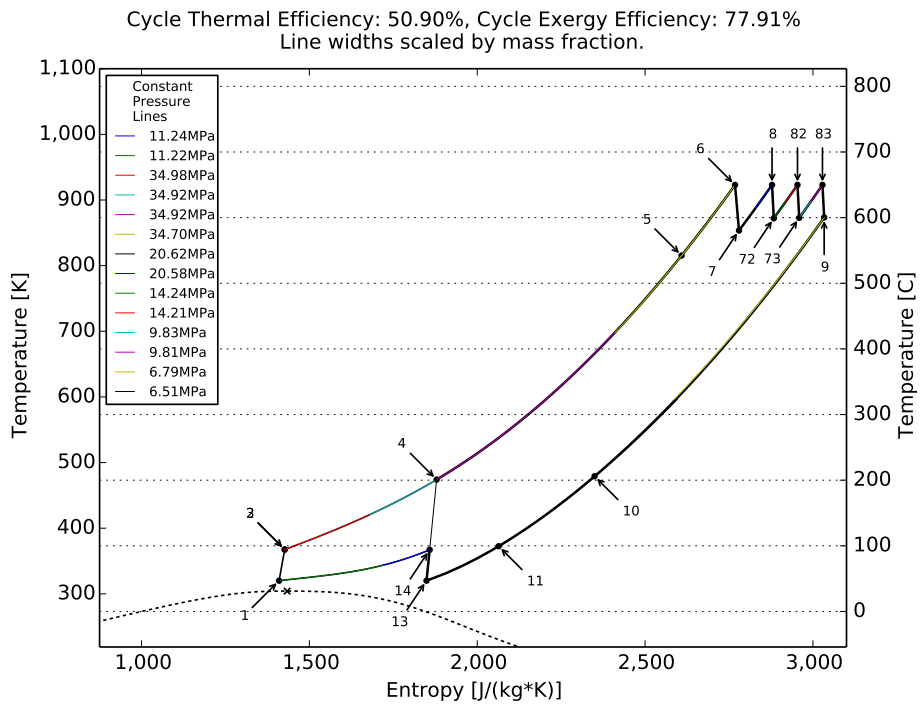


Figure 2.46: Temperature Entropy Diagram for the System Layout With Reheat and 2 InterTurbine Reheat Stages

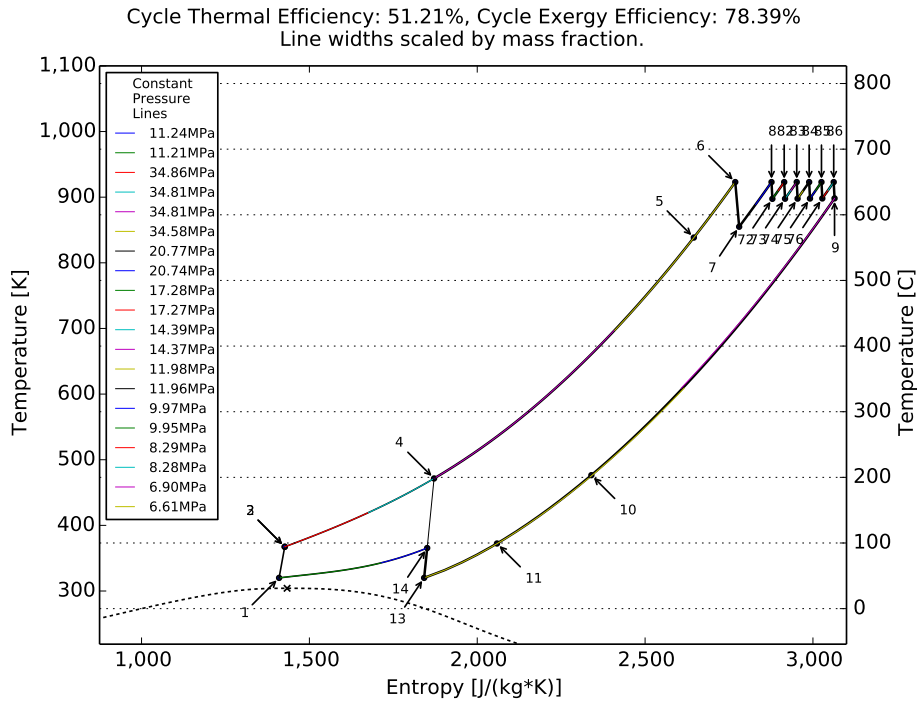


Figure 2.47: Temperature Entropy Diagram for the System Layout With Reheat and 5 InterTurbine Reheat Stages

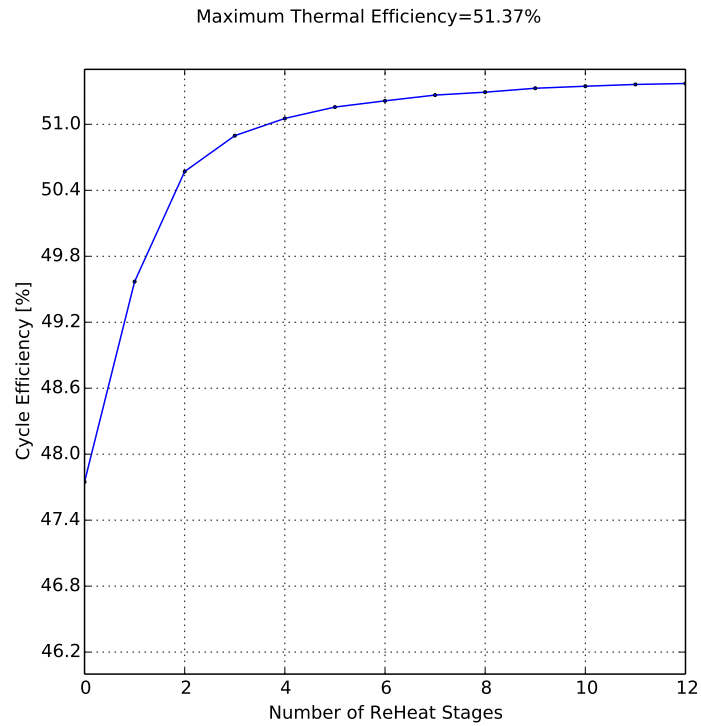


Figure 2.48: Cycle Efficiency vs Number of Reheat Stages

added in between turbine stages in the power turbine.

Figure 2.48 summarizes the impact of the number of reheat stages on cycle performance. Although 0, 1, and 3 reheat stages are the most likely, values for 0 through 12 are still plotted as a reference. The most significant increase is from 0 to 1 reheat stage. After 3 stages of reheat, the benefits begin to diminish, but there still is an increase all the way up to 12 stages. With more reheat stages the high temperature end of the cycle begins to more closely mimic that of a Carnot cycle with a constant heat addition temperature. One limit to increasing the number of reheat stages is that the smaller turbines that power the compressors will be difficult to add reheat within, and therefore reducing the range of heat addition is constrained by the temperature drop across those turbines. This begins to become more evident when reviewing Figure 2.47.

2.5 Conclusions and Recommended Future Work

A cycle analysis code has been developed and used to identify a high efficiency optimized design for a stand alone Recuperated, Recompression, Precompression Supercritical Carbon Dioxide Power Cycle with Intercooling, Improved Regeneration, and Reheat. The unique shaft layout proposed would allow for an incremental design and testing process as well as more design freedom when developing the turbomachinery components. As part of this cycle analysis code a detailed 0-D heat exchanger model was developed and used in order to appropriately consider the variable fluid properties. A number of parameter sweeps were conducted for this cycle layout and have been presented in detail.

Limitations of the present code include the lack of ability to model cycles below the critical temperature (condensing cycles) where a discontinuous change in phase and two phase region may exist. The pressure drop formulation in the heat exchangers could also be improved and individual relationships applied to different heat exchangers. Fluid specific heat, pressure drop and pumping power of the atmospheric pressure side of the heat exchangers that transfer heat to and from the engine is currently not rigorously addressed. The code is presently limited such that the precompressor inlet temperature must be equal to the main compressor inlet temperature, and further flexibility could be incorporated to allow for this parameter to be changed independently. The code could also allow for different turbomachinery efficiencies for the turbines that power

the compressors and a selectable mass flow split between these turbines that operate in parallel. It would also be very beneficial to incorporate turbomachinery efficiencies that are variable as a function of inlet temperature and pressure as well as pressure ratio.

Chapter 3

A Closed Loop Recuperated Lenoir Cycle using Supercritical Carbon Dioxide

Inspired by the efficiency gains predicted for cycles that aim to approximate the Humphrey cycle (such as a pulse detonation engine, or PDE), variation in fluid properties of carbon dioxide near the critical point, and the large amounts of recuperation used in the cycle presented in Chapter 2, a study was conducted of a recuperated Lenoir cycle. A standard Lenoir cycle features a constant volume heating process where the pressure rise happens purely due to heat transfer. After a temperature and pressure rise, the working fluid expands and work is extracted. After expansion, the fluid is cooled and compressed at constant pressure by rejecting heat to the atmosphere. Some work is done on the fluid during the cooling process because the density is changed. Because the Lenoir cycle does not compress the working fluid to a higher pressure after being cooled, more heat is added in the cycle at lower temperatures, and therefore the cycle is less efficient than other competing cycles, and as a result, the Lenoir cycle did not see extensive industrial use.

No known studies of a recuperated Lenoir cycle have been identified, where the heat addition could occur at a higher temperature due to the recuperation, achieving higher efficiencies than a standard Lenoir cycle. No known studies have been conducted using supercritical carbon dioxide with a Lenoir cycle. One motivation for exploring such a cycle is because of the highly variable compressibility factor near the critical point. It was thought that the minimum temperature and

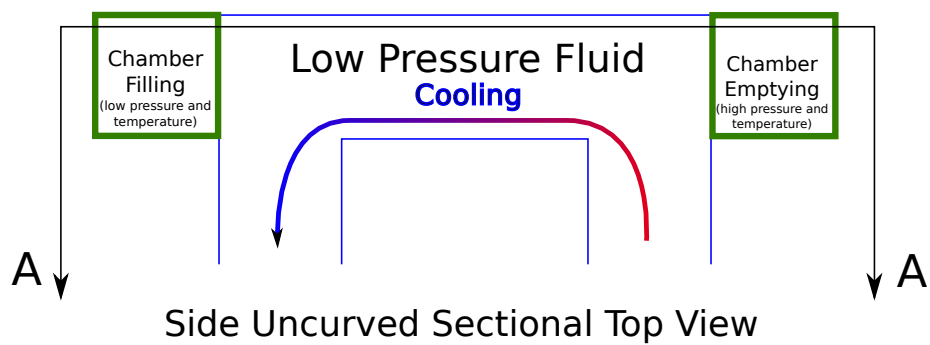
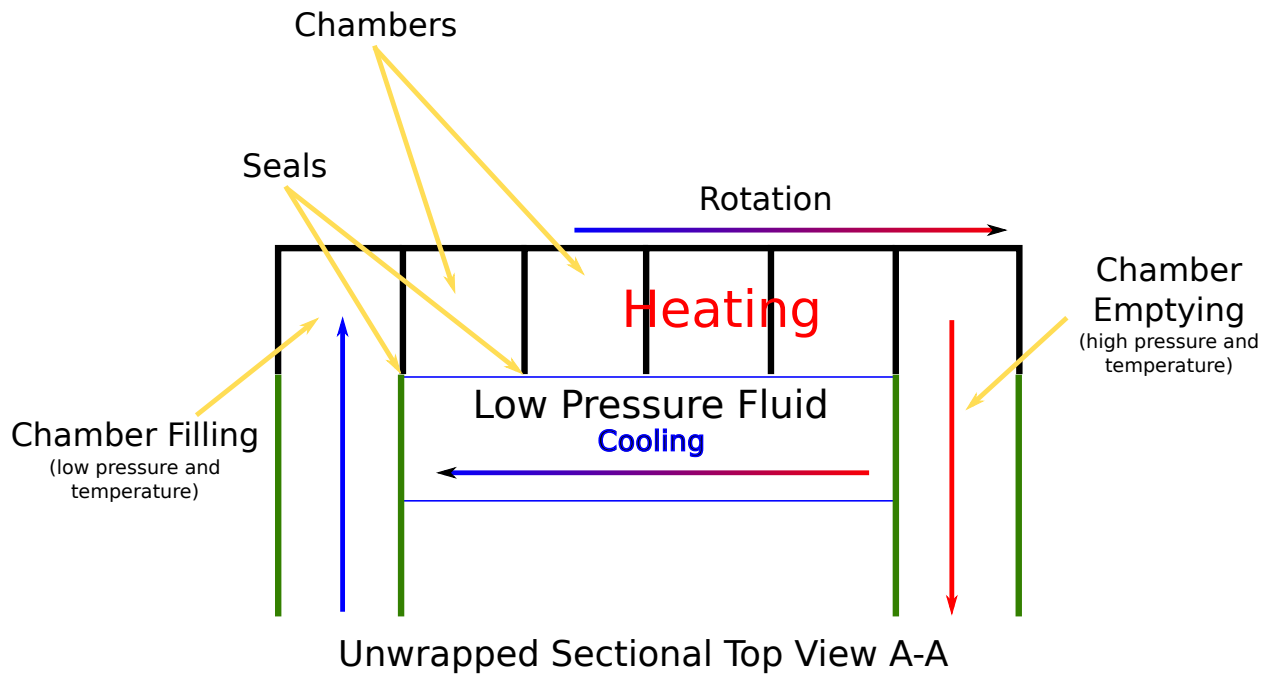


Figure 3.1: Constant Volume Heat Exchanger Concept

pressure in the cycle may be able to be tuned for a better cycle efficiency if the compressibility factor varies.

The concept of a heat exchanger with constant pressure cooling and constant volume heating is not a common configuration, especially when the temperature difference between the high and low pressure sides is minimized, as it is in a counter flow heat exchanger. Some effort was done exploring ideas of how such a heat exchanger could be created. In order for such an ideal heat exchanger to be created, the chambers with constant volume heating must be moving relative to the passage with constant pressure cooling, such that the rate of transient heating in the chamber heated at constant volume appropriately matches the steady constant pressure cooling, such that the the constant pressure fluid appears to be cooled by another fluid that is steadily moving.

Figure 3.1 is a very simplified schematic of how a heat exchanger could work with constant volume heating on the high heated side and constant pressure cooling on the low cooled side. For simplicity Figure 3.1 is a flattened version of a portion of a geometry that would be curved and rotating about a central axis. A small number of chambers is also depicted. In a real design many chambers would be used in order to allow for a better approximation of a counterflow heat exchanger that has lower temperature differences between the heated and cooled sides. In theory, an infinite number of chambers could be used and the temperature difference between the heated and cooled sides could approach zero. However, no study was conducted to determine what discrete number of chambers reasonably approximated an infinite number of chambers. The configuration also relies on low leakage seals in order to maintain pressure in each chamber. It's possible that a design could be developed that instead has high speed valves that securely seat, rather than moving seals, however, the current design allows for some wall shear in both the heated and cooled fluid streams to facilitate better heat transfer. Some work will be required to overcome the wall shear in the rotating heat exchanger, but this is assumed to be negligible.

Although just a simple concept has been presented, which in a real design would be much more complex, the feasibility of producing such a rotating heat exchanger is believed to be possible through the use of additive manufacturing, especially as part quality is rapidly improving with such technologies. Additive manufacturing will allow for very intricate and small passages and chambers to be produced, better approximating the goal of an infinite number of chambers, which is desired in order to better approximate a counter flow heat exchanger and reduce the amount of entropy

production in the heat exchanger. The idealization of the heat exchanger also relies on chamber walls with very low heat capacity and thermal conductivity (except on the wall in contact with the cooled fluid) because during the filling process, the wall temperatures will be much higher than that of the entering fluid temperature, so there will be some additional entropy produced with heat transfer between a large temperature difference. There is also a desire for little heat conduction between chambers.

Because the heat exchanger just described was believed to be possible, although very complex, analysis of a hypothetical cycle was then carried out assuming that an ideal heat exchanger with such a description could be created. Such an approach was taken because the usefulness of spending efforts to create such a heat exchanger may not necessarily be warranted if the overall cycle does not provide significant advantages. The cycle code and heat exchanger model described in Chapter 2 were modified to allow for a constant volume heating process, both from external heat addition and with a heat exchanger with constant pressure cooling and constant volume heating.

When modeling the Lenoir cycle, a minimum cycle temperature of 320K (47C) and a maximum temperature of 923K (650C) were used. An aggressive maximum pressure of 35MPa was used for this hypothetical cycle and counterflow constant volume heat exchanger. The minimum pressure was a design parameter that could be changed that represented the pressure in the constant pressure side of the recuperator, as well as the starting pressure of the constant volume side of the recuperator. The maximum pressure was the pressure at the end of the constant volume heating process and the starting pressure of the expander. If the maximum pressure was reached due to the chosen minimum pressure, the maximum temperature was limited. If the maximum temperature was reached due to the chosen minimum pressure, the maximum pressure was limited. The Lenoir cycles currently considered are ideal cycles that have an expander with an isentropic efficiency of 100% and no pressure losses during the inflow and outflow of the heating chambers. The recuperated cycle was also idealized in that it had a 0 minimum temperature difference in the heat exchangers and no pressure losses in the constant pressure side of the heat exchanger and no pressure losses during the inflow and outflow of the heating chambers.

First as a baseline, a standard ideal Lenoir cycle was modeled with carbon dioxide as the working fluid and the minimum pressure swept in order to identify the optimum efficiency. The results from this parameter sweep are presented in Figure 3.2. A maximum cycle thermal efficiency of

Maximum Thermal Efficiency=17.92%, Maximum Exergy Efficiency=32.91%

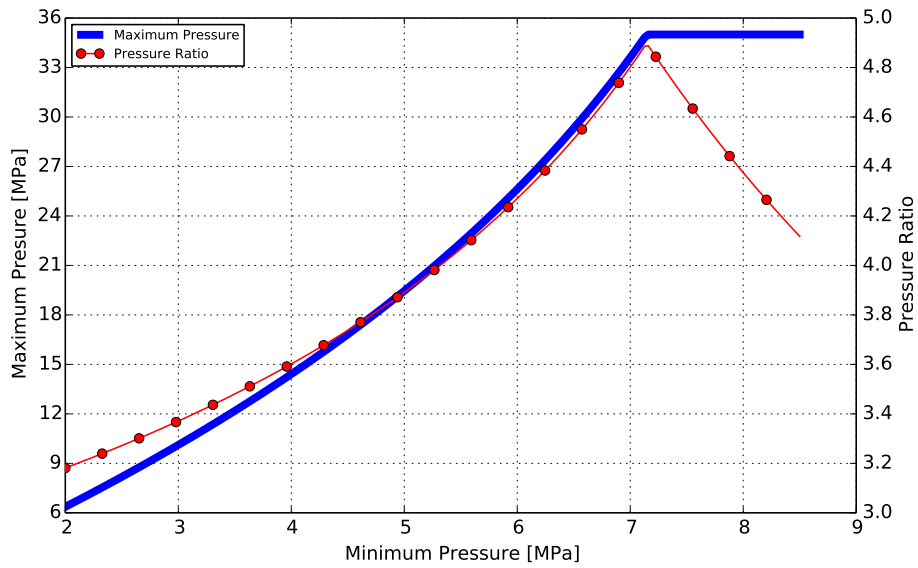
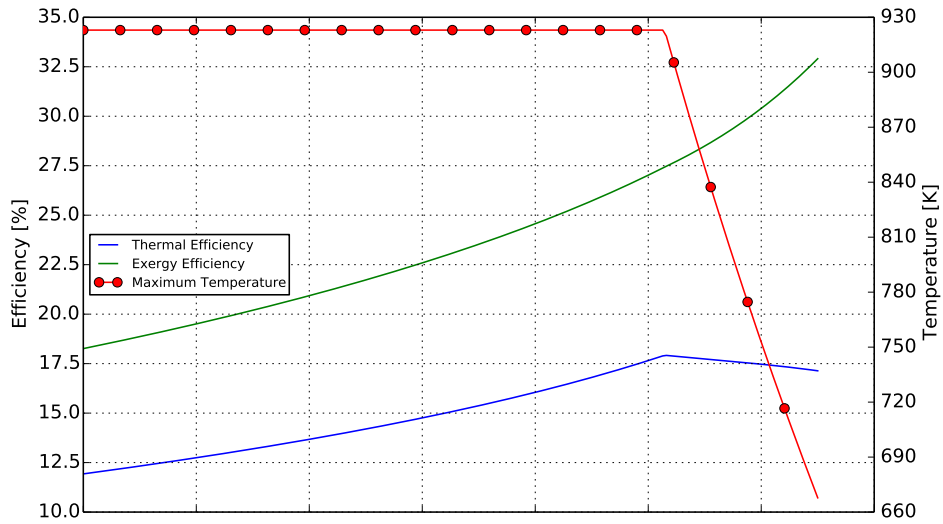


Figure 3.2: Lenoir Cycle - Efficiency, Maximum Pressure, Maximum Temperature, and Pressure Ratio vs Minimum Pressure

Maximum Thermal Efficiency=45.62%, Maximum Exergy Efficiency=69.87%

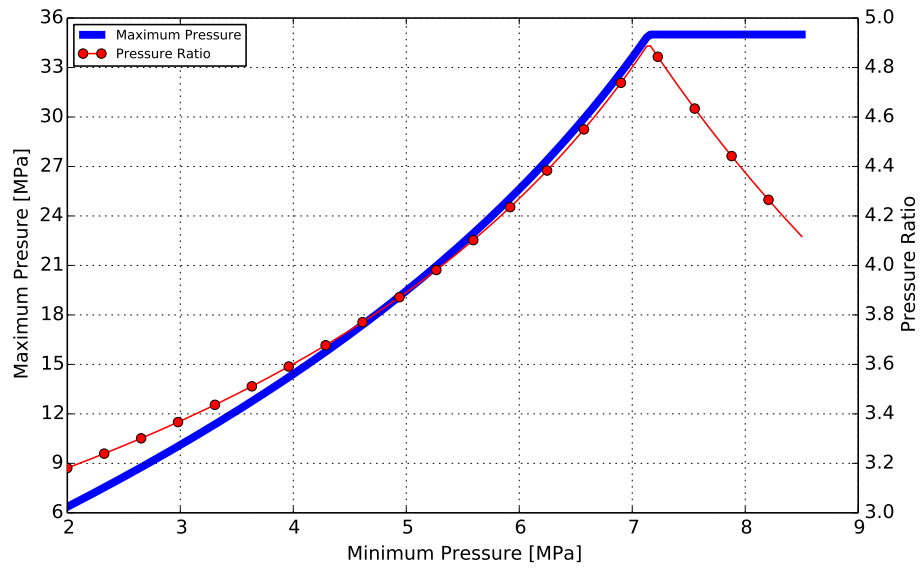
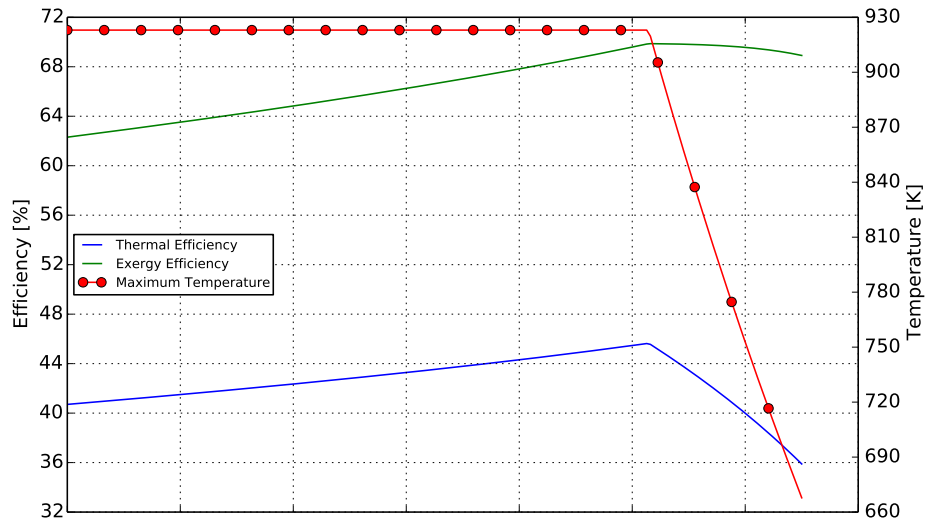


Figure 3.3: Recuperated Lenoir Cycle - Efficiency, Maximum Pressure, Maximum Temperature, and Pressure Ratio vs Minimum Pressure

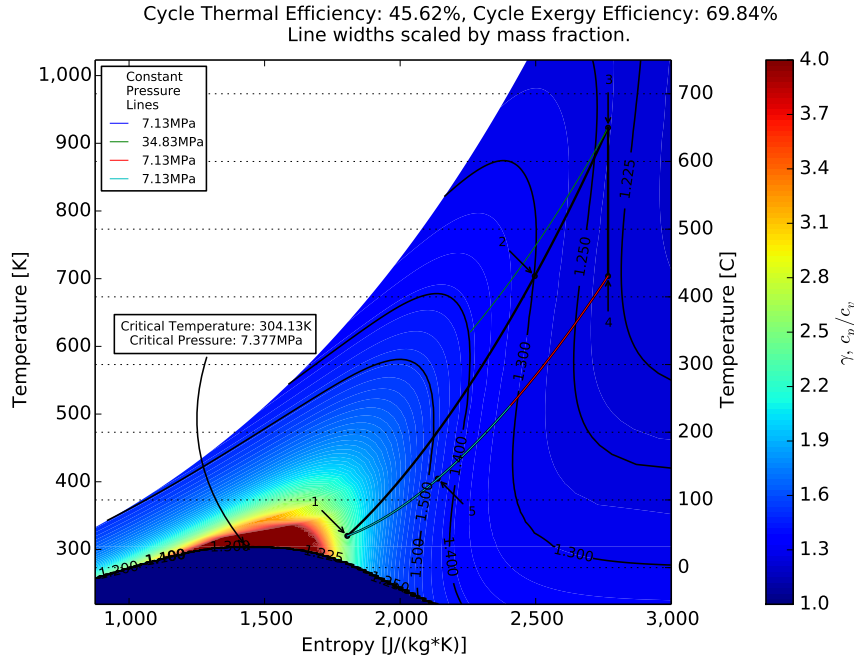


Figure 3.4: Recuperated Lenoir Cycle - Temperature Entropy, contour background is $\gamma, c_p/c_v$

17.9% and a maximum cycle exergy efficiency of 32.9% were determined. A recuperator was then added and the minimum pressure swept again. The results from this parameter sweep for an ideal recuperated Lenoir cycle can be seen in Figure 3.3. A maximum a cycle thermal efficiency of 45.6% and a maximum cycle exergy efficiency of 69.9% were determined. There was a considerable gain in efficiency by considering the use of a recuperator. In both Figures it is evident where the maximum pressure begins limiting the maximum temperature. Once the maximum pressure begins limiting the maximum temperature, the thermal efficiency begins to drop. For the standard Lenoir cycle, the exergy efficiency continues to rise with increases in minimum pressure even after the maximum pressure is reached, but the recuperated Lenoir cycle sees a slight reduction in exergy efficiency as the minimum pressure is increased after the maximum pressure is reached. As a thought experiment, the maximum pressure constraint was lifted up to 49MPa, and the minimum pressure swept again. Although the results are not presented here, the thermal efficiency did continue to increase and did not have any local maximum below a 49MPa maximum pressure.

Figures 3.4 through 3.12 depict the recuperated Lenoir cycle layout in Temperature - Entropy, Temperature - Pressure, and Pressure - Specific Volume planes, for the case with the optimum minimum pressure, given the maximum temperature and pressure constraints. Various contour

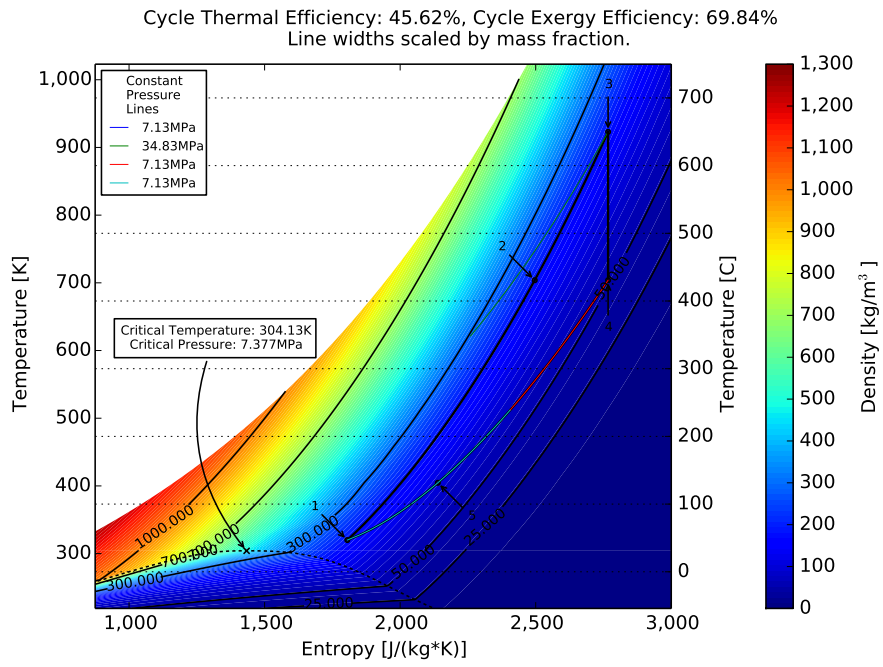


Figure 3.5: Recuperated Lenoir Cycle - Temperature Entropy, contour background is Density

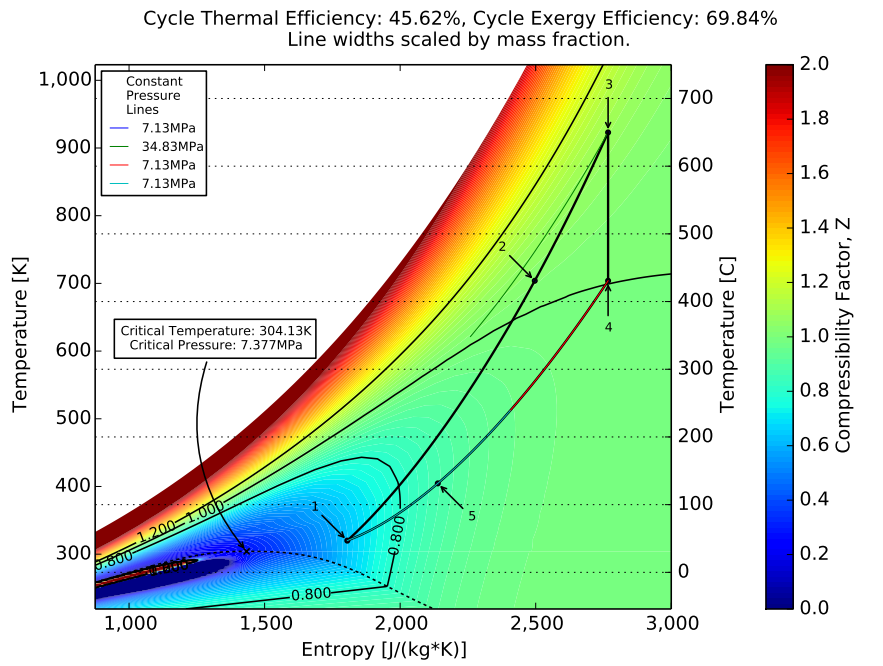


Figure 3.6: Recuperated Lenoir Cycle - Temperature Entropy, contour background is Compressibility Factor

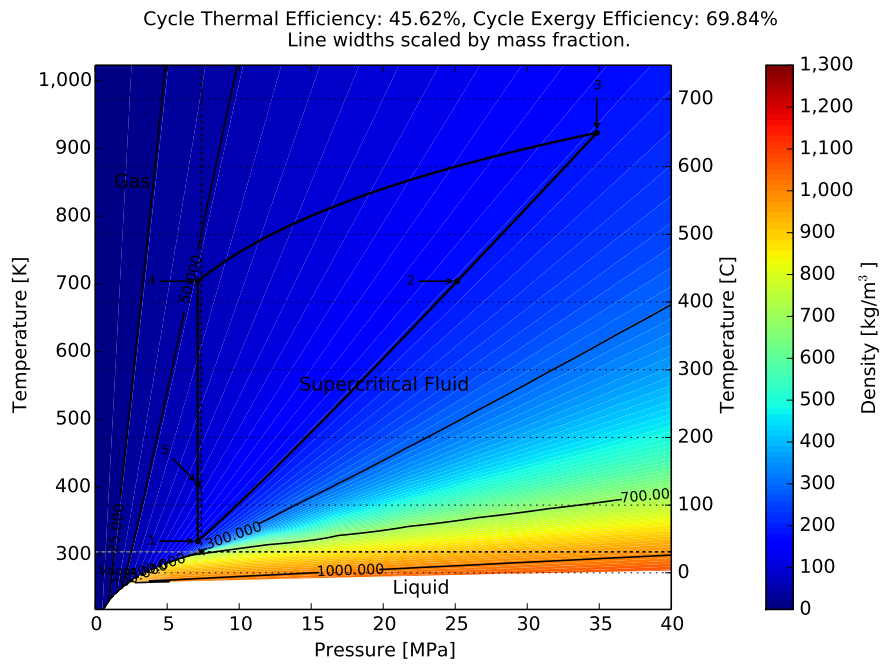


Figure 3.7: Recuperated Lenoir Cycle - Temperature Pressure, contour background is Density

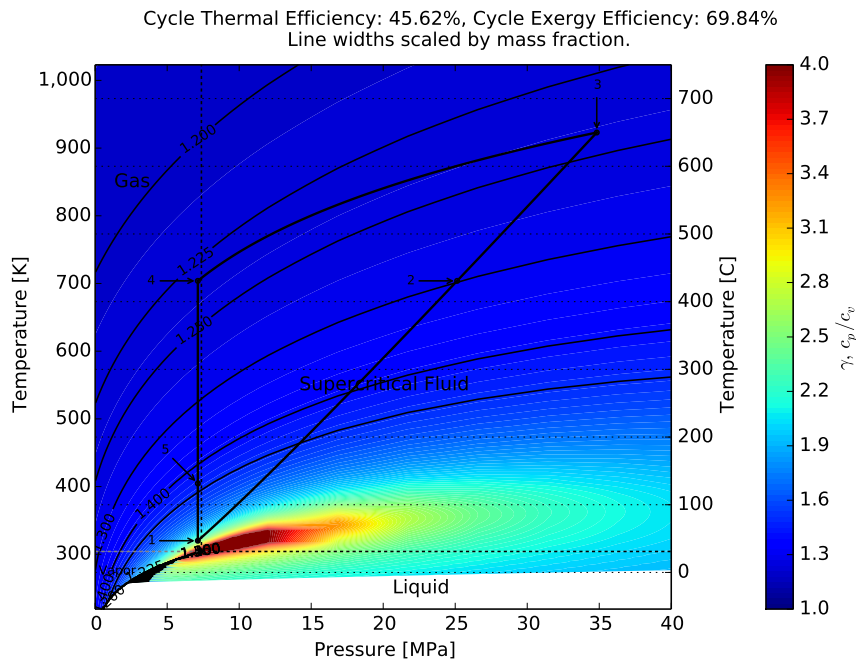


Figure 3.8: Recuperated Lenoir Cycle - Temperature Pressure, contour background is $\gamma, c_p/c_v$

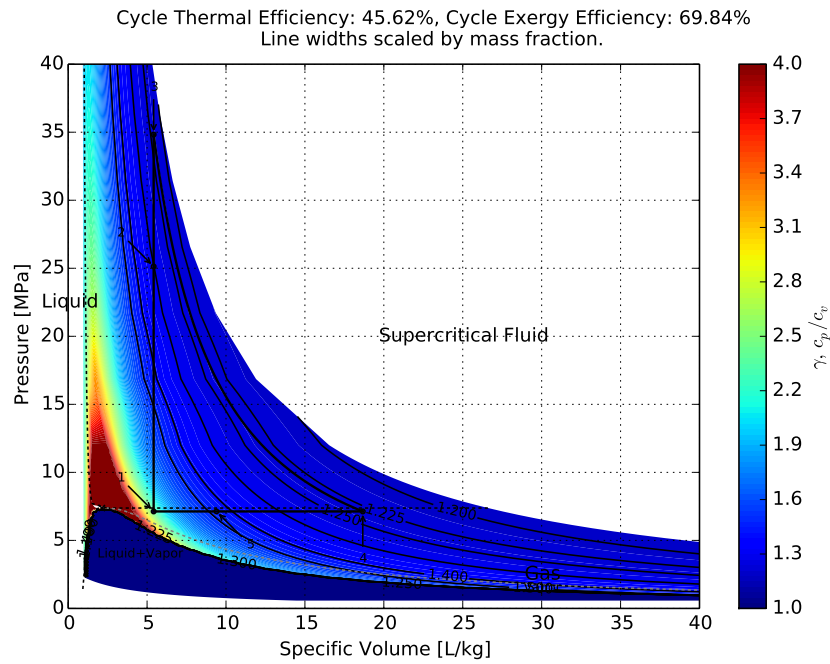


Figure 3.9: Recuperated Lenoir Cycle - Pressure Specific Volume, contour background is $\gamma, c_p/c_v$

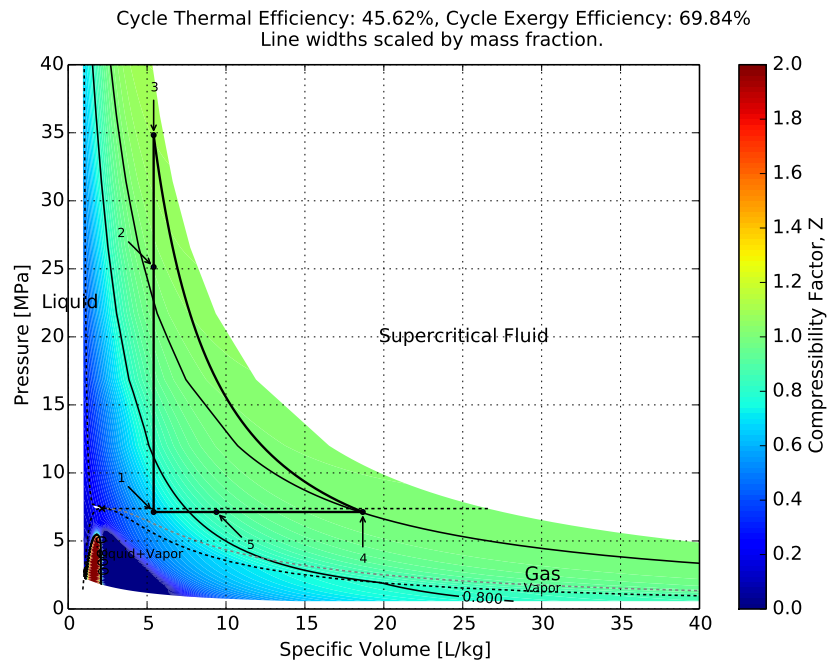


Figure 3.10: Recuperated Lenoir Cycle - Pressure Specific Volume, contour background is Compressibility Factor

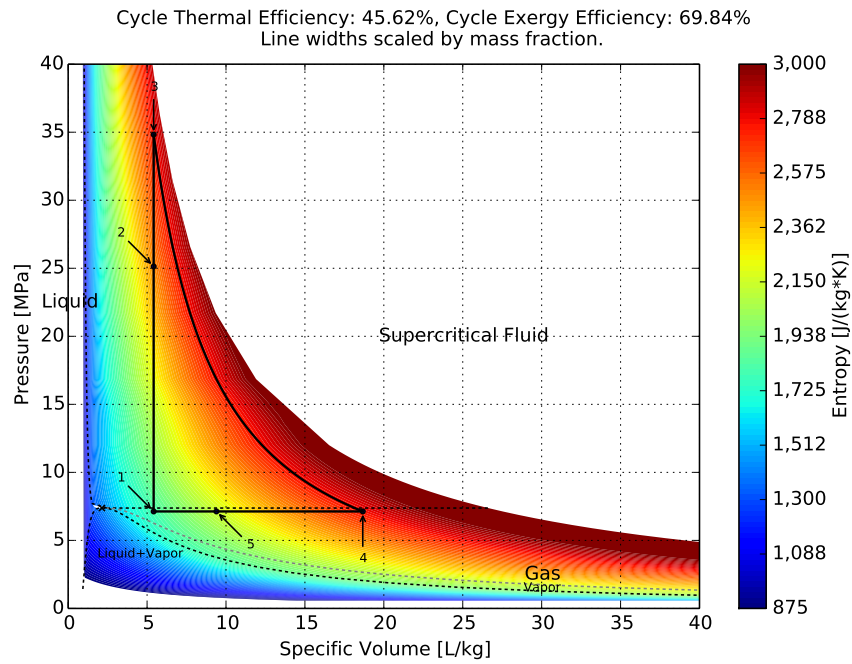


Figure 3.11: Recuperated Lenoir Cycle - Pressure Specific Volume, contour background is Entropy

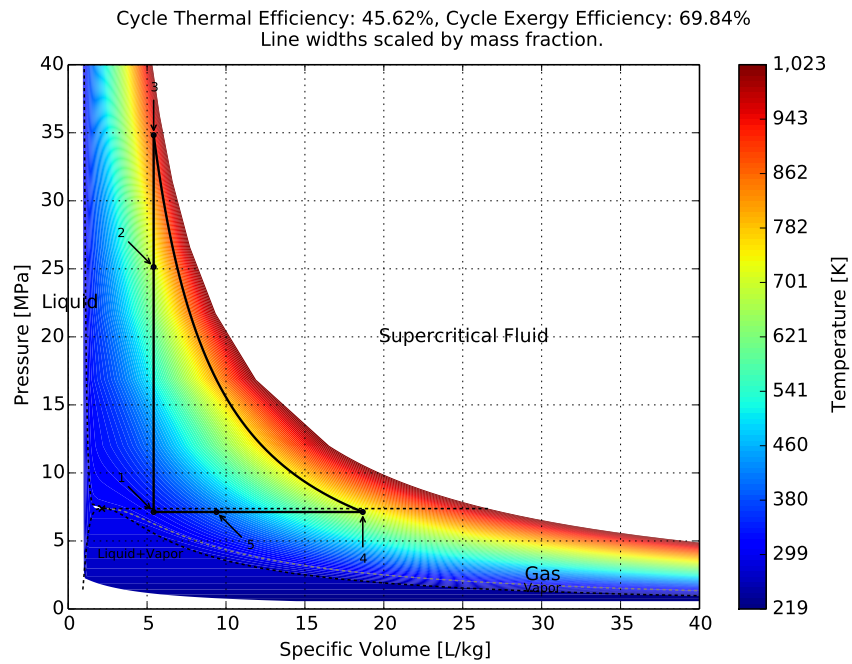


Figure 3.12: Recuperated Lenoir Cycle - Pressure Specific Volume, contour background is Temperature

level backgrounds are utilized in the Figures in order to place the cycle in context with the fluid property variations. The efficiency of this recuperated Lenoir cycle, even when idealized, was a bit lower than was originally anticipated.

The state points defined in Figures 3.4 through 3.12 are as follows: Point 1 is the end of the constant pressure cooling process where heat was rejected to the surroundings and the start of the constant volume heating process where the fluid is heated through recuperation. At point 1, the fluid enters one of the moving heating chambers previously described. Point 2 is the end of constant volume heating due to recuperation and the beginning of constant volume heating due to an external heat source. Point 3 is the end of constant volume heating due to the external heat source and the start of the constant entropy expansion process. In Figure 3.1 it's not clearly articulated how the high pressure fluid would be isentropically moved to another chamber for expansion, but the present thought experiment assumes it can be done. The expansion process could be a piston or a turbine. In the present work, a piston is considered for the Lenoir cycles for the sake of simplicity because a single piston would be pushed by a fixed mass of fluid. It's possible that the piston could be rotating with the chambers and avoid the unexplained step (just mentioned) where the fluid moves isentropically from the heating chamber. Point 4 is the end of the constant entropy expansion processes and the beginning of the constant pressure cooling due to recuperation. At point 4 a valve opens to the constant pressure cooler. As the fluid moves from point 4 to 1 it is pushed back out of the expansion chamber by the piston. In order for the system to work with the concept constant volume heat exchanger with moving chambers, there must be many chambers and many pistons (the present work assumed 200 chambers, although as mentioned previously, no work was conducted to determine if this was a sufficiently large number or if the number of chambers could be reduced). As soon as one piston empties a chamber by pushing the fluid through the constant pressure side, a valve closes and another chamber's (whose piston just finished expanding to point 4) valve opens it and immediately begins emptying, such that a sufficient mass of fluid on the low, constant pressure side of the heat exchanger exists that a small minimum temperature difference can exist in the heat exchanger. Point 5 is the end of constant pressure cooling due to recuperation and the beginning of constant pressure cooling where heat is rejected to the atmosphere. Constant pressure cooling where heat is rejected to the atmosphere occurs between points 5 and 1 through the use of a standard counterflow heat exchanger.

The concept heat exchanger previously described which features constant volume heating and constant pressure cooling through the using of moving chambers consists of points 1-2 and 4-5 as a recuperator. Presently points 2-3 assume a constant heat flux heat source and therefore a complex heat exchanger with moving chambers *may* not necessarily be needed.

It turns out that because the high ratio of specific heats, much of the heat on the low pressure side could not be recuperated to the high pressure side and had to be rejected to the atmosphere. The initial thought was that if there was no mechanical compression from low pressure to high pressure, more heat could be recuperated because recuperation would not be limited by the compressor outlet temperature. This turned out to not be true. Much of the energy that had to be rejected to the atmosphere had to be input into the fluid at the inlet of the low pressure side of the heat exchanger in order to maintain the constant pressure that occurred during the cooling as the density was increased (the decrease in specific volume during constant pressure cooling is clearly evident in Figure 3.12). This resulted in a back work ratio of 48.6% for the recuperated Lenoir cycle, which was much higher than the recompression cycle presented in Chapter 2. It was originally anticipated that the back work ratio for the recuperated Lenoir cycle would be lower since no work would be done compressing from a high pressure to a low pressure, but this proved to be incorrect. In more traditional recuperated cycles such as a recuperated Brayton cycle, the work required to maintain constant pressure during compression is typically not accounted for explicitly because both the high pressure heating and the low pressure cooling sides are both at constant pressure and are analyzed using a control volume approach. In this case of the Lenoir cycle with constant volume heating, a control mass, or system approach had to be used and therefore the work input had to be accounted for explicitly.

The amount of energy transferred to the high pressure fluid from the low pressure side and the external heat source was equal to the change in internal energy between points 1 and 3. The use of a piston (instead of a turbine) as the expander worked well with the control mass approach and eliminated the need to understand the interactions between pressure pulses from many different heating chambers onto a single turbine, as well as the need to transition between control volume (for the turbine) formulations and control mass formulations (for the constant volume heating chambers). The work extracted by the piston was equal to the change in internal energy (rather than a change in enthalpy which is used with a turbine using control volume approach) between points 3 and 4.

With the Lenoir cycle, some of the work extracted between points 3 and 4 by the piston expander had to be input back into the fluid between points 4 and point 1 as the fluid is pushed by the piston out of the expansion chamber into the constant pressure cooler. This work input is not necessarily obvious from the Temperature - Entropy cycle plots, but must still be considered. The work that had to be input during the constant pressure cooling process was equal to the difference between the enthalpy change and internal energy change of the fluid during cooling. The energy extracted from the fluid during the constant pressure cooling process and transferred to the high pressure side and rejected to the atmosphere was equal to the change in enthalpy between points 4 and 1.

Because the efficiency of the ideal recuperated Lenoir cycle was not a monumental improvement upon the cycle presented in Chapter 2, more extensive efforts with this cycle are not planned. It's possible that a recompression, precompression, or reheat process could be combined with this cycle in order to improve it, but the increased cycle layout complexity coupled with the complexity of the constant volume recuperator make it less attractive than further improving the cycle presented in Chapter 2 with additional reheat stages. Reducing the minimum pressure and adding a compressor to the layout (increasing the overall pressure ratio) to convert the cycle from a recuperated Lenoir cycle to a recuperated Humphrey cycle is believed to also be a drawback because that will just increase the back work ratio and increase the temperature of heat rejection and decrease the temperature of heat addition. Another option would be to have a compressor and constant pressure heating with a traditional heat exchanger and then employ constant volume heating after recuperation by the external heat source, similar to a concept suggested by Bellini for pulse detonation engines[38]. This approach will still require the complex layout described in Chapter 2 and the very complex (not yet designed) constant volume heat exchanger. It's believed that additional reheat stages may be a more practical approach to improving the cycle efficiency than employing a constant volume heat addition when heated by the external heat source. The primary conclusion from this study is that although constant volume heating may be beneficial in unrecuperated open loop airbreathing engines without reheat, it's not very beneficial or practical in closed loop engines using working fluids in operating ranges that prefer recuperation and have implemented reheat.

Chapter 4

Combined Cycle Engine Cascades Achieving High Efficiency

4.1 Introduction

The current work explores the use of a Brayton cycle engine as a topping cycle in combination with a series of supercritical carbon dioxide power cycles as intermediate and bottoming cycle engines. An earlier work of Mohagheghi explored a supercritical carbon dioxide power cycle as part of a combined cycle, but only with a single bottoming cycle, and the results were presented in terms of power output, rather than non-dimensionalized combined cycle efficiency, providing limited usefulness[39]. Other researchers at SoftInWay have studied combined cycles with supercritical carbon dioxide, but fixed important supercritical carbon dioxide power cycle design parameters such as pressure ratio, operating pressure, and recompression fraction. They were also focused on power output, rather than non-dimensionalized combined cycle efficiency. Their study concentrated on exhaust heat source temperature, rather than a coupling with a topping cycle[40]. The configuration studied in this work is the use of a cascade of supercritical carbon dioxide power cycles in place of a single bottoming cycle which is traditionally proposed to be a steam based Rankine cycle. The application of this configuration is base load electrical power generation. This approach aims to increase the overall combined cycle efficiency, as well as leverage a power cycle with a high power density. A second approach uses a fuel cell in combination with a Brayton cycle engine and supercritical

carbon dioxide power cycles in order to achieve even higher combined cycle efficiencies. The use of a fuel cell in combination with a Brayton cycle was inspired by earlier works of Roberts [41, 42], except the combustion process was changed to occur after the fuel cell, rather than before the fuel cell. This change was motivated by a desire for higher efficiency rather than higher power density. Other researchers have studied the use of supercritical carbon dioxide engines in a combined cycle configuration with fuel cells, however, their work replaced the traditional Brayton cycle engine with the supercritical carbon dioxide cycle engine, rather than compliment it [43, 44].

4.2 Methodology

4.2.1 Cycle Layouts

In this work, two combined cycle power plant configurations are studied. The first is a combined cycle engine that uses a simple brayton cycle as the topping cycle and a series of supercritical carbon dioxide power cycles as intermediate and bottoming cycles. The topping cycle is expected to use methane (natural gas, CH_4) or kerosene/diesel as it's fuel. Waste heat from the topping cycle is used to power the intermediate and bottoming cycles.

The second combined cycle configuration is similar to the first, except the topping cycle is a modified Brayton cycle that includes a solid oxide fuel cell inside the pressurized environment. The fuel cell simultaneously produces heat and direct current (DC) electrical work from methane (natural gas, CH_4) fuel. 80% of the fuel is utilized by the fuel cell and then the remaining 20% is later burned in a combustor. The fuel cell heats the products and reactants up to 1,273 K [1,000°C]. Incorporating the solid oxide fuel cell inside the Brayton cycle allows for high temperature fuel and air to be provided by compression of those fluids. Waste heat produced by the fuel cell's electrochemical inefficiency heats the high pressure fluids even further, recovering energy that would otherwise be unusable in a stand alone fuel cell configuration. The excess fuel that is unusable by the fuel cell is then able to be burned in the Brayton cycle engine's combustor. Waste heat from the topping cycle is used to power the intermediate and bottoming cycles, just as with the combined cycle that does not use a solid oxide fuel cell.

The most general representation for these two topping cycle layouts is presented in Figure 4.1.

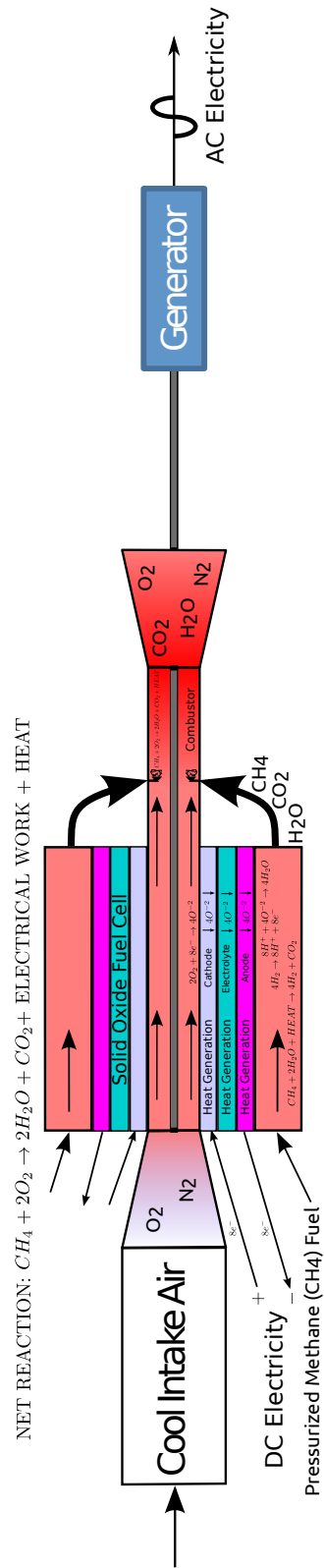


Figure 4.1: Solid Oxide Fuel Cell integrated into a Brayton Cycle Engine

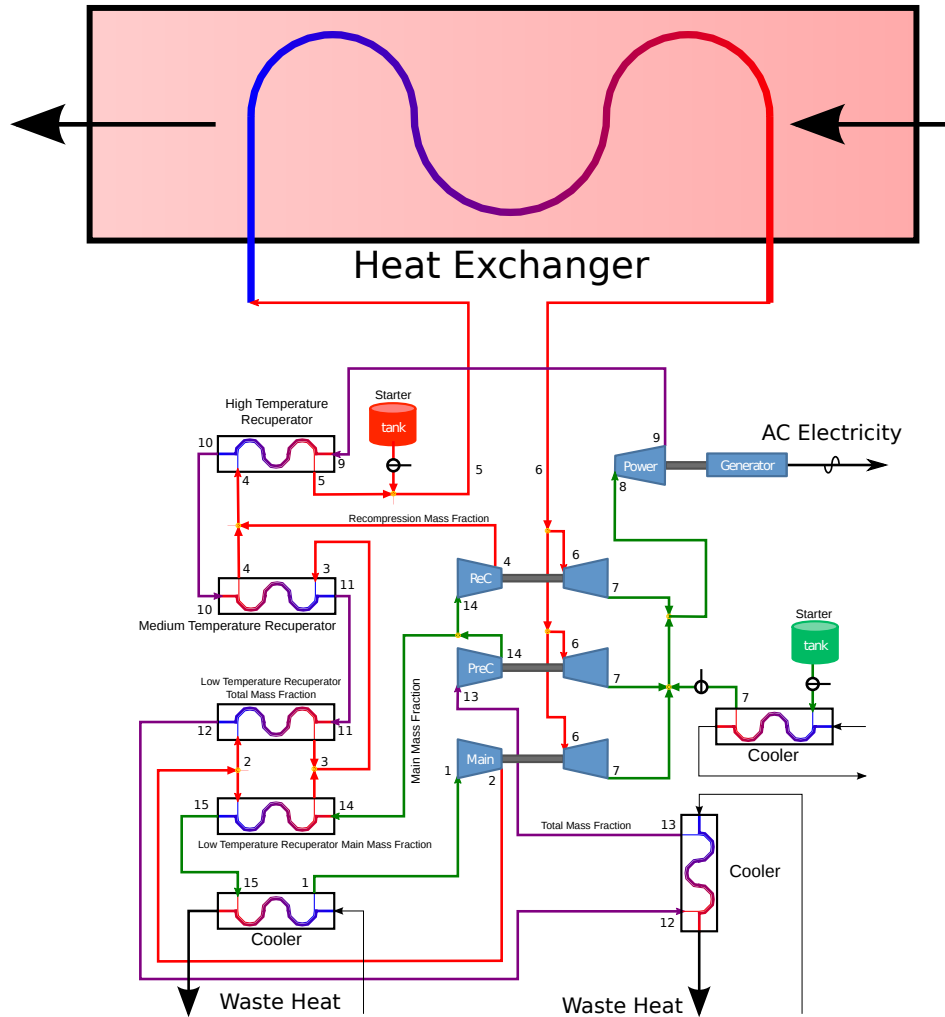


Figure 4.2: General Supercritical Carbon Dioxide Cycle

In the case of the cycle with no fuel cell, the fuel cell will just be omitted from the engine and fuel added directly to the flame holders in the combustor, or one can think of the fuel cell components being inactive. If no load is applied to the fuel cell's electrical circuit, no electrochemical reactions will occur and the fuel will pass through to the combustor to be burned.

Figure 4.2 depicts the intermediate and bottoming $S - CO_2$ cycle engines. This configuration is nearly identical to a layout described in detail in Chapter 2, with the exception of reheat being removed. The layout is a recompression, precompression, recuperated $S - CO_2$ cycle with intercooling and improved regeneration. This combined cycle effort builds on that generality in search of the optimal, peak efficiency design. A combination of these topping, intermediate, and bottoming cycles is shown in Figure 4.3. Depending on the configuration, a different number of

$S - CO_2$ engines can be used in the cascade.

A high pressure ratio is used to heat the fuel and air up to the required inlet temperature of the solid oxide fuel cell rather than a recuperator, which also could have been done. Although use of a recuperator allows for much lower system pressures (could be as low as 0.101MPa), it is believed that such low pressure air to air heat exchangers would be very large and expensive. Additionally, work would not be able to be extracted from the waste heat produced by the fuel cell or from combustion of the unspent fuel. It's possible that a recuperator in combination with a moderate pressure ratio could provide a more balanced configuration and a higher efficiency because the temperature of the waste heat being provided to the supercritical carbon dioxide power cycles would be higher. This configuration of the topping cycle was not presently explored due to the increased modeling complexity and uncertainty on the costs and performance of the air to air heat exchangers.

Although the development of fuel cell technologies has been ongoing for decades, solutions have not yet received widespread market penetration due to the lower technical maturity and higher capital costs compared to competing equipment. Their use is growing however. The configuration presented in this work anticipates some increased maturity of such devices in order for the entire system to be practical.

The solid oxide fuel cell has a temperature inlet requirement of 923 K [650°C]. The design actually considers the use of two different types in series which utilize materials more appropriate for their temperature ranges. However, the two are not distinguished in Figure 4.1. The lower temperature fuel cell uses silver interconnects and the high temperature fuel cell uses platinum interconnects. The outlet temperature of the lower temperature fuel cell and the inlet temperature of the higher temperature fuel cell is 1,093 K [820°C]. The outlet temperature of the higher temperature fuel cell is 1,273 K [1,000°C]. This configuration was suggested by Dr. Rory Roberts.

4.2.2 Fuel Cell and Combustion Chemistry

There are a number of processes occurring within the fuel cell. The fuel cell is depicted as part of the gas turbine engine in Figure 4.1. The methane fuel needs to first be reformed. The reformation process absorbs some waste heat from the fuel cell and some water by-product and converts CH_4

into hydrogen gas (H_2) and carbon dioxide (CO_2):



The hydrogen gas then is split into positively charged hydrogen ions (H^+) and electrons that are transferred to the anode:



The electrons transferred to the anode then flow through the electrical circuit which has a load on it, and then back to the cathode. On the other side of the fuel cell oxygen (O_2) in the supply air is combined with the electrons received on the anode and split into negatively charged oxygen ions (O^{-2}):



The negatively charged oxygen ions then permeate through the cathode, electrolyte, and anode. At the anode, the negatively charged oxygen ions are combined with the positively charged hydrogen ions to form water:



The net reaction for these processes is a conversion of methane and oxygen into water, carbon dioxide, electrical work, and heat:



Internal to the fuel cell, there is some heat generation in the electrolyte and at the anode and cathode. This heat generation causes the fuel cell's electrochemical efficiency to be lower than ideal. The heat generated is transferred to the fluid which heats up while keeping the fuel cell cool. The heat absorbed in the fuel reformation process is a form of chemical recuperation. The heat absorbed by the water, excess fuel, carbon dioxide, nitrogen, and excess air are pre-heating the air for the brayton cycle.

After the fuel cell, combustion occurs with the remaining methane and excess oxygen. This

combustion reaction is similar to that of the fuel cell, without the electrical work output:



This assumes reactions with nitrogen are not significant to the overall energy balance. The combined reaction of the fuel cell and combustion process is of the same form as the fuel cell by itself presented in Equation (4.5), except there is some additional heat produced instead of electrical work.

The fuel cell based combined cycle is specified to have 26.3% excess air overall, which is closer to stoichiometric than a traditional gas turbine.

Because the CO_2 is produced in the fuel cell is isolated from the bulk air flow, a potential benefit of a fuel cell is that it may be easier to sequester the CO_2 as part of the process. In order to do so, the reformation process in Equation (4.1) may need to be a separate step.

4.2.3 Cycle Analysis and Optimization

The variable fluid property cycle analysis code described in Chapter 2 for studying $S - CO_2$ cycle engines was used as a basis for the analysis, parameter exploration, and optimization. The cycle analysis code was run with no reheat in use. No reheat is desired in an intermediate or bottoming cycle in a combined cycle power plant because the goal is to extract as much heat from the topping cycle's exhaust gases. The heat transfer from the exhaust gases to the intermediate or bottoming cycle engine is an internal process to the entire system and therefore there is no need to introduce reheat as one may want to do when heat is being added to the system. The maximum pressure was set to 35MPa for the $S - CO_2$ cycles. The minimum system temperature was set to 306 K [33°C]. All other assumptions and component efficiencies utilized for the $S - CO_2$ cycle engines is described in Chapter 2.

In the development of the combined cycle analysis code, many functions were enhanced from the supercritical carbon dioxide power cycle analysis code presented in Chapter 2. The electrochemical reaction of Equation (4.5) was implemented for varying equivalence ratios with air. The REFPROP fluid property routines were utilized for air, fuel, and the combustion products [13]. Although very useful for obtaining non-linear fluid properties, REFPROP has many limitations and robustness issues. As a result, combustion products could not be computed below ~ 338 K [65°C] because the

water vapour began to condense at that temperature and REFPROP could not operate.

REFPROP's methane model had a limited temperature range at 625 K [352°C]. Because of this, the enthalpy of methane at the compressed pressure was extrapolated beyond this limit using ideal gas laws and constant specific heats, in order to calculate the work required to compress the fuel.

The heat exchanger between the exhaust gases and the supercritical carbon dioxide was considerably simpler than the CO_2 to CO_2 heat exchanger model. The CO_2 to exhaust gases heat exchanger assumed negligible pressure drop on the exhaust gas side. It also assumed an infinitesimally small (nearly zero) minimum temperature difference between the CO_2 and exhaust gases. These two assumptions will likely cause a small reduction in overall cycle performance from the current predictions. The current CO_2 to exhaust gas heat exchanger also has been designed such that the average heat capacities of the CO_2 and exhaust gases are nearly equal. Although the specific heat capacities are different between CO_2 and the exhaust gases, the mass flow rate of each CO_2 cycle can be varied such that its average heat capacity (not specific heat capacity) is matched to the exhaust gases. This ability to vary the mass flow rate (and corresponding engine size) of each CO_2 to match the heat capacities of the fluids on both sides of the heat exchanger is believed to be one of the key benefits of the CO_2 compared to a steam based Rankine cycle.

For both combined cycle configurations, a 306 K [33°C] temperature was used at the topping cycle compressor inlet. In the combined cycle configuration without a fuel cell, the compressor pressure ratio was optimized, but limited to 45. For the combined cycle with a fuel cell, the pressure ratio was fixed to 37.15 in order to meet the requirement of a 923 K [650°C] inlet temperature to the fuel cell. A topping cycle compressor efficiency of 84% and turbine efficiency of 90% were used. The combustor in the simple Brayton cycle had a pressure drop of $\sim 1.5\%$ and peak temperature of 1,890 K [1,617°C]. The hybrid fuel cell Brayton cycle topping cycle does not currently consider any pressure drop in the fuel cell or combustor. The fuel cell was set to have a 58.5% electrochemical efficiency based on the fuel's higher heating value (65% based on the fuel's lower heating value). The fuel cell cycle was configured to have 26.3% excess air and 80% fuel utilization relative to the ideal stoichiometric chemical reactions. It is believed that 85% fuel utilization may be possible; however, a more conservative value of 80% was utilized because of some uncertainty in the performance of the fuel cell under the elevated pressure of 4.35MPa. The values for the fuel cell electrochemical efficiency, percent excess air, and fuel utilization were based on guidance from Dr. Rory Roberts.

4.3 Results

4.3.1 Combined Cycle With Simple Gas Turbine

For the combined cycle configuration with a simple Brayton cycle engine with no integrated fuel cell as the topping cycle, a combined cycle efficiency of 65.0% was predicted. Figure 4.4 shows a combined temperature entropy diagram for all 4 engines in the design that resulted from the optimization process. The color of the lines for each cycle matches the borders around each engine in Figure 4.3. The topping Brayton cycle engine has a much higher pressure ratio than the $S - CO_2$ cycle engines. Each engine in the cascade has a progressively lower peak temperature than the previous engine in the cascade. Figures 4.5 through 4.8 depict temperature entropy diagrams for the 4 different engines in the cascade with appropriate axis ranges for their temperature of operation. The $S - CO_2$ cycle engines' Figures 4.6 - 4.8 feature a contour level background emphasizing the high degree of variation in specific heat in the operating regime. The different engines in the cascade feature some or all of the components depicted in the most general layout shown in Figure 4.2. Depending on the flow split mass fractions, temperatures, pressures, and pressure ratios, some of these components may not exist.

Table 4.1 shows the work distribution, marginal gain in efficiency due to each engine, the individual engine efficiencies, as well as the exergy efficiency of each individual engine and the combined cycle. The exergy efficiency is defined as the ratio of the actual cycle efficiency to that of an ideal Carnot cycle operating within the same minimum and maximum temperatures. The gas turbine topping cycle produces the majority of the work at 70.05% of the total work output of the combined cycle engine. Each engine produces a diminishing amount of work and marginal gain in combined cycle efficiency. As the temperature drops there is a decreased amount of energy available and the efficiency of each individual engine drops as well.

The topping Brayton cycle engine has a thermal efficiency of 45.5%. This is slightly higher than the advertised production engine efficiency of 44%^[5] mentioned previously, however, is believed to be feasible with upcoming technological developments. The topping Brayton cycle engine has an exergy efficiency of 54.28%, which is considerably lower than the second and third engine (the first and second $S - CO_2$ engines) at 75.02% and 63.79%. Low exergy efficiency of the Brayton

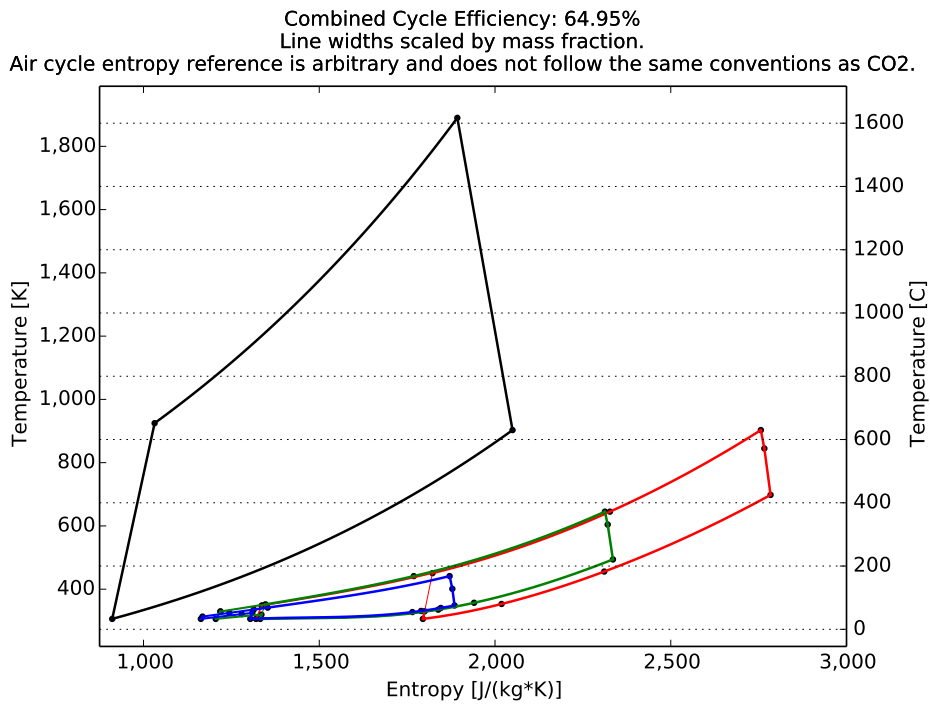


Figure 4.4: Combined Cycle With Simple Gas Turbine, All Engines: Temperature Entropy Diagram

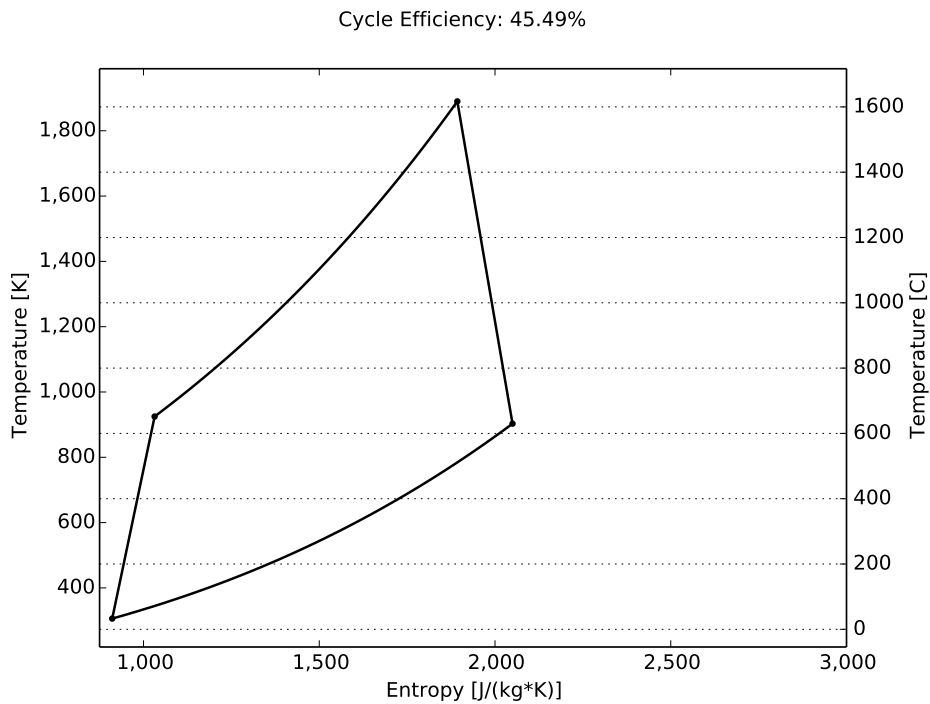


Figure 4.5: Combined Cycle With Simple Gas Turbine, Engine Number 1: Brayton Cycle, Temperature Entropy Diagram

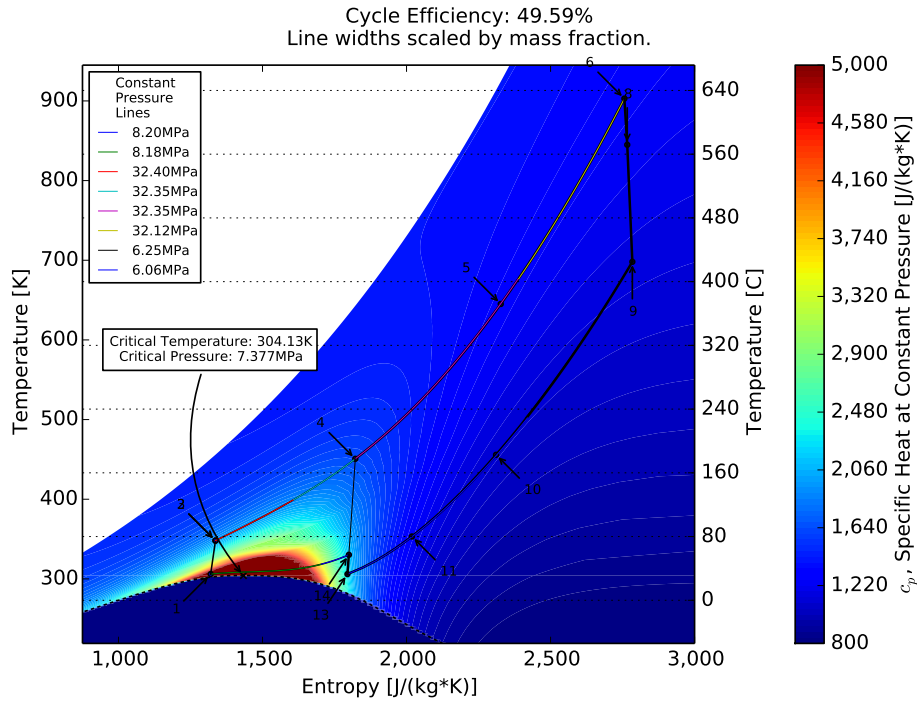


Figure 4.6: Combined Cycle With Simple Gas Turbine, Engine Number 2: $S - CO_2$ Cycle, Temperature Entropy Diagram with Specific Heat at Constant Pressure Contour Level Background

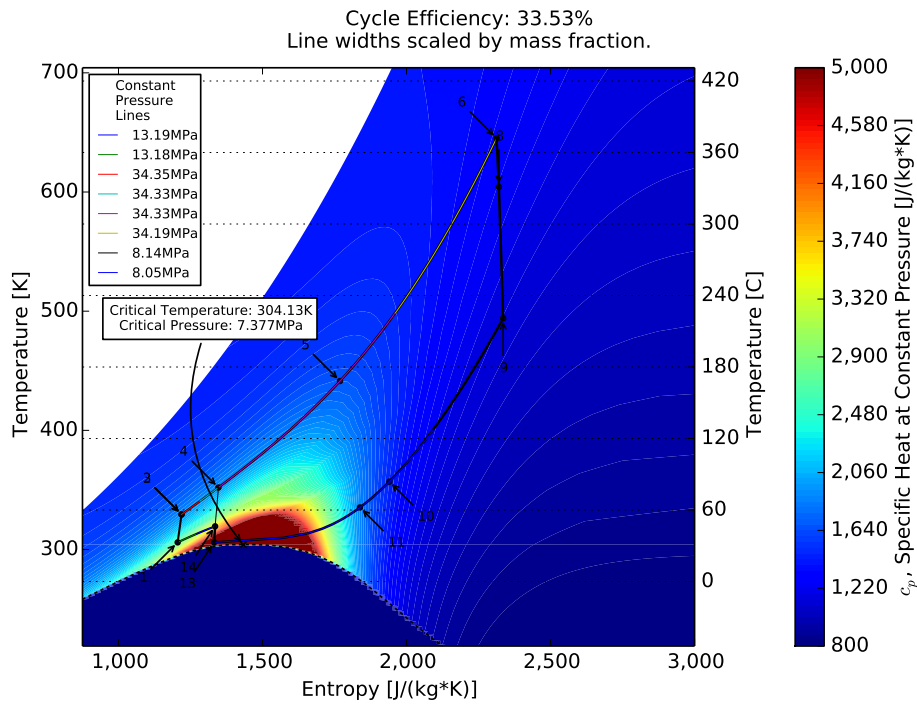


Figure 4.7: Combined Cycle With Simple Gas Turbine, Engine Number 3: $S - CO_2$ Cycle, Temperature Entropy Diagram with Specific Heat at Constant Pressure Contour Level Background

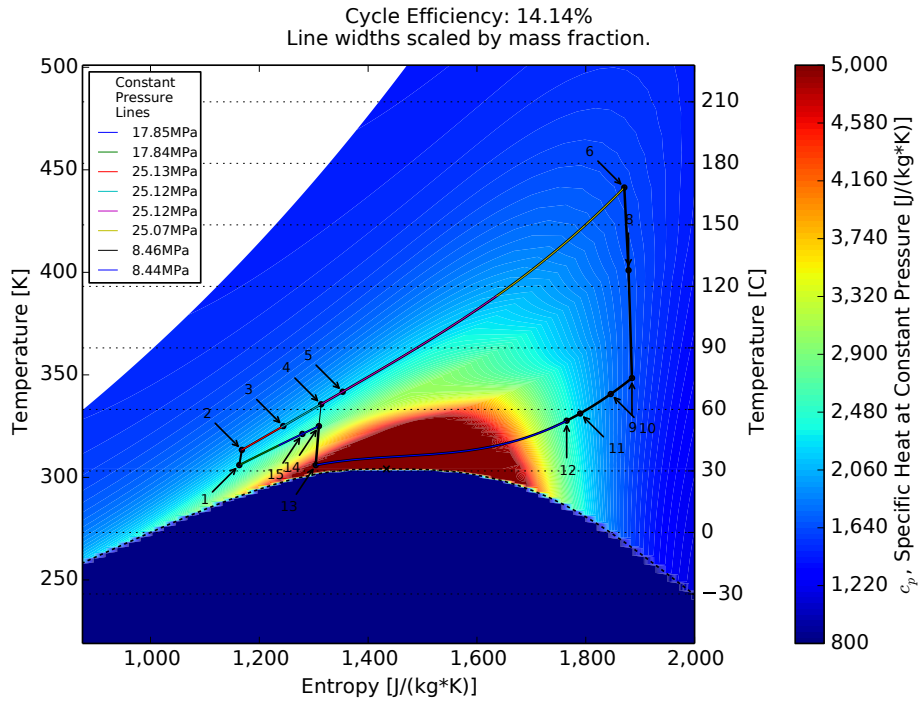


Figure 4.8: Combined Cycle With Simple Gas Turbine, Engine Number 4: $S - CO_2$ Cycle, Temperature Entropy Diagram with Specific Heat at Constant Pressure Contour Level Background

Engine		Work Fraction	Marginal Combined Cycle Efficiency	Engine Efficiency	Engine Exergy Efficiency
Type	Number	%	%	%	%
Gas Turbine	1	70.05	45.49	45.49	54.28
$S - CO_2$ Engine	2	18.60	12.08	49.59	75.02
$S - CO_2$ Engine	3	9.45	6.14	33.53	63.79
$S - CO_2$ Engine	4	1.90	1.23	14.14	46.10
Combined		100.00	64.95	64.95	77.5

Table 4.1: Work Split and Efficiencies: Combined Cycle

Engine		Exhaust Gas Heat Exchanger		Power Turbine	Main Compressor
Type	Number	Inlet Temperature	Outlet Temperature	Exit Temperature	Exit Temperature
		K [°C]	K [°C]	K [°C]	K [°C]
Gas Turbine	1	-	903 [630]	903 [630]	925 [652]
$S - CO_2$ Engine	2	903 [630]	645 [372]	698 [425]	348 [75]
$S - CO_2$ Engine	3	645 [372]	441 [168]	494 [221]	329 [56]
$S - CO_2$ Engine	4	441 [168]	342 [69]	348 [75]	313 [40]

Table 4.2: Selected Temperatures: Combined Cycle

cycle engine can be explained by high back work ratio, which is the ratio of work required in the compressor relative to the work extracted in the turbine. The large amount of work required to drive the compressor results in additional losses because of inefficiencies in the turbine and compressor. Additional causes for the low exergy efficiency are due to the large range of heat rejection and heat addition by the cycle.

The $S - CO_2$ cycle engines feature moderate back work ratios, locally narrow ranges of heat addition, and narrow ranges of heat rejection, which is what drives their high exergy efficiencies. Unfortunately, there is a limit to how much energy each $S - CO_2$ engine can extract from the exhaust gases so the range of heat addition of the combined cascade of $S - CO_2$ engines is still high. The heat addition of the $S - CO_2$ engines over a large range is an internal process however, so the main penalty on the overall cycle is the large range of heat addition of the topping cycle.

When looking at the high exergy efficiency of the $S - CO_2$ engines, one may be inspired to replace the topping cycle completely with a $S - CO_2$ engine. There are several reasons doing so is not practical. The first reason is because of the very high working pressures in the $S - CO_2$ engines (up to 35MPa), it is not practical from a strength of materials perspective to operate at higher temperatures than the current configuration. The second reason is that with the $S - CO_2$ engines being closed loop cycles, an external combustion process would require large amounts of regeneration to pre-heat the incoming air in order to maintain a high temperature and narrow temperature range of heat addition. The burner would also have to operate very lean if a narrow temperature range of heat addition were implemented. Recuperators with low pressure, low density air would likely be very large and costly.

The combined cycle exergy efficiency of 77.5% shown in Table 4.1 is a very high overall exergy efficiency possible through the use of this unique engine cascade that extracts heat from the exhaust gases over limited temperature ranges by different engines. The fourth engine in the cycle features a small overall gain for the system so it's uncertain whether that engine would be economical to include in the system.

Table 4.2 shows the temperatures at the inlets and outlets of each heat exchanger transferring heat from the exhaust gases to the $S - CO_2$. Also displayed is the main compressor exit temperatures and the power turbine exit temperatures. The temperature difference between the power turbine and the heat exchanger exit can be significant due to the large specific heat mismatches between

the high and low temperature sides of the $S - CO_2$ engine. Because of this larger specific heat mismatch, the high temperature recuperator in the $S - CO_2$ engine is limited because the mass flow rates of the high and low pressure sides have to be equal in the high temperature recuperator.

Although fluid properties were available up to 2,000 K [1,727°C] for nitrogen, water, oxygen, and carbon dioxide, REFPROP could not operate above 1,724 K [1,451°C] with combustion product mixtures because of its inability to work with water vapour in the mixture. A real gas turbine can operate up to ranges of 1,900 K [1,627°C] and higher. Chemically reacting flows were not considered for the combined cycle configuration where no fuel cell was in use. Without a fuel cell, a standard Brayton cycle engine will operate much leaner. As a result, the mass fraction of the fuel during compression is reasonably low and the mass fraction of combustion products is reasonably low. Using pure air is believed to be a reasonable approximation for this engine and allowed for operating up to 1,890 K [1,617°C] without significant issues. When comparing results from pure air based analysis, the efficiencies are to be compared to the lower heating value (LHV) efficiencies of an analysis which considers chemically reacting flows.

Some additional studies were conducted to explore the impacts of some design choices on the overall system. In these efforts, a design parameter was varied, from the fixed or optimized values defined previously, to see its impact. Figure 4.9 shows the combined cycle efficiency vs the $S - CO_2$ engines' peak pressure (the main compressor outlet pressure). This parameter is important because the proposed system pressures are typically very high in $S - CO_2$ engines that it's useful to know the marginal gain of an increased operating pressure and compare that to the marginal cost, and possibly later constrain an optimization at a certain peak pressure. It's also interesting to note that an increase in peak pressure does not always result in an increase in efficiency as in Figure 2.35; there is an optimal peak pressure below 49MPa. The cause for this relationship needs further investigation. It's possible that the maximum allowed compressor pressure ratios specified in Table 2.2 are too low for $S - CO_2$ engines *without* reheat, at high main compressor outlet pressures. In addition to reheat possibly playing a role on the optimal peak pressure, the $S - CO_2$ minimum and maximum temperatures were shown in Figure 2.26 to play a role in the optimal peak pressure.

In this parameter sweep, all $S - CO_2$ engines were fixed with the same peak pressure. More flexibility would be allowed if each engine could have its peak pressure optimized, while sweeping the maximum constraint on that optimization of peak pressure instead. This approach would allow

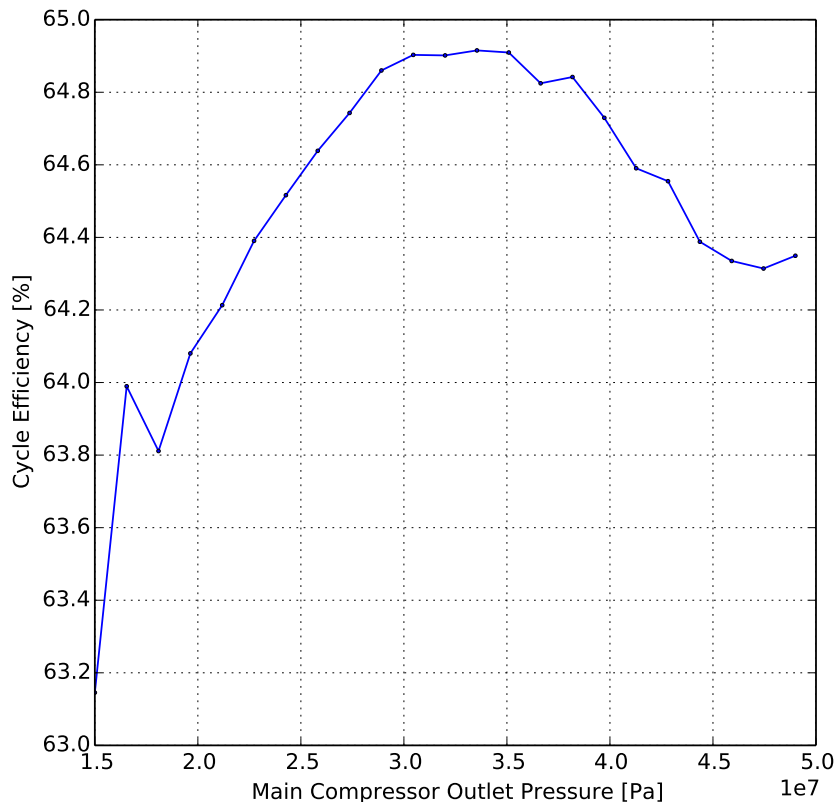


Figure 4.9: Combined Cycle Efficiency vs $S - CO_2$ Engine Peak Pressure

some engines that would prefer a lower peak pressure while still allowing engines that prefer the higher pressure to utilize the higher pressure. Looking at Figures 4.6 through 4.8, it is evident that different engines will optimize to different peak pressures with different maximum temperatures.

Further investigation is recommended if operation at pressures higher than 35MPa is believed to be possible from a structural standpoint. A first step would be to study the impact of the main compressor outlet pressure on cycle efficiency and optimal compressor pressure ratios at various turbine inlet temperatures for a stand alone $S - CO_2$ engine *without* reheat. After further exploring the stand alone $S - CO_2$ engine *without* reheat, then the influence of the same parameters should be explored for the combined cycle.

Figure 4.10 shows the overall combined cycle efficiency vs the topping cycle turbine rotor inlet temperature at various ambient temperatures. The maximum temperature is a very important parameter from a cost perspective because higher operating temperatures result in higher initial and

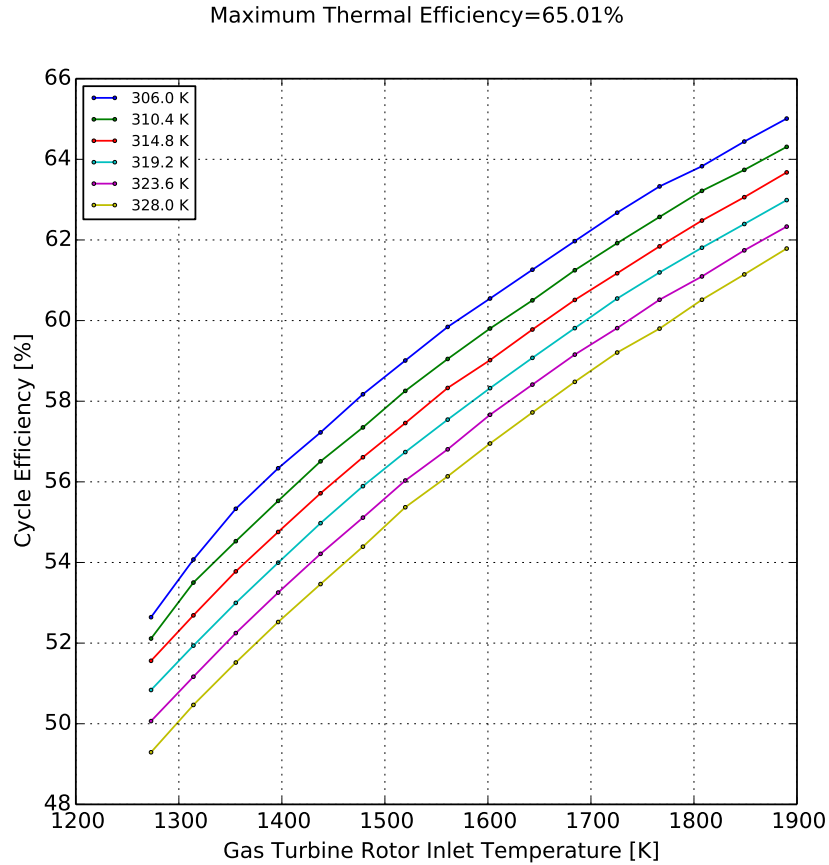


Figure 4.10: Combined Cycle Efficiency vs Topping Cycle Turbine Inlet Temperature at Various Ambient Temperatures

maintenance costs. Variation in efficiency with ambient temperature is very relevant as it indicates how the configuration could perform if designed and applied to different climates, seasons, and the size and type of the heat rejection heat exchangers.

Figure 4.11 shows the variation in exergy efficiency over the same range of temperatures as in Figure 4.10. Comparing to Figure 2.24, one will notice that the maximum exergy efficiency is actually lower for the combined cycle than a single cycle, despite the fact that the maximum temperature is considerably higher. However, the thermal efficiency of the combined cycle is still higher, and as mentioned previously, it's not practical to use a $S - CO_2$ cycle engine at higher temperatures due to the high operating pressures, and the single $S - CO_2$ engine is configured for fuels which can supply all of their energy over a high, narrow temperature range, which the combustion of natural gas cannot easily do.

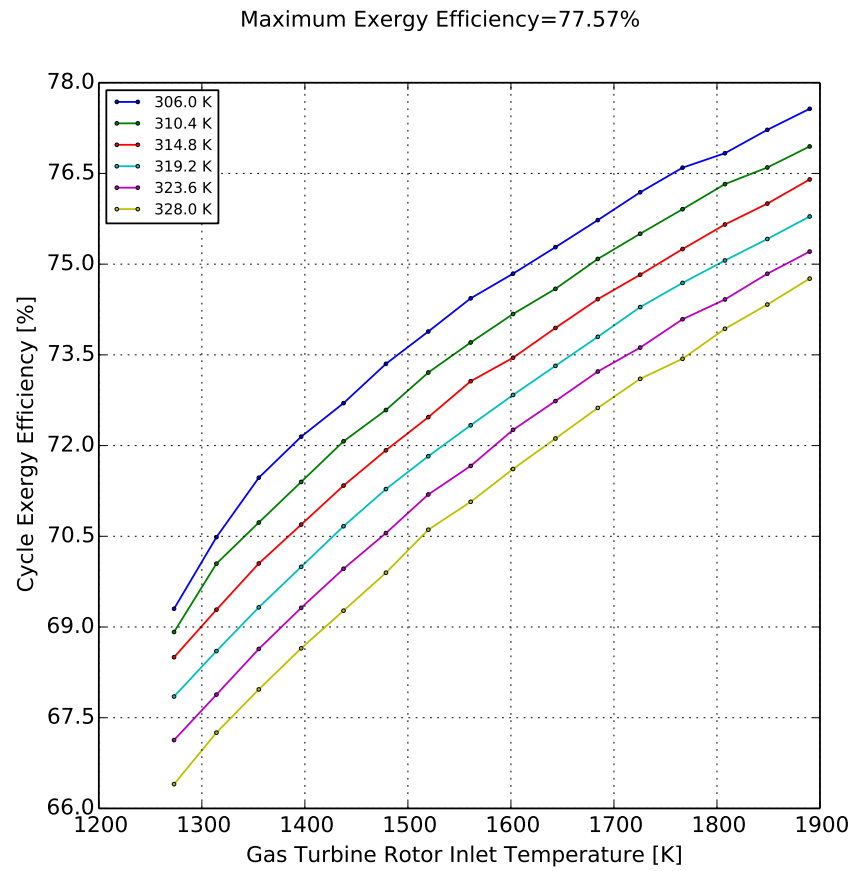


Figure 4.11: Combined Cycle Exergy Efficiency vs Topping Cycle Turbine Inlet Temperature at Various Ambient Temperatures

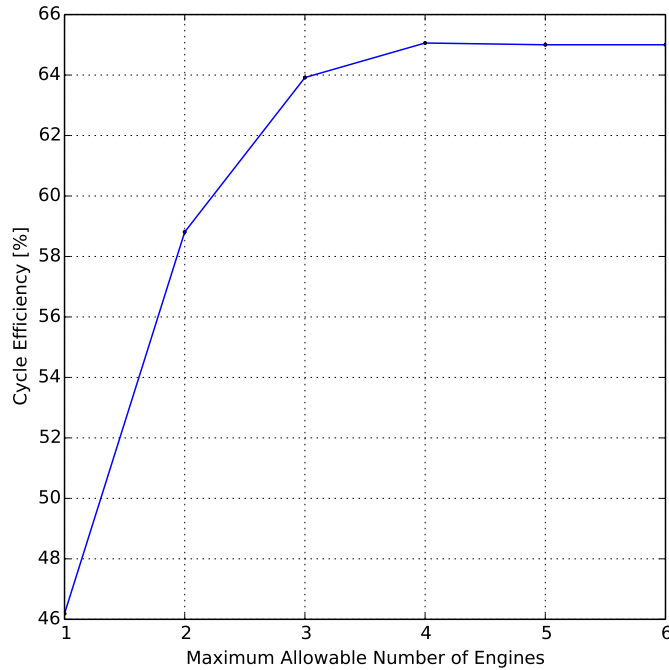


Figure 4.12: Combined Cycle Efficiency vs Total Number of Engines

Figure 4.12 shows the combined cycle efficiency vs the number of engines in the cascade, one engine being a simple gas turbine cycle. In this study, the optimal design was found given the constraint on the maximum allowable number of engines, therefore, the results are different than those presented in Table 4.1. There is no increase in efficiency with more than four engines and therefore there will not be more than four engines.

Figure 4.13 shows the overall combined cycle efficiency vs the topping cycle's isentropic efficiency. Because the topping cycle has a much larger pressure ratio and back work ratio, it's important to understand the sensitivity of this component's performance to the overall system because a more efficient component will come at a higher cost. It's important to make note when reviewing all of these parameter sweeps that there appears to be some "noise" in the results. This is caused by the optimization process not being an exact one. Each time a new optimization run is conducted, a new random starting population is selected. Reducing the variability between runs can be done by increasing the population size as well as the tolerance on the optimizer's convergence. However, doing so will increase the run time and there is a trade off between run time and accuracy and repeatability.

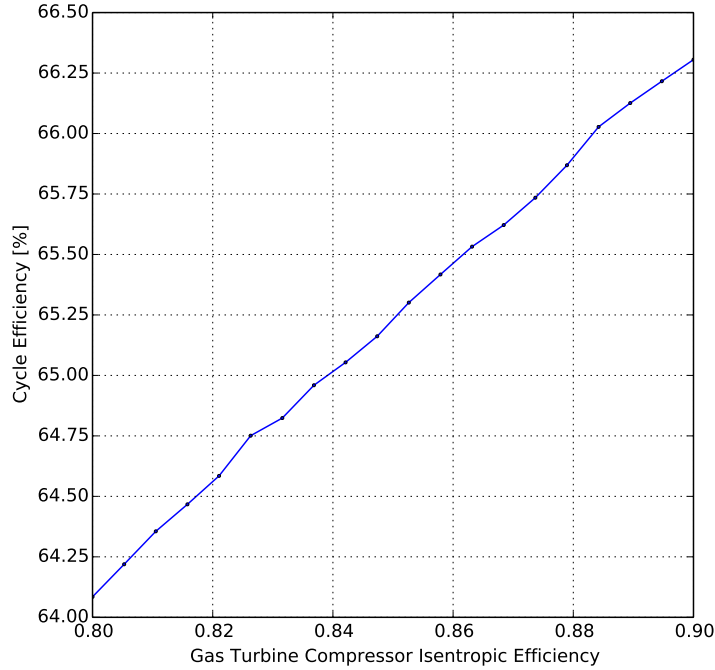


Figure 4.13: Combined Cycle Efficiency vs Topping Cycle Compressor Isentropic Efficiency

4.3.2 Combined Cycle With Fuel Cell

Using the design optimization process, for the combined cycle configuration with a Brayton cycle engine and integrated fuel cell as the topping cycle, a combined cycle efficiency of 73.1% was predicted using the lower heating value (LHV) of the fuel and 65.8% using the higher heating value (HHV) of the fuel.

Figure 4.14 depicts the temperature entropy diagrams for all engines in the cascade. Figures 4.15 through 4.17 depict temperature entropy diagrams for the three different engines in the cascade with appropriate axis ranges for their temperature of operation. Compared to the combined cycle configuration without the integrated fuel cell just presented, there are only two $S - CO_2$ engines instead of three. Shown in Table 4.3, the topping cycle has a much larger work fraction at 91.15% for the combined fuel cell and gas turbine. The fuel cell has a work fraction of 71.14% and the gas turbine has a work fraction of 20.01%.

Because of these reduced work fractions, the $S - CO_2$ engines contribute much less in improving the overall combined cycle efficiency although they still have fairly high exergy efficiencies. The

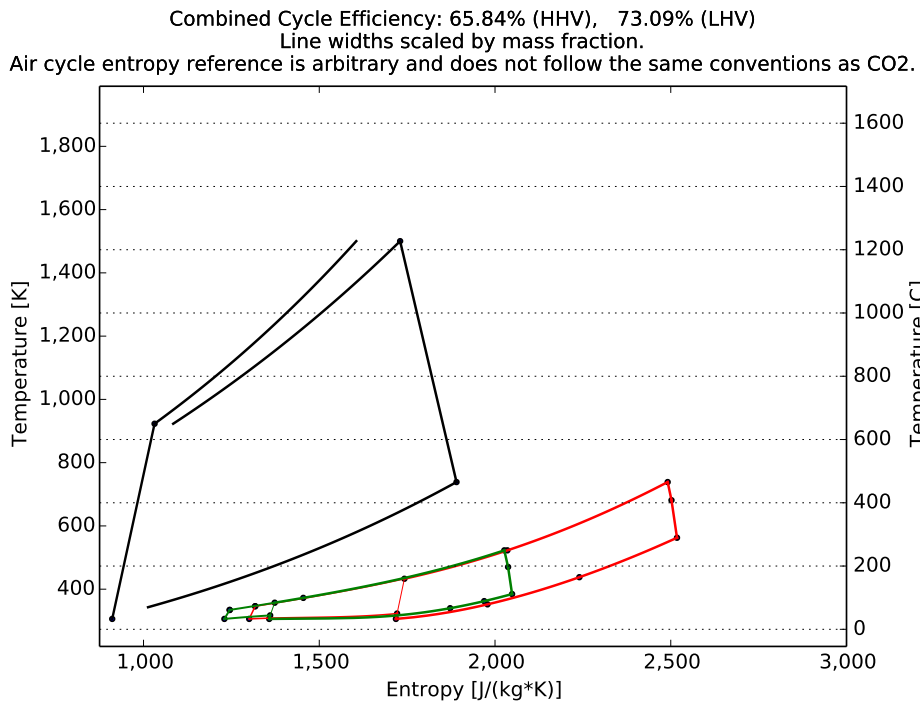


Figure 4.14: Combined Cycle With Fuel Cell, All Engines: Temperature Entropy Diagram

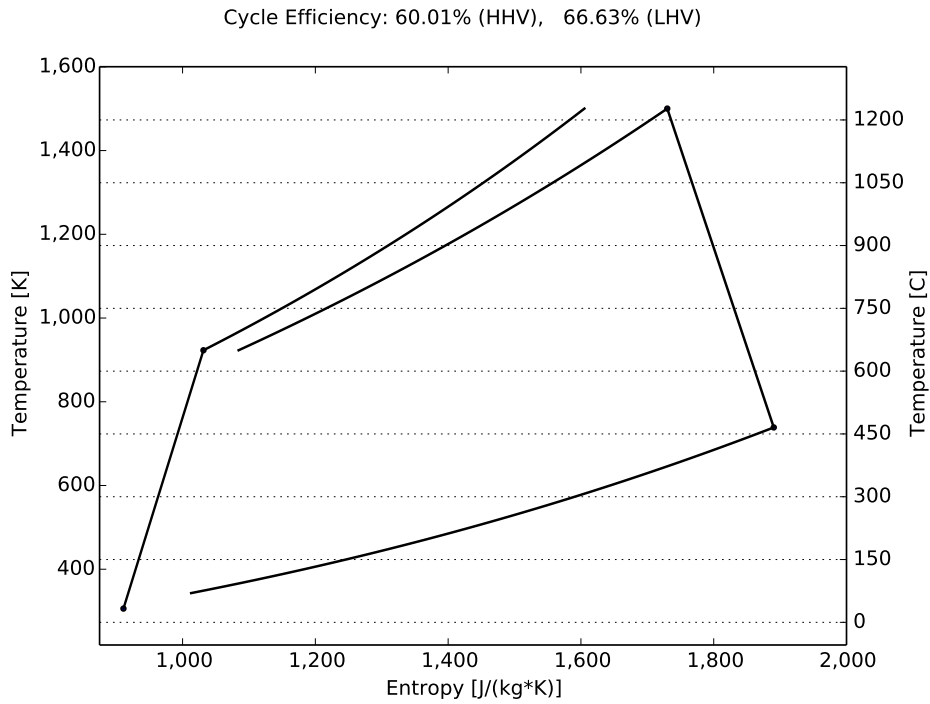


Figure 4.15: Combined Cycle With Fuel Cell, Engine Number 1: Hybrid Fuel Cell and Brayton Cycle, Temperature Entropy Diagram

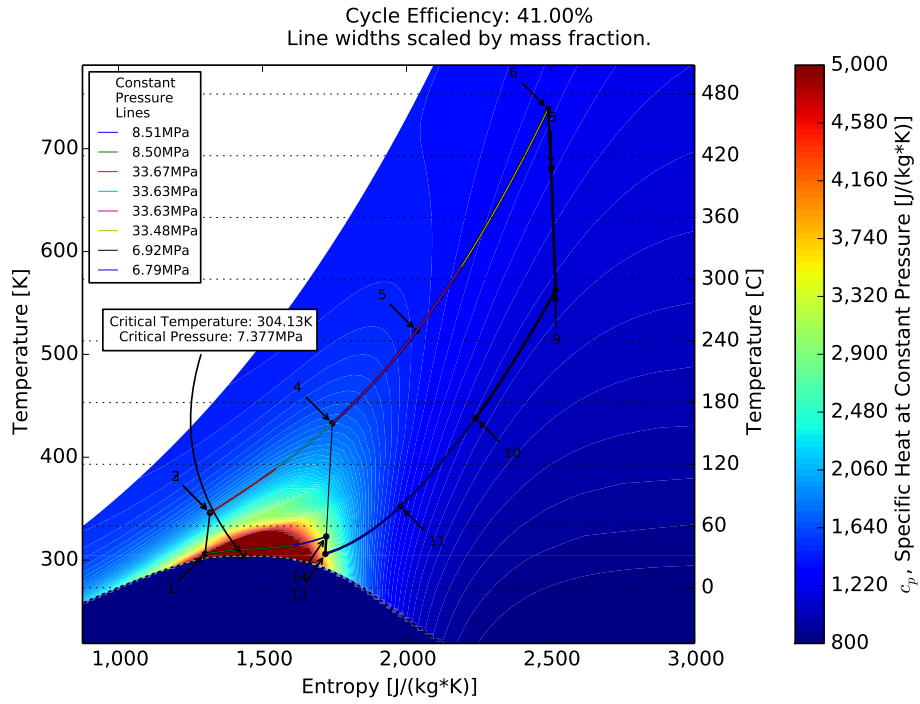


Figure 4.16: Combined Cycle With Fuel Cell, Engine Number 2: $S - CO_2$ Cycle, Temperature Entropy Diagram with Specific Heat at Constant Pressure Contour Level Background

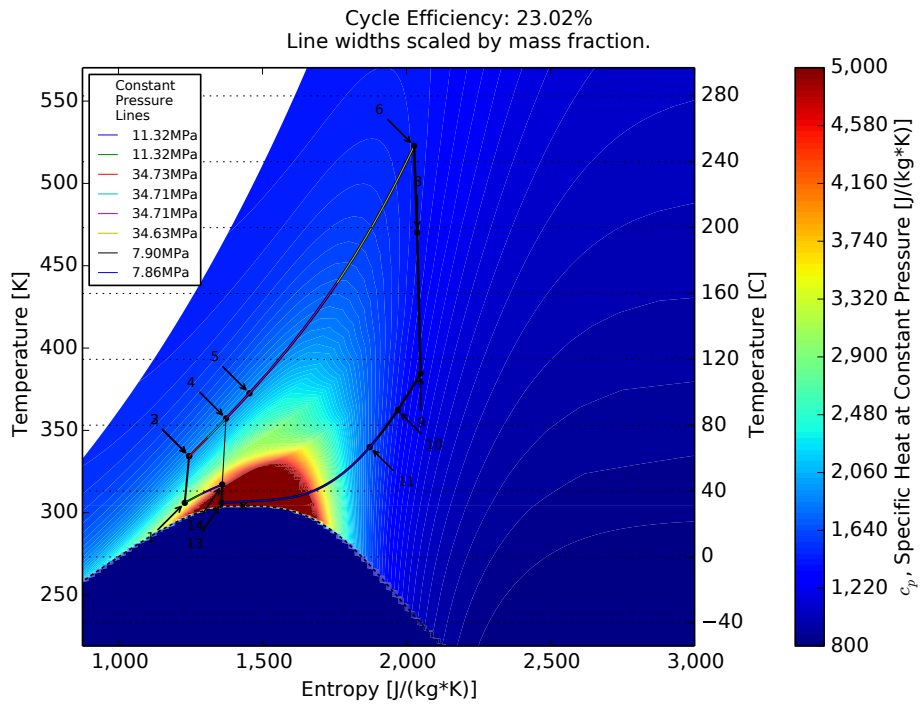


Figure 4.17: Combined Cycle With Fuel Cell, Engine Number 3: $S - CO_2$ Cycle, Temperature Entropy Diagram with Specific Heat at Constant Pressure Contour Level Background

Engine		Work Fraction		Marginal Combined Cycle Efficiency				Engine Efficiency		Engine Exergy Efficiency
Type	Number	%		HHV, %		LHV, %		%		%
Fuel Cell	1	71.14	91.15	46.84	60.01	52.00	66.63	52.00 (LHV)	66.63 (LHV)	-
Gas Turbine		20.01		13.17		14.63		30.47 (LHV)		
$S - CO_2$ Engine	2	6.44		4.24		4.71		41.00		69.99
$S - CO_2$ Engine	3	2.41		1.59		1.76		23.02		55.52
Combined		100.00		65.84				73.09%		-

Table 4.3: Work Split and Efficiencies: Combined Cycle With Fuel Cell

Engine		Exhaust Gas Heat Exchanger		Power Turbine	Main Compressor
Type	Number	Inlet Temperature	Outlet Temperature	Exit Temperature	Exit Temperature
		K [°C]	K [°C]	K [°C]	K [°C]
Fuel Cell + Gas Turbine	1	-	739 [466]	739 [466]	923 [650]
$S - CO_2$ Engine	2	739 [466]	523 [250]	563 [289]	346 [73]
$S - CO_2$ Engine	3	523 [250]	373 [99]	385 [111]	334 [61]

Table 4.4: Selected Temperatures: Combined Cycle With Fuel Cell

low work fraction can be explained by observing the inlet temperatures shown in Table 4.4 for the exhaust gas heat exchangers and comparing them to the combined cycle without a fuel cell shown in Table 4.2. The highest temperature a $S - CO_2$ engine receives is 739 K [466°C] compared to 903 K [630°C] for the previous combined cycle without a fuel cell.

The fuel cell is naturally a more efficient process than a stand alone Brayton cycle, and the two combined have a LHV efficiency of 66.63%. This is higher than the entire previous combined cycle without a fuel cell! Naturally, there is less waste heat for the $S - CO_2$ to utilize. The combustor also only burns the excess fuel not able to be utilized by the fuel cell, so the peak cycle temperature is 1,500 K [1,227°C], compared to 1,890 K [1,617°C] for the previous combined cycle without a fuel cell. Naturally, the turbine exit temperature will be lower if the turbine inlet temperature is reduced, with a similar pressure ratio. Regardless of the reduced contribution of the $S - CO_2$ cycle engines in this combined cycle configuration, they do still increase the cycle efficiency by over 6 percentage points on a lower heating value basis.

Another important point to note is the itemized fuel cell efficiency listed in Table 4.3 may be a little unfairly high relative to the gas turbine. Since the two components are so closely coupled, it's difficult to decide how much of the losses due to fuel and air compression should be attributed to the fuel cell and how much to be attributed to the gas turbine. Presently, all of these losses

are attributed to the gas turbine, so the fuel cell gets its fuel and air compressed (and heated) for “free”. The combined fuel cell and gas turbine efficiencies are not as ambiguous though because they treat the two components as one combined system, sharing the losses. It’s also important to point out that the exergy efficiency is not specified in Table 4.3 for the fuel cell, gas turbine, or the overall combined cycle. The present work has not focused on a detailed exergy flow analysis. A follow on work may be useful to properly identify exergy destruction in each component and more clearly identify the losses that should be attributed to the fuel cell and the gas turbine and to define an overall combined cycle exergy efficiency.

It should be noted that there are some gaps in the lines for the topping air cycle in Figures 4.14 and 4.15. The current combined cycle analysis code lumps the heat generation of the fuel cell and combustor into a single component that considers the fuel utilization of each. As a result, there is no distinction on the temperature entropy diagram at the fuel cell exit. Also no intermediate species concentrations were computed inside the fuel cell or combustor. As a result, the entropy inside the fuel cell and combustor is not known. A constant pressure line is computed for air from the compressor exit temperature, up to the combustor exit temperature. There is also a constant pressure line computed for combustion products from the compressor exit temperature up to the combustor exit temperature. The actual constant pressure line considering the local species concentration will be somewhere in between these two constant pressure lines. The actual fuel cell and combustor will have some small pressure loss as well, so a constant pressure line is an idealization.

It’s important to make some distinction between lower heating value (LHV) and higher heating value (HHV) efficiencies. A LHV efficiency is an efficiency which assumes that the latent heat of vaporization of water in the combustion by-products is energy that is virtually unobtainable. Thermodynamically, this is not correct. The approach does not conserve energy. Nevertheless, industry has primarily adopted a convention where LHV efficiencies are presented. Using the LHV of a fuel when performing analysis of a Brayton cycle engine for the most part allows for ideal gas analysis to be used with reasonable accuracy because dealing with the non-linearity of the condensation of the water vapour is avoided. Another motivation for the use of LHV efficiencies is because the relative LHV and HHV of different fuels aren’t the same. Comparing a HHV efficiency of an engine configuration with a HHV of a similar engine configuration with a different fuel will not

result in the same efficiency because they both have different amounts of “unobtainable” energy in the water vapour relative to the rest of the energy in the fuel. Using a LHV efficiency and LHV of a fuel allows one to compare engines and fuels without considering the chemical reactions involved.

The temperature at which the water vapour condenses in combustion gases is very low, due to the low partial pressure of the water vapour due to the dominance of nitrogen in air compared to oxygen as well as the very lean operation of most open loop gas turbines. If the water were to completely condense, it would be at such a low temperature that it would not be able to do much useful work. The latent heat of vaporization can still be used for combined heat and power applications though. So, considering a LHV efficiency is not appropriate when an engine can use the latent heat of vaporization of the fuel.

There was some question as to whether there could be any benefit to running the fuel cell at a fuel utilization less than its maximum, combusting more fuel. Similar to the parameter sweeps that were conducted for the combined cycle engine without a fuel cell, a parameter sweep was conducted for the combined cycle engine with a fuel cell, varying the fuel utilization. The results indicated that the combined cycle efficiency increases nearly linearly with fuel utilization and the maximum fuel utilization results in the highest combined cycle efficiency. If the fuel utilization could reach 100%, that would be preferred, but is not a reality due to the way the electrochemical reactions must occur in the fuel cell in an environment with excess fuel present.

4.4 Conclusions

The present work demonstrates two different combined cycle configurations that utilize supercritical carbon dioxide power cycles as a means to increase the efficiency by extracting more work from heat in exhaust gases that otherwise would be wasted. One concept uses a traditional open loop gas turbine engine (Brayton cycle) with a combustor as the topping cycle and a series of supercritical carbon dioxide ($S-CO_2$) engines as intermediate cycles and a bottoming cycle. A global optimization of the engine design parameters was conducted to maximize the combined efficiency of all of the engines. A combined cycle efficiency of 65.0% is predicted with three ($S - CO_2$) engines. This assumes dry-cooling.

The other combined cycle configuration concept utilizes a fuel cell inside of the topping cycle

in addition to a combustor. The fuel cell utilizes methane fuel. The waste heat from the fuel cell is used to heat the high pressure air. A combustor is also used to burn the excess fuel not usable by the fuel cell. After being heated, the high pressure, high temperature air expands through a turbine to atmospheric pressure. The low pressure, intermediate temperature exhaust air is then used to power a cascade of supercritical carbon dioxide engines. A combined efficiency of 73.1% using the fuel lower heating value is predicted with this combined fuel cell and gas turbine and two ($S - CO_2$) engines. This is also for a dry-cooling configuration.

The complexity of the layout is high, but each engine in the ($S - CO_2$) engine cascade is a nearly independent module that could be designed, built, and tested independently. Because of the power density of the ($S - CO_2$) engine, its size and weight are much smaller than a comparable steam turbine, in addition to the efficiency benefits.

The general supercritical carbon dioxide engine layout explored is a little studied concept that will require effort to commercialize and mature, but all of the necessary components in the system are believed to be possible to construct. The fuel cell component plays a dominant role in the second combined cycle configuration. Fuel cell technology is still evolving and has not yet reached cost parity with gas turbines. The current cycle layout increases the scale and operating pressure of such devices. It's anticipated that configurations such as the proposed layout could motivate further efforts towards cost reduction in fuel cells due to improved design and manufacturing processes. The studied combined cycle configurations, although complex, are believed to be very feasible.

4.5 Recommended Future Work

There may be some benefits of using the latent heat of vaporization of water in the combustion products. Because of the higher exergy efficiency of the supercritical carbon dioxide power cycles, there still may be some beneficial work that can be extracted from the condensation of the water, even though the thermal efficiency may be low. It's possible an increase of ~ 0.5 percentage points of cycle efficiency could be obtained by extracting heat from this condensing water. In order to investigate these possibilities, more exhaustive and realistic exploration can be conducted by increasing the range of operation of the code with combustion products to higher and lower temperatures.

The ranges of the compressor pressure ratios used in the optimization were limited to the same ranges used in Chapter 2, which were defined in Table 2.2. In Chapter 2 these ranges were determined to be appropriate for a $S - CO_2$ cycle with reheat because the absolute maximum efficiency was far from the upper and lower limits, which was shown in the parameter sweep displayed in Figure 2.27. In the combined cycle, where reheat is not used, it's possible a higher pressure ratio may be more beneficial. Further work could be conducted to explore larger allowed ranges of compressor pressure ratios in the $S - CO_2$ engines of the combined cycles.

The present analysis considered a cascade of engines where each engine extracted some heat from the topping cycles exhaust gases over a limited range. This approach allows for simpler modeling, design, testing, and controls. An alternate approach could be used where the first supercritical carbon dioxide cycle (the second engine in the cascade) extracts all of the heat down to it's compressor exit temperature. It's waste heat then would be exchanged to the next engine in the cascade, all the way down to that engine's compressor exit temperature. This approach would be more complex to model, test, and control, but it may be simpler from a plumbing perspective and allow for some lower cost components because the temperature difference in the heat exchangers may be higher because the exhaust gases are utilized all the way down to ambient temperature, including the condensation of the water vapour.

The present work focused on steady, on-design analysis. The strengths and weaknesses of the studied configurations in transient and part load conditions have not been considered. It's anticipated that the benefits of each different component in this combined cycle could be harnessed during different load conditions to provide a more stable operation than may be achievable with a simpler combined cycle configuration. Further work should be conducted to explore these design conditions.

The $S - CO_2$ engine cycle analysis code used as a basis for this work does not currently have the capability to model engines which operate below the critical temperature of carbon dioxide. Implementing such capability could identify designs with higher efficiency due to the condensation of carbon dioxide that would occur. This assumption means that all the simulations conducted have dry-cooling which can have huge advantages in many applications. If wet-cooling was available, the carbon dioxide would condense, and an even more efficient cycle would likely result.

Chapter 5

Conjugate Heat Transfer With Supercritical Carbon Dioxide As the Working Fluid

5.1 Introduction

As was emphasized in the previous Chapters, heat exchangers play a pivotal roll in proposed power cycles that utilize supercritical carbon dioxide as their working fluid. In these proposed supercritical carbon dioxide power cycles, massive amounts of recuperation occurs. The recuperative power is typically larger than the heat transfer entering the system from the external fuel source. In combined cycle power plants where there are multiple engines operating in a cascade in order to extract the maximum amount of energy from the the fuel source, there is even more heat transfer required.

In the operating range of heat exchangers in such proposed power cycles, there is typically a large variation in fluid properties that occurs within the heat exchangers. This variation in fluid properties is both from the high pressure side to the low pressure side, as well as from the high temperature end to the low temperature end in each respective fluid stream. With these large variations, design and analysis is not nearly as straightforward as heat exchanger design that involves fluid streams with constant and equal specific heats or constant but dissimilar specific heats, or a constant specific heat on one side and a condensation or boiling process on the other side.

Much of the prior work in the field has focused on characterizing heat transfer coefficients of supercritical carbon dioxide in flow configurations representative of printed circuit heat exchangers, which likely may be used in such power cycles. Many of the studies identified by the author were focused on heat transfer coefficients and not isolation of the impacts of specific heat. All of the studies identified also did not focus on conjugate heat transfer between two supercritical carbon dioxide fluid streams, but rather, typically focused on heat transfer between supercritical carbon dioxide and a nearly isothermal fluid, such as water, or a constant heat flux boundary[45, 46].

Many researchers studying supercritical carbon dioxide power cycles utilize some type of simplified heat exchanger model in order to rapidly facilitate the analysis of the overall cycle configuration of interest. Often times, little detail is provided by the researchers on these heat exchanger models and their applicability to real heat exchangers. The simplified 0-D heat exchanger model described in Section 2.3.3 did not consider any geometry, effectiveness, surface area, or convection coefficients to be defined, but instead relied on a minimum temperature difference and pressure drop to be defined. Such an approach was chosen in order simplify the heat exchanger model as well as eliminate any direct assumptions about the heat exchanger geometry or flow and heat transfer and their dependency on fluid properties, while still accommodating for losses in a heat exchanger.

5.2 Problem Scope and Methodology

The present work has several goals. The first is to understand the impacts of variable fluid properties on flow and conjugate heat transfer in a simple geometric configuration. The second is to assess the feasibility of conducting numerical simulations of fluid flow and heat transfer with variable fluid properties with computational fluid dynamics tools, as well as assess the resolution needs for the fluid property data used. The work also aims to better investigate the applicability of the previously mentioned 0-D simplified heat exchanger model to high level supercritical carbon dioxide power cycle analysis.

Figure 5.1 illustrates the simple flow configuration studied: two straight, two dimensional channels separated by a solid. This 2-D infinite channel configuration would not be practical in a real heat exchanger from a structural standpoint, especially one with a high pressure difference between the two fluid streams. The use of straight channels also limits the power density of the

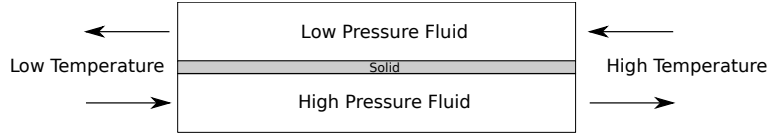


Figure 5.1: Heat Exchanger Sketch

heat exchanger, and therefore would not be economically effective. However, the present work is still believed to be useful as a foundation for understanding flow and heat transfer with variable fluid properties. Complex phenomenon can occur in real fluid heat exchangers, in the absence of complex flow geometries.

5.2.1 Details of Computational Tools Utilized

Initially, the ANSYS Fluent[47] computational fluid dynamics tool was utilized. Fluent features an inbuilt REFPROP fluid property interface. This feature, coupled with the author's previous extensive experience[48] with the software package motivated its initial use. Two modes were available for the REFPROP fluid property interface. The first mode utilizes a direct call to the REFPROP FORTRAN codes for each fluid property state needed. This approach resulted in the highest accuracy achievable, as far as fluid property data quality goes. However, it was extremely slow. The one good case that was able to be converged with Fluent, took several weeks of continuous run time with a simple 2-D flow configuration, an unpractical process. The second method available in Fluent allowed a data table to be pre-generated based on user instruction every time the solver was launched. Control of the resolution of the data tables generated was very limited to the user. This approach proved to be much faster to iterate, however, no good solutions were able to be obtained. Typically the solutions would diverge or have very high residuals and were not able to be trusted. Over a month of effort was dedicated towards trying to obtain a meaningful solution process with the Fluent software package, with negligible success.

After this experience, it was decided to explore the use of the Star-CCM+[49] solver instead. Star-CCM+ does not have any in built REFPROP fluid property database interface. Star-CCM+ does has the ability to configure a user defined equation of state. One option is to specify the user defined equation of state in terms of temperature and pressure in the form of a data table. Although less convenient in that the user has to supply their own data tables for Enthalpy, Density, Speed of

Sound, Dynamic Viscosity, and Thermal Conductivity, this solution does provide the user with vast control on the range and resolution of the data tables. The primary drawback in Star-CCM+'s data table fluid property mode is that it only allows for piecewise linear interpolation between data points.

Having already developed wrapper functions for REFPROP[13] using Python, as part of the supercritical carbon dioxide power cycle analysis code, those functions were then used to generate data tables in the required CSV format that Star-CCM+ accepted. No considerable reduction in solver performance was identified when using the user defined equation of state utilizing data tables. In general the Star-CCM+ solver and simulation suite proved to be much more stable, user friendly, modular, and capable than the Fluent software package, and therefore is recommended for any future simulations.

5.2.2 Flow Configuration and Simulation Setup

A structured mesh was generated utilizing Star-CCM+'s built in meshing tool. A simple rectangular channel and wall geometry was first created using the solid modeling tool. The "Directed Meshing" procedure was then used to create a structured 3-D mesh for the two fluid streams as well as the solid wall. The resultant 3-D mesh, which was aligned normal to the Z axis, was then converted to a 2-D mesh. The resultant 2-D mesh of fluid and solid regions had 250,368 cells.

Each channel was 3mm tall, but only 1.5mm were modeled. The solid wall was defined to be 0.5mm thick. The length of the channel was 1 m for Cases I through IV and 10 m for Cases V and VI. Because of this aspect ratio, all contour plot Figures presented do not have equal horizontal and vertical scaling. A 100:1 scaling was applied to the horizontal axis of the 1 m cases and a 1000:1 scaling was applied to the 10 m cases in order to make the figures a more manageable shape. Figure 5.2 depicts the geometry as well as boundary condition definitions.

Details regarding each case are defined in Table 5.1. For Cases I through V the inlet total temperature on the high pressure side of the heat exchanger was defined to be a uniform 305 K, and on the low pressure side, a uniform 450 K. The outlet static pressure on the low pressure side was defined to be 5 MPa, and the outlet static pressure on the high pressure side was defined to be 25 MPa. For Case VI, the inlet total temperature on the high pressure side of the heat exchanger

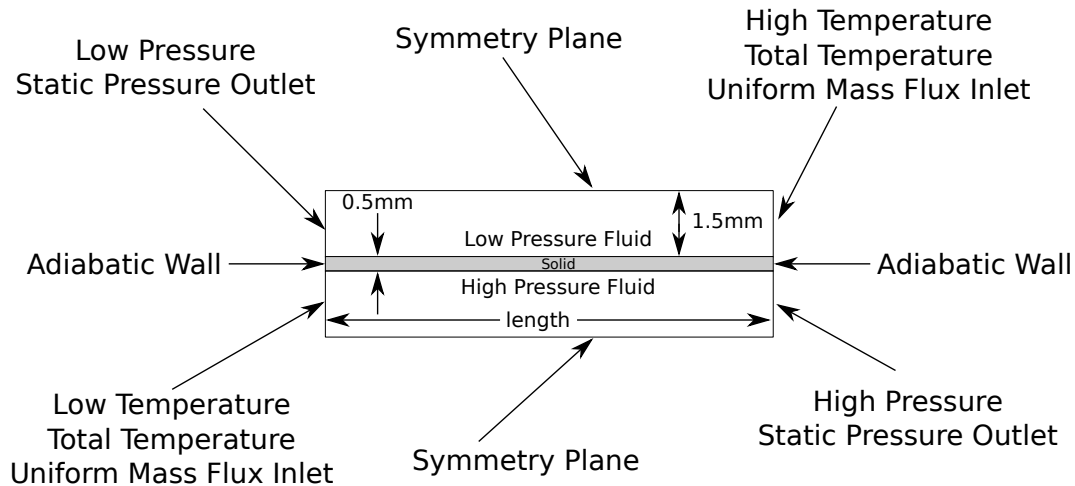


Figure 5.2: Heat Exchanger Boundary Conditions

was defined to be a uniform 600 K, and on the low pressure side, a uniform 700 K. The outlet static pressure on the low pressure side was defined to be 1 MPa, and the outlet static pressure on the high pressure side was defined to be 5 MPa. For all cases, inlet boundary conditions were defined to have a uniform mass flux. Because the inlet mass fluxes and total temperatures were uniform, the flow hydrodynamically and thermally develops at the entrance. No buoyancy forces due to gravity were modeled.

As mentioned previously, only 1/2 of each channel was actually modeled. At the center-line/boundary of the channel a symmetry boundary condition was imposed. This basically assumes that there is an infinite series of stacked channels with alternating pressure levels and flow directions. This is another thing that may be an over idealization about this flow configuration because it may be too difficult to configure such a manifold configuration at the inlets and outlets. At the ends of the solid material, an adiabatic boundary condition was assumed. Such assumptions are definitely an idealization, but was made in order to simplify the configuration such that the focus can be on the physics and heat transfer involved with the simplest case.

For all cases except Case VI, the mass flux on high pressure side was defined to be 0.565 of that of the mass flux on the low pressure side. This relative mass flux was chosen based on explorations conducted with the previously mentioned simplified 0-D heat exchanger model, which were used to identify a case with a well matched heat capacity between the two fluid streams. This mass fraction is similar to what one could design a recompression supercritical carbon dioxide cycle to utilize,

however, not necessarily an optimized design. Rather than choosing an optimized mass fraction based on a good fit with a recompression supercritical carbon dioxide cycle, the 0.565 mass fraction was chosen to more clearly distinguish some of the unusual effects that occur in a heat exchanger with a low minimum temperature difference and variable and dissimilar fluid properties. For Case VI, the mass flux was defined to be 1.0.

The actual mass fluxes imposed are adjusted in order to study different Reynolds numbers. The Reynolds number is based on the hydraulic diameter of an infinite channel, which is defined to be twice the channel height. Because of the variation in viscosity with temperature, due to the heat transfer in the heat exchanger, the Reynolds number is different from the inlet to the exit of each channel and is plotted as a reference for each case studied. Also, because the mass fluxes differed between the channels, the Reynolds numbers also different between channels. Because of this, the minimum Reynolds number was used to identify each case. The minimum Reynolds number occurred at the high pressure inlet. For flows that were expected to be turbulent (based on the Reynolds number), Star-CCM+ was configured to use the standard $k - \omega$ turbulence model without a wall function.

The user defined equation of state model in Star-CCM+ was used for the fluid streams with Carbon Dioxide fluid properties defined as a function of temperature and pressure in the generated data tables that were imported into Star-CCM+. The coupled flow and coupled energy models were selected. The flow solution was configured to be independent of time (steady flow). The solid region was configured to be 316 Stainless Steel, using Star-CCM+'s in built material property database. This material property database featured a constant density of $8,000 \text{ kg}/\text{m}^3$, constant thermal conductivity of $16.0 \text{ W}/(\text{m} * \text{K})$, and a constant specific heat of $502.0 \text{ J}/(\text{kg} * \text{K})$. Any variation in Stainless Steel material properties with temperature was assumed to have a minimal impact on the overall solution. Researchers are actively studying the applicability of 316 Stainless Steel for heat exchangers in supercritical carbon dioxide power cycles[50].

Because of the different operating pressures between the two fluid streams in the studied configuration (5 MPa and 25 MPa or 1 MPa and 5 MPa), two nearly identical fluid continua were generated in Star-CCM+ in order to be able to define two different reference pressures. Appropriately defining the solver reference pressure, as well as using the double precision solver was essential in order to obtain low solver residual levels.

Case	Re_{D_h} , High Pressure Inlet	Viscous Model	Low Pressure Inlet Total Temperature	Low Pressure Outlet Static Pressure	High Pressure Inlet Total Temperature	High Pressure Outlet Static Pressure	High Pressure Mass Fraction	Length	Notes
I	10	Laminar	450 K	5 MPa	305 K	25 MPa	0.565	1 m	Low Re, Low ΔT_{min}
II	50	Laminar	450 K	5 MPa	305 K	25 MPa	0.565	1 m	Low Re, Medium ΔT_{min}
III	3,000	Turbulent	450 K	5 MPa	305 K	25 MPa	0.565	1 m	High Re, High ΔT_{min}
IV	4,000	Turbulent	450 K	5 MPa	305 K	25 MPa	0.565	1 m	High Re, High ΔT_{min}
V	3,000	Turbulent	450 K	5 MPa	305 K	25 MPa	0.565	10 m	High Re, Low ΔT_{min}
VI	3,000	Turbulent	700 K	1 MPa	600 K	5 MPa	1.000	10 m	Nearly Constant and Nearly Similar Specific Heats

Table 5.1: 2-D Heat Transfer Cases

5.2.3 Post Processing

All contour plots were done directly within Star-CCM+ with its built in post processor. A separate python/numpy/matplotlib based post processing script was created in order to do averaging and other analysis not possible directly within Star-CCM+. Data tables were exported from Star-CCM+ in ASCII text file format in order to facilitate this process.

Total temperature and temperature are used where appropriate, although Mach numbers were very low, approximately .01, and therefore the difference between stagnation and static values was typically negligible. Mass flux at each horizontal position was averaged based on the channel cross sectional area. Other parameters were averaged with a weighting of mass flux of the channel at that horizontal location. Average fluid properties (density, viscosity, thermal conductivity and specific heat) were computed based on the mass flux averaged static temperatures and pressures at that horizontal location, using the REFPROP fluid property functions. It should be noted that the fluid properties themselves were not averaged directly (they could have been), but it was deemed more appropriate to utilize values based on average temperatures and pressures because those are the

parameters that would be measured in an experiment.

The local Reynolds number was computed based on the hydraulic diameter, the average mass flux, and the local average dynamic viscosity. The local Nusselt number was computed based on the hydraulic diameter, the local heat transfer coefficient, and local average fluid thermal conductivity.

It was thought that a total enthalpy weighted average total temperature would be more appropriate than a mass flux averaged total temperature. This was because the total temperature would not have an specific heat weighting if that were the averaging technique. Therefore, a mass flux weighted average total enthalpy and pressure were computed and then the corresponding total temperature was computed from those values using the REFPROP fluid property functions.

5.3 Results

5.3.1 Grid Dependency Studies

Two grid dependency studies were conducted simultaneously. One was a grid dependency study of the fluid property grid and the other was a grid dependency study for the geometry grid. Rather than the typical 3 cases compared in a grid dependency study, 9 cases were conducted instead. A separate study was also conducted for both laminar and turbulent flow, coming to a total of 18 cases. Details regarding the fluid property grids used for the grid dependency study as well as Cases I through V are presented in Table 5.2. Details regarding the geometry grids used for the grid dependency study as well as all cases are presented in Table 5.3. The 00 fluid property and geometry grids were used for all cases and the grid dependency study was a grid coarsening study to verify that the 00 grid used was appropriate. The laminar grid coarsening study was done for Case I and the turbulent grid coarsening study was done for Case V. Validation using those two cases was assumed to be an appropriate reference to use for establishing the quality of the grid for use with the other laminar and turbulent cases. Case VI utilized a different fluid property grid because of its different operating range, but no grid dependency was conducted because the grid resolution was higher and the property variations in that operating range were significantly lower. The number of grid points in the laminar and turbulent geometry grids were the same, but the grid point clustering was different. Both the laminar and turbulent grid dependency study cases utilized

Grid Level	Minimum Temperature	Maximum Temperature	Temperature Points	Minimum Pressure	Maximum Pressure	Pressure Points	Total Points
00	304.22 K	500 K	3001	4.4 MPa	26.0 MPa	217	651,217
11	304.22 K	500 K	1501	4.4 MPa	26.0 MPa	109	163,609
22	304.22 K	500 K	751	4.4 MPa	26.0 MPa	55	41,305

Table 5.2: Fluid Property Grid I

Grid	Top Half Channel Points	Top Channel First Point Spacing From Wall	Bottom Half Channel Points	Bottom Channel First Point Spacing From Wall	Solid Wall Points	Length Points	Total Points
00	41	1.00E-5 m (laminar), 2.50E-6 m (turbulent)	41	1.00E-5 m (laminar), 5.00E-6 m (turbulent)	17	2,609	258,291
11	21	2.00E-5 m (laminar), 5.00E-6 m (turbulent)	21	2.00E-5 m (laminar), 1.00E-5 m (turbulent)	9	1,305	66,555
22	11	4.00E-5 m (laminar), 1.00E-5 m (turbulent)	11	4.00E-5 m (laminar), 2.00E-5 m (turbulent)	5	653	17,631

Table 5.3: Geometry Grids

the same fluid property grid.

The grid level terminology 0, 1, and 2 was borrowed from that which is used by Numeca International[51] in their products, where grid level 0 indicates that every $2^0 = 1$ grid points of the finest grid are used, 1 indicates every $2^1 = 2$ grid points of the finest grid are used, and 2 indicates every $2^2 = 4$ grid points of the finest grid are used. The terminology 00, 11, and 22 just means that the same skipping of grid points applies to both dimensions of the grid. Because Star-CCM+ did not have the ability to automatically skip points in both the geometry grid and fluid property grid, this skipping was conducted manually in order to coarsen the grid.

Laminar

Results from the laminar grid dependency study are presented in Figures 5.3 through 5.6. Figure 5.3 shows the heat exchanger effectiveness vs geometry grid level for each fluid property grid level. Figure 5.4 shows the heat exchanger effectiveness vs fluid property grid level at each geometry grid level. Both of these Figures clearly show the variation between fluid property grid level 22 and 11 is small and the variation between fluid property grid level 11 and 00 is extremely small, such that the 00 grid level mostly likely does not need to be used. The change from geometry grid level 22 to 11 is similar to that of the change between grid level 11 and 00, but both of these changes are still very small (~ 0.1 percentage points) such that the 00 grid can be considered sufficient.

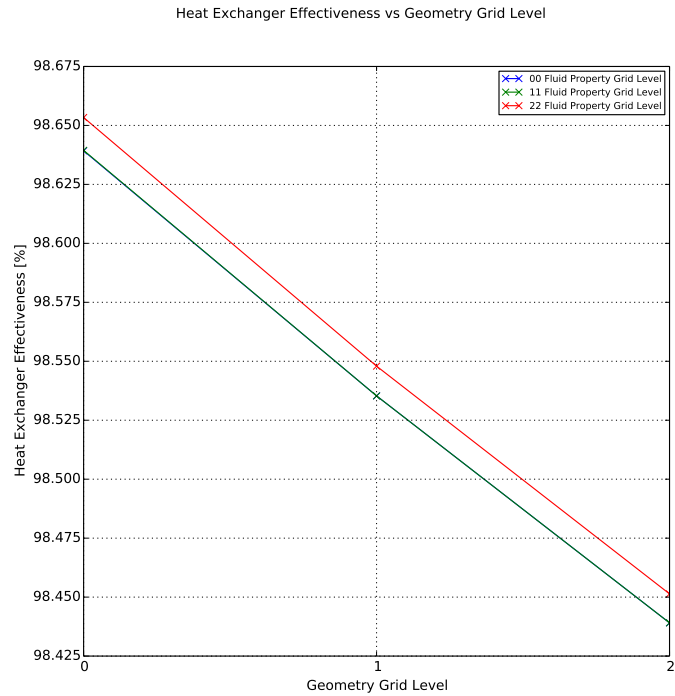


Figure 5.3: Laminar Grid Dependency Study, Effectiveness vs Geometry Grid Levels at Various Fluid Property Grid Levels

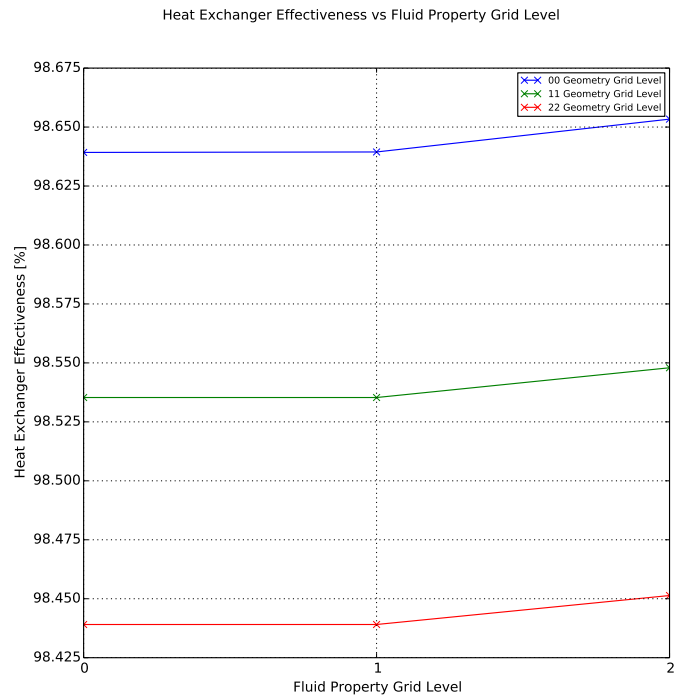


Figure 5.4: Laminar Grid Dependency Study, Effectiveness vs Property Grid Levels at Various Geometry Grid Levels

Figures 5.5 and 5.6 show the local variation in temperature difference between the low and high pressure sides for all 9 grid levels. There is a very small difference between all cases and the highest resolution case in most locations, and 4.9% being the maximum.

Temperature Difference, Low Pressure Channel to High Pressure Channel

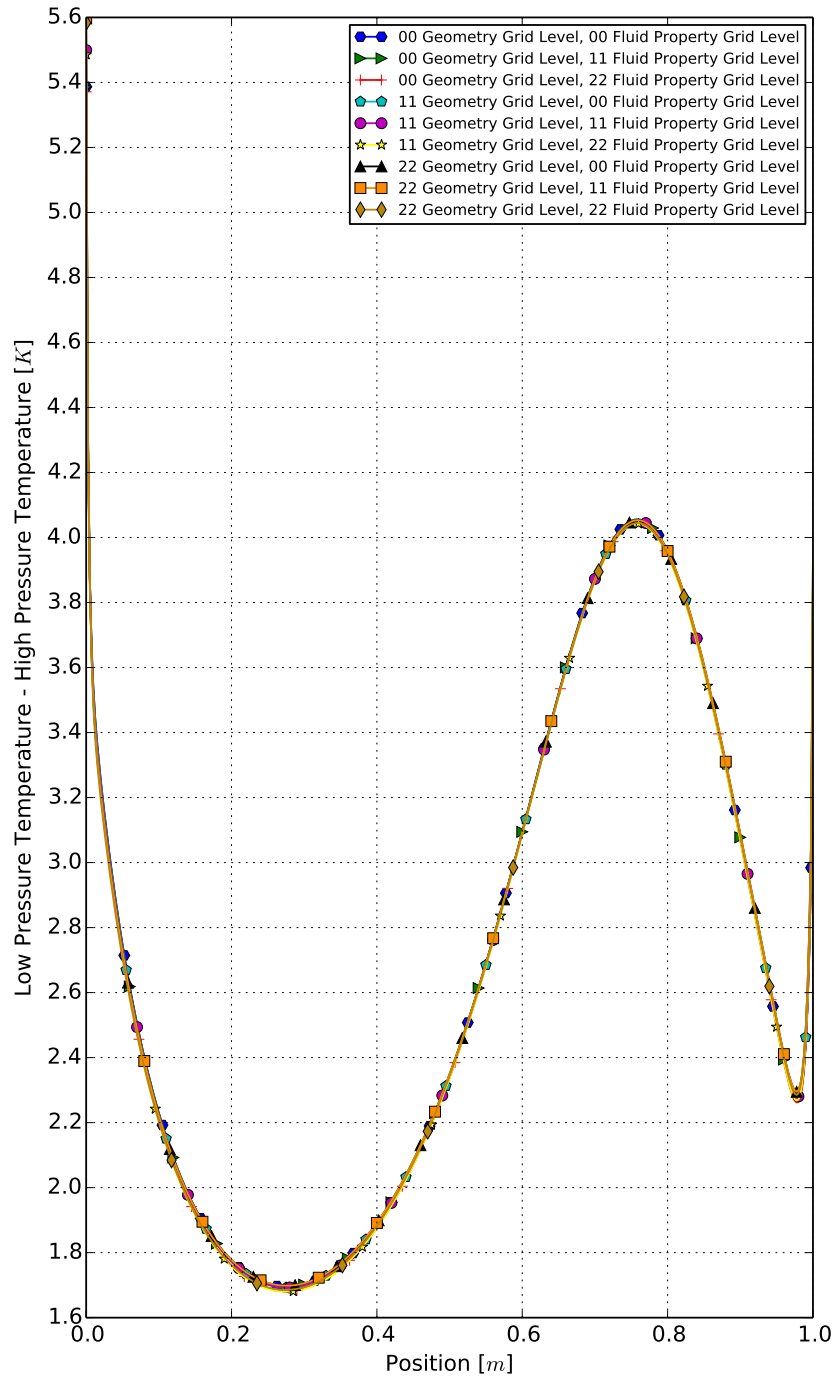


Figure 5.5: Laminar Grid Dependency Study, Temperature Difference vs Position at Each Grid Level

Temperature Difference, Low Pressure Channel to High Pressure Channel

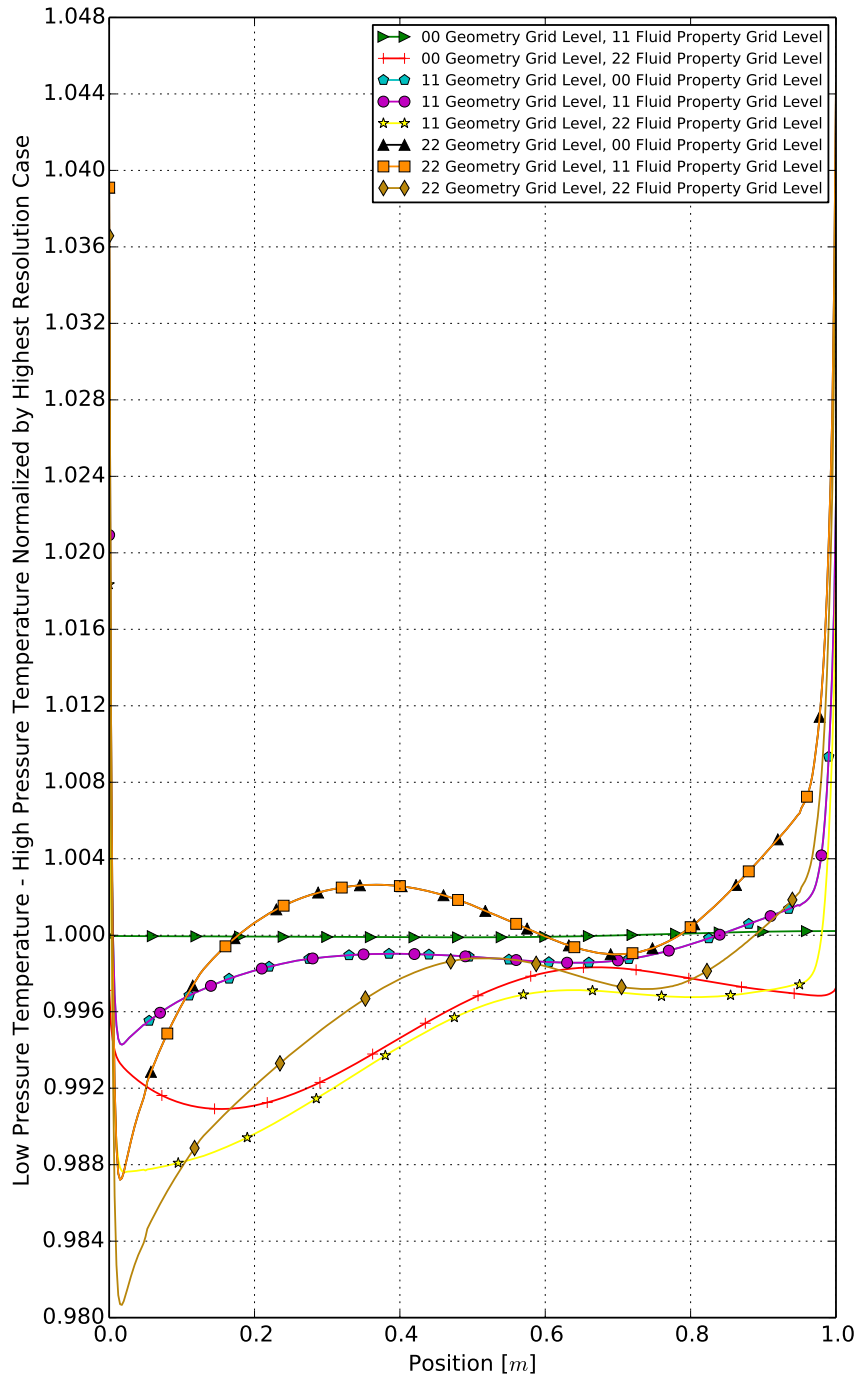


Figure 5.6: Laminar Grid Dependency Study, Temperature Difference vs Position at Each Grid Level Normalized by Highest Resolution Case

Turbulent

Results from the turbulent grid dependency study are presented in Figures 5.7 through 5.12. Overall, the change from geometry grid level to grid level was much larger than the laminar case, but similar for the fluid property grids. The variation in effectiveness from geometry grid level 11 to 00 was ~ 0.3 percentage points, which was approximately 3 times higher than the laminar case. Figures 5.9 and 5.10 show the local variation in temperature difference between the low pressure and high pressure sides. As with the effectiveness, the variation from geometry grid to geometry grid is higher than that of the laminar case, but the peak variation from the 11 to 00 grid is less than 5% and is believed to be acceptable for the purposes of the present study. Figures 5.11 and 5.12 show the variation in y^+ values for the first grid point from the wall for the low pressure and high pressure sides, respectively. For the low pressure side, the y^+ value is less than 1.4 nearly everywhere for the 22 geometry grid (but peaks at 3.40 for the 22 geometry grid) and less than 0.7 nearly everywhere for the 11 and 00 geometry grids (but peaks at 2.30 for the 11 geometry grid and 1.50 for the 00 geometry grid). For the high pressure side, the y^+ value is less than 0.95 nearly everywhere for the 22 geometry grid (but peaks at 1.80 for the 22 geometry grid) and less than 0.5 nearly everywhere for the 11 and 00 geometry grids (but peaks at 1.18 for the 11 geometry grid and 0.77 for the 00 geometry grid). There does not appear to be any variation in y^+ values with the fluid property grids. y^+ values less than 1 are typically recommended when no wall function is used with the turbulence model and the 00 geometry grid is sufficiently below this recommendation nearly everywhere. Although the y^+ does peak greater than 1, these peaks are for very small spatial regions. It's difficult to be below 1 everywhere, especially when there is developing flow. Because the regions where y^+ is greater than 1 are so small, it is considered acceptable.

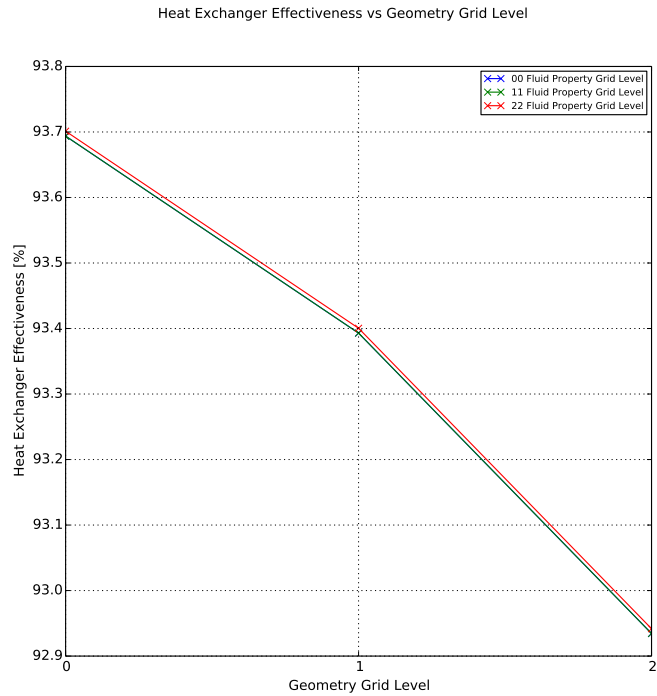


Figure 5.7: Turbulent Grid Dependency Study, Effectiveness vs Geometry Grid Levels at Various Fluid Property Grid Levels

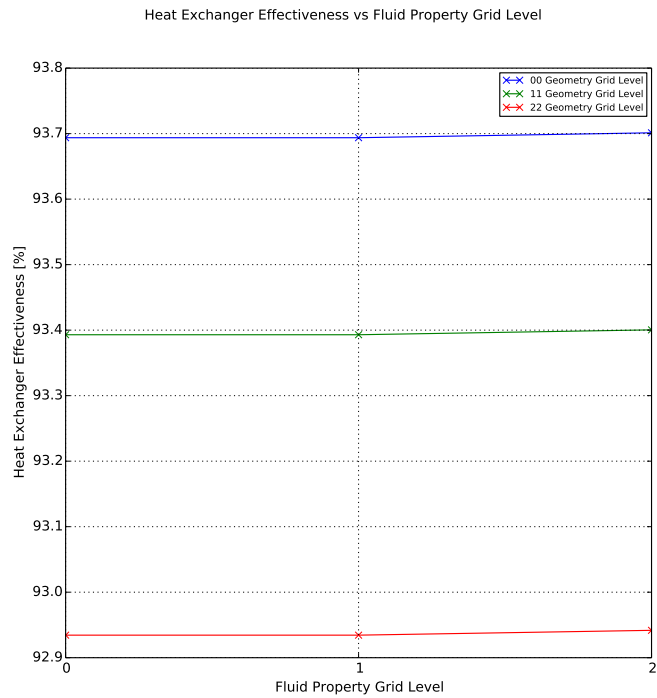


Figure 5.8: Turbulent Grid Dependency Study, Effectiveness vs Property Grid Levels at Various Geometry Grid Levels

Temperature Difference, Low Pressure Channel to High Pressure Channel

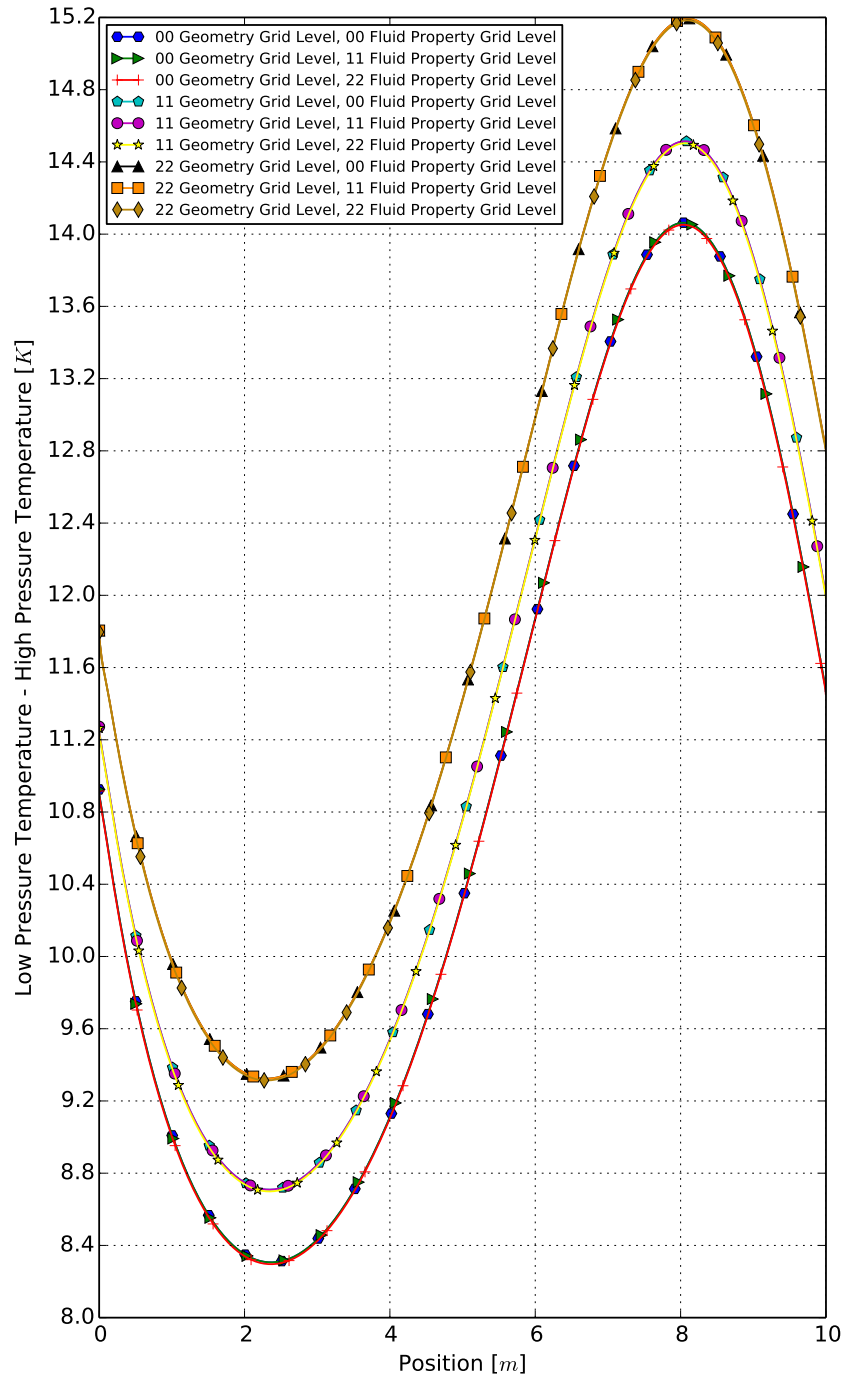


Figure 5.9: Turbulent Grid Dependency Study, Temperature Difference vs Position at Each Grid Level

Temperature Difference, Low Pressure Channel to High Pressure Channel

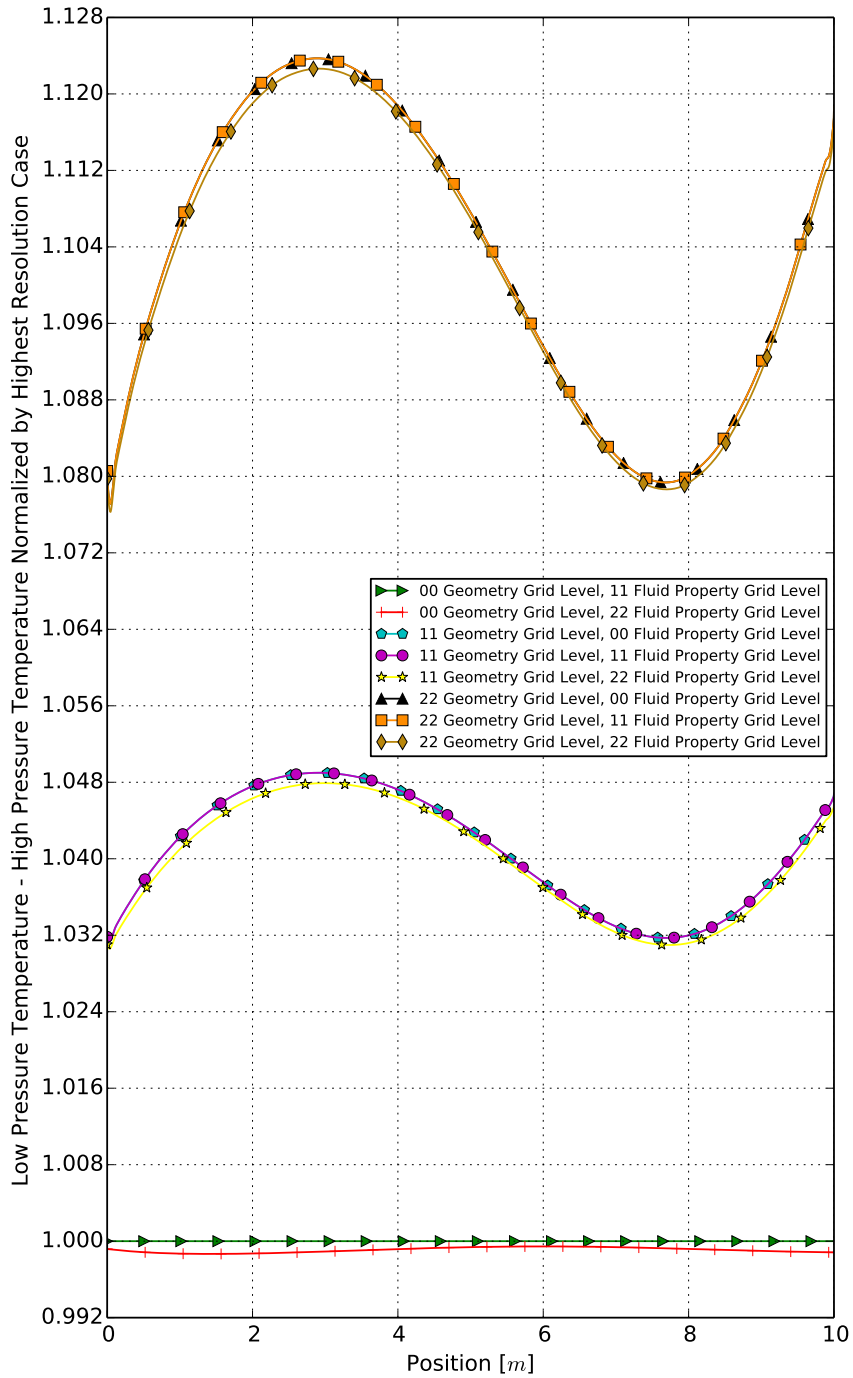


Figure 5.10: Turbulent Grid Dependency Study, Temperature Difference vs Position at Each Grid Level Normalized by Highest Resolution Case

Low Pressure Side

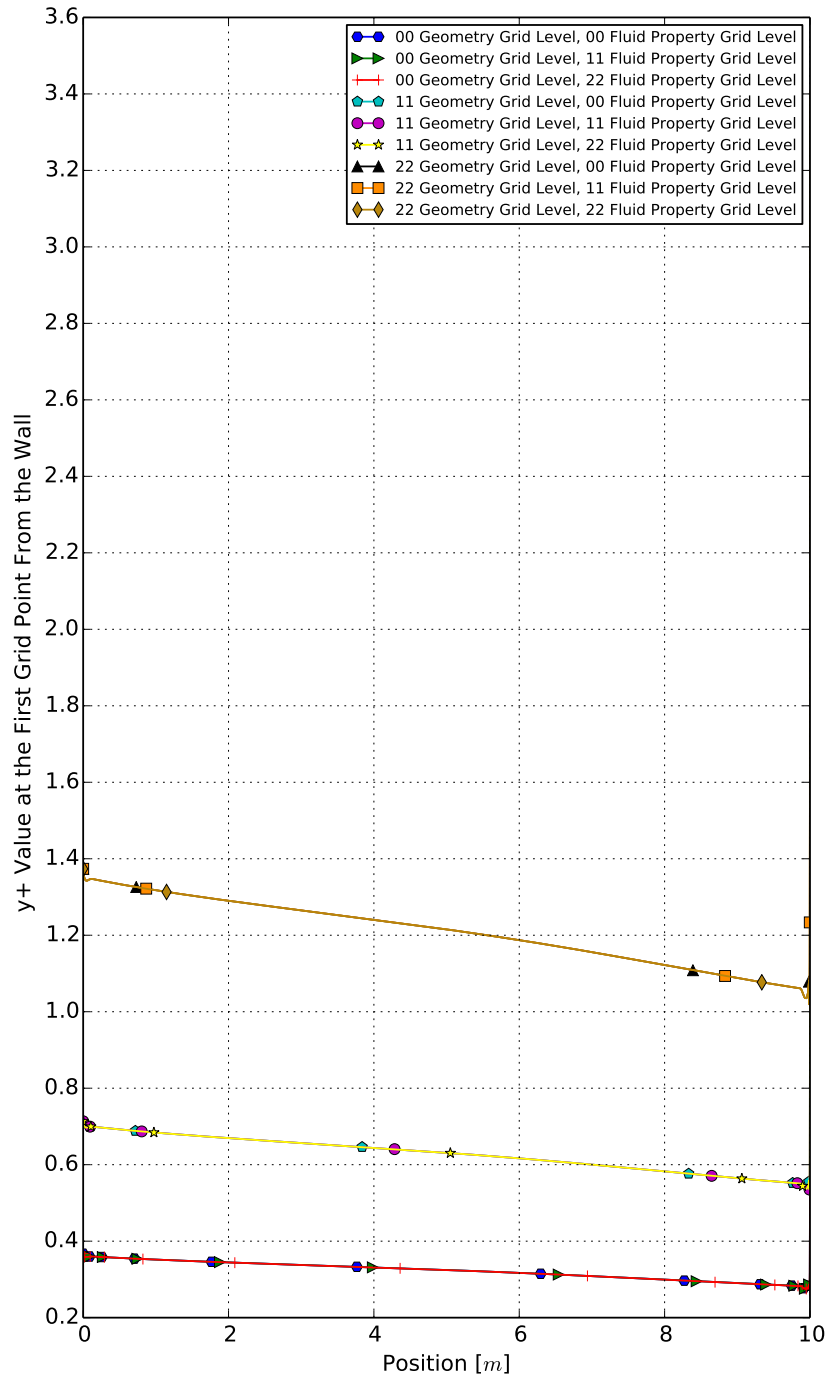


Figure 5.11: Turbulent Grid Dependency Study, y^+ vs Position at Each Grid Level, Low Pressure Half Channel

High Pressure Side

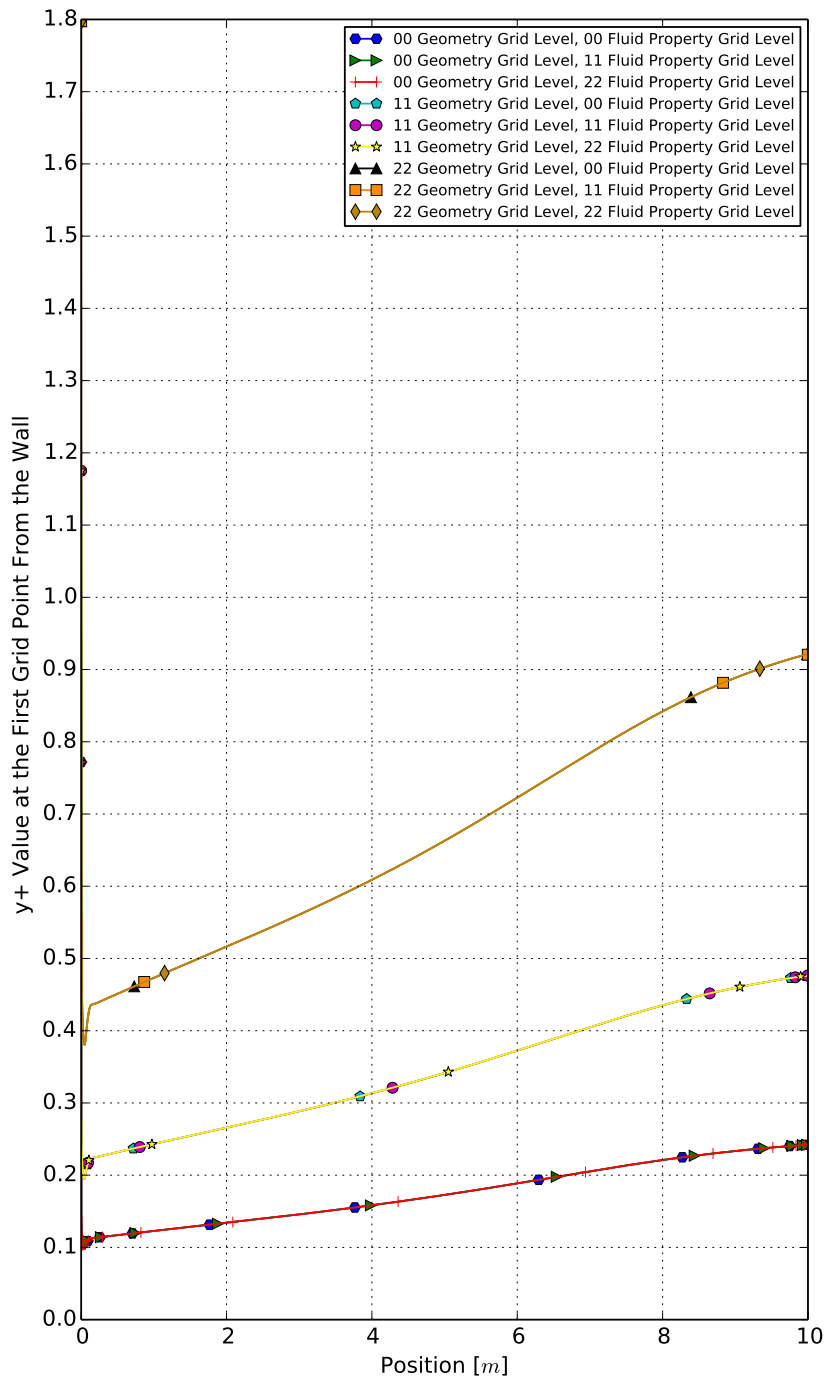


Figure 5.12: Turbulent Grid Dependency Study, y^+ vs Position at Each Grid Level, High Pressure Half Channel

5.3.2 Case I: High Pressure Inlet $Re_{D_h}=10$, Laminar, 1m Long

For Case I, the high pressure inlet Reynolds number based on the hydraulic diameter (Re_{D_h}) was set to 10. Because of the very low Reynolds number, this case was assumed to be laminar. Star-CCM+ was configured to use its laminar solver in both fluid streams. In this case, the maximum Reynolds number reached 99.2 at the low pressure outlet. The variation of Reynolds number with respect to position in both the high and low pressure channels is depicted in Figure 5.13, and is driven by the variation in dynamic viscosity with respect to fluid temperature. The high pressure channel mass flux was $0.15844kg/(m^2 * s)$ and the low pressure channel mass flux was $0.28043kg/(m^2 * s)$. The heat exchanger effectiveness for this case is 98.64%.

As a comparison, the viscosity computed using the Sutherland Law of Viscosity is also presented in Figure 5.13. The Sutherland Law for viscosity states that [52]

$$\frac{\mu}{\mu_0} \approx \left(\frac{T}{T_0}\right)^{3/2} \frac{T_0 + S}{T + S} \quad (5.1)$$

where μ_0 is the fluid reference viscosity, T_0 is the fluid reference temperature, and S is the Sutherland constant. For Carbon Dioxide, these parameters are $1.370 * 10^{-5} N * s/m^2$, $273K$, and $222K$, respectively [53]. As can be seen, on the high pressure (25MPa) side there is a huge discrepancy between the viscosity computed using Sutherland's Law and the viscosity computed using REFPROP. For the low pressure (5MPa), the difference between Sutherland's Law is evident, although not as clearly emphasized relative to itself due to the large range of the vertical axis. This is due to the fact that the plot is shared with the high pressure viscosity which has a much larger magnitude as well as variation.

Figure 5.14 shows contours of total temperature in both fluids and the solid. Because of the 100:1 scaling of the horizontal axis, visualization of the temperature variation within the channel height is not as obvious for this low temperature difference case. There is a small variation in temperature across the cross section of the solid. It's important to note that because of the difference in scaling of the horizontal and vertical axes in the Figures presented in this work, it would appear based on the slope of the temperature contour lines that the dominant direction of heat transfer in the solid is along the length of the solid. This is in fact incorrect. Although the Stainless Steel has a medium thermal conductivity, the wall thickness is thin and the channel length is long, therefore there is

Local Reynolds Number and Dynamic Viscosity

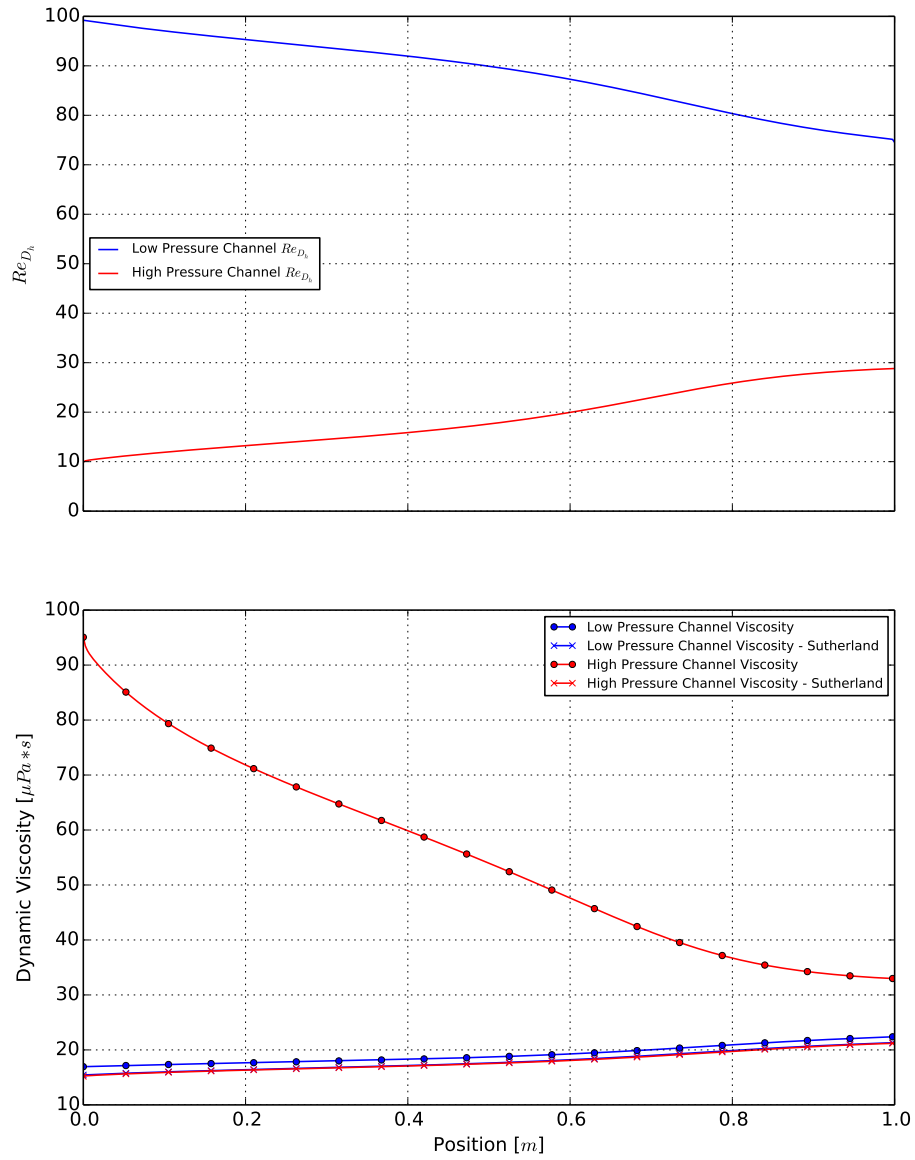
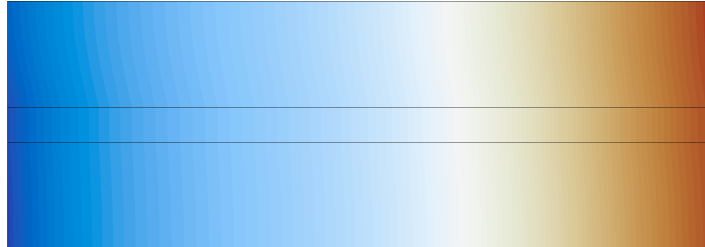


Figure 5.13: Case I: Reynolds Numbers and Average Dynamic Viscosities vs Length Position

Low Reference Pressure (5MPa)



High Reference Pressure (25MPa)



Figure 5.14: Case I: Total Temperature Contours

significant thermal resistance in the length direction but negligible thermal resistance along the thickness.

Figure 5.15 shows the variation in centerline, wall, and enthalpy weighted average total temperatures throughout each channel position, for each channel. For this low temperature difference case, both wall temperatures are nearly identical. The high pressure centerline total temperature and high pressure enthalpy weighted average total temperature were nearly identical. For the low pressure side, some distinction is visible.

Figure 5.16 depicts the difference in enthalpy weighted total temperature on the low and high pressure sides, using the Star-CCM+ 2-D solution, as well as the solution obtained using the simplified 0-D heat exchanger solver. The 0-D solver was configured to have the same minimum temperature difference as the 2-D solution provided, as well as the same high pressure inlet and low pressure inlet temperatures and pressures. Because the 0-D solver had no spatial dimensions associated with its solution, the temperature differences are presented relative to the temperature on the low pressure side. Observing the relative temperatures in Figure 5.16, the interesting phenomenon of this case begin to be revealed. First, entrance effects in the heat exchanger are

Temperatures

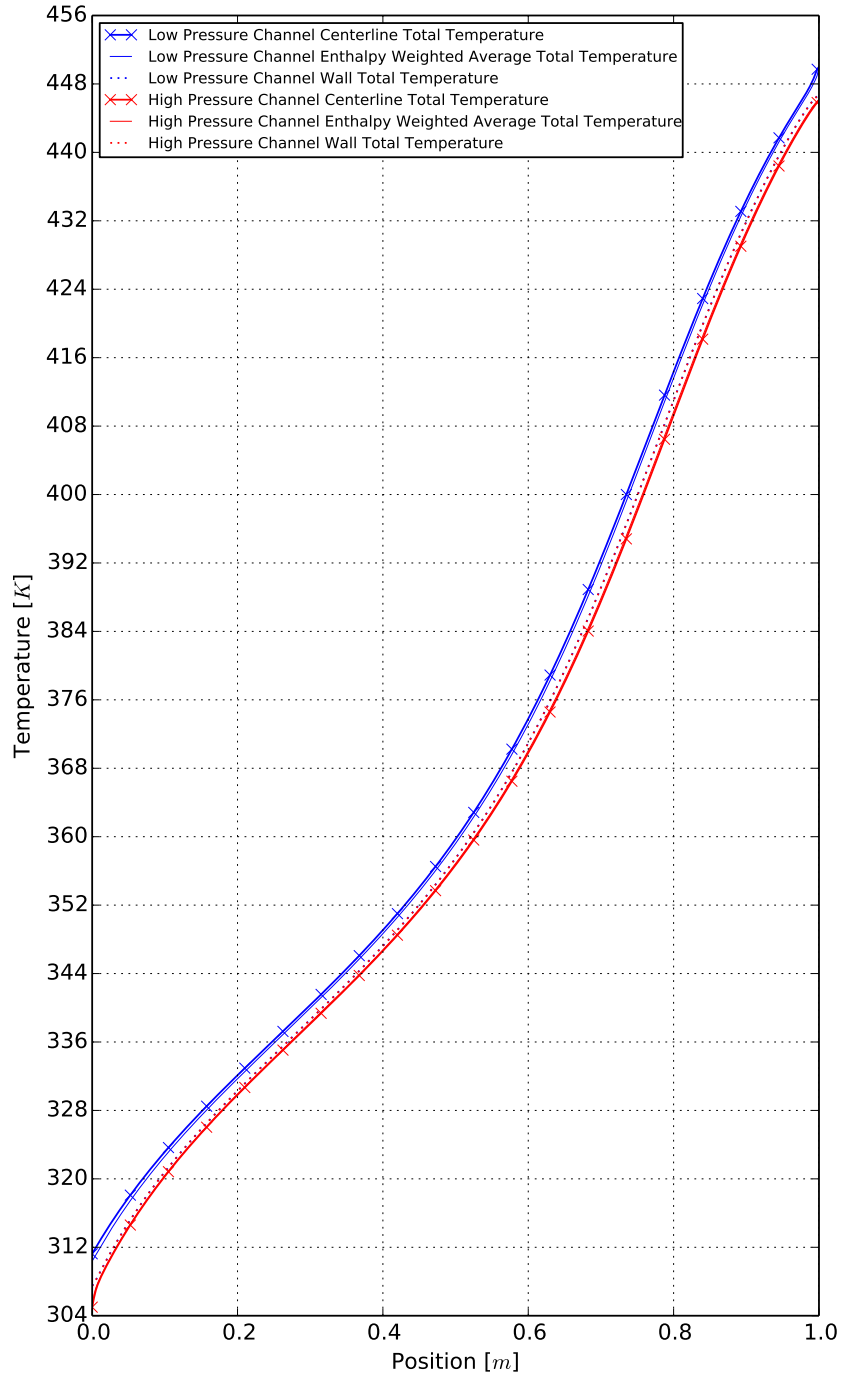


Figure 5.15: Case I: Temperatures vs Length Position

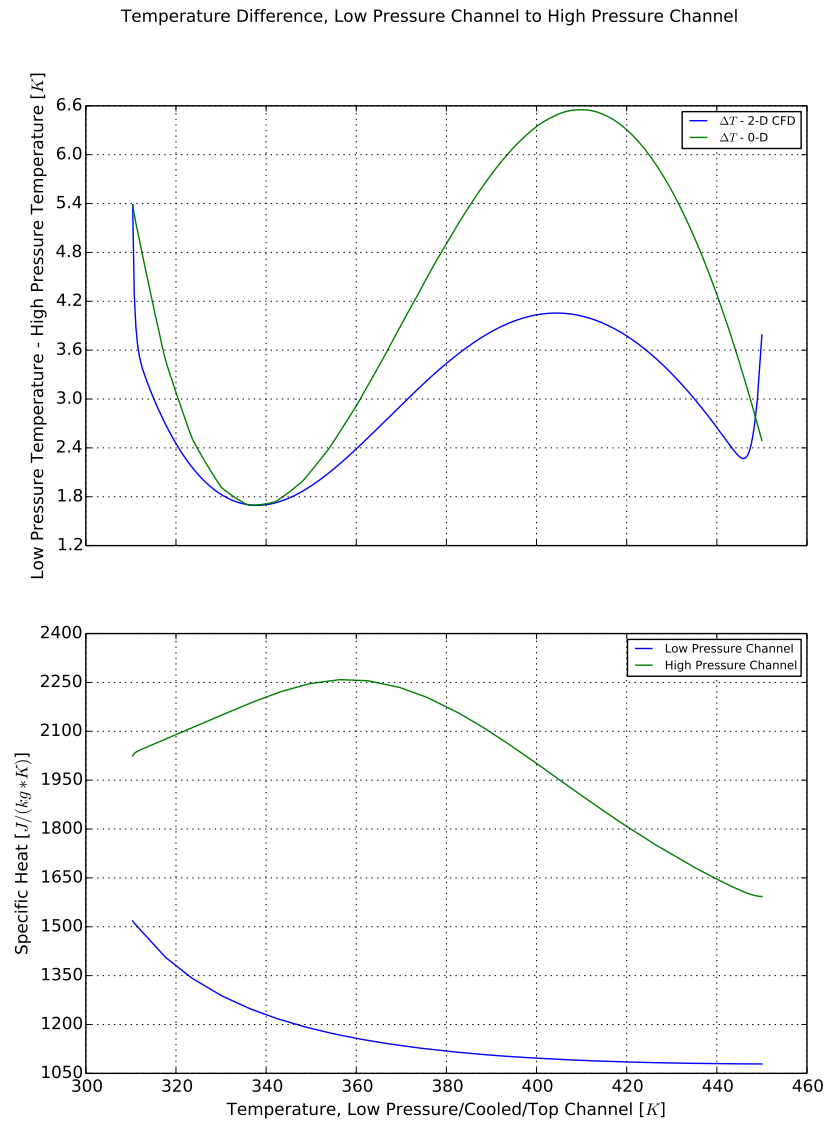


Figure 5.16: Case I: Average Temperature Difference and Specific Heats vs Temperature on the Low Pressure Side

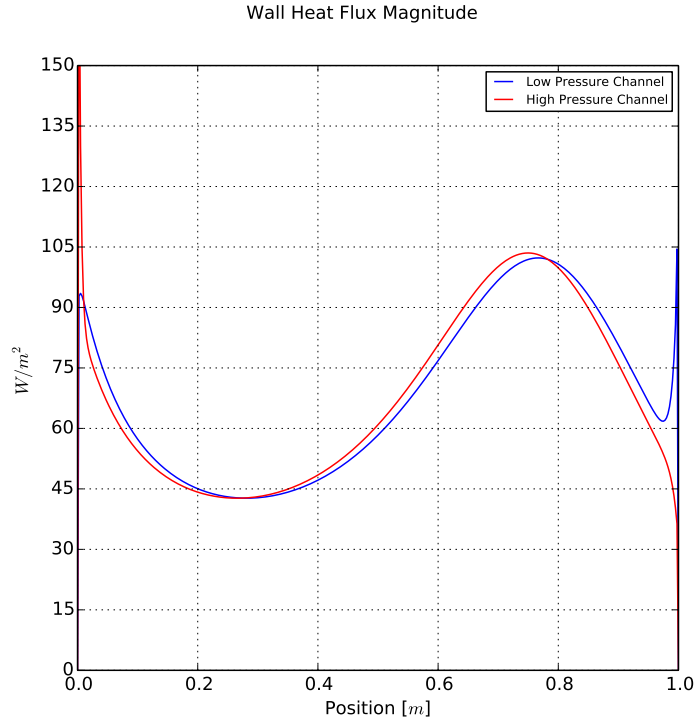


Figure 5.17: Case I: Heat Fluxes vs Length Position

evident with the 2-D solution. Second, the 2-D solution features two local minima in the middle of the heat heat exchanger and one local maxima in the middle of the heat exchanger. The minimum temperature difference is 1.69K. Such effects are not believed to be found in typical heat exchangers with constant specific heats. The relative and variable specific heats depicted in the bottom portion of Figure 5.16 provide an explanation for this phenomenon. The 0-D model does not match the 2-D solution very well in this case with a low minimum temperature difference and a well matched heat capacity. The reason being the 0-D model assumes thermally fully developed flow at the inlets to the heat exchanger.

Figure 5.17 shows the heat flux vs length on both walls of the solid. Entrance effects are very obvious because the flow began both thermally and hydrodynamically undeveloped. It's also important to note that the heat flux is extremely low, less than $1/10^{th}$ that of the intensity of the Sun's already small nominal heat flux of $1,000W/m^2$ that reaches earth.

In Figure 5.18, the non-dimensional heat transfer coefficient, Nu_{D_h} , shows a small variation in the fully developed regions. The dimensional heat transfer coefficient does vary considerably, driven by variations in thermal conductivity that are dependent on the fluid temperature. For a

Heat Transfer Coefficient and Thermal Conductivity

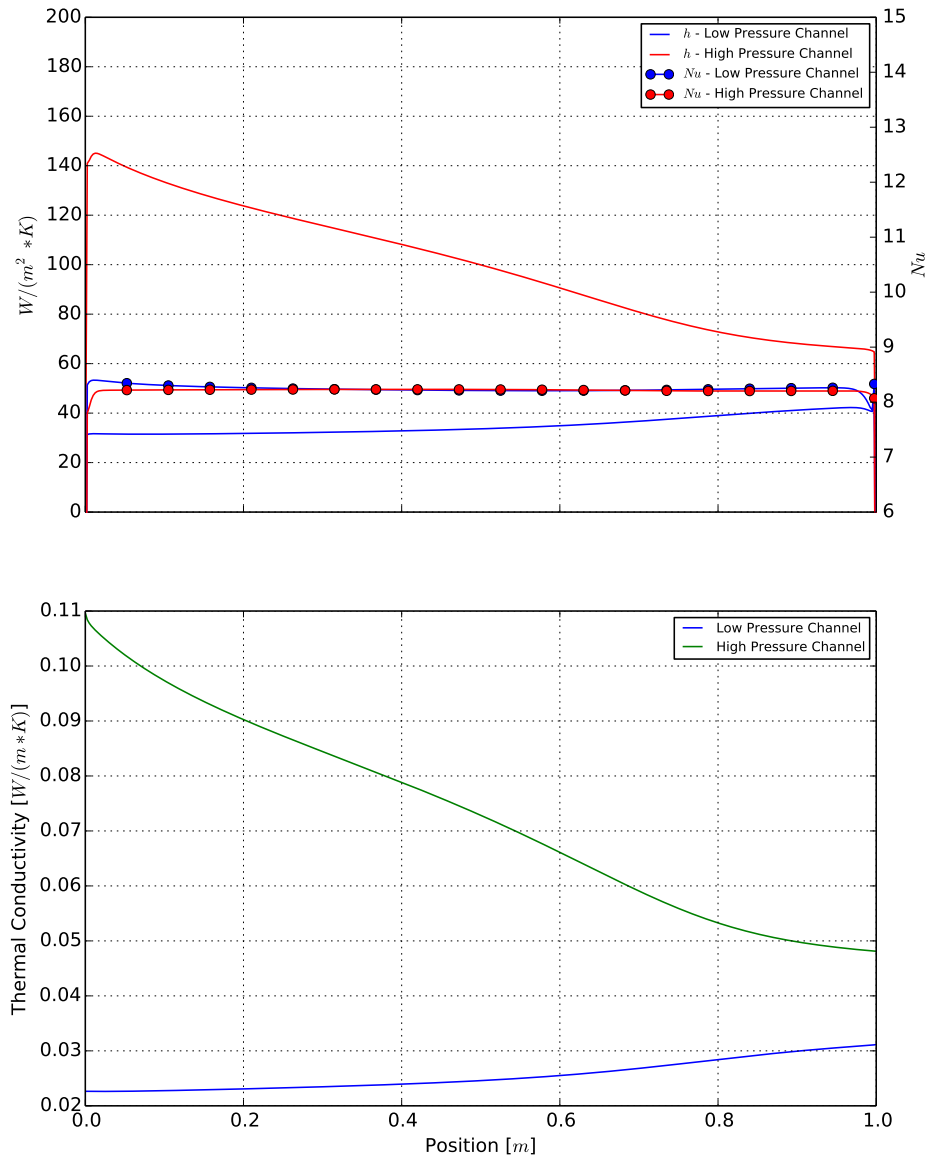


Figure 5.18: Case I: Heat Transfer Coefficients and Average Thermal Conductivities vs Length Position

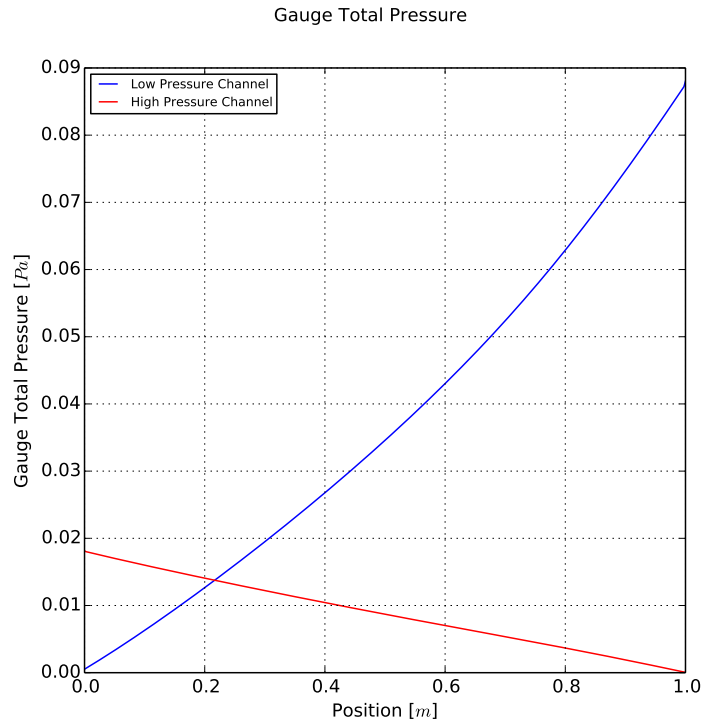


Figure 5.19: Case I: Average Gauge Total Pressures vs Length Position

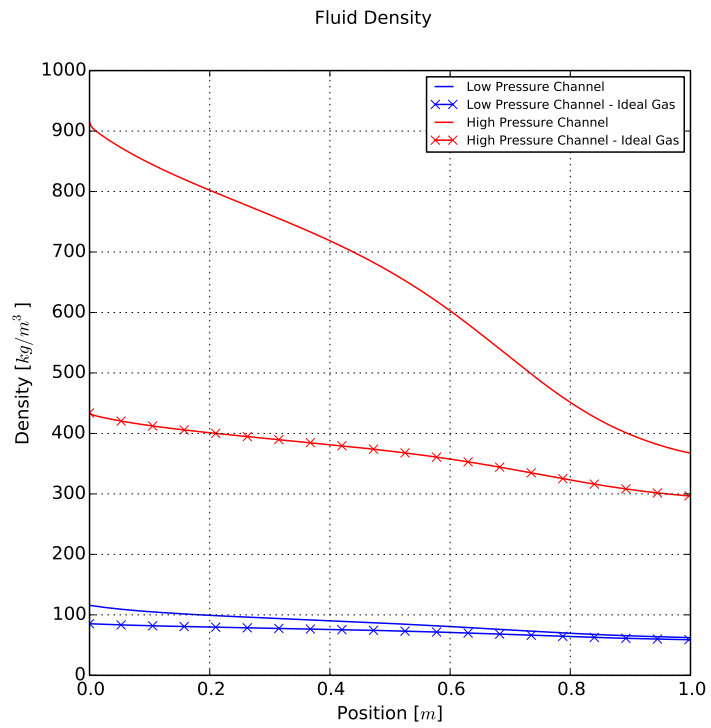


Figure 5.20: Case I: Average Densities vs Length Position

constant property laminar fully developed infinite channel flow, the theoretical Nusselt number for a constant and equal surface heat flux on both is 8.2353 and 7.5407 for a constant and equal surface temperature on both walls[54].

Gauge total pressure drop shown in Figure 5.19 is minuscule compared to the reference pressures. Although these pressure drops are very low, this is one example where this laminar flow configuration is likely impractical for a real heat exchanger design because the heat flux is too low.

Figure 5.20 shows the extreme variation in fluid densities with channel position, which is driven by the large temperature changes due to heat transfer. Although the densities of the high temperature fluids are lower than the low temperature fluids, they are still considerably high for the low pressure end of a heat engine. This is due to the high working fluid pressures.

As a comparison, the density is also computed using the ideal gas model using the temperature and pressure. It's readily evident that there is a huge difference between the density computed using the ideal gas model and the density computed using REFPROP for the high pressure (25MPa) fluid. For the low pressure (5MPa) fluid, there is also a large relative difference at the low temperature end, but at the high temperature end the ideal gas law computed density and the REFPROP computed density begin to agree.

Additional contour plots can be found in Appendix B.

5.3.3 Case II: High Pressure Inlet $Re_{D_h}=50$, Laminar, 1m Long

For Case II, the high pressure inlet Reynolds number based on the hydraulic diameter (Re_{D_h}) was set to 50, 5 times higher than the previous case. The variation of Reynolds number with respect to position in both the high and low pressure channels is depicted in Figure 5.21. The maximum Reynolds number reached was 490 at the low pressure outlet. Because the Reynolds numbers are all still low enough everywhere, Star-CCM+ was configured to use its laminar solver in both fluid streams. The high pressure channel mass flux was $0.79221kg/(m^2 * s)$ and the low pressure channel mass flux was $1.40214kg/(m^2 * s)$.

Figure 5.22 shows the temperatures vs channel position. The temperature difference is larger than Case I and the centerline and average values are more distinguishable.

The heat exchanger effectiveness was 92.42% and shown in Figure 5.23 one can see that the

Local Reynolds Number and Dynamic Viscosity

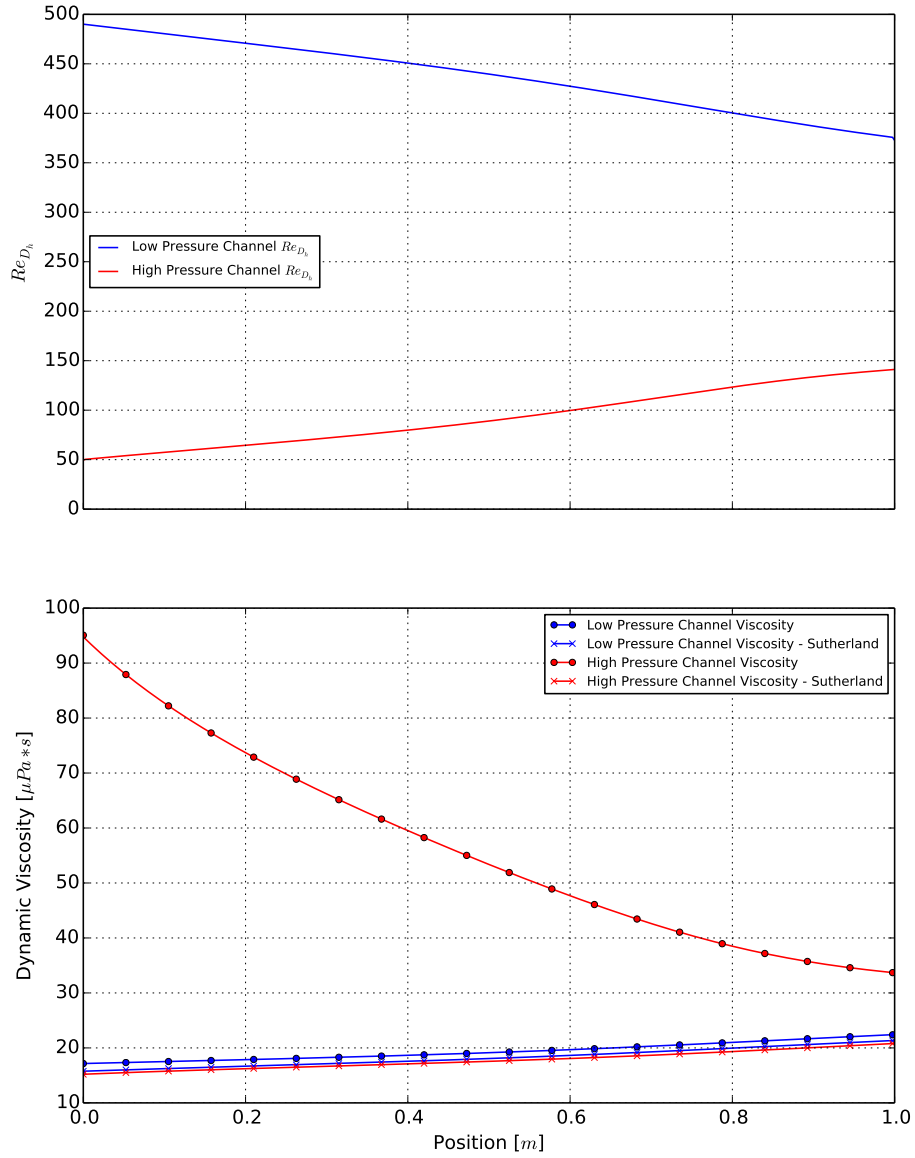


Figure 5.21: Case II: Reynolds Numbers and Average Dynamic Viscosities vs Length Position

Temperatures

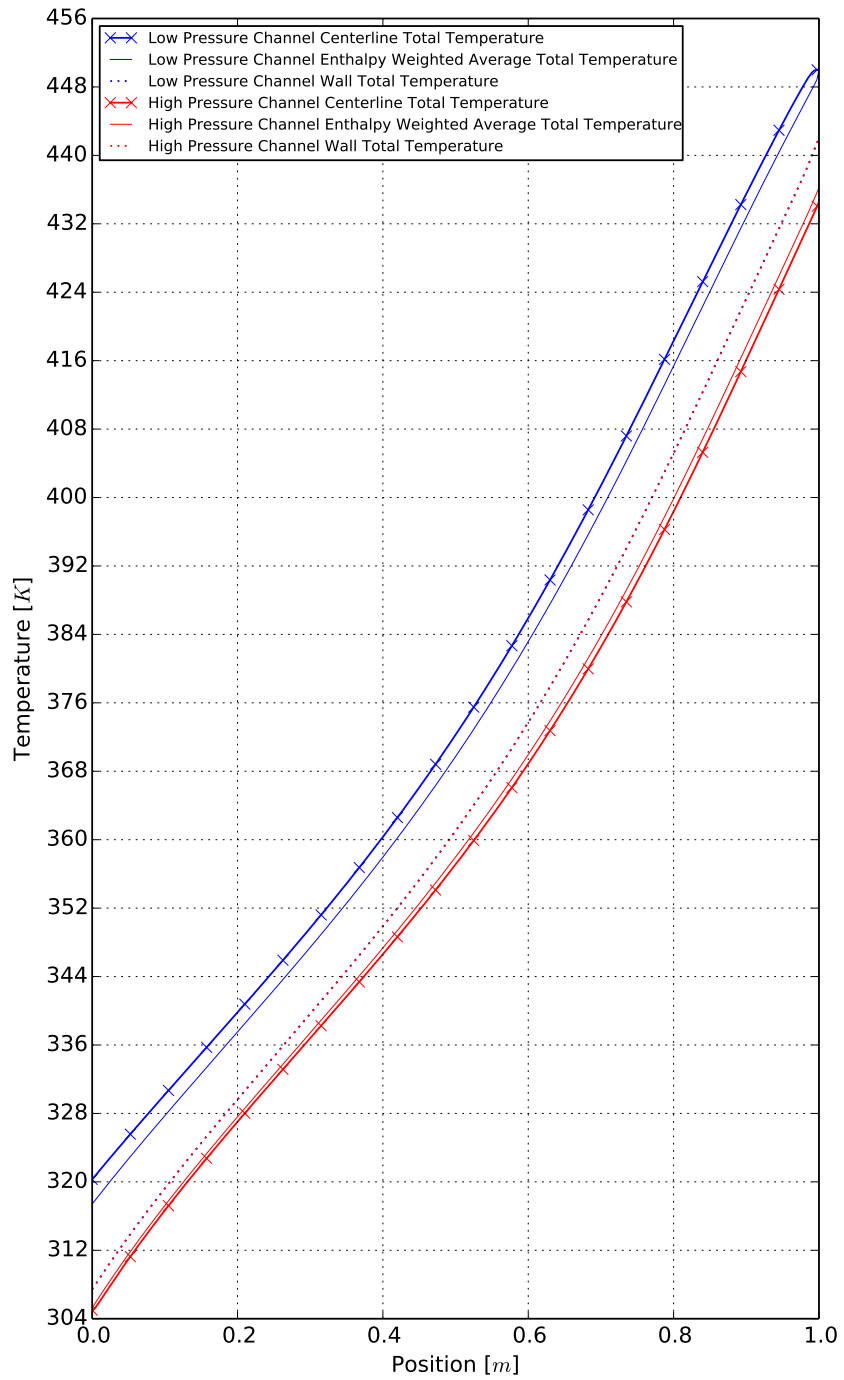


Figure 5.22: Case II: Temperatures vs Length Position

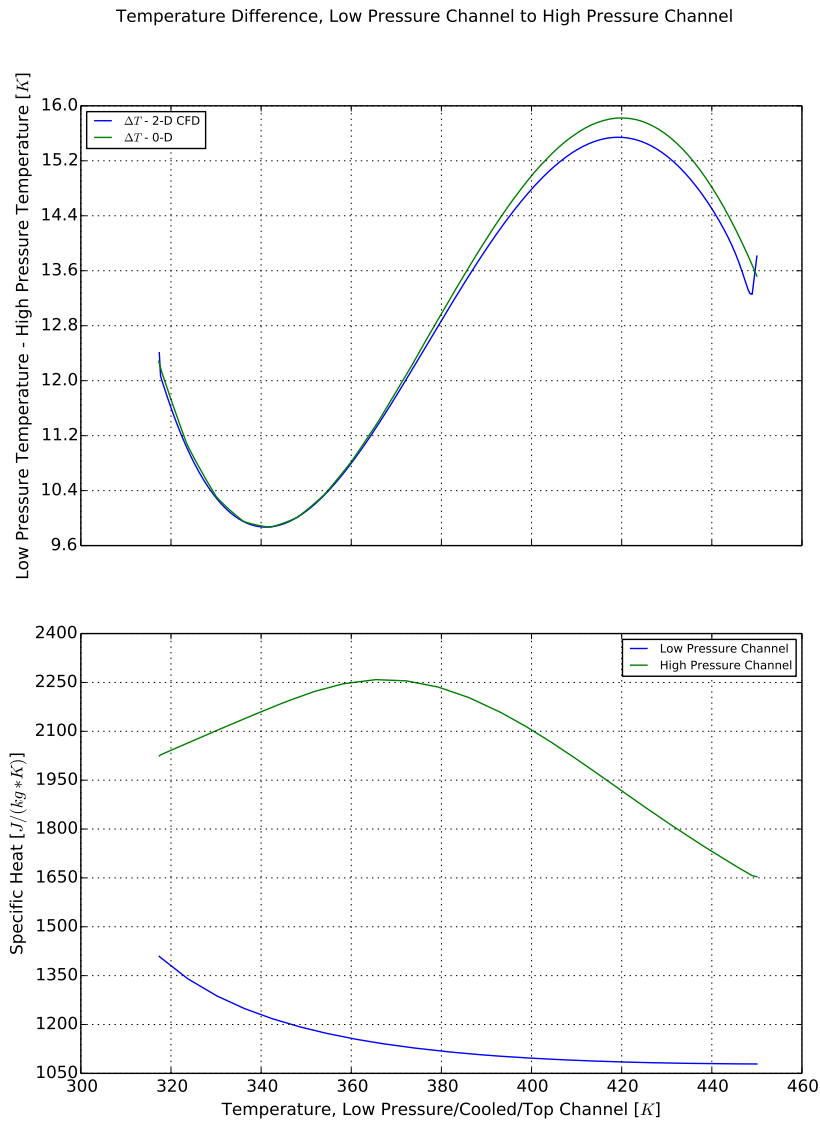


Figure 5.23: Case II: Average Temperature Difference and Specific Heats vs Temperature on the Low Pressure Side

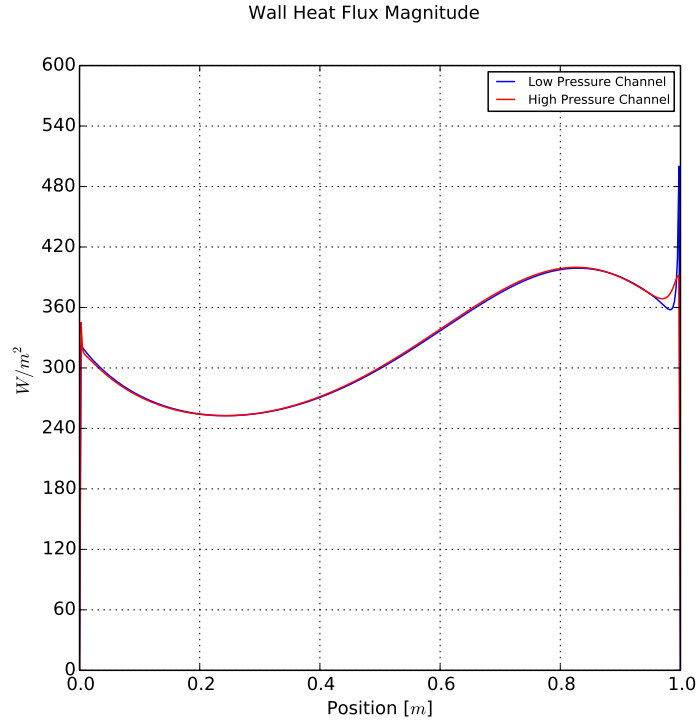


Figure 5.24: Case II: Heat Fluxes vs Length Position

minimum temperature difference is 9.87K, a more realistic minimum temperature difference for a real heat exchanger. Comparing Figure 5.23 to Figure 5.16, one can see that both feature a similar shape, but the local maxima and minima are at different levels. Also, the entrance effects are much less pronounced and the 0-D solver solution more closely matches the 2-D solution.

The wall heat flux, shown in Figure 5.24 is much higher than Case I. The heat fluxes of both walls are much closer to the same level, indicating less relative conduction along the length of the solid. The heat transfer coefficients in Figure 5.25 are similar and also still varying due to the variation in thermal conductivities. Outside of the entrance regions, the non-dimensional heat transfer coefficients are also still relatively constant and similar to the analytical constant property constant heat flux solution.

Heat Transfer Coefficient and Thermal Conductivity

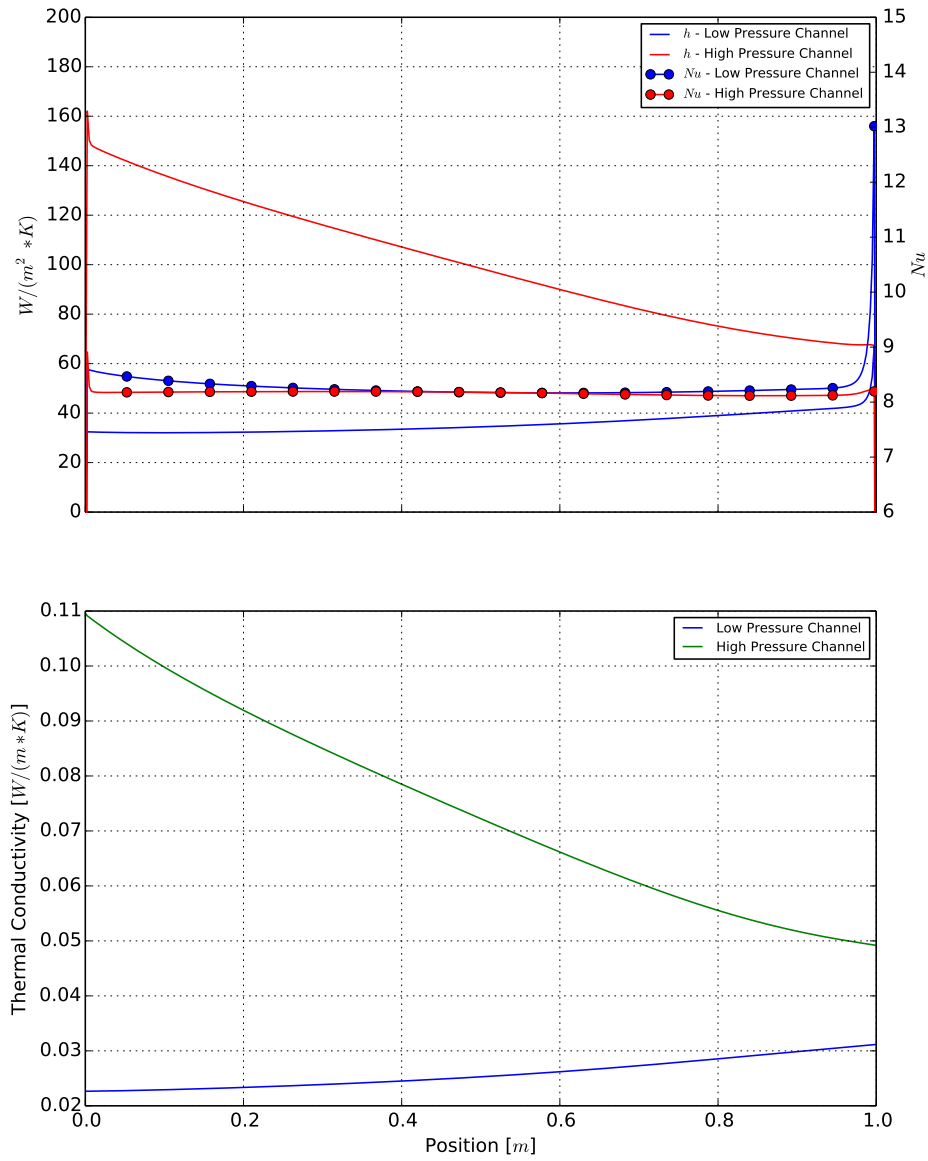


Figure 5.25: Case II: Heat Transfer Coefficients and Average Thermal Conductivities vs Length Position

5.3.4 Case III: High Pressure Inlet $Re_{D_n}=3,000$, Turbulent, 1m Long

For Case III, the high pressure inlet Reynolds number based on the hydraulic diameter (Re_{D_H}) was set to 3,000. Everywhere else in the two fluids the Reynolds number was higher and therefore this case was assumed to be fully turbulent. As shown in Figure 5.26, the peak Reynolds number is 26,520. As was mentioned previously, for turbulent flows Star-CCM+ was configured to use a turbulence model in both fluid streams and the standard $k - \omega$ turbulence model was used without a wall function.

With the large temperature difference shown in Figures 5.27-5.29, there is a significant variation in fluid properties along the cross section of the channels and along the channel lengths. In Figure 5.27 there is a very interesting effect near the low temperature end. There is a point where the temperature in the heat exchanger reaches a local maximum and a local minimum along the length of the channels. In this configuration there is a very large temperature difference, variation in specific heat capacity, and rapid change in heat transfer coefficient. All of these things coupled together result in some heat transfer in the reverse direction along the length of the channel.

Although there is a local maximum and minimum in temperature, the average difference is so large that these effects are not able to produce a local maximum or minimum temperature difference. The temperature difference is always increasing with temperature, but still does feature some nonlinearity. The 0-D heat exchanger solver also matches this case much better than the previous cases. The minimum temperature difference is 62.20K. The heat exchanger effectiveness is 55.01%. The large minimum temperature difference is driven by the much larger mass fluxes. $47.53239kg/(m^2 * s)$ on the high pressure side and $84.12812kg/(m^2 * s)$ on the low pressure side. The heat fluxes shown in Figure 5.30 are much larger and the heat transfer coefficients are also much larger than the previous cases, but not enough to compensate for the additional energy that would needed to be transferred in order to keep the minimum temperature difference lower. Therefore, more surface area would be required to maintain these mass fluxes at lower temperature differences.

Figure 5.31 shows several times higher dimensional and non-dimensional heat transfer coefficients. The non-dimensional heat transfer coefficients are dissimilar and have much higher relative variation. The laminar fully developed constant property analytical solution no longer applies. The gauge total pressure shown in Figure 5.32 shows a considerably higher pressure loss than the laminar

Local Reynolds Number and Dynamic Viscosity

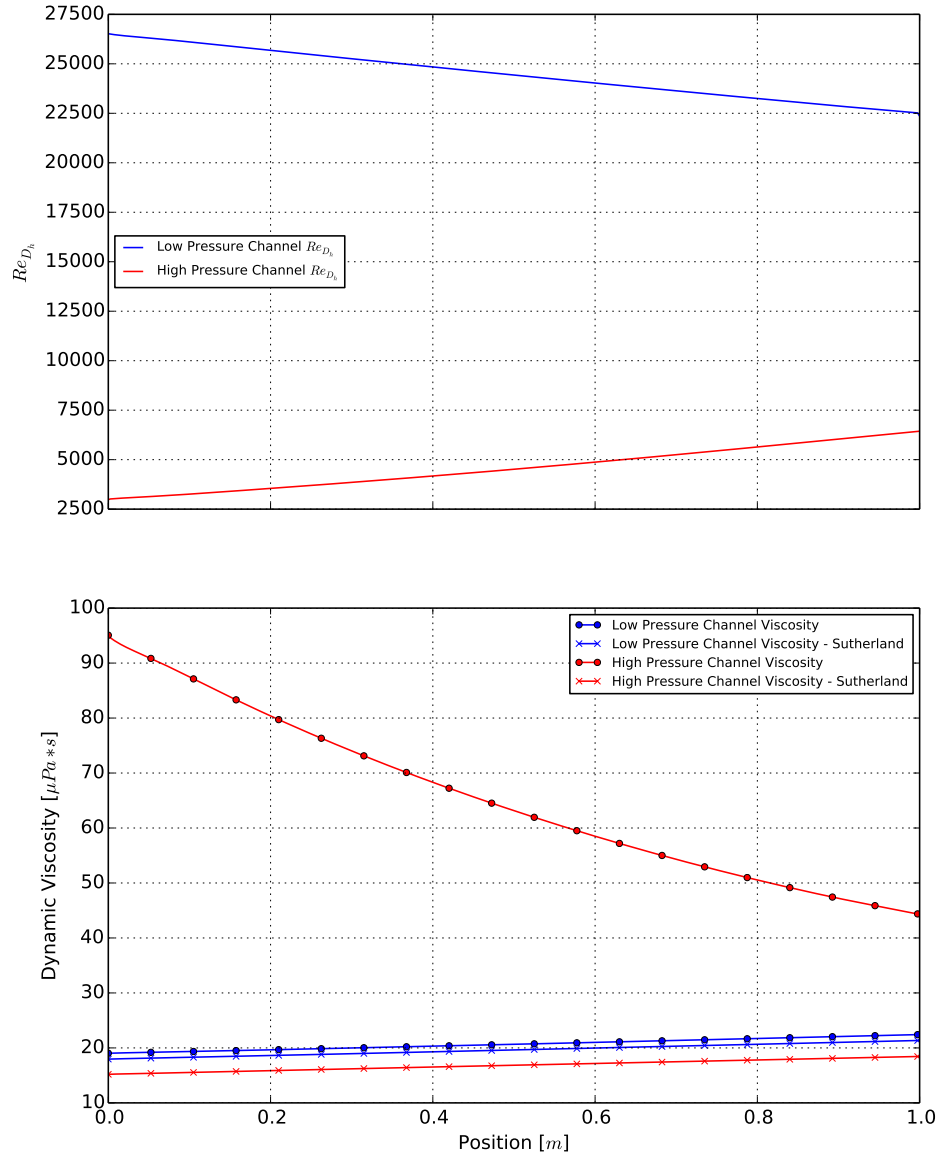


Figure 5.26: Case III: Reynolds Numbers and Average Dynamic Viscosities vs Length Position

Low Reference Pressure (5MPa)



High Reference Pressure (25MPa)



Figure 5.27: Case III: Total Temperature Contours

Temperatures

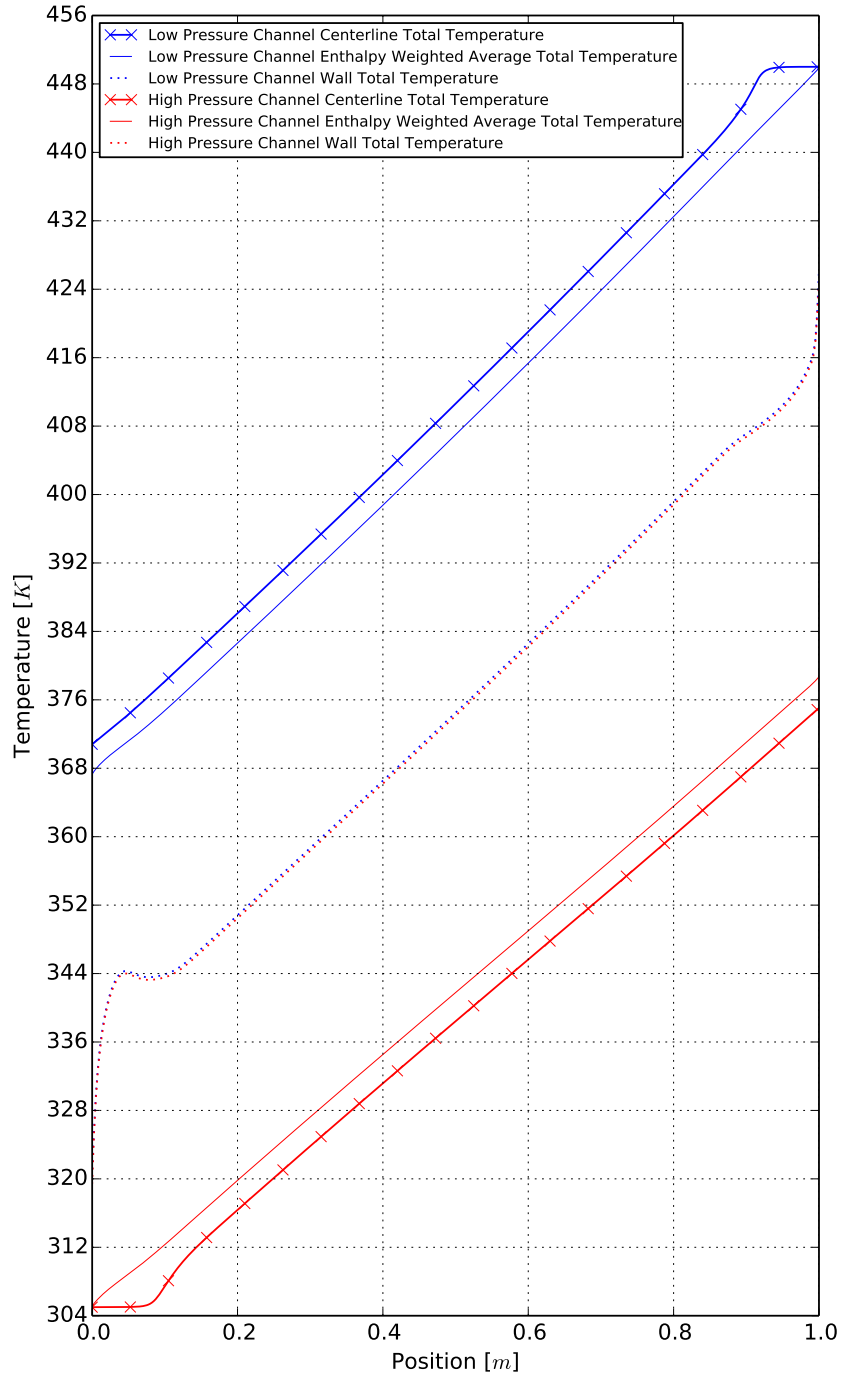


Figure 5.28: Case III: Temperatures vs Length Position

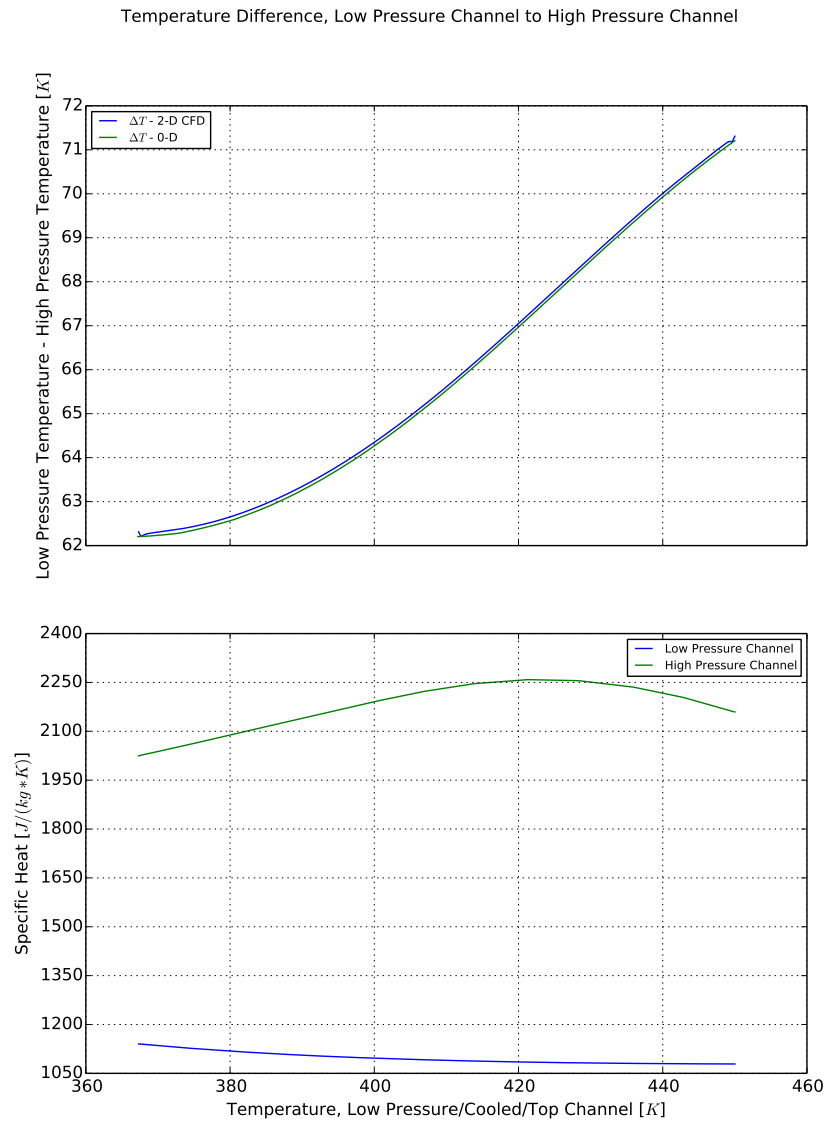


Figure 5.29: Case III: Average Temperature Difference and Specific Heats vs Temperature on the Low Pressure Side

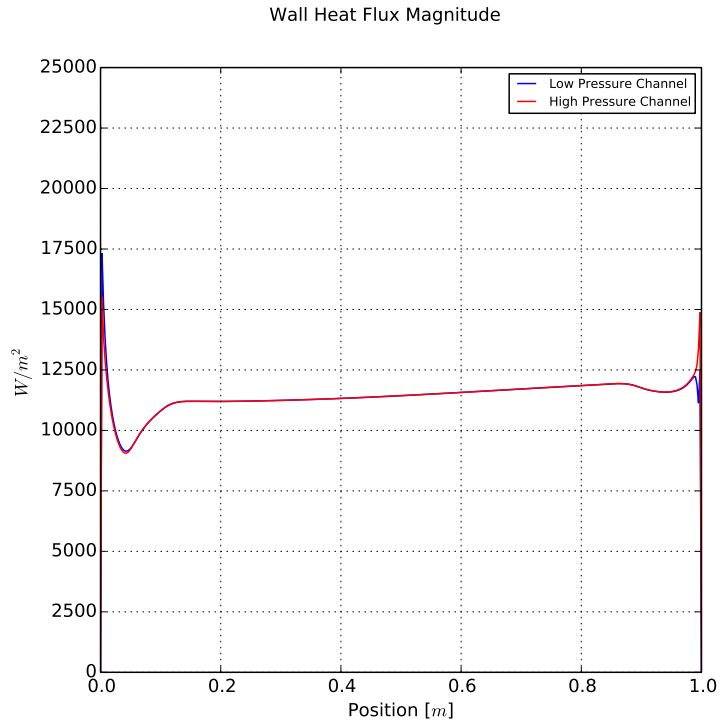


Figure 5.30: Case III: Heat Fluxes vs Length Position

cases, a compromise required in order to obtain the higher heat transfer coefficients. The density variation (Figure 5.33) is of similar magnitude as previous cases, but shows less non-linearity.

Additional contour plots can be found in Appendix B.

Heat Transfer Coefficient and Thermal Conductivity

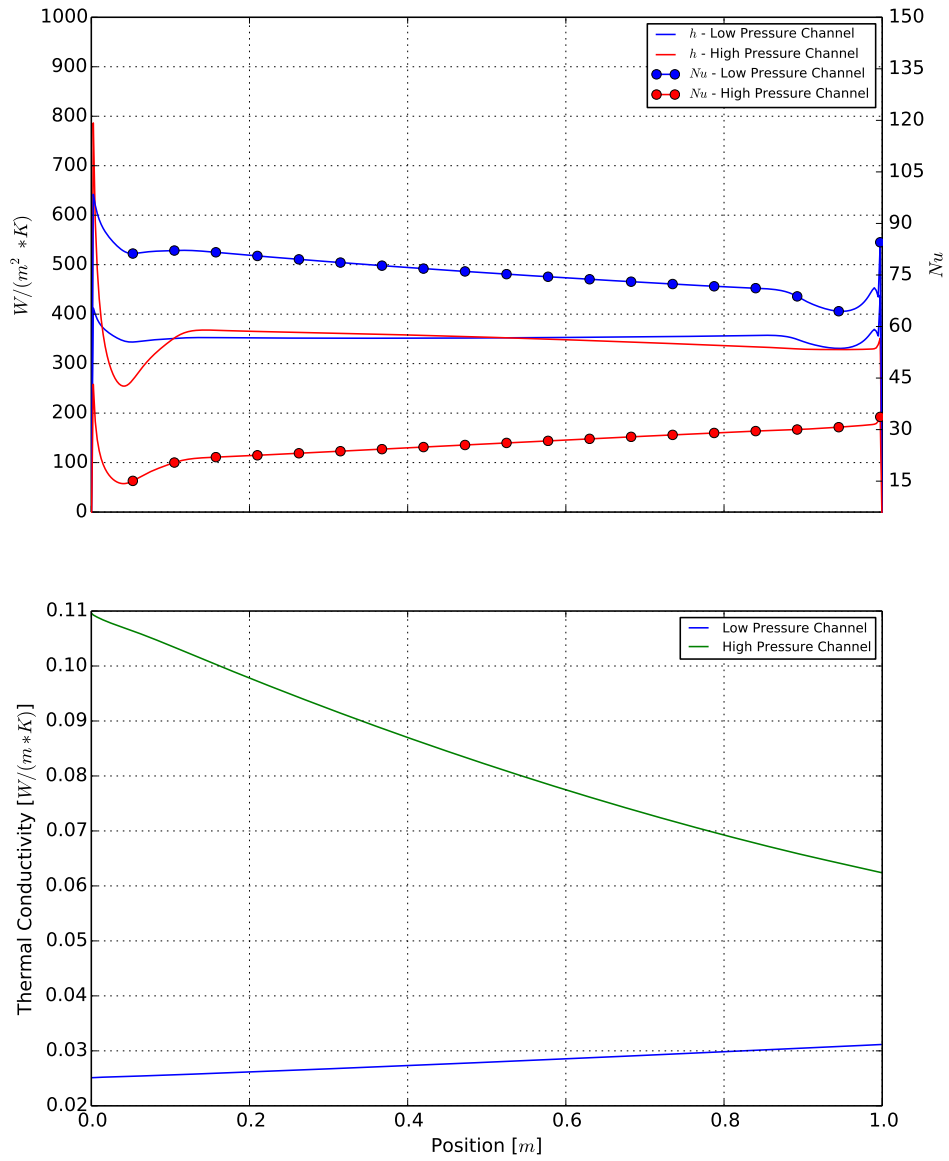


Figure 5.31: Case III: Heat Transfer Coefficients and Average Thermal Conductivities vs Length Position

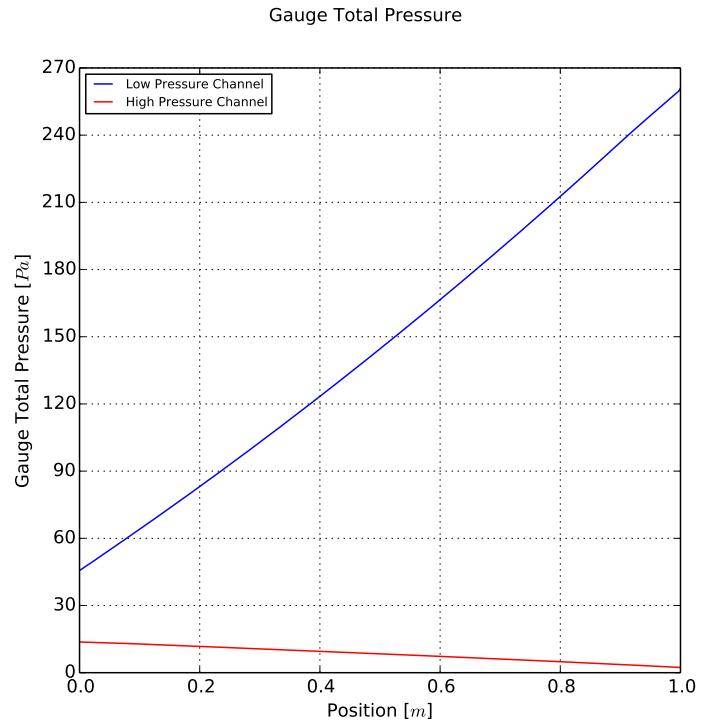


Figure 5.32: Case III: Average Gauge Total Pressures vs Length Position

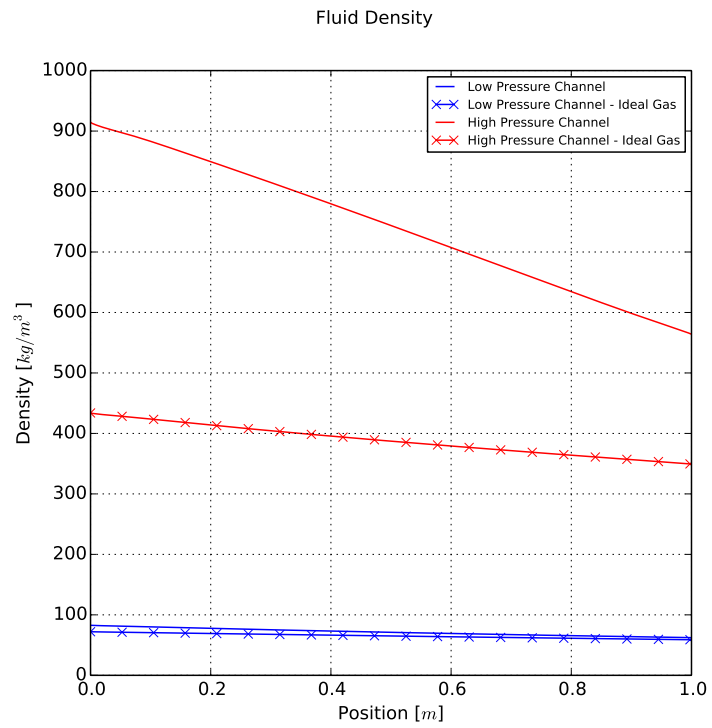


Figure 5.33: Case III: Average Densities vs Length Position

5.3.5 Case IV: High Pressure Inlet $Re_{D_h}=4,000$, Turbulent, 1m Long

Case IV had a high pressure inlet Reynolds number set to 4,000. The peak Reynolds number at the low pressure outlet was 35,129. The high pressure mass flux was $63.37651 \text{ kg}/(\text{m}^2 * \text{s})$ and the low pressure mass flux was $112.17082 \text{ kg}/(\text{m}^2 * \text{s})$.

Qualitatively, Figures 5.34-5.38 appear similar to that of Case III. The minimum temperature differences was slightly higher at 65.27K and the heat exchanger effectiveness slightly lower at 52.90%. It is important to note that the heat transfer coefficients have increased as Reynolds number increased, rather than staying nearly the same, as they did in the laminar cases.

Local Reynolds Number and Dynamic Viscosity

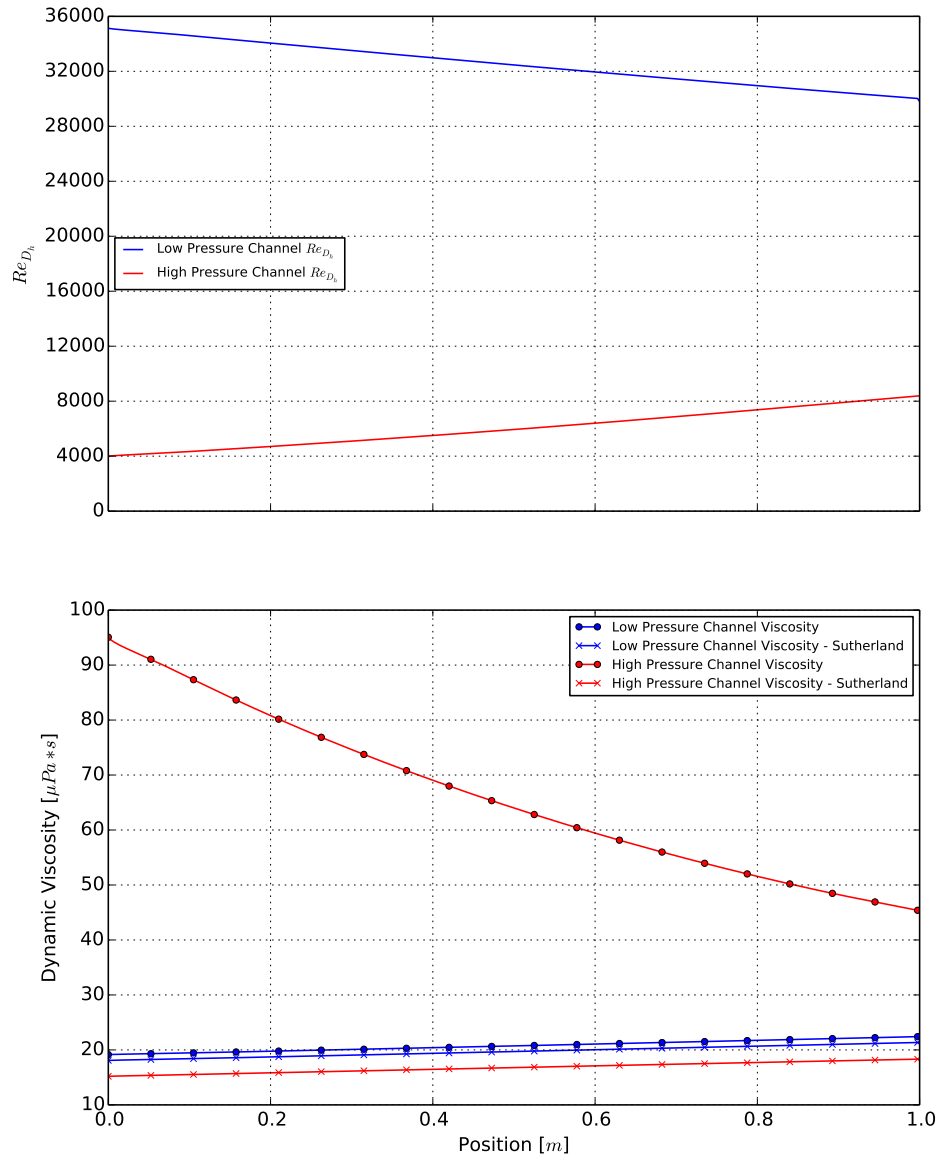


Figure 5.34: Case IV: Reynolds Numbers and Average Dynamic Viscosities vs Length Position

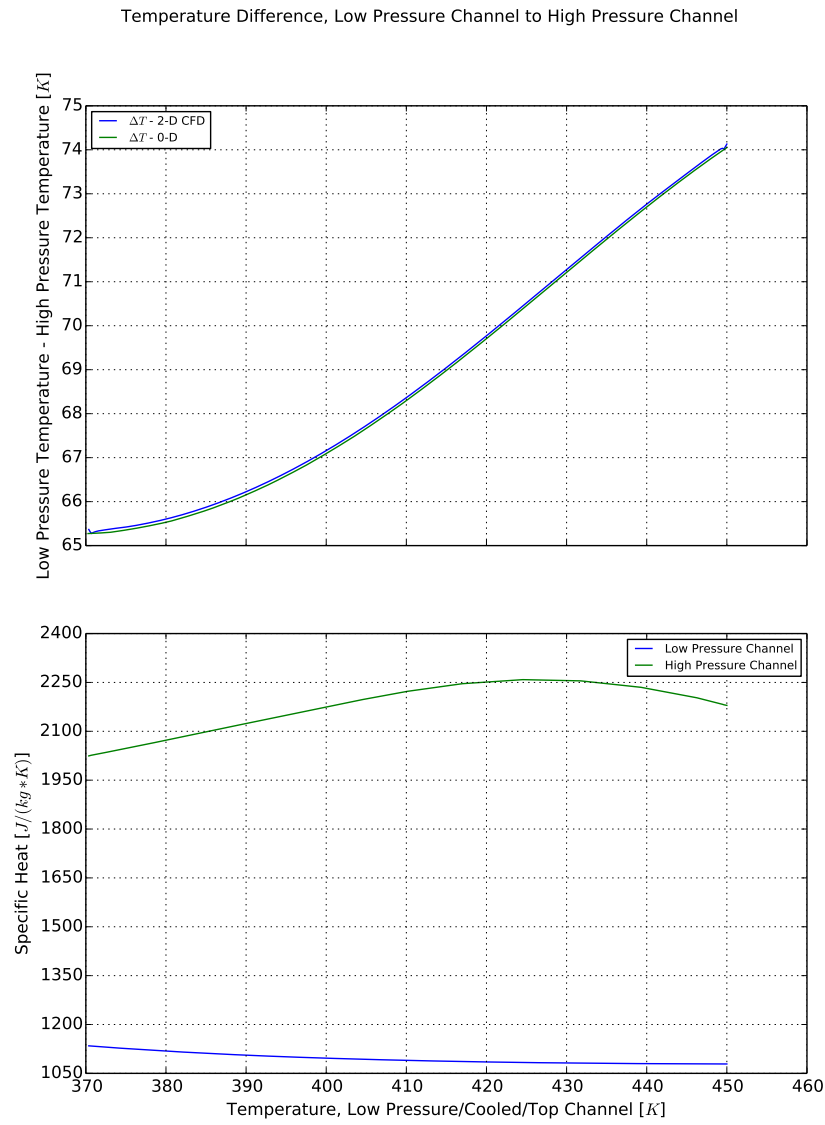


Figure 5.35: Case IV: Average Temperature Difference and Specific Heats vs Temperature on the Low Pressure Side

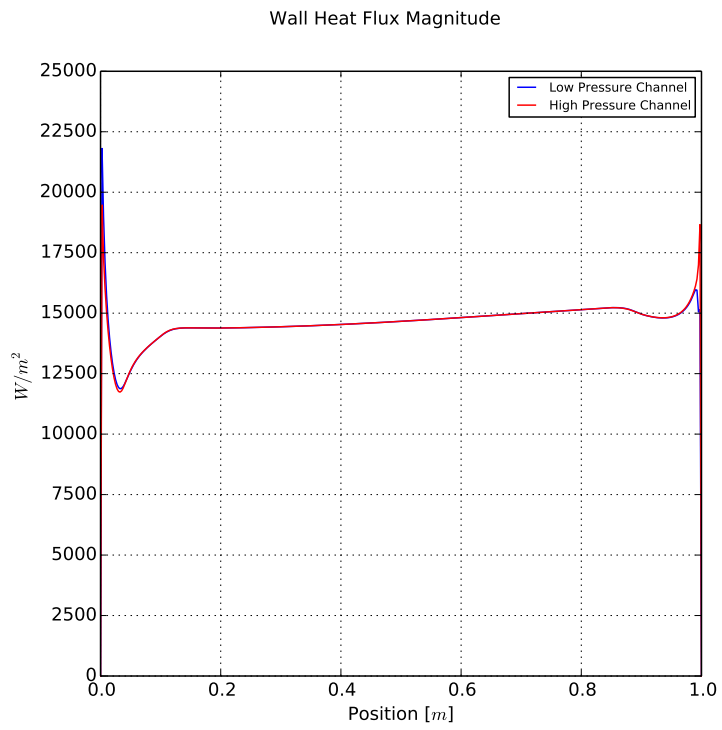


Figure 5.36: Case IV: Heat Fluxes vs Length Position

Heat Transfer Coefficient and Thermal Conductivity

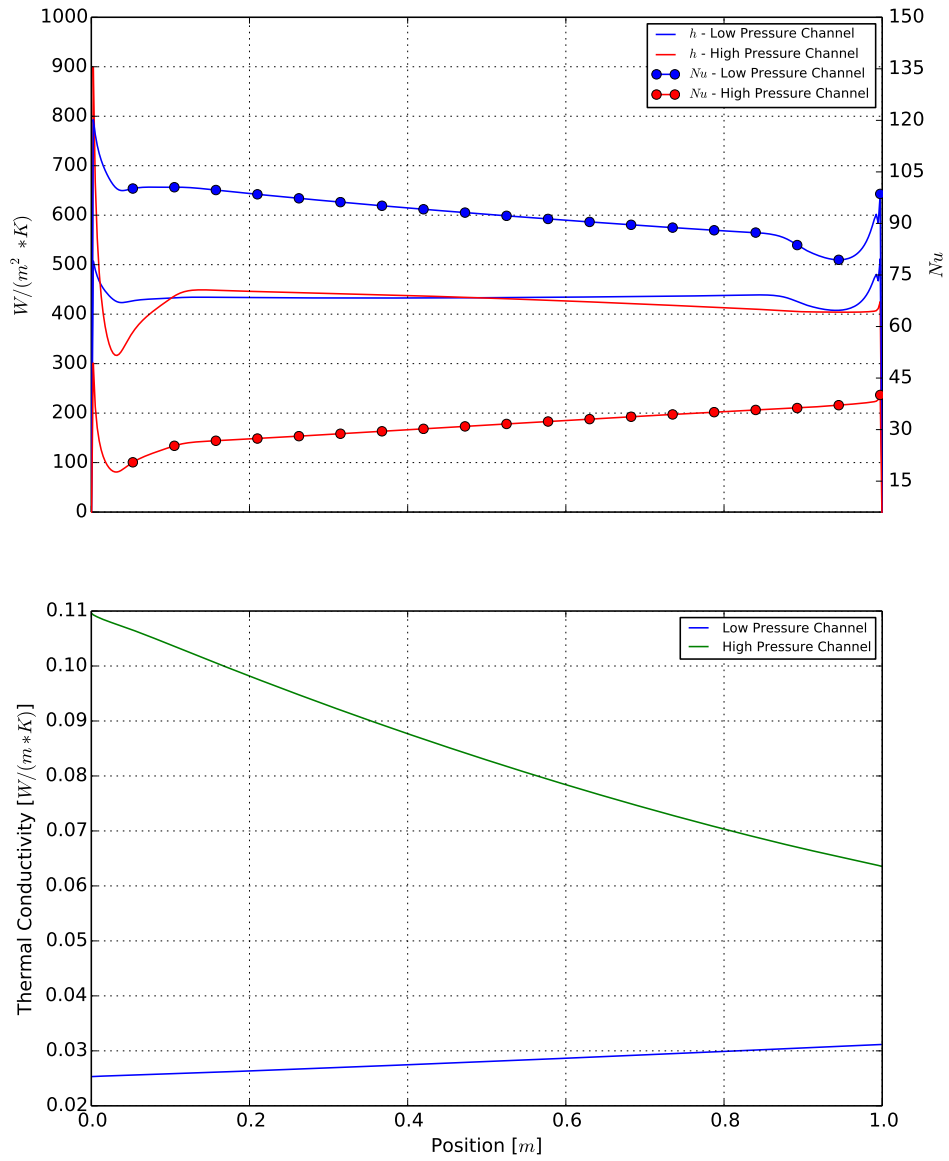


Figure 5.37: Case IV: Heat Transfer Coefficients and Average Thermal Conductivities vs Length Position

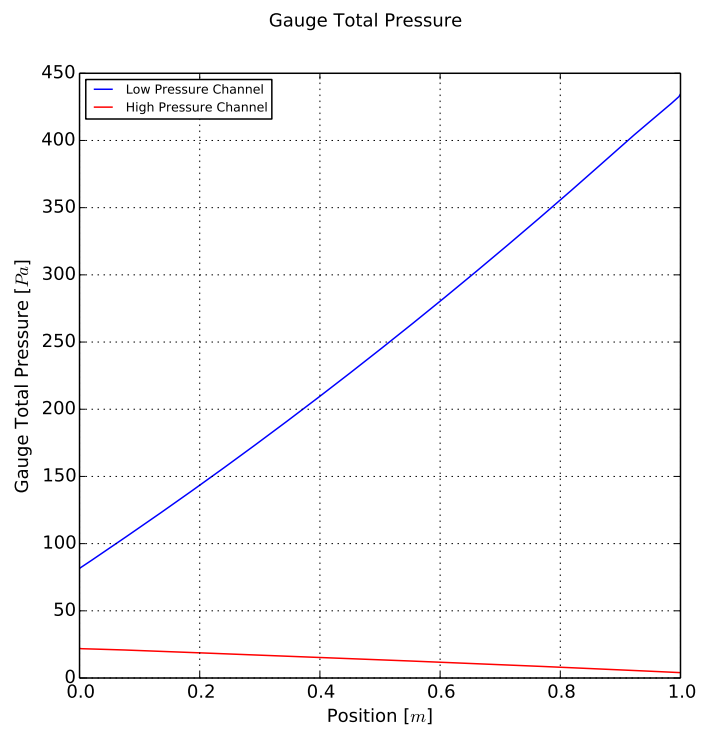


Figure 5.38: Case IV: Average Gauge Total Pressures vs Length Position

5.3.6 Case V: High Pressure Inlet $Re_{D_h}=3,000$, Turbulent, 10m Long

Results for Case V are shown in Figures 5.39 through 5.45. With the much larger surface area, Case V had a much lower minimum temperature difference than Case III at the same Reynolds number. With the increased length, entrance effects are negligible. In Figure 5.41, the highly non-linear temperature difference is much more pronounced than the high temperature difference Case III, shown in Figure 5.29. The 0-D results match up very closely in Figure 5.41 to the 2-D results. With this, one can conclude that the 0-D solver is indeed appropriate for heat exchangers with sufficient length. It's very likely that most heat exchangers will have much higher convection coefficients and more than 1 m passage length given the curvy nature of most real heat exchanger passages, and therefore, the 0-D solver should be appropriate. Figure 5.43 shows the local Nusselt number and heat transfer coefficient. Despite being the same Reynolds number, the results vary from Figure 5.31 at similar length percentages. This is likely due to the different temperatures which result in different local Reynolds numbers.

Local Reynolds Number and Dynamic Viscosity

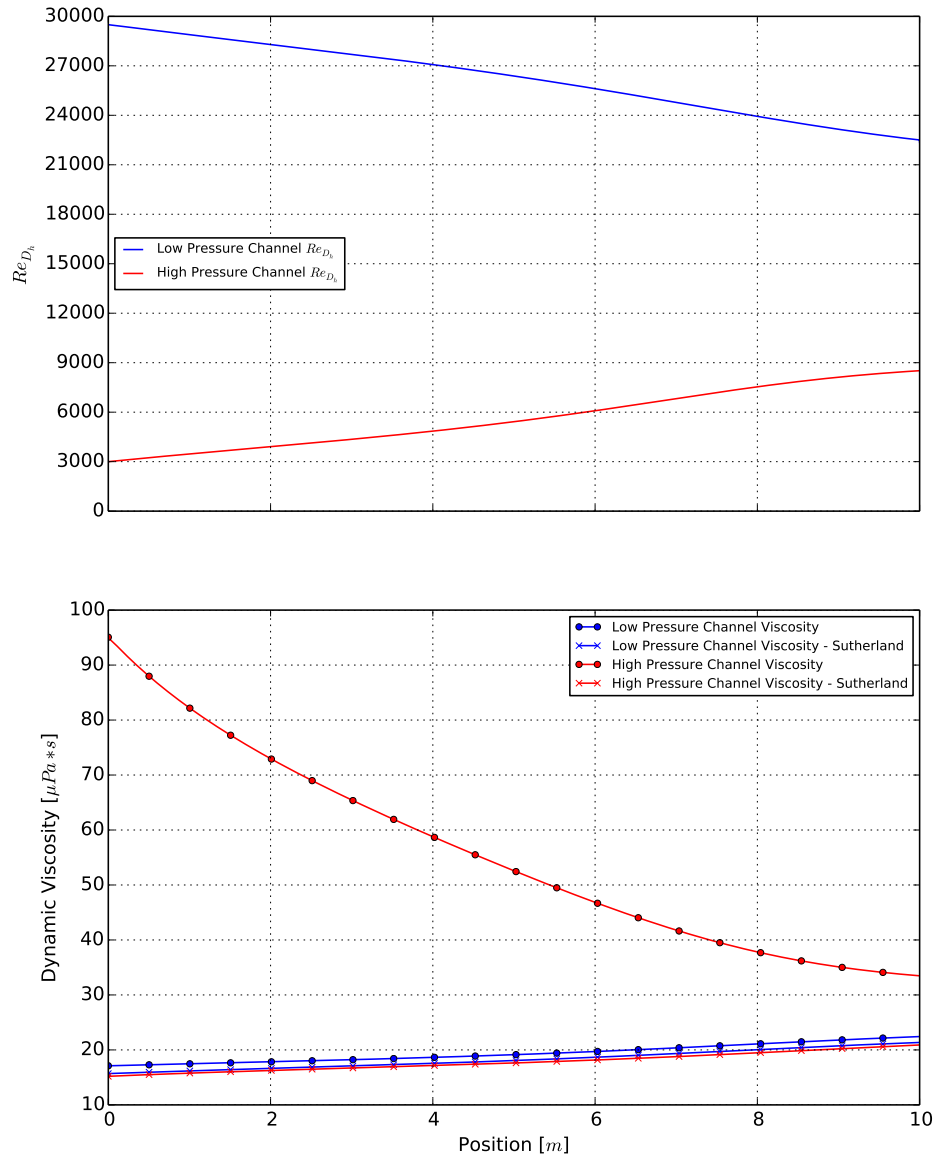


Figure 5.39: Case V: Reynolds Numbers and Average Dynamic Viscosities vs Length Position

Temperatures

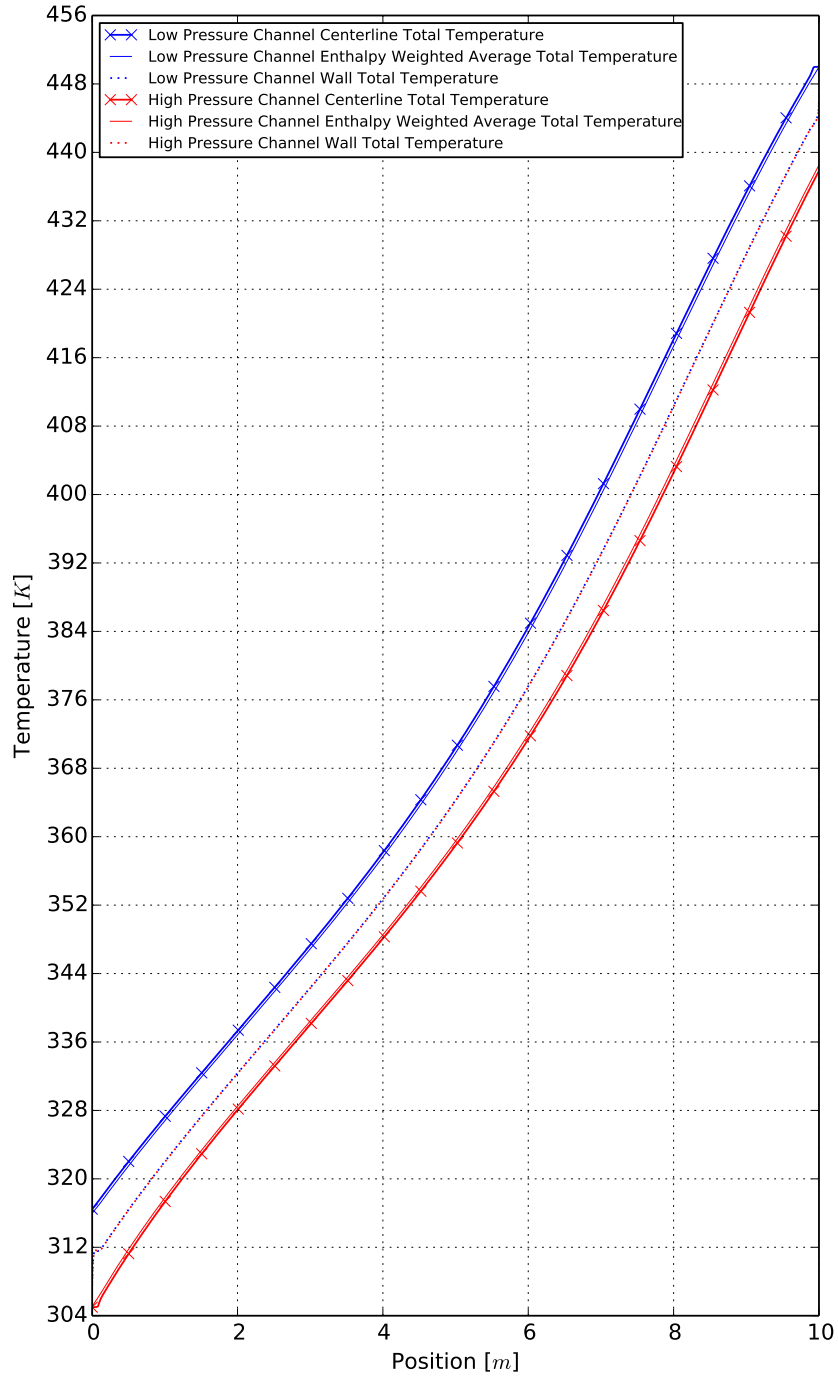


Figure 5.40: Case V: Temperatures vs Length Position

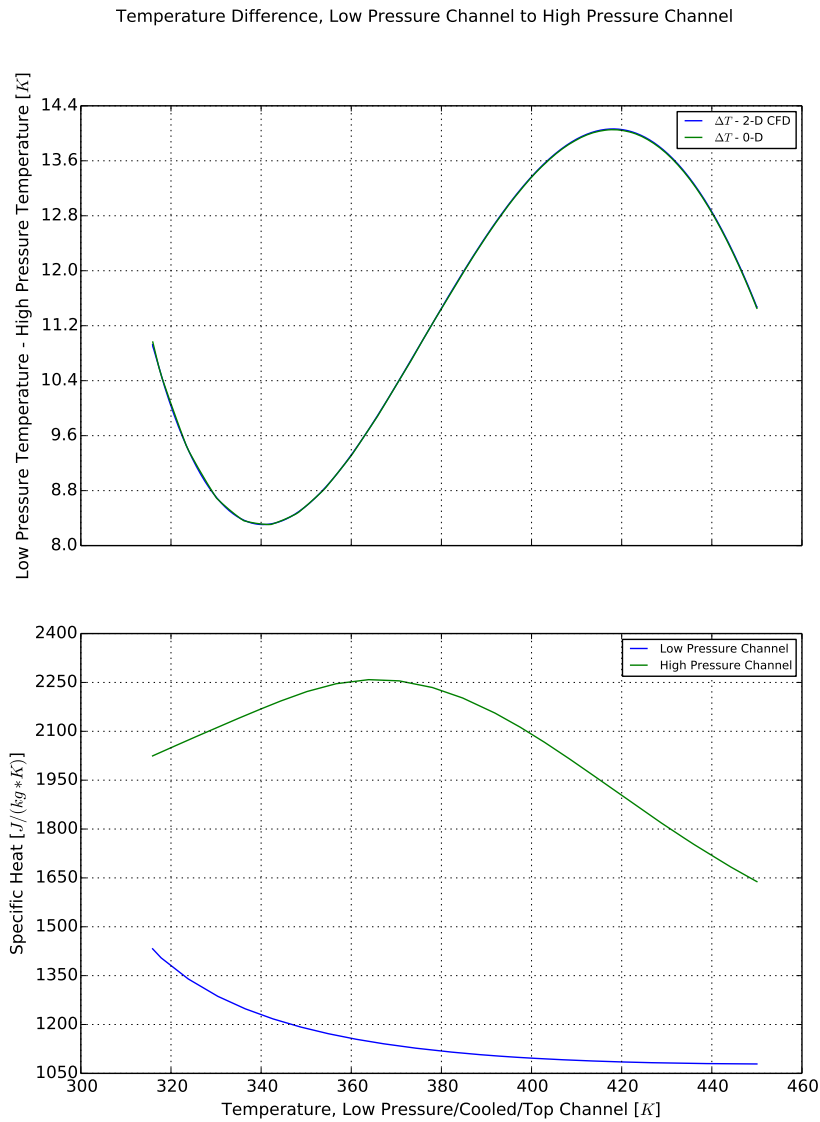


Figure 5.41: Case V: Average Temperature Difference and Specific Heats vs Temperature on the Low Pressure Side

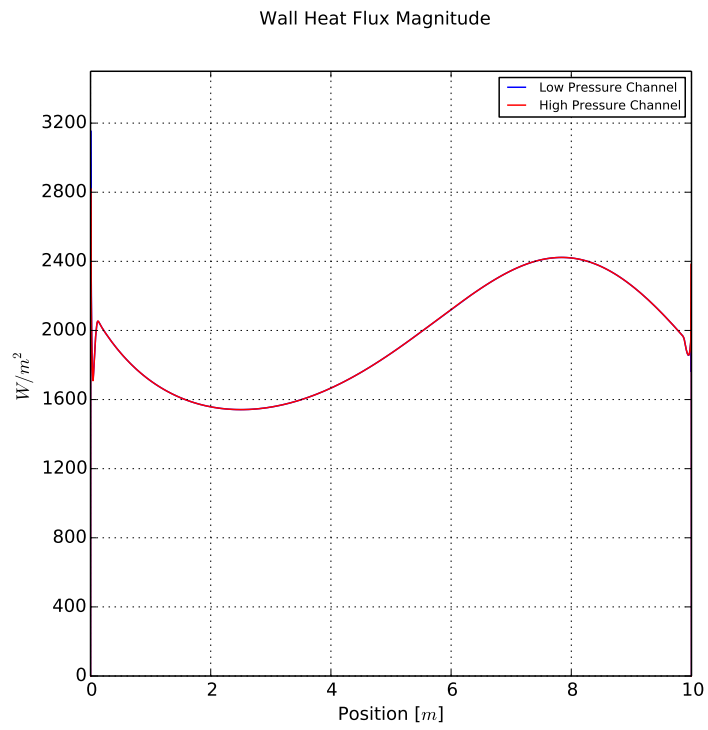


Figure 5.42: Case V: Heat Fluxes vs Length Position

Heat Transfer Coefficient and Thermal Conductivity

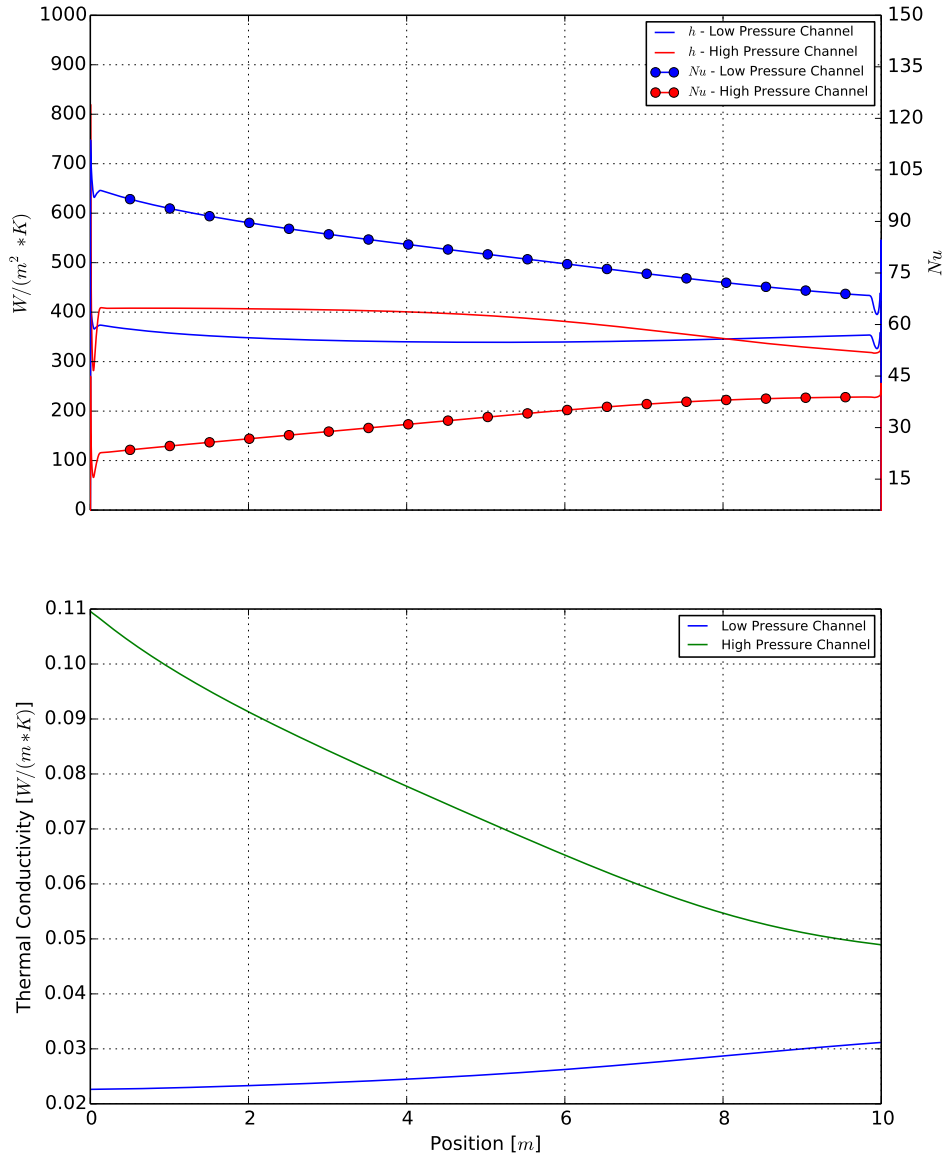


Figure 5.43: Case V: Heat Transfer Coefficients and Average Thermal Conductivities vs Length Position

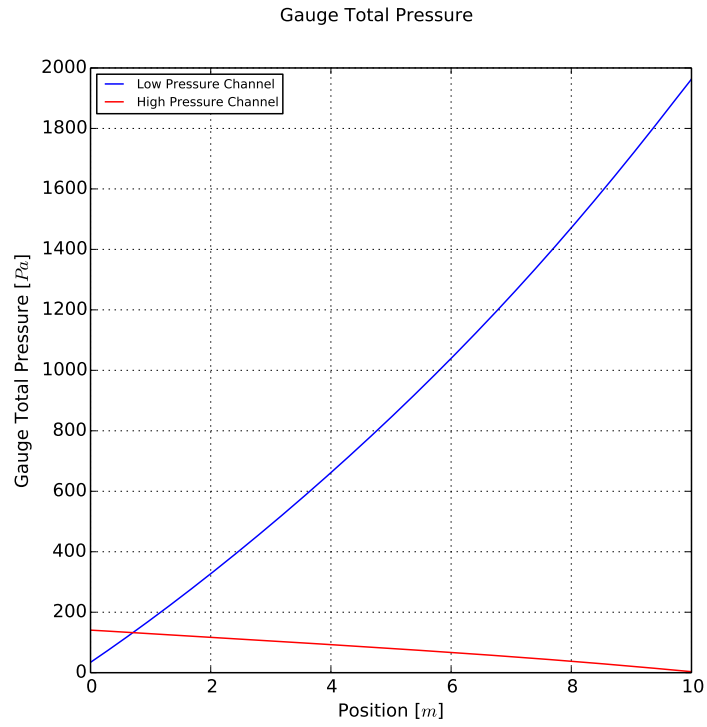


Figure 5.44: Case V: Average Gauge Total Pressures vs Length Position

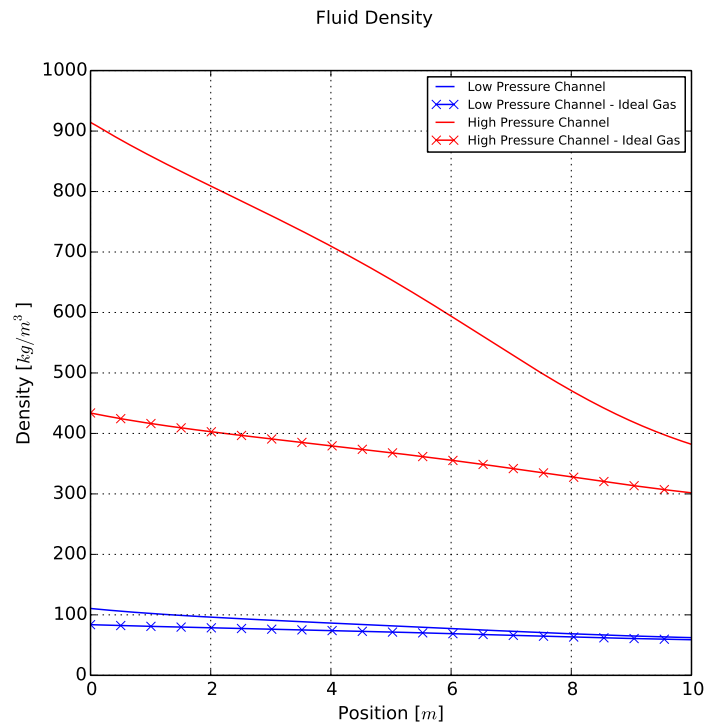


Figure 5.45: Case V: Average Densities vs Length Position

5.3.7 Case VI: High Pressure Inlet $Re_{D_h}=3,000$, Turbulent, 10m Long, Nearly Constant and Nearly Similar Specific Heats

Case VI was conducted in order to have a reference solution with a small variation in fluid properties in order to acquaint the reader with the simpler solutions found in many heat exchanger applications. These results are shown in Figures 5.46 through 5.52. As was mentioned in Section 5.3.1, a different fluid property grid was used for this case and details of that fluid property grid are shown in Table 5.4. The boundary conditions are further defined in Table 5.1. Although a solution could have been conducted for the same fluid at the same pressure levels in both channels, a different pressure was chosen in order to demonstrate what a solution looks like with slightly dissimilar specific heats. Because every fluid's properties vary some with temperature and pressure, there is some variation with temperature and pressure in this case as well, although not nearly as significant as the previous cases. The variations in fluid properties are primarily due to changes in temperature in this case. In Figure 5.46 one can see that there is a difference of a few percent between the viscosities computed using the Sutherland Law and using REFPROP. There is also a small difference in viscosity between the two pressure levels (1MPa and 5MPa). The variation in viscosity with temperature still drives a variation in Reynolds number within each channel. The mass flow rates in each channel are the same, therefore, the Reynolds numbers in the high and low pressure channels are nearly the same. Also, a small curvature exists in the temperature difference shown in Figure 5.48, due to the small variation in specific heats. The heat flux shown in Figure 5.49 varies nearly linearly except for at the ends where some entrance effects occur. In Figure 5.50 one can see that there is some variation in heat transfer coefficient and Nusselt number, but it is small and nearly linear. Nusselt numbers are nearly the same for the low and high pressure sides, except at the ends where entrance effects are involved. It's also interesting to note that the Nusselt numbers are significantly lower than that of Case V with the same Reynolds number but different pressures. The densities presented in Figure 5.52 show a close agreement between the ideal gas law and the REFPROP, particularly for the low pressure (1MPa) fluid. The high pressure fluid (5MPa) has a small difference of just a few percent near the low temperature end.

Grid Level	Minimum Temperature	Maximum Temperature	Temperature Points	Minimum Pressure	Maximum Pressure	Pressure Points	Total Points
00	590 K	710 K	3001	1 MPa	5 MPa	217	651,217

Table 5.4: Fluid Property Grid II

Local Reynolds Number and Dynamic Viscosity

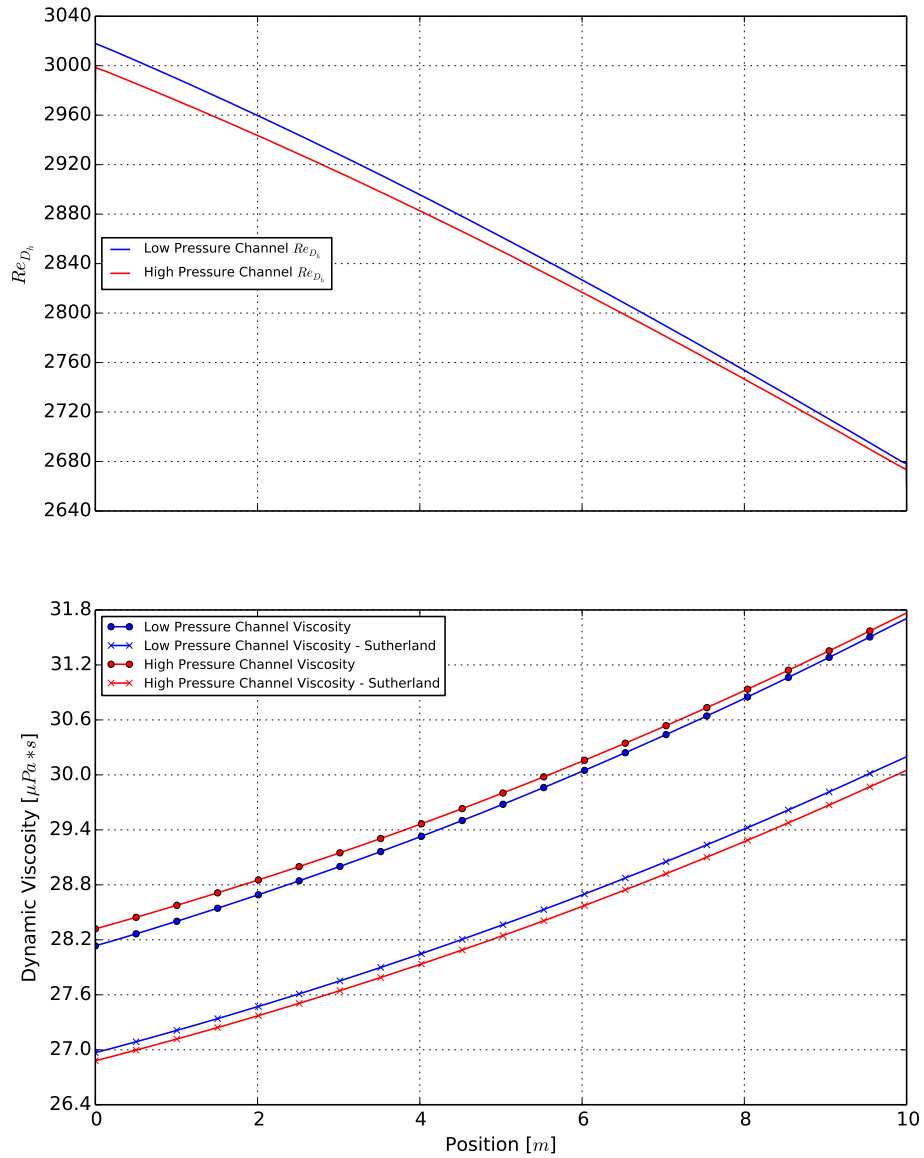


Figure 5.46: Case VI: Reynolds Numbers and Average Dynamic Viscosities vs Length Position

Temperatures

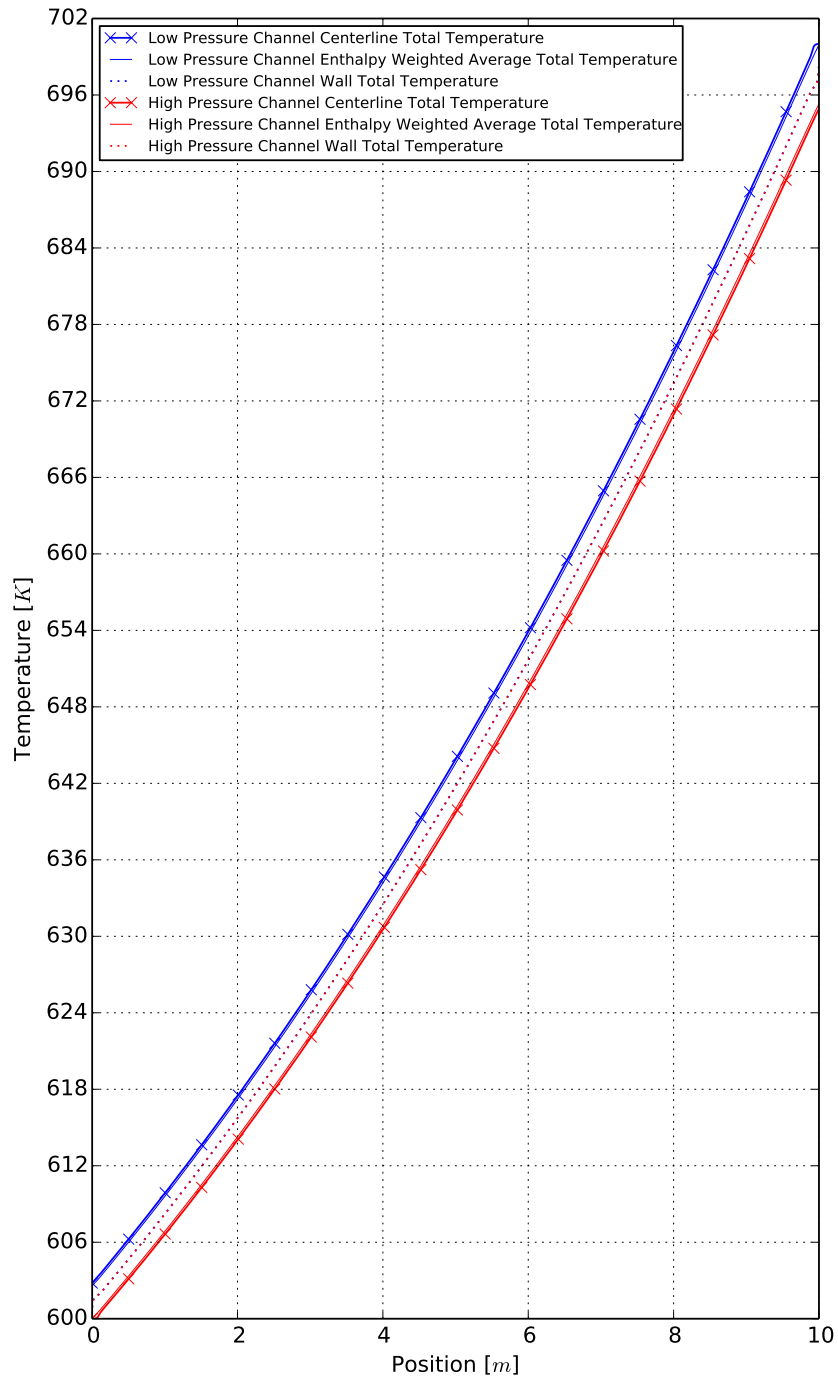


Figure 5.47: Case VI: Temperatures vs Length Position

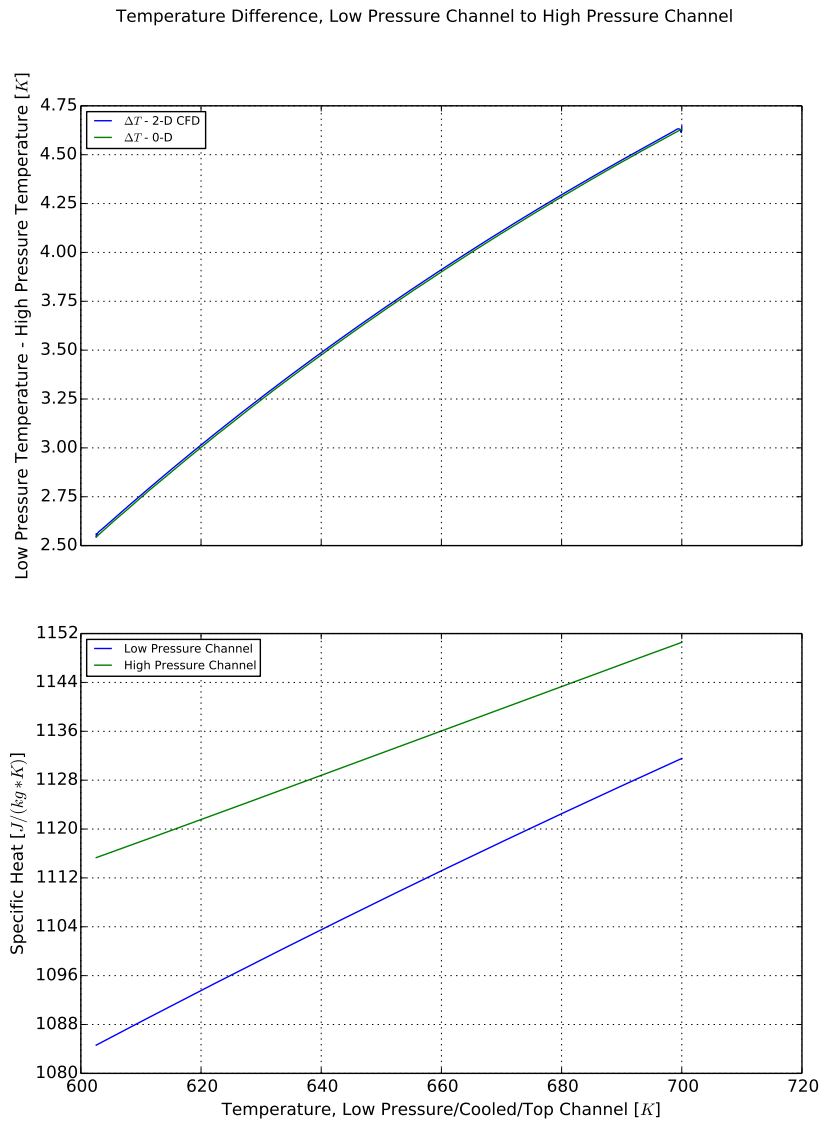


Figure 5.48: Case VI: Average Temperature Difference and Specific Heats vs Temperature on the Low Pressure Side

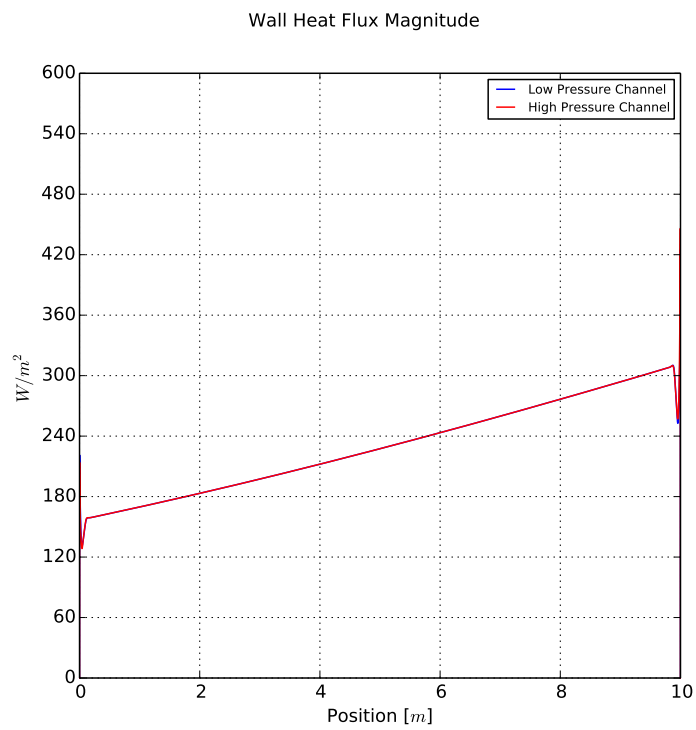


Figure 5.49: Case VI: Heat Fluxes vs Length Position

Heat Transfer Coefficient and Thermal Conductivity

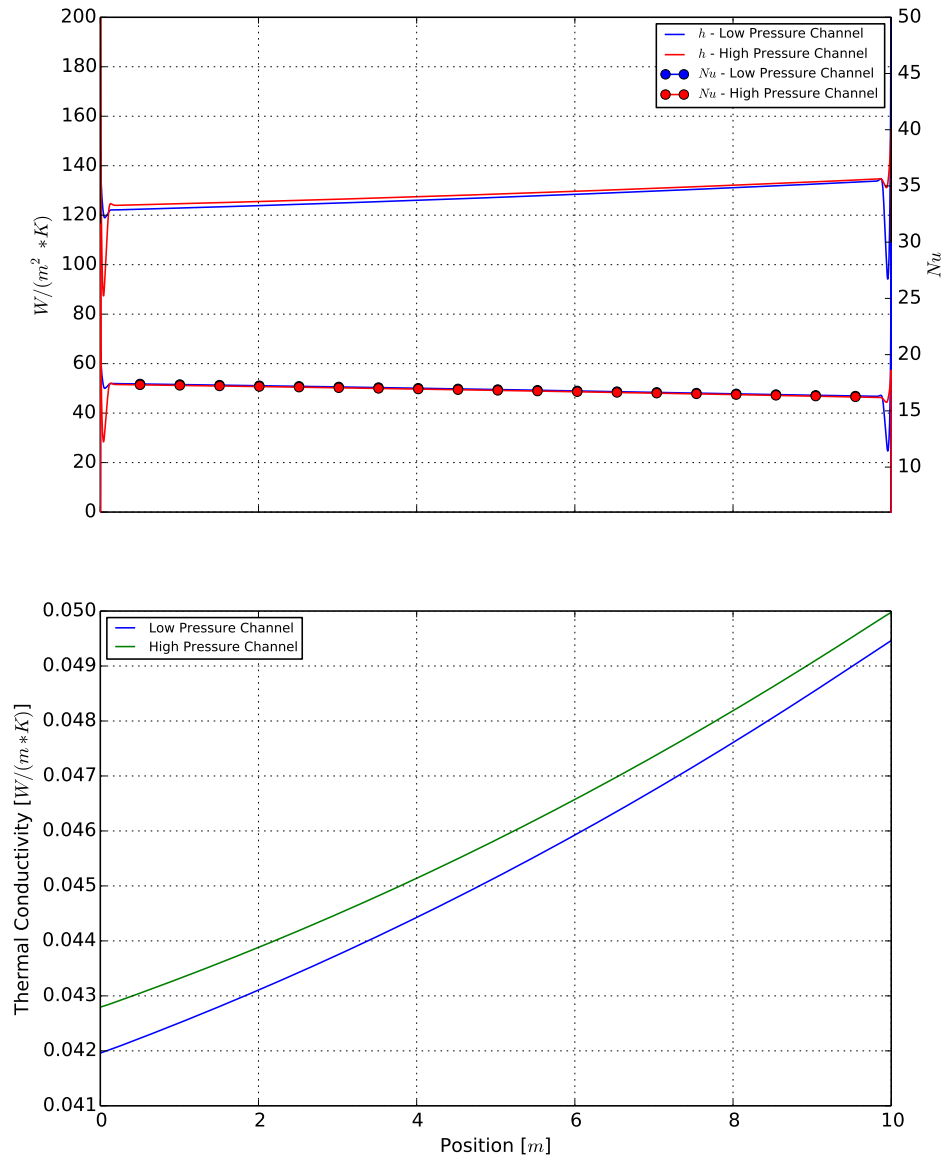


Figure 5.50: Case VI: Heat Transfer Coefficients and Average Thermal Conductivities vs Length Position

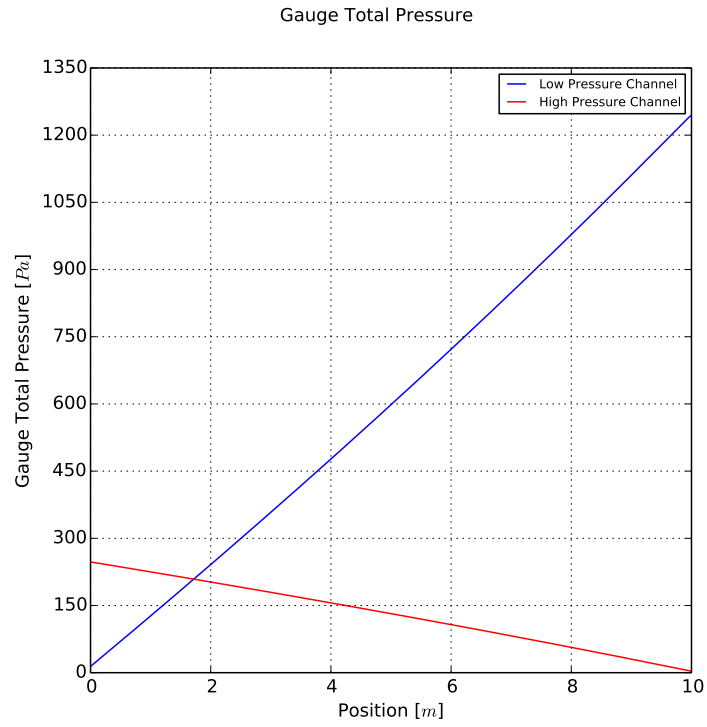


Figure 5.51: Case VI: Average Gauge Total Pressures vs Length Position

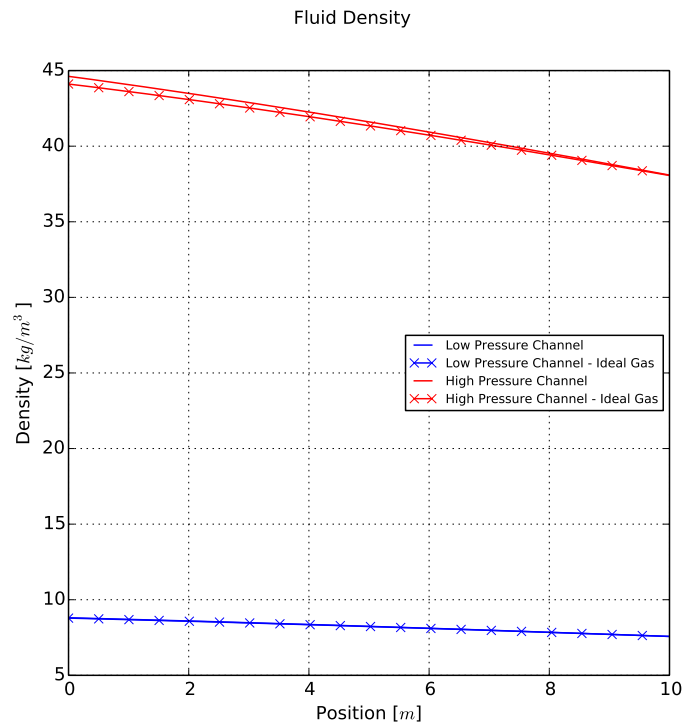


Figure 5.52: Case VI: Average Densities vs Length Position

5.4 Conclusions and Recommended Future Work

The present work has displayed some unique characteristics of heat transfer with supercritical carbon dioxide operating near the critical point. Non-dimensionalization of the heat transfer coefficient based on the local thermal conductivity does seem to result in a less varying heat transfer coefficient in the fully developed laminar regions. The author's simplified 0-D heat exchanger solver does have some issues matching the same temperature difference profile with very low minimum temperature difference heat exchangers with a reduced length. This is due to the entrance effects that are not accounted for in the 0-D solver. It's likely that this error is not significant in the overall performance predictions of a supercritical carbon dioxide power cycle since most heat exchangers will be longer than 1 m and have much higher convection coefficients than this straight, smooth channel. In the worst case, the error in temperature difference at the outlet was less than 1.5K, the outlet being the critical metric. The bottom line is that the 0-D heat exchanger solver should be able to accurately predict the heat exchanger temperature differences of fluids with non-linear and dissimilar specific heats, given a defined minimum temperature difference and a sufficient length, regardless of the shape of the heat exchanger. Further work could be conducted with more heat exchanger geometries and flow configurations to increase the certainty of the applicability of the 0-D heat exchanger model.

Based on the results of the present work, it's likely that a laminar flow heat exchanger would be unpractical, despite the extremely low pressure loss, because the heat transfer coefficient and corresponding heat fluxes are too low. It was thought that it may be possible using additive or some other advanced manufacturing process to develop a heat exchanger with very small micro channels, achieving a very large surface area to volume ratio, and a thin wall thickness. Further investigation could be conducted on this concept, but it's likely that the design will not be laminar.

The present work avoided configurations where there was a transition to turbulent flow within a channel, or one channel was laminar and one channel was turbulent. It's possible some additional interesting solutions may result from such a configuration. However, it's likely no practical designs will ever operate near turbulent transition because off design operation will result in dramatic changes in heat transfer coefficients when changing from laminar to turbulent flow, and then back again, which is not desired from an operability and controls standpoint.

Additional work can involve studying more realistic geometries, taking insight from this simpler flow configuration. Complexity with meshing may increase due to the required heat exchanger length and number of repeated features in order to achieve appropriately low minimum temperature differences and high effectivenesses. It's likely that these more complex geometries will have a better balance of higher pressure loss and higher heat flux. There will need to some assessment of the appropriate balance between heat exchanger length and the number of parallel passages in the heat exchanger. Increased length will result in a larger mass flow rate through each channel, which in turn will result in a larger pressure drop. Too many parallel channels, however, will result in too much pressure loss in the entrance and exit manifolds of the heat exchanger. Additionally, with a chosen heat exchanger solid material (and its thermal conductivity) there will be a balance in heat exchanger wall thickness and heat exchanger length in order to avoid too much axial conduction in the heat exchanger. The results from those efforts could help to better estimate the heat exchanger volume and cost.

It's believed that given a common minimum temperature difference, but different geometry patterns between heat exchangers (but the patterns do not change *within* the heat exchangers), relative changes due to fluid property variations will be mostly independent of the geometry pattern because those property variations are driven primarily by the temperature variation in each side of the heat exchanger. Pressure losses in the heat exchanger will still be fairly low such that there will not be significant variation in fluid properties due to the pressure losses.

Chapter 6

Conclusions and Recommended Future Work

Supercritical CO₂ Power Cycles have the potential for improvements in efficiency over traditional power cycles and traditional combined cycle power plants, at a reduced system size. However, the highly nonlinear fluid properties present significant challenges in cycle and component design. A multi-shaft layout with smaller turbomachinery components placed in pressure vessels has been presented which may help to eliminate some of the design challenges with the design, construction, and testing of supercritical carbon dioxide engines. The smaller compressor-turbine pairs on independent shafts are packaged in a similar way as a turbocharger. The present work demonstrates a cycle analysis code that was written from scratch specifically to explore a wide range of design parameters for the very general proposed layout. The present work indicates that a cycle efficiency of 49.6% may be achievable in a stand alone engine configuration with a maximum heat source temperature of 923 K (650°C) and a minimum coolant temperature of 320 K (47°C).

A recuperated Lenoir cycle using supercritical carbon dioxide was explored. Although the efficiency predicted of this hypothetical engine configuration could be considered high, in an ideal analysis it did not present significant advances over more established technologies and did not present considerable potential advantages over the former supercritical carbon dioxide cycle that was studied in significantly more detail. Because of the increased complexity of actually creating a constant volume counterflow heat exchanger, further efforts with this layout are not recommended.

Solutions using both the custom developed 0-D heat exchanger solver as well as 2-D conjugate heat transfer solutions using the Star-CCM+ computational fluid dynamics software suite were compared. On an averaged basis there was good agreement for highly non-linear cases when the heat exchanger length was sufficiently long that entrance effects were negligible. Although considerable efforts were involved, the present heat exchanger work is just a start for fluids with such a complex operating range. More detailed investigation and review of the current results would be beneficial. Utilization of more appropriate pressure loss relationships for the given minimum temperature differences would improve the accuracy of the results in the cycle analysis code. In the studies of conjugate heat transfer, more realistic three dimensional flow geometries and Reynolds numbers could be studied.

The two engine cascade configurations that were studied predicted very high combined cycle efficiencies.. The first optimized design, which consisted of a traditional open loop gas turbine, coupled with a series of recuperated, recompression, precompression supercritical carbon dioxide power cycles had a predicted combined cycle thermal efficiency of 65.0% using a peak temperature of 1,890 K [1,617°C]. The second optimized configuration which consisted of a hybrid natural gas powered solid oxide fuel cell and gas turbine, coupled with a series of recuperated, recompression, precompression supercritical carbon dioxide power cycles had a predicted combined cycle thermal efficiency of 73.1%.

The hybrid stochastic and gradient based optimization technique was used throughout these studies as a balance between optimization time and identification of the most optimal configuration. This approach fared much better than a previously used brute force approach in terms of optimization time, although its results tended to be “noisy” at times. Because the optimization time was so dramatically reduced, the “noise” in the results was tolerated.

For all cycle layouts, the use of fixed turbomachinery component efficiencies was believed to drive the optimization process in a somewhat unrealistic way. As a result, interpretation of some results where the turbomachinery efficiencies were swept dramatically can be misleading. By incorporating turbomachinery efficiencies that are a function of inlet temperature and pressure as well as pressure ratio, the optimization process could be more generalized.

The present cycle code uses REFPROP to obtain fluid properties. REFPROP is an older software package and has many instabilities in its solver which can be a nuisance for the user. Its

use is also taxed by the United States Secretary of Commerce and therefore it is not able to be freely distributed along with software codes that utilize it. The present cycle code could be modified to also allow for the use of CoolProp[55], a free, open source, modern fluid property database that has seen a lot of activity and enhancements in recent times.

These studies have been currently limited to temperatures above the critical temperature. Further increases in efficiency are expected if the low temperature side of the cycle can operate below the critical temperature of carbon dioxide, either above the critical pressure or below it. In many climates where the proposed engine cycles would be operating, the ambient temperature does drop significantly below the critical temperature of carbon dioxide. Additionally, when evaporative cooling (of water) is used, the low temperature end of the engine can be reduced below the ambient air temperature, making operation below critical temperature of carbon dioxide possible during more seasons and regions. The cycle code created in the present work limited the low temperature to the critical temperature because condensation and boiling have not yet been implemented. It's possible to not have condensation and boiling below the critical temperature, but limiting to the critical temperature was the simplest way to avoid the discontinuous phase changes introduced by condensation and boiling. The cycle analysis, optimization, and parameter sweeps would be very beneficial if the cycle analysis code were expanded to contain this larger potential operating range. Performing such analysis at reduced temperatures will make more appropriate comparisons to high efficiency Rankine cycles which typically utilize evaporative cooling in order to obtain the efficiencies that are quoted.

All studies considered on-design operation only. The cycle analysis and optimization could be expanded to allow for off-design, as well as transient simulations, providing optimized results that would apply to the entire use of each system. An estimated system cost could also be computed and the engine layout optimized based on operating cost rather than efficiency. Development of accurate cost models will be an ongoing task as many specific components in the system have not yet been designed or constructed yet. Detailed collaboration between researchers and industry professionals can better help these efforts.

References

- [1] M.J. Moran and H.N. Shapiro. *Fundamentals of engineering thermodynamics*. Wiley, 2004.
- [2] Alstom/GE. Pulverised coal steam power plant. <http://alstomenergy.gepower.com/products-services/product-catalogue/power-generation/coal-and-oil-power/coal-and-oil-power-plants/pulverised-coal-steam-power-plant/> Accessed: November 23rd, 2015.
- [3] Frank Cziesla, Jurgen Bewerunge, and Andreas Senzel. Siemens - Lunen - State-of-the-Art Ultra Supercritical Steam Power Plant Under Construction. POWER-GEN Europe 2009, May 2009.
- [4] Johna Marion, Frank Kluger, Michael Sell, and Adrian Skea. Advanced Ultra-Supercritical Steam Power Plants. POWER-GEN Asia 2014, September 2014.
- [5] GE Power & Water. Marketing Document, LMS100 gas turbine. https://powergen.gepower.com/content/dam/gepower-pgdp/global/en_US/documents/product/lms100-60hz-fact-sheet.pdf Accessed: November 23rd, 2015.
- [6] Snecma, Military Aircraft Engines, M53-P2 - brochure. http://snecma.com/IMG/files/fiche_m53_ve_2013_modulvoir_file_fr.pdf.
- [7] The GE90 Engine. <http://www.geaviation.com/commercial/engines/ge90/>.
- [8] GE Power & Water. Marketing Document, 7HA.01/.02 GAS TURBINE. https://powergen.gepower.com/content/dam/gepower-pgdp/global/en_US/documents/product/gas%20turbines/Fact%20Sheet/7ha-fact-sheet-oct15.pdf Accessed: November 23rd, 2015.

- [9] Siemens Energy Sector. Siemens pushes world record in efficiency to over 60 percent while achieving maximum operating flexibility. http://www.siemens.com/press/en/pressrelease/?press=/en/pressrelease/2011/fossil_power_generation/efp201105064.htm Accessed: November 23rd, 2015.
- [10] FuelCell Energy, Inc. World's Largest Fuel Cell Park Completed in South Korea. <http://globenewswire.com/news-release/2014/02/19/611481/10068981/en/World-s-Largest-Fuel-Cell-Park-Completed-in-South-Korea.html> Accessed: November 23rd, 2015.
- [11] Tildy Bayar, Power Engineering International. Fuel cell power scales up. <http://www.powerengineeringint.com/articles/print/volume-22/issue-7/features/fuel-cell-power-scales-up.html> Accessed: November 23rd, 2015.
- [12] M. F. Platzer, W. Sanz, and H. Jericha. Renewable Power Via Energy Ship And Graz Cycle. 15th International Symposium on Transport Phenomena and Dynamics of Rotating Machinery, February 2014.
- [13] National Institute of Standards and Technology, Standard Reference Data Program. NIST Standard Reference Database 23: Reference Fluid Thermodynamic and Transport Properties-REFPROP.
- [14] Sulzer. Verfahren zur Erzeugung von Arbeit aus Warme, 1948. Swiss Patent 269 599.
- [15] G Angelino. Perspectives for the liquid phase compression gas turbine. *Journal of Engineering for Gas Turbines and Power*, 89(2):229--236, 1967.
- [16] G Angelino. Carbon dioxide condensation cycles for power production. *Journal of Engineering for Gas Turbines and Power*, 90(3):287--295, 1968.
- [17] Ernest G Feher. The supercritical thermodynamic power cycle. *Energy conversion*, 8(2):85--90, 1968.
- [18] V. Dostal. *A Supercritical Carbon Dioxide Cycle for Next Generation Nuclear Reactors*. PhD thesis, Massachusetts Institute of Technology, Dept. of Nuclear Engineering, 2004.

- [19] Steven A. Wright, Tom M. Conboy, and Gary E. Rochau. Break-even Power Transients for two Simple Recuperated S-CO₂ Brayton Cycle Test Configurations. SCO₂ Power Cycle Symposium, May 2011.
- [20] Steven A Wright, Ross F Radel, Milton E Vernon, Gary E Rochau, and Paul S Pickard. Operation and Analysis of a Supercritical CO₂ Brayton Cycle. SANDIA REPORT, SAND2010-0171, Advanced Nuclear Concepts Department, Sandia National Laboratories, Albuquerque, New Mexico, September 2010.
- [21] Kenneth J Kimball, Kevin D Rahner, Joseph P Nehrbauer, and Eric M Clementoni. Supercritical Carbon Dioxide Brayton Cycle Development Overview. In *ASME Turbo Expo 2013: Turbine Technical Conference and Exposition*. American Society of Mechanical Engineers, June 2013.
- [22] Echogen Power Systems, LLC. Our Story. <http://www.echogen.com/about/our-story/> Accessed: February 22nd, 2014.
- [23] Energy Department Announces New Concentrating Solar Power Technology Investments to American Industry, Universities. <http://energy.gov/articles/energy-department-announces-new-concentrating-solar-power-technology-investments-american>.
- [24] SunShot CSP R&D 2012, June 12, 2012. http://www1.eere.energy.gov/solar/pdfs/csp_rd_awardees_2012.pdf.
- [25] Concentrating Solar Power SunShot Research and Development. <http://energy.gov/eere/sunshot/concentrating-solar-power-sunshot-research-and-development>.
- [26] Python. <https://www.python.org/>.
- [27] NumPy. <http://www.numpy.org/>.
- [28] SciPy. <http://scipy.org/>.
- [29] matplotlib. <http://matplotlib.org/>.
- [30] python-refprop. <https://github.com/AndySchroder/python-refprop>.
- [31] Andy Schroder. Real Fluid Cycle Analysis Code, Source Code. <http://andyschroder.com/CO2Cycle/SourceCode>.

- [32] Andy Schroder and Mark Turner. Mapping the Design Space of a Recuperated, Recompression, Precompression Supercritical Carbon Dioxide Power Cycle with Intercooling, Improved Regeneration, and Reheat. 4th International Supercritical CO₂ Power Cycles Symposium, September 2014.
- [33] Andy Schroder. Supercritical Carbon Dioxide Power Cycles. <http://andyschroder.com/CO2Cycle/>.
- [34] J.D. Mattingly. *Elements of Propulsion: Gas Turbines and Rockets*. AIAA education series. American Institute of Aeronautics and Astronautics, 2006.
- [35] F.P. Incropera and D.P. DeWitt. *Fundamentals of Heat and Mass Transfer*, pages 641–697. J. Wiley, 2002.
- [36] Differential Evolution, SciPy. http://docs.scipy.org/doc/scipy/reference/generated/scipy.optimize.differential_evolution.html.
- [37] Heatric. Features & capabilities of high pressure Printed Circuit Heat Exchangers (PCHEs). http://www.heatric.com/efficiency_and_effectiveness.html/ Accessed: March 26th, 2016.
- [38] Rafaela Bellini. *Ideal cycle analysis of a regenerative pulse detonation engine for power production*. PhD thesis, The University of Texas at Arlington, 2011.
- [39] Mahmood Mohagheghi and Jayanta Kapat. Thermodynamic Optimization Of Recuperated S-CO₂ Brayton Cycles For Waste Heat Recovery Applications. 4th International Supercritical CO₂ Power Cycles Symposium, September 2014.
- [40] Leonid Moroz, Petr Pagur, Oleksii Rudenko, Maksym Burlaka, and Clement Joly. Evaluation for Scalability of a Combined Cycle Using Gas and Bottoming SCO₂ Turbines. In *ASME 2015 Power Conference collocated with the ASME 2015 9th International Conference on Energy Sustainability, the ASME 2015 13th International Conference on Fuel Cell Science, Engineering and Technology, and the ASME 2015 Nuclear Forum*. American Society of Mechanical Engineers, 2015.

- [41] Rory A. Roberts. *A Dynamic Fuel Cell-Gas Turbine Hybrid Simulation Methodology to Establish Control Strategies and an Improved Balance of Plant*. PhD thesis, University Of California, Irvine, 2005.
- [42] Rory A. Roberts, Mitch Wolff, Sean Nuzum, and Adam Donovan. Assessment Of The Vehicle Level Impact For A SOFC Integrated With The Power And Thermal Management System Of An Air Vehicle. ASME 2015 Dynamic Systems and Control Conference, October 2014.
- [43] Seong Jun Bae, Yoonhan Ahn, Jekyoung Lee, and Jeong Ik Lee. Hybrid System of Supercritical Carbon Dioxide Brayton Cycle and Carbon Dioxide Rankine Cycle Combined Fuel Cell. In *ASME Turbo Expo 2014: Turbine Technical Conference and Exposition*. American Society of Mechanical Engineers, 2014.
- [44] D Sanchez, JM Munoz de Escalona, R Chacartegui, A Munoz, and T Sanchez. A comparison between molten carbonate fuel cells based hybrid systems using air and supercritical carbon dioxide brayton cycles with state of the art technology. *Journal of Power Sources*, 196(9):4347-4354, 2011.
- [45] Alan Kruiuzenga, Mark Anderson, Roma Fatima, Michael Corradini, Aaron Towne, and Devesh Ranjan. Heat transfer of supercritical carbon dioxide in printed circuit heat exchanger geometries. *Journal of Thermal Science and Engineering Applications*, 3(3):031002, 2011.
- [46] SM Liao and TS Zhao. An experimental investigation of convection heat transfer to supercritical carbon dioxide in miniature tubes. *International Journal of Heat and Mass Transfer*, 45(25):5025--5034, 2002.
- [47] ANSYS Fluent. <http://www.ansys.com/Products/Fluids/ANSYS-Fluent>.
- [48] Andy Schroder. Experimental and Numerical Study of Impingement Jet Heat Transfer. Master's thesis, University of Cincinnati, May 2011.
- [49] Star-CCM+, CD-adapco. <http://www.cd-adapco.com/products/star-ccm>.
- [50] M. D. Carlson, C. Schalansky, A. K. Kruiuzenga, and D. F. Fleming. Sandia Progress On Advanced Heat Exchangers For SCO2 Brayton Cycles. 4th International Supercritical CO₂ Power Cycles Symposium, September 2014.

- [51] Numeca International. <http://www.numeca.com/en>.
- [52] W. Sutherland. LII. The viscosity of gases and molecular force. *Philosophical Magazine Series 5*, 36(223):507--531, 1893.
- [53] J. Hilsenrath, CW Beckett, WS Benedict, L. Fano, HJ Hoge, JF Masi, RL Nuttall, YS Touloukian, and HW Woolley. Tables of thermodynamic and transport properties. *US Nat. Bur. Stand. Circ*, 564, 1955.
- [54] R.K. Shah and A.L. London. Laminar Flow Forced Convection Heat Transfer and Flow Friction in Straight and Curved Ducts -- A Summary of Analytical Solutions. Technical Report No. 75, Department of Mechanical Engineering, Stanford University, Stanford, California, November 1971.
- [55] Ian Bell. CoolProp: Fluid properties for the masses. <http://coolprop.sourceforge.net/>.

Appendix A

Zero Dimensional Heat Exchanger Parameter Sweeps

A.1 Sweep ΔT_{min}

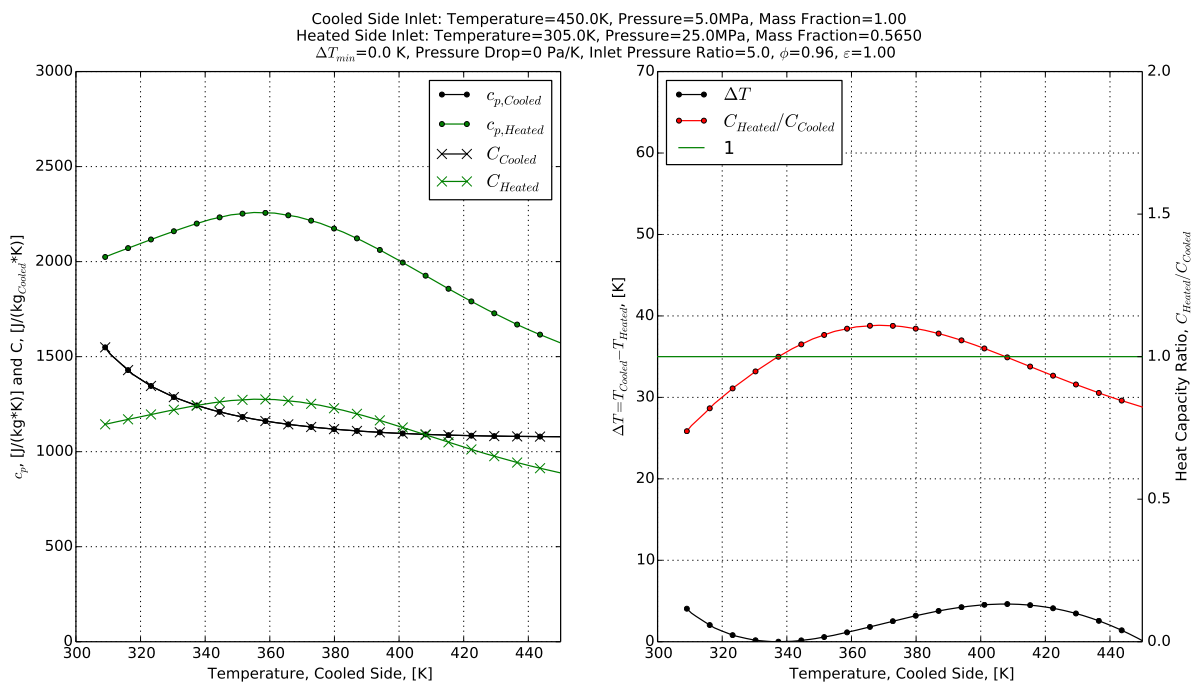


Figure A.1: Sample Heat Exchanger Solution, $\Delta T_{min} = 0K$

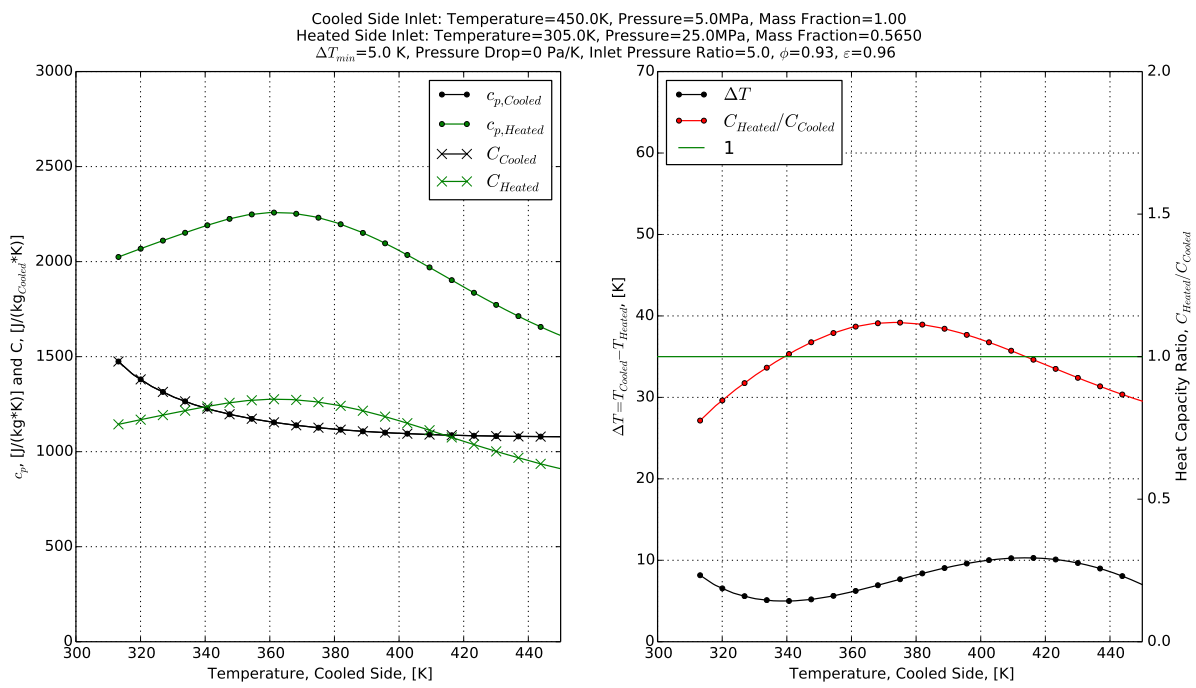


Figure A.2: Sample Heat Exchanger Solution, $\Delta T_{min} = 5K$

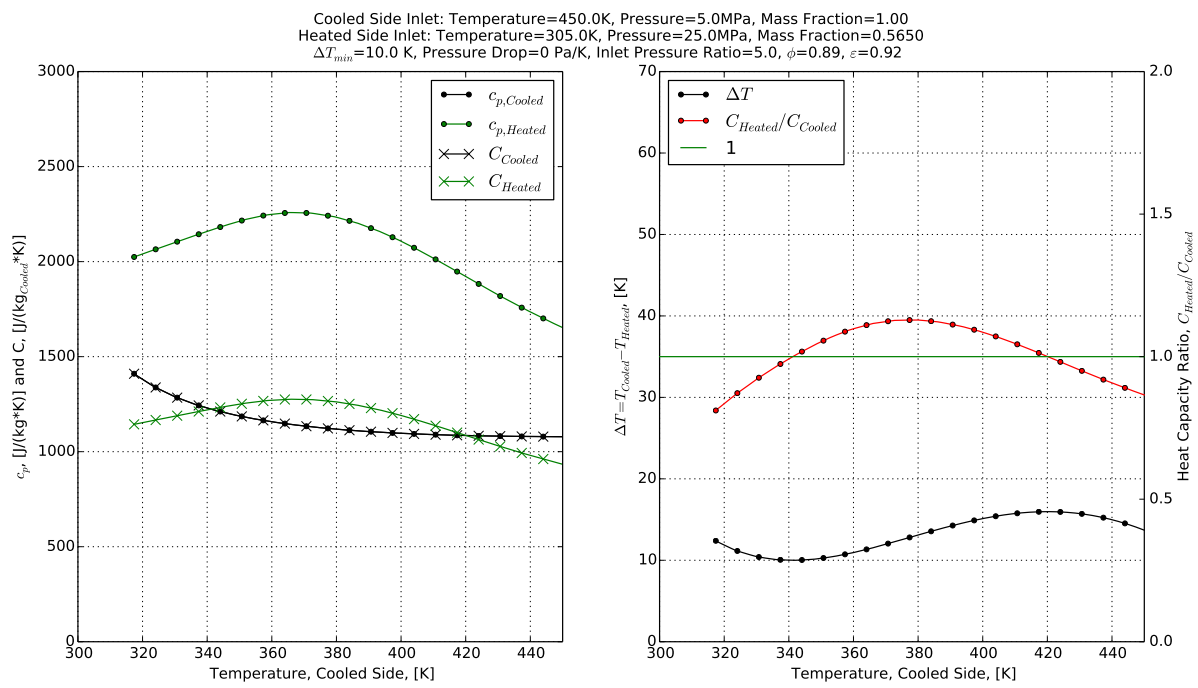


Figure A.3: Sample Heat Exchanger Solution, $\Delta T_{min} = 10K$

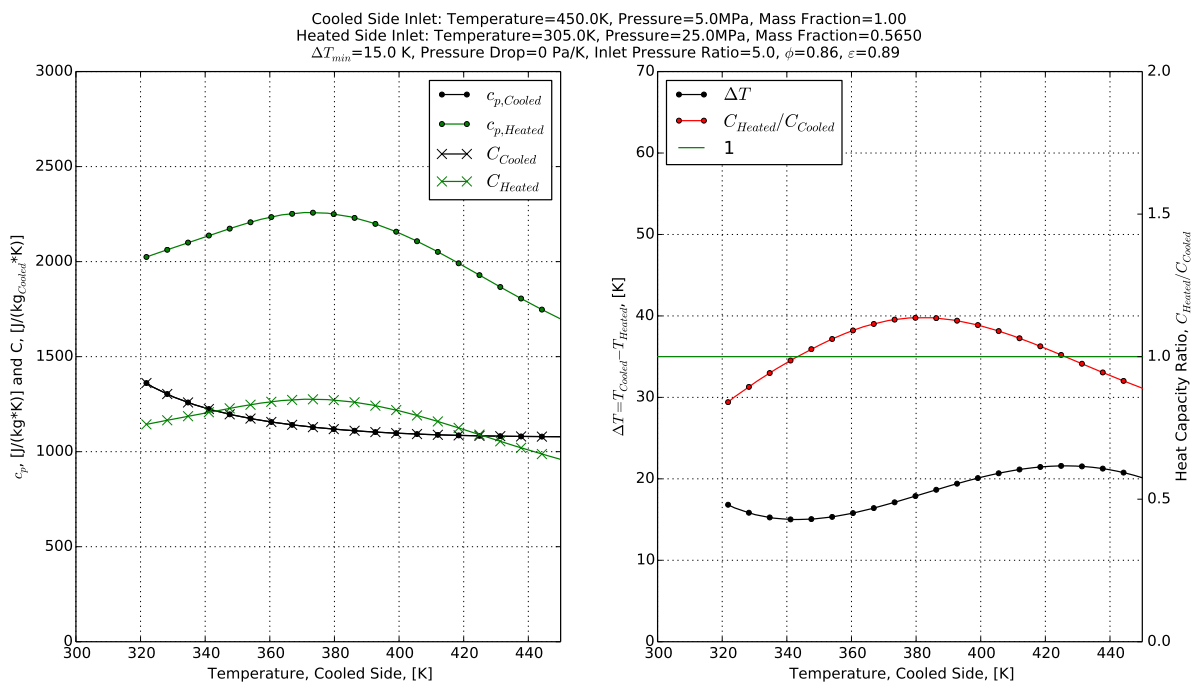


Figure A.4: Sample Heat Exchanger Solution, $\Delta T_{min} = 15K$

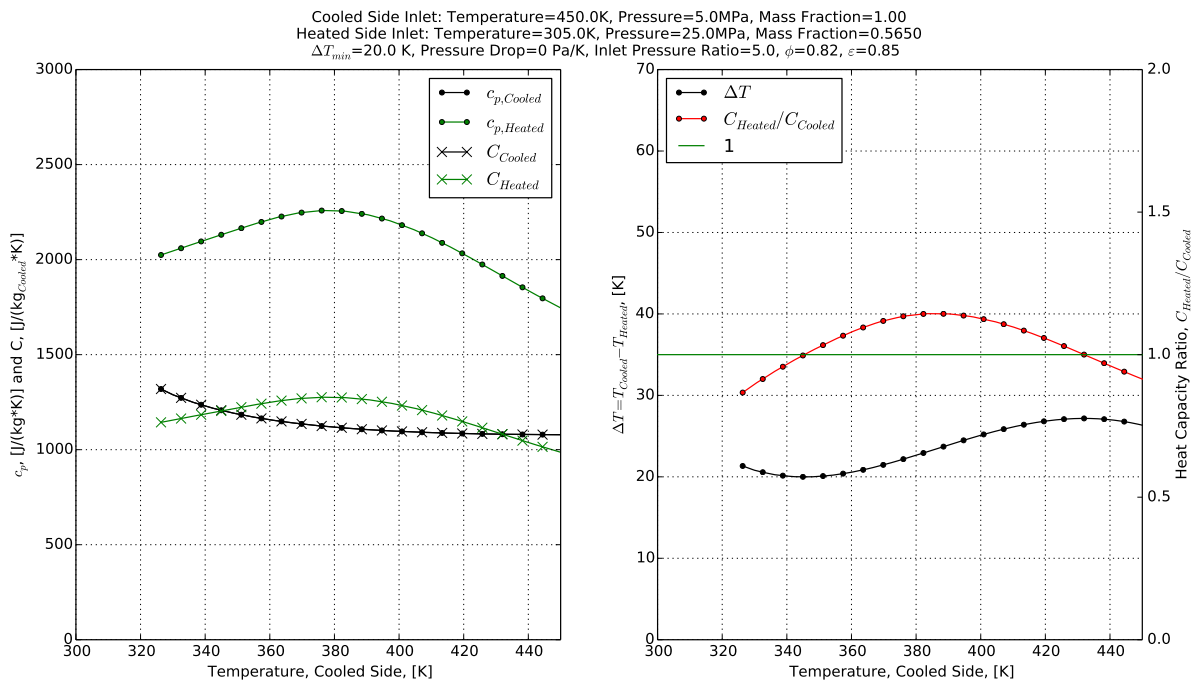


Figure A.5: Sample Heat Exchanger Solution, $\Delta T_{min} = 20K$

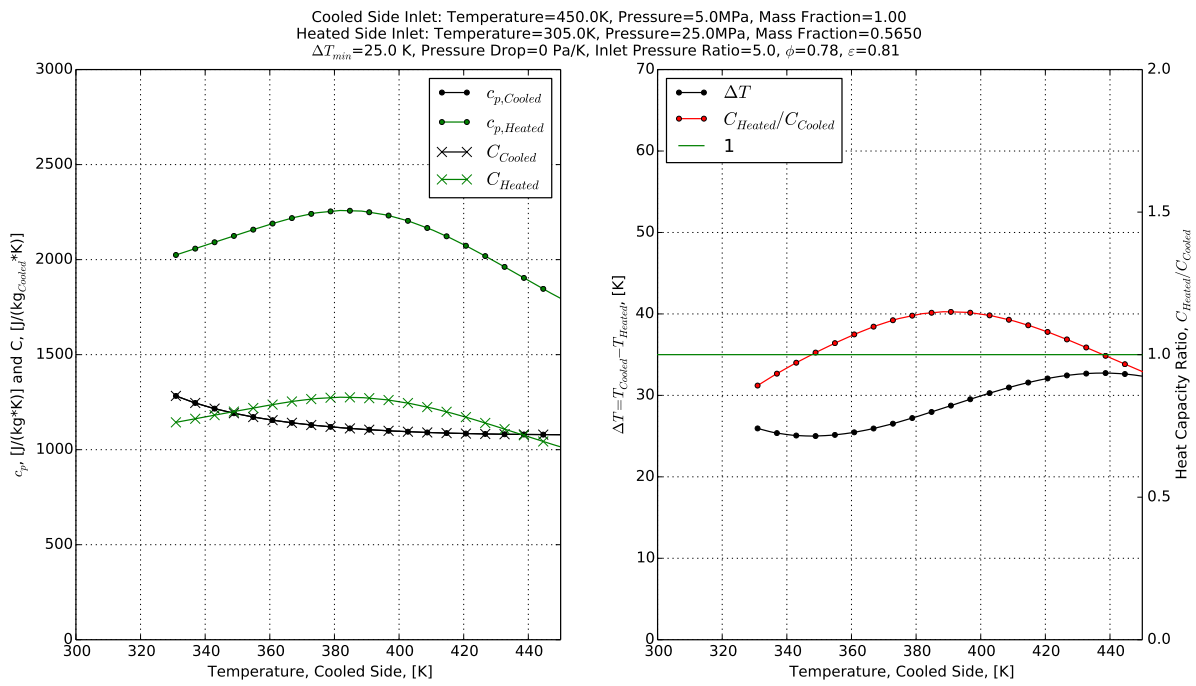


Figure A.6: Sample Heat Exchanger Solution, $\Delta T_{min} = 25K$

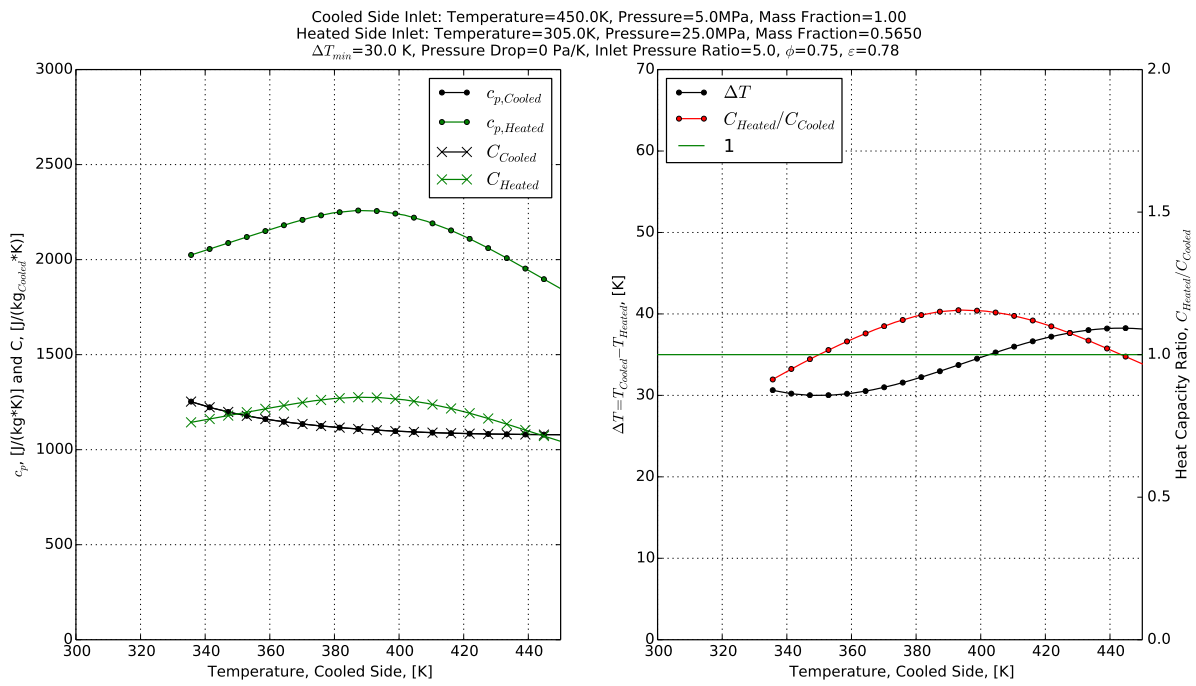


Figure A.7: Sample Heat Exchanger Solution, $\Delta T_{min} = 30K$

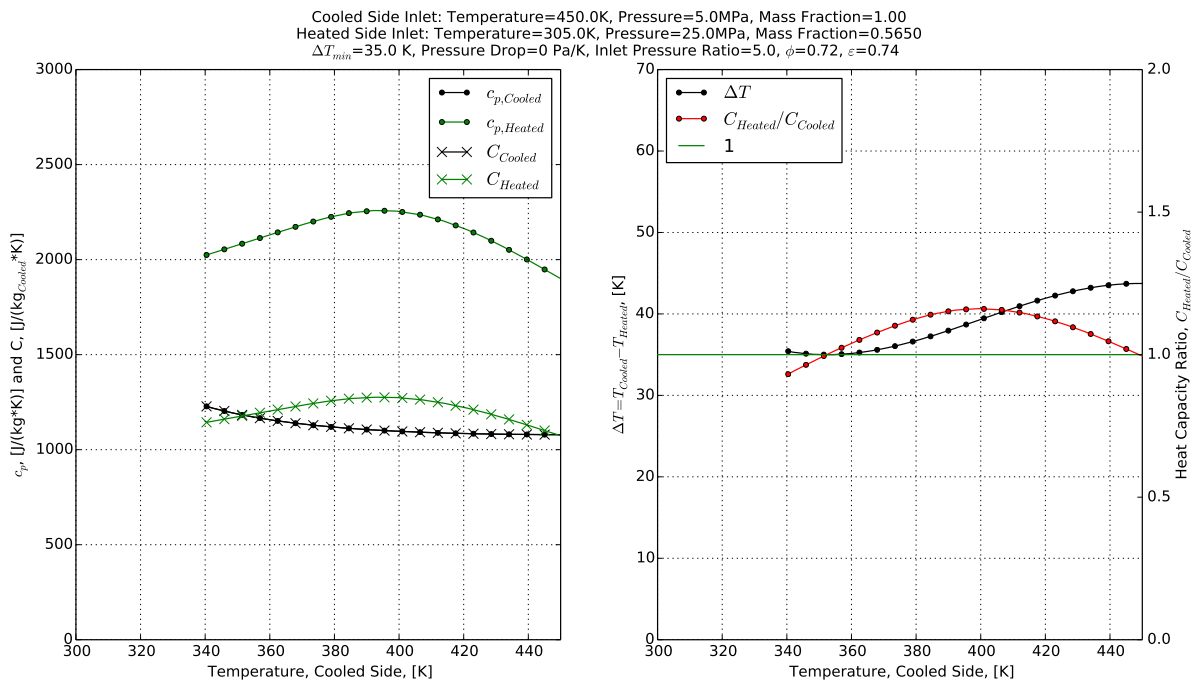


Figure A.8: Sample Heat Exchanger Solution, $\Delta T_{min} = 35K$

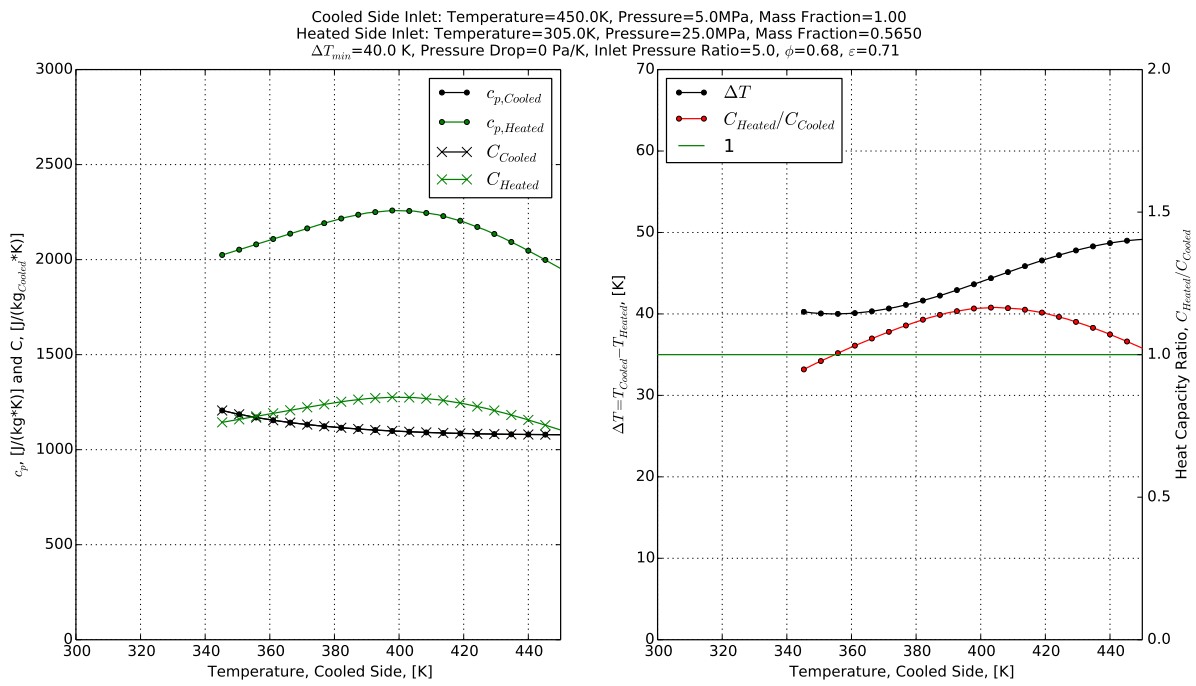


Figure A.9: Sample Heat Exchanger Solution, $\Delta T_{min} = 40K$

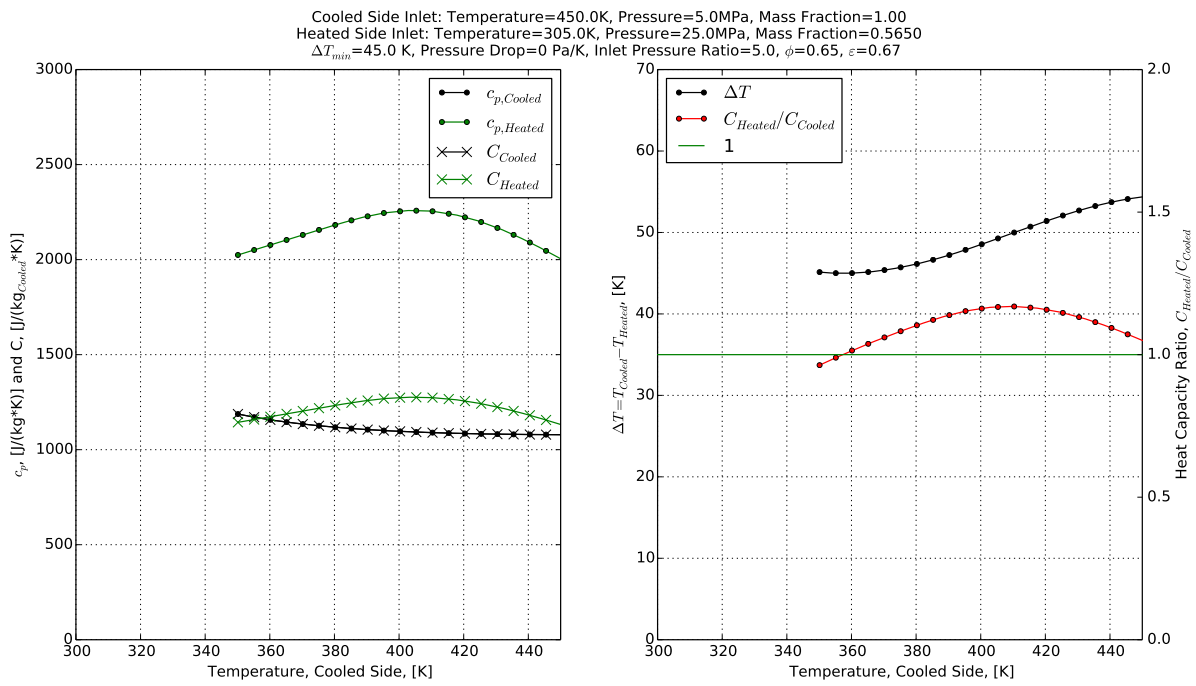


Figure A.10: Sample Heat Exchanger Solution, $\Delta T_{min} = 45K$

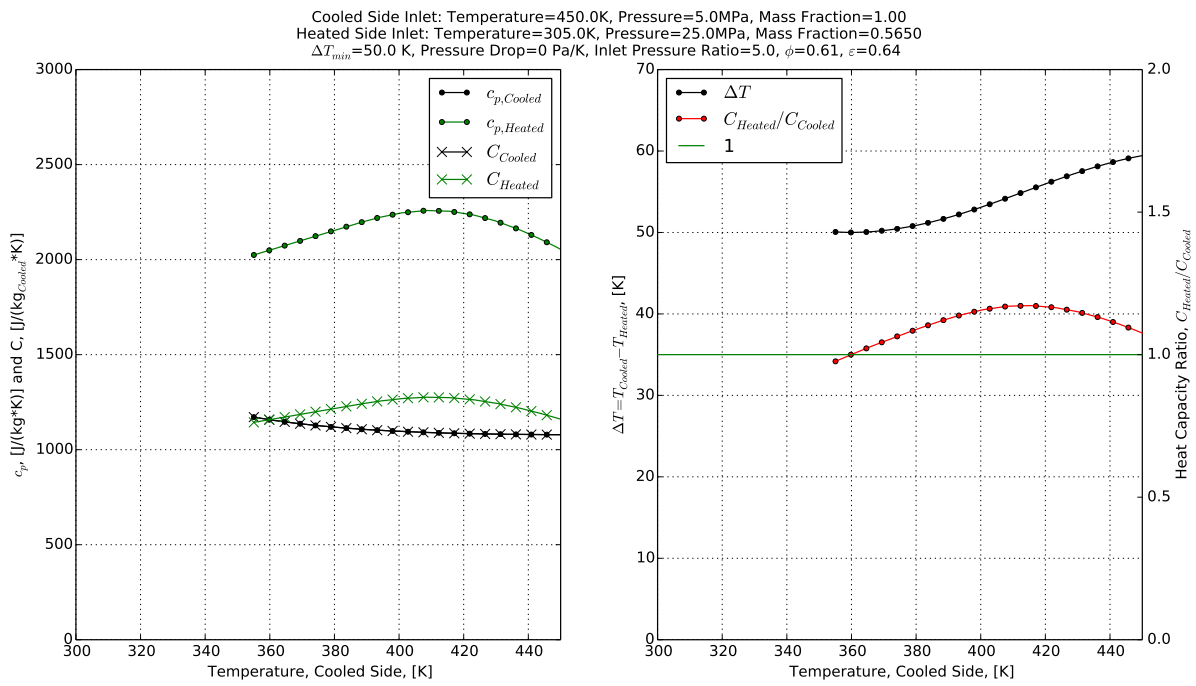


Figure A.11: Sample Heat Exchanger Solution, $\Delta T_{min} = 50K$

A.2 Sweep Mass Fraction

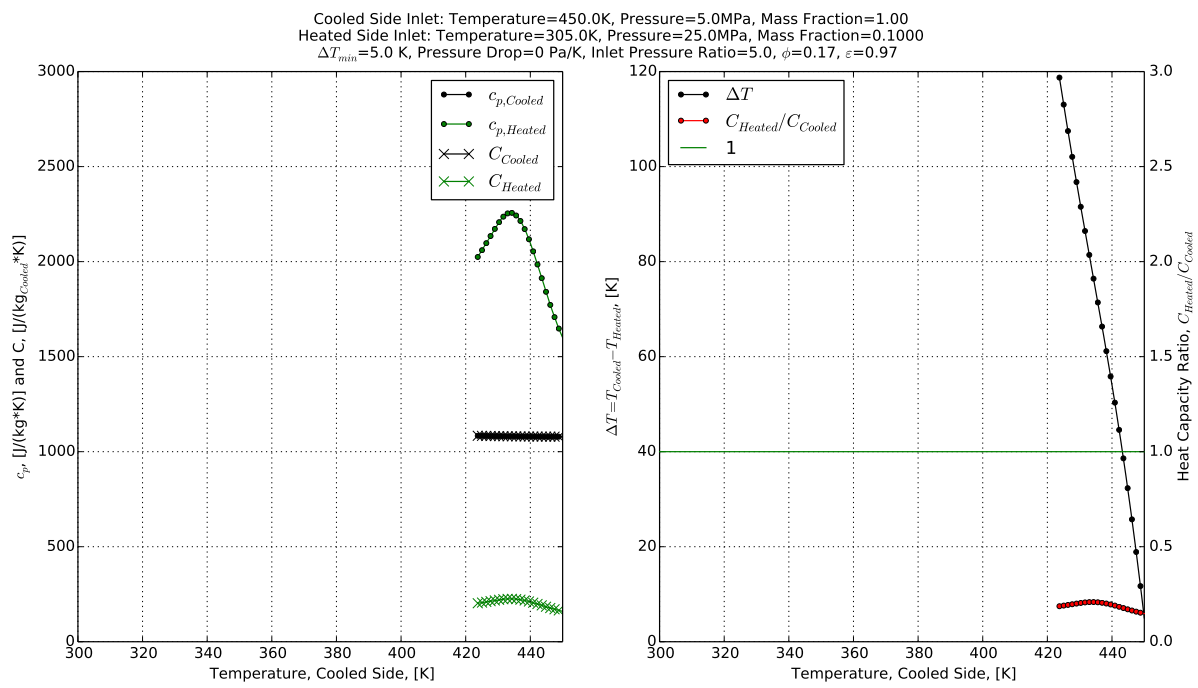


Figure A.12: Sample Heat Exchanger Solution, Mass Fraction=0.1

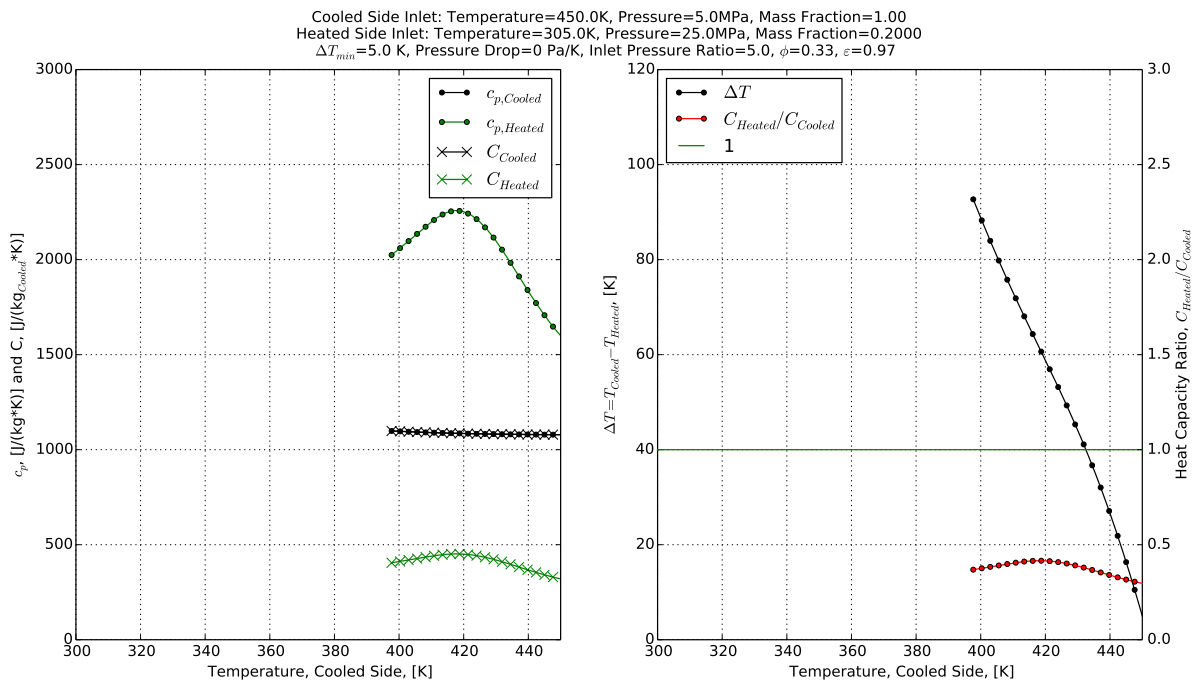


Figure A.13: Sample Heat Exchanger Solution, Mass Fraction=0.2

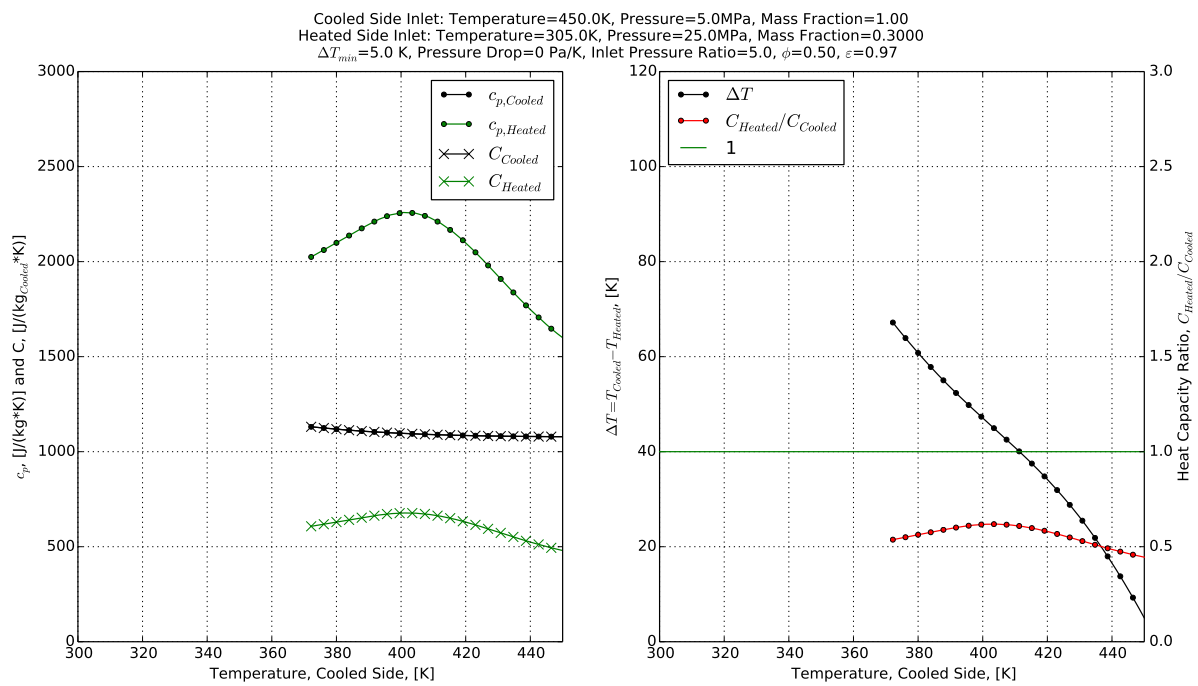


Figure A.14: Sample Heat Exchanger Solution, Mass Fraction=0.3

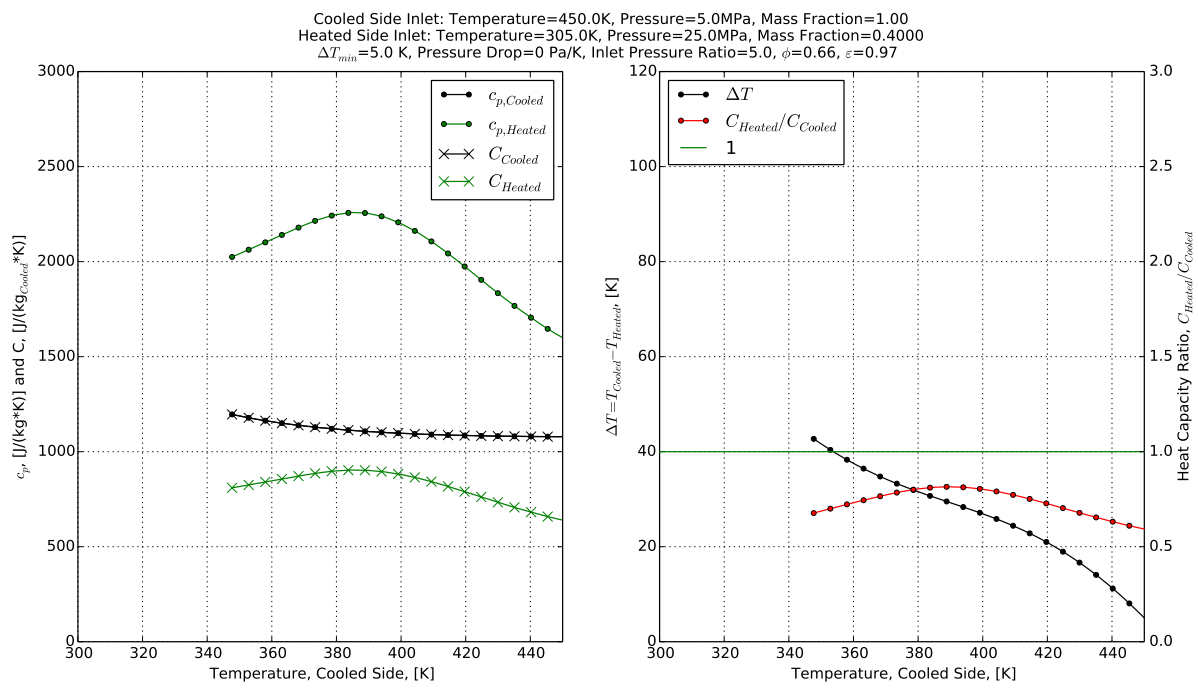


Figure A.15: Sample Heat Exchanger Solution, Mass Fraction=0.4

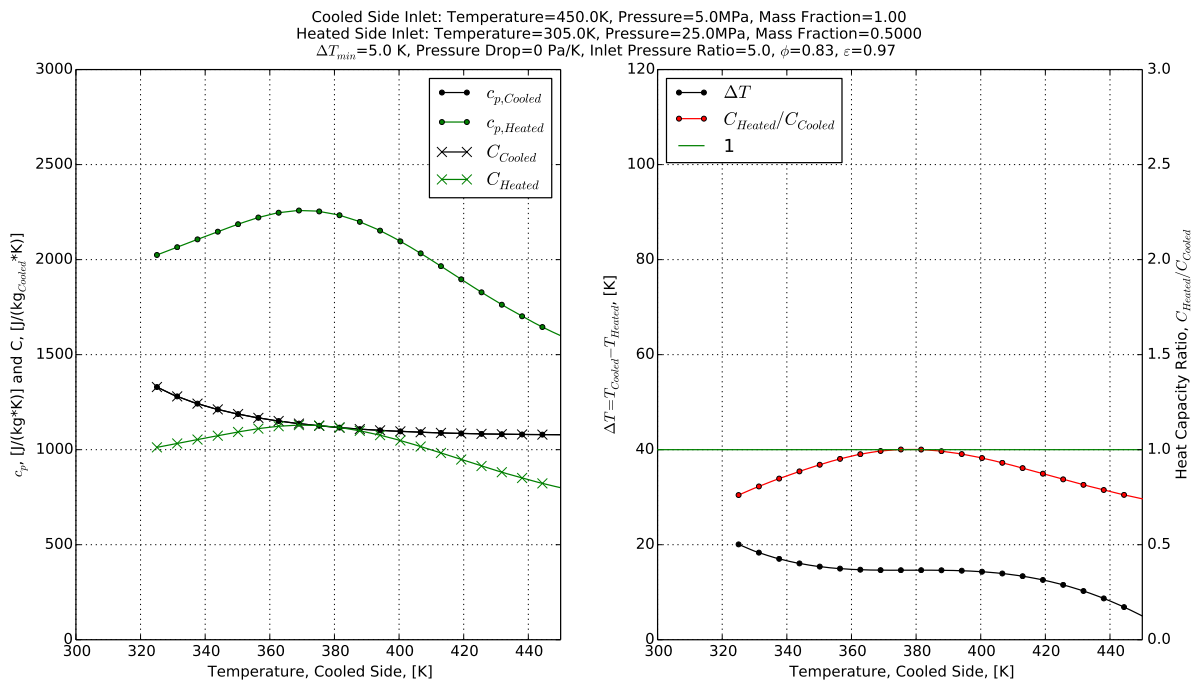


Figure A.16: Sample Heat Exchanger Solution, Mass Fraction=0.5

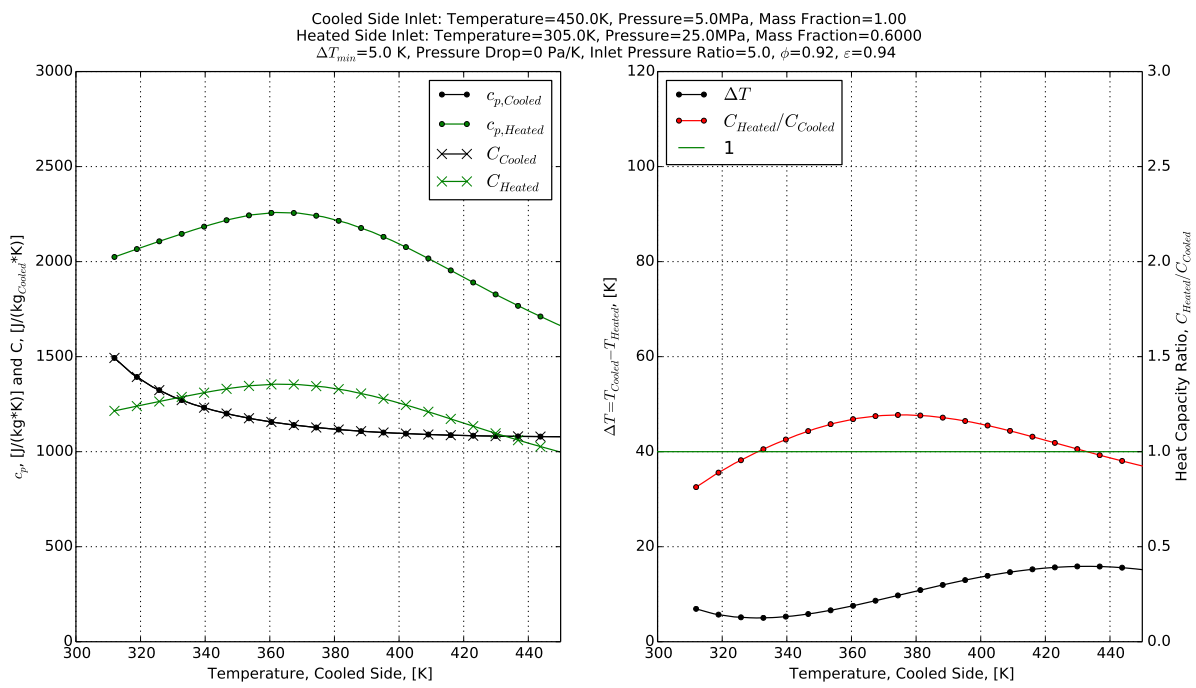


Figure A.17: Sample Heat Exchanger Solution, Mass Fraction=0.6

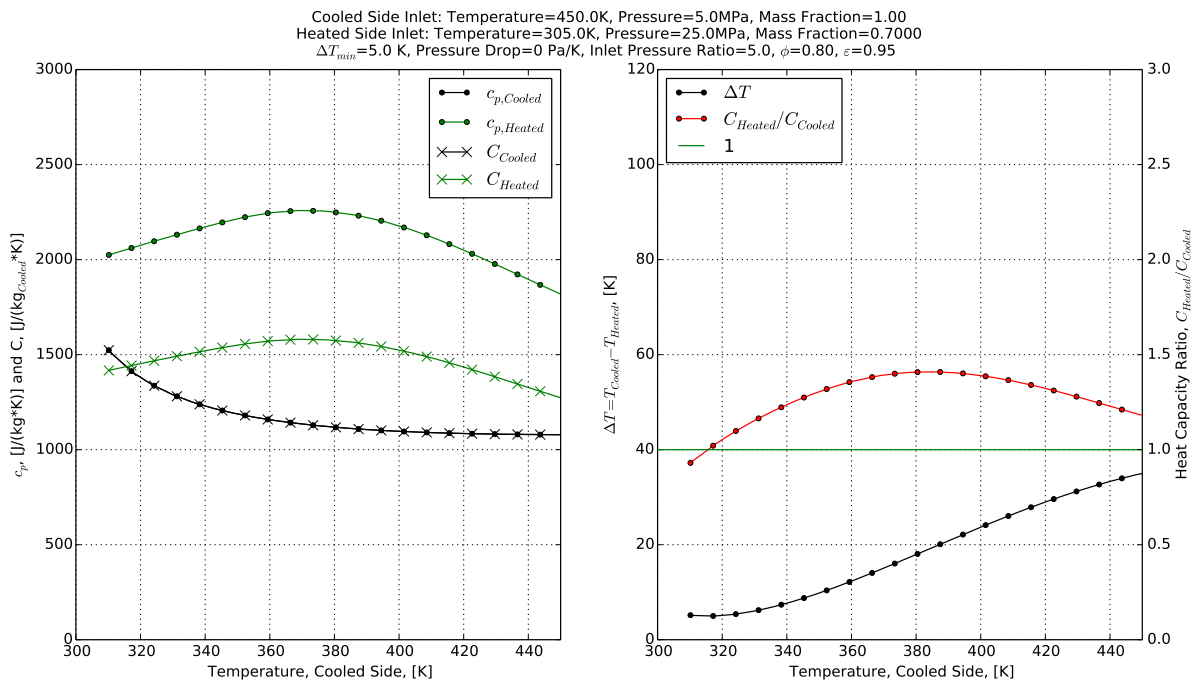


Figure A.18: Sample Heat Exchanger Solution, Mass Fraction=0.7

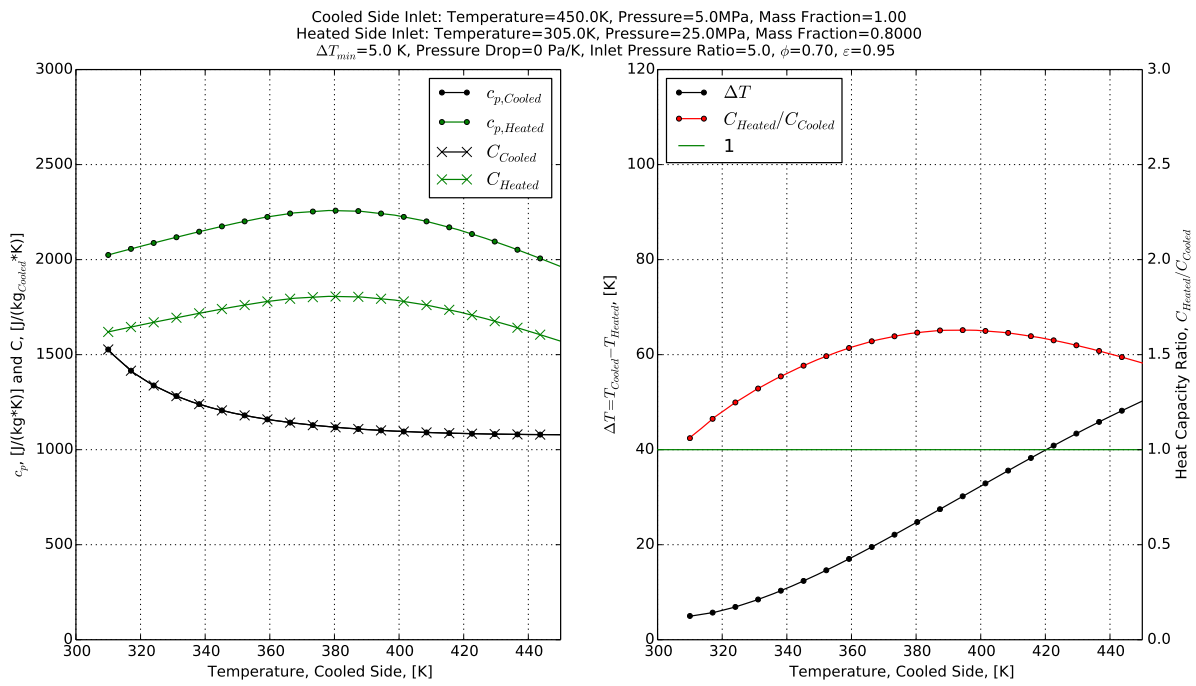


Figure A.19: Sample Heat Exchanger Solution, Mass Fraction=0.8

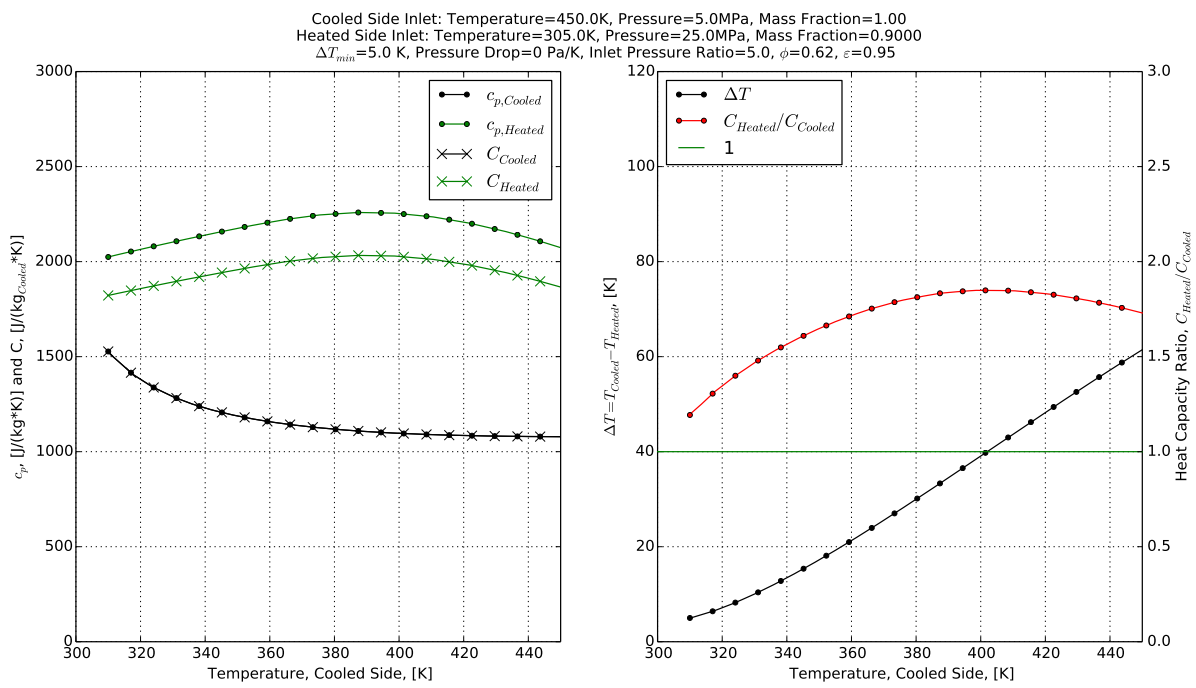


Figure A.20: Sample Heat Exchanger Solution, Mass Fraction=0.9

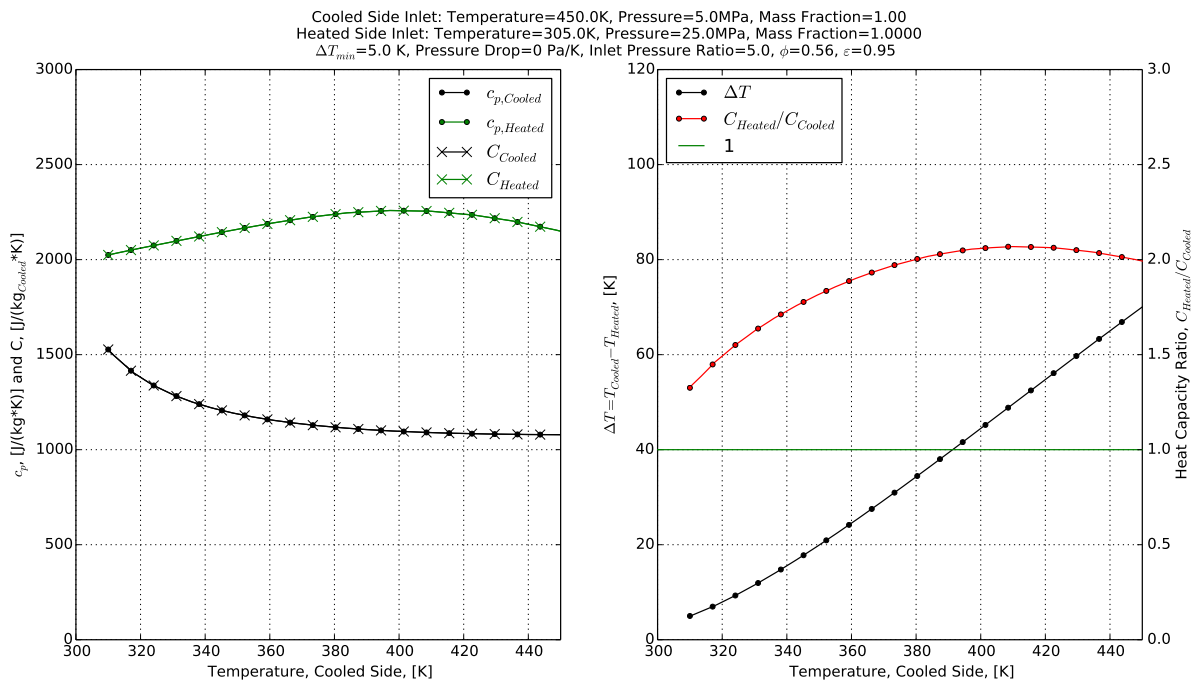


Figure A.21: Sample Heat Exchanger Solution, Mass Fraction=1.0

Appendix B

Additional Conjugate Heat Transfer Results

B.1 Case I: High Pressure Inlet $Re_{D_h}=10$, Laminar, 1m Long

Low Reference Pressure (5MPa)



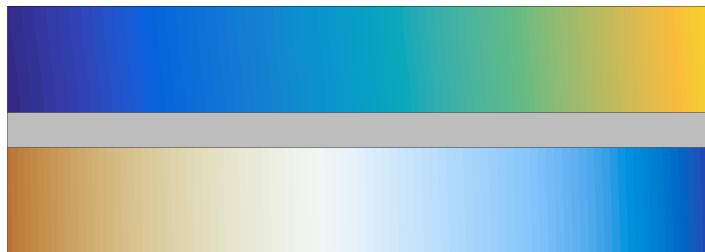
High Reference Pressure (25MPa)



Figure B.1: Case I: Specific Heat Contours



Low Reference Pressure (5MPa)



High Reference Pressure (25MPa)



Figure B.2: Case I: Total Pressure Contours

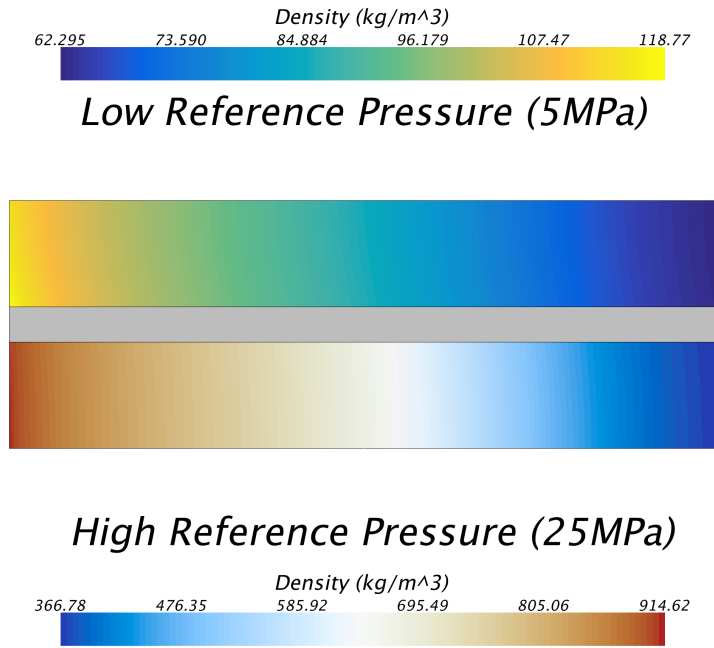


Figure B.3: Case I: Density Contours

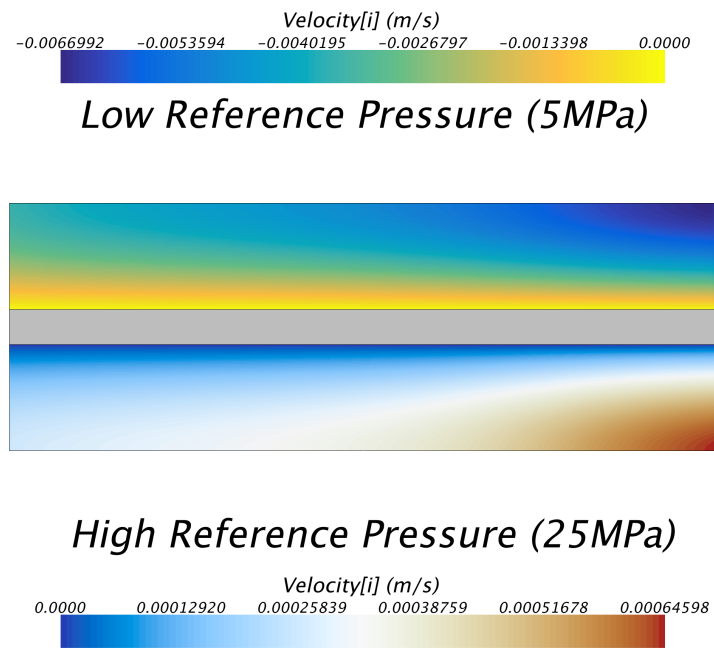


Figure B.4: Case I: Axial Velocity Contours

Dynamic Viscosity (Pa-s)
1.6876e-05 1.8264e-05 1.9653e-05 2.1041e-05 2.2429e-05

Low Reference Pressure (5MPa)



High Reference Pressure (25MPa)

Dynamic Viscosity (Pa-s)
3.2946e-05 4.5370e-05 5.7793e-05 7.0217e-05 8.2641e-05 9.5065e-05

Figure B.5: Case I: Dynamic Viscosity Contours

B.2 Case III: High Pressure Inlet $Re_{D_h}=3,000$, Turbulent, 1m Long

Low Reference Pressure (5MPa)



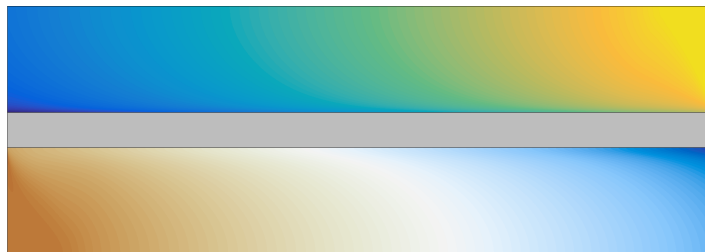
High Reference Pressure (25MPa)



Figure B.6: Case III: Specific Heat Contours



Low Reference Pressure (5MPa)



High Reference Pressure (25MPa)



Figure B.7: Case III: Total Pressure Contours

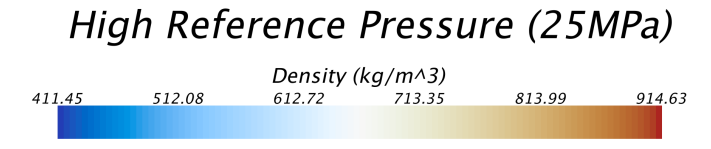
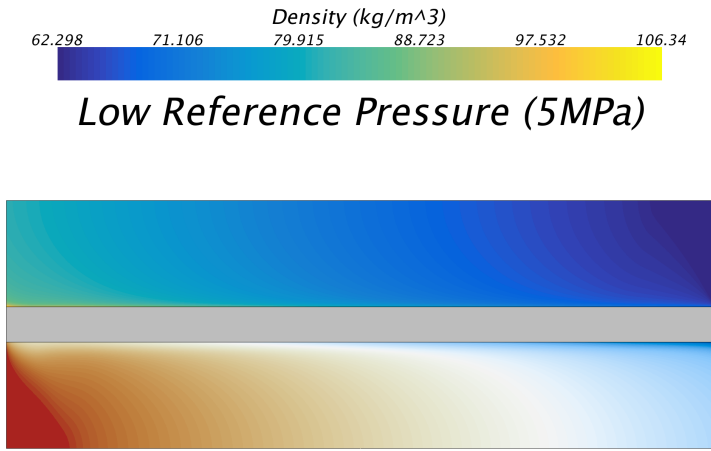


Figure B.8: Case III: Density Contours

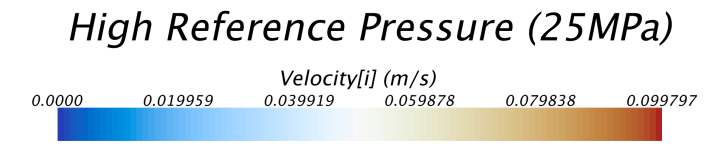
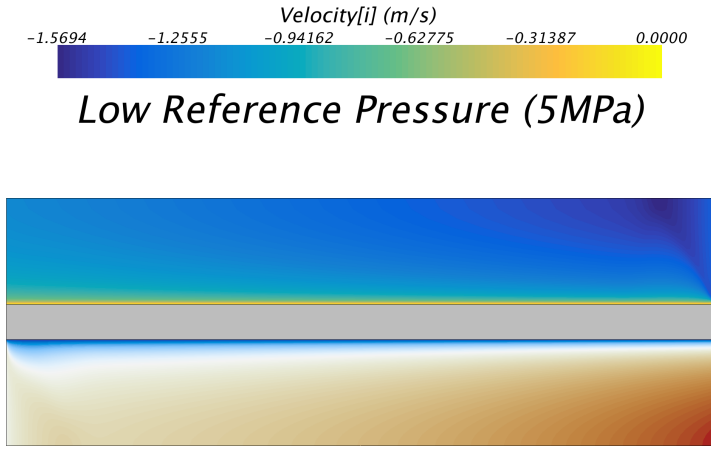
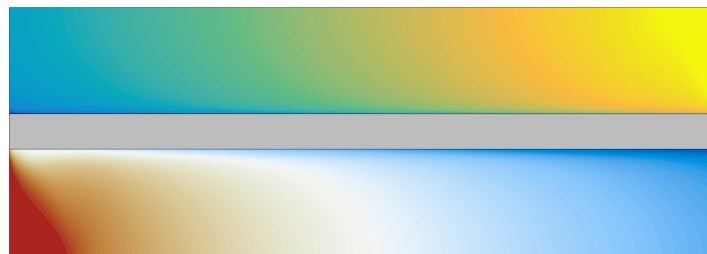
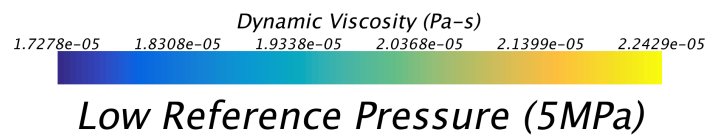


Figure B.9: Case III: Axial Velocity Contours



High Reference Pressure (25MPa)



Figure B.10: Case III: Dynamic Viscosity Contours

